UNIVERSITY OF CALIFORNIA
RIVERSIDE

Probing the Reaction Dynamics of Energetic Materials: the Influence of Physical Properties and Heat Transfer on Ignition and Combustion Characteristics

A Dissertation submitted in partial satisfaction
of the requirements for the degree of

Doctor of Philosophy

in

Chemical and Environmental Engineering

by

Yujie Wang

June 2024

Dissertation Committee:
Dr. Michael R. Zachariah, Chairperson
Dr. Bryan M. Wong
Dr. Lorenzo Mangolini

The Dissertation of Yujie Wang is approved:

Committee Chairperson

University of California, Riverside

Acknowledgements

First and foremost, I express my deepest gratitude to my advisor, Dr. Michael R. Zachariah, for his unwavering support and guidance throughout the entirety of my four and a half years in this endeavor. I extend my heartfelt appreciation to my dissertation committee members, Dr. Mangolini and Dr. Wong. Special thanks are also due to Dr. Haiyang Wang and Dr. Miles Rehwodlt for imparting the essential skills that set me on this path at the outset of my journey in the lab. I am indebted to the former and current members of Dr. Zachariah's research group, including Dr. Prithwish Biswas, Dr. Ashvin K. Vasudevan, Dr. Feiyu Xu, Dr. Yuxin Zhou, Dr. Dylan J. Kline, Dr. Pankaj Ghildiyal, Dr. Lucas Algrim, Dr. Zaira Alibay, Erik Hagen, Keren Shi, Mahbub Chowdhury, Afrida Anis, Drake Aure, and George Issac Paul, for their invaluable contributions and camaraderie. Gratitude is also extended to collaborators from other research groups, namely Emmanuel Vidales Pasos, Brandon Wagner, Dr. Lorenzo Mangolini, Dr. Yue Jiang, Dr. Xiaolin Zheng, Dr. Kelsea Miller, Quan Tran, Nicholas Jaramillo, and Dr. Michelle Pantoya. I am deeply appreciative of the financial support provided by the Office of Naval Research, Air Force Office of Scientific Research, Army Research Office, and Defense Threat Reduction Agency Materials Science in Extreme Environments, which enabled me to conduct my research at UCR. Finally, I am profoundly grateful to my family and friends, including Peiyu, Lingling, Yulong, Ruoshui, Jiyoung, Joyce, Pei, Rainie, Atefe, Shuting, Xin, Ali, Ben, Bin, Yen, and Lan, for their unwavering encouragement and support throughout this dissertation journey.

To my parents, Guanghui Wang and Huazhi Xiao, and my fiancé, Weihao Xie, for your unconditional love and constant support through this process

ABSTRACT OF THE DISSERTATION

Probing the Reaction Dynamics of Energetic Materials: the Influence of Physical Properties and Heat Transfer on Ignition and Combustion Characteristics

by

Yujie Wang

Doctor of Philosophy, Graduate Program in Chemical and Environmental Engineering
University of California, Riverside, June 2024
Dr. Michael R. Zachariah, Chairperson

Energetic materials convert chemically stored potential energy to kinetic energy through combustion. A current focus within this field is to address the constraints related to mass transfer, which hinder the rapid release of energy from solid-state energetic materials. Nanomaterials have emerged as a promising avenue for overcoming these limitations by reducing the distance between fuels and oxidizers, thereby increasing energy release rates. This dissertation focuses on understanding reaction mechanisms and combustion behavior of solid nanoenergetic composite materials by tuning chemical and physical properties of the components as well as manipulating heat transfer of the composites. Specifically, it sheds light on the crucial role of oxidizer physical properties in influencing the ignition behavior of nanoscale boron, as well as the dominant effect of physical properties of fuels and their corresponding oxides on the microscopic combustion characteristics of

composites containing different fuels. A significant portion of this dissertation focuses on tuning the energy release rate of nanoenergetic composites by manipulating heat transfer through various approaches, including: a) Altering the equivalence ratio between fuel and oxidizer, b) Decreasing agglomerate surface tension using an additive, and c) Incorporating carbon fiber to intercept and retain hot agglomerates near the burning surface. These approaches share a common objective of controlling the residence time of agglomerates on or near the burning surface, with longer residence times resulting in increased heat feedback and, consequently, higher energy release rates. Additionally, this dissertation explores the development of energetic biocidal agents using a series of metal iodates by studying their decomposition mechanisms and combustion behavior of assembled composites with nanoscale aluminum as the fuel.

Table of Contents

List of Figures

1 Introduction

1.1 General overview on energetic materials

Energetic materials refer to compounds or composites that release large amounts of chemically stored energy on a short time scale. The most common exothermic process is combustion, where a fuel and an oxidizer undergo redox reaction and release heat. Energetic materials find applications in various fields such as fireworks, demolition, space technology, mining, and automobile airbags[1–4]. They are typically classified into three main categories: propellants, pyrotechnics, and explosives. These compositions ignite when the heat released from the redox reaction surpasses the energy dissipation rate, leading to the establishment of a self-sustaining chemical reaction. The distinction between these categorizations lies in the rate at which the reactions progress after ignition. The energy release rate does not solely depend on reaction enthalpy; rather, the reaction time scale is the primary factor influencing the energy release rate. The time scale of the reaction depends on both intrinsic chemical kinetics and the diffusion rates of the reacting species. Explosives incorporate fuel and oxidizer constituents within the same molecule, reducing the mass transfer distance and increasing the diffusion rate of the reacting species, thereby significantly enhancing reactivity. Energy release in explosives occurs through detonation, generating shock waves that propagate at supersonic speeds[5]. Commonly used explosives include trinitrotoluene (TNT), cyclotrimethylenetrinitramine (RDX), cyclotetramethylenetetranitramine (HMX), and hexanitrohexaazaisowurtzitane (CL-20).

Pyrotechnics and propellants, often made of heterogenous composites of fuel and oxidizer from physical mixing, combust with a deflagration event that has lower energy release rate compared to explosives due to mass transfer limitations[2,3,6]. The black powder, consisting of a physical mixture of sulfur and charcoal as the fuel and potassium nitrate as the oxidizer, is one of the earliest documented composite energetic materials. The key distinction between pyrotechnics and propellants lies in their gas generation capabilities. Propellants reliably produce sufficient gas to sustain thrust for propelling objects, whereas pyrotechnics have limited gas release capabilities[6]. Solid-state propellants offer several advantages over liquid propellants, including ease of handling, storage stability, safety, simplicity, and high mass flow rates[3,4,6,7].

However, traditional micron-scale metal energetics suffer from slow reaction kinetics due to the relatively long diffusion length between the fuel and oxidizer[8]. A primary strategy to enhance the reactivity of metal fuel-based energetics is to decrease the particle size, which facilitates better contact and reduces the diffusion distance between the fuel and oxidizer[8–12]. The utilization of nanoscale particles has shown dramatically increased reactivity. It has been reported that incorporating aluminum nanoparticles into a composite propellant can increase the combustion rate of propellant by 5–10 times compared to traditional micron-sized particles[13]. Thermites consisting of nanoscale metals and metal oxides have demonstrated reaction rates approximately 1000 times higher than the thermites with micron-sized particles, along with significantly reduced ignition temperatures[14–16]. These materials are commonly referred to as nanothermites and metastable intermolecular composites (MICs)[17].

1.2 Combustion mechanism of metal particles

From the perspective of energy release during combustion, fuels with high energy density, both in terms of weight and volume, are beneficial in terms of both economy and energy efficiency. Despite having a high energy release rate, explosives often exhibit lower energy density and no stoichiometric control compared to metal fuels[6]. Figure 1-1 demonstrates that metal fuels, such as Al, B, Ti, Mg, Si, have much higher volumetric and gravimetric energy density compared to the commonly used monomolecular compounds. The oxidation and combustion mechanism of these metal particles have been widely studied. Commercial metal particles have a passivating oxide shell. The distinct physical and chemical properties of these oxide shells and metallic cores lead to significantly different combustion mechanisms. For example, while the cores of Al and Mg particles melt and vaporize at relatively low temperatures, their oxide shells exhibit high-temperature resistance[18–22]. In contrast, the core of B particles remains solid while its oxide shell melts at a relatively low temperature[23–25]. For Si and Ti particles, both the oxide shells and the cores maintain resistance to phase changes until exposed to high temperatures[26–32].

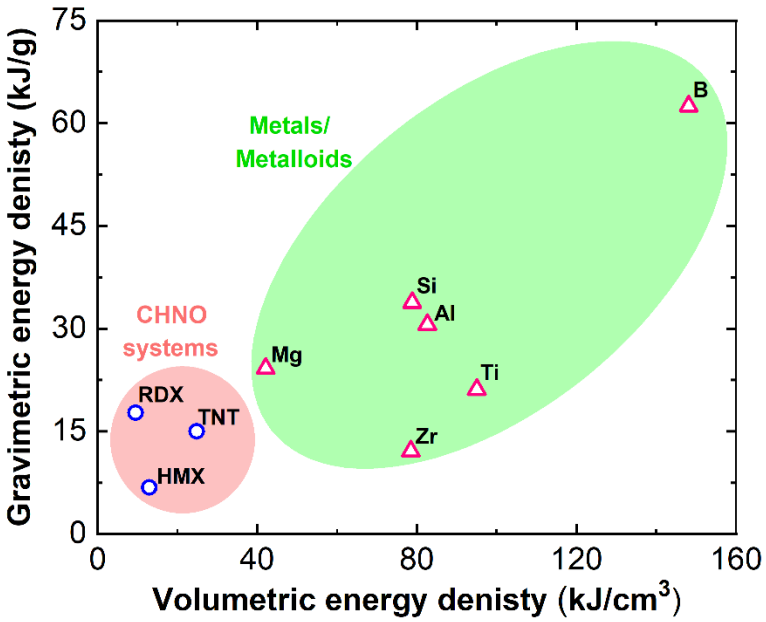

Figure 1-1 Gravimetric and volumetric energy density of metals and monomolecular compounds.

Among all the metal fuels listed in Figure 1-1, Al has received the most thorough investigation because of its availability, low cost, high energy density, and favorable ignition properties[33–35]. Aluminum has been widely utilized as an additive to rocket propellant for improving specific impulse and enhancing combustion stability[20,36]. For example, the incorporation of aluminum in solid propellants has the capability of increasing the specific impulse by as much as 15%[33].

Aluminum combustion in air suggests that it burns as a vapor, and the combustion process is governed by the diffusion of both the fuel and oxidizer[22]. Combustion of Al particles produces aluminum oxide smoke resulted from the combustion of Al vapor[20]. The ignition process of aluminum particles initiates with a relatively brief phase of heterogeneous combustion, which rapidly transitions into a quasi-steady diffusion flame[37].

Figure 1-2 (a) shows the heterogenous oxidation mechanism of nanoscale aluminum at low heating rate developed by Dreizin and coworkers[38]. This mechanism suggests that the phase transition of the alumina shell into different polymorphs at elevated temperatures may result in the formation of cracks or discontinuities in the shell. These cracks or discontinuities in the shell enable rapid diffusion of gaseous oxygen to reach the Al core, thereby facilitating oxidation[38]. Other studies have proposed an alternative Al particle oxidation mechanism based on experimental observation and molecular dynamics simulation that Al particle becomes hollow at elevated temperatures (Figure 1-2 (b))[13,39]. These studies have suggested that the difference in charge density between the inner and outer surfaces of the oxide shell suggests the induction of an electric field, which prompts aluminum cations near the core/shell interface to migrate towards the outer surface, where they come into contact with oxygen and undergo oxidation[13,39]. They have also concluded that the diffusivity of aluminum cations through the oxide shell is significantly higher than the diffusion rate of oxygen anions towards the core. Therefore, both the inward diffusion of oxygen and the outward diffusion of aluminum collectively contribute to the oxidation process of aluminum particles.

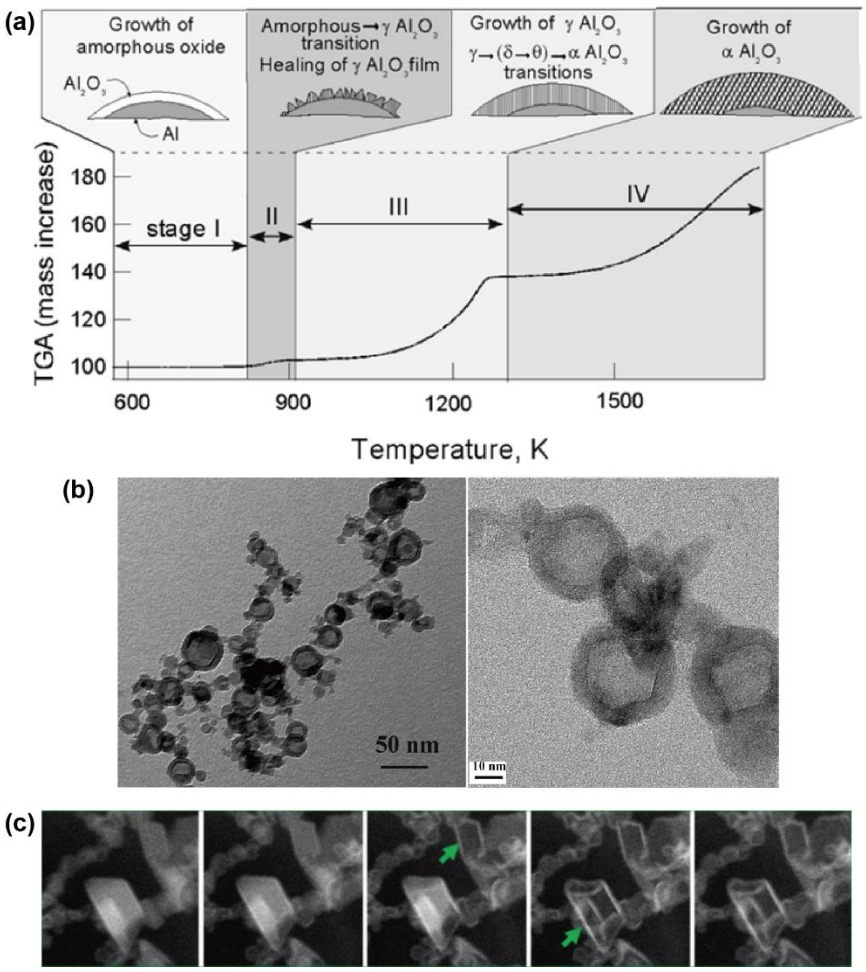

Figure 1-2 Schematic of the proposed oxidation of aluminum particles (a)[38] (*Reproduced with permission from Taylor & Francis*). TEM images of hollow Al nanoparticles after oxidation (b)[13] (*Reproduced with permission from Taylor & Francis*). TEM images of hollowing process of Mg nanoparticles from in-situ heating (c)[18]. (*Reproduced with permission from American Chemical Society*).

Similar to aluminum, magnesium also undergoes combustion in the vapor phase. However, a notable difference arises due to the extremely high vapor pressure of magnesium at relatively low temperatures. This high vapor pressure results in the complete vaporization of the magnesium core in magnesium nanoparticles through the porous magnesium oxide shell at ~900 K and leads to the oxidation of magnesium vapor in the gas

phase (Figure 1-2 (c))[18]. Furthermore, the rapid sintering of Al nanoparticles before oxidation results in the loss of nanostructure, which compromises the oxidation and energy release kinetics. In contrast, the combustion of magnesium initiated in the vapor phase with most oxidizers should eliminate sintering due to rapid vaporization. Therefore, magnesium nanoparticles have significantly faster oxidation kinetics and more complete energy extraction compared to aluminum nanoparticles[18].

Among all the metals listed in Figure 1-1, boron (B) stands out due to its significantly higher volumetric and gravimetric energy density compared to other metal fuels. However, unlikely aluminum and magnesium, boron suffers from low ignitibility and slow oxidation kinetics due to its native oxide shell, boron oxide (B_2O_3), which has a low melting point (723 K) and a high boiling point (2130 K) [24,40–45]. These temperatures are lower than the melting point (2349 K) and boiling point (4200 K) of boron. Therefore, the solid boron core is covered by a liquid shell during oxidation when the temperature is lower than 2130 K. This liquid oxide layer lacks physical voids and acts as a barrier for oxygen or boron diffusion, consequently impeding reactivity [24,40–45]. Further oxidation and full-fledged combustion of boron particle occurs when the oxide shell is completely removed, and the bare boron reacts heterogeneously with the surrounding oxidizer[24,41,46,47]. These two stages are generally referred to the two stages of boron particle combustion. During the first stage, the oxidation rate of boron particle is limited by the diffusion of reacting species through the liquid oxide shell. While during the second stage, the oxidation rate is limited by the reaction of bare boron with the gaseous oxidizer. Another limiting factor for extracting the energy from boron is the reduced energy release from boron

combustion in gases containing hydrogen due to the thermodynamically favored formation of HOBO. This compound "traps" boron, preventing it from forming gaseous B_2O_3 and releasing its full potential energy[41,48].

Similar to B, the oxidation of Ti and Si takes place in the condensed phase and oxygen must diffuse through the oxide shell to react with the metallic core[26,27,29]. However, the melting point of the oxide shell of Ti and Si is significantly higher than that of B, leading to difference in oxidation mechanism. The oxide shell of Ti contains high concentrations of oxygen vacancies as Ti has multiple oxidation states. These vacancies promote oxygen diffusion through the oxide shell. Consequently, Ti has the lowest ignition temperature in gaseous oxidizers among these commonly used metal fuels. However, unlike Al and Mg, the Ti core cannot melt or vaporize and react with oxygen ions on the metal oxide surface, it has poor reactivity with condensed phase oxidizers[29,31,49]. The oxide shell of Si nanoparticles contains less oxidation vacancies and melts at a lower temperature than that of Ti nanoparticles, therefore the oxidation kinetics of Si nanoparticle is inhibited[26].

Overall, the different physical properties of these metal fuels and their corresponding oxides dictate their distinct oxidation mechanisms and energy release rates. It has been demonstrated that manipulation of the oxide shell to increase the vacancies for enhancing oxygen diffusion or break the continuity of the liquid oxide shell favors the oxidation kinetics. For example, the reactivity of B particles has been shown to increase by coating them with fluorides, oxides, and polymers[50–54]. Additionally, it has demonstrated that pre-stressed aluminum nanoparticles exhibit increased reactivity attributed to

accelerated ion migration through the surface under tensile strain[55]. Apart from these, tunable energy release rates can be achieved by mixing different metal nanoparticles in energetic composites. For instance, it has been shown that the combination of B and Al nanoparticles with copper oxide (CuO) exhibits higher reactivity compared to compositions containing only B/CuO or Al/CuO[17].

1.3 Assembling fuel and oxidizer particles in polymer matrices

Nanoscale metal fuels and oxidizers have demonstrated enhanced reactivity compared to their micron size counterparts due to improved contact and reduced diffusion distance with oxidizers[8–11]. The most straightforward method to achieve an intimate mixture between the nanoscale fuels and oxidizers is by physically mixing the nanoparticles[56]. However, the direct usage of nanothermite as loose powder in practical applications, such as propellants, is impractical due to the high impact, friction, and electrostatic discharge sensitivities associated with the physically mixed nanothermites. These sensitivities can lead to the uncontrollability and irreproducibility, rendering the approach unsuitable. Hence, there is a need to develop techniques for fabricating compact composites with reproducible characteristics. Traditional casting methods used for fabricating solid propellants suffer from long processing times and restriction in the types of architectures that can be achieved. These limitations have motivated the exploration of alternative techniques to assemble thermites into polymer matrices, with additive manufacturing techniques such as electro-spraying, electrospinning, and direct ink writing (3D printing) being investigated (Figure 1-3 (a))[56–61]. Among these techniques, 3D printing stands out as the most ubiquitous due to its simplicity, higher productivity, greater control,

higher compatibility with nanothermites employing a variety of polymers[6,58,62–66]. Therefore, 3D printing has been widely employed to fabricate free-standing propellants and pyrotechnics (Figure 1-3 (b)).

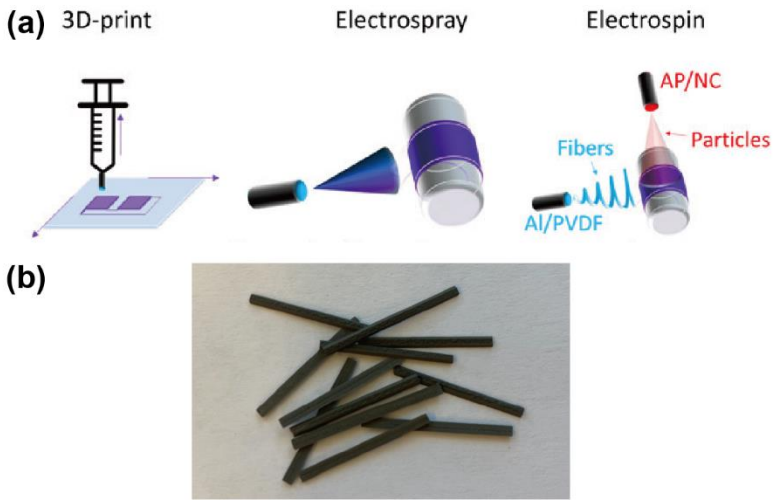

Figure 1-3 Different additive manufacturing techniques for fabricating polymer composites of metal and metal oxides (a) [58]. (*Reproduced with permission from American Chemical Society*) A photo of free-standing energetic stands from 3D printing (b).

While the reactivity of metal-based energetic materials improves with the utilization of nanoscale particles, the nanostructure of metal nanoparticles is often compromised by sintering and agglomeration before or during the combustion process. The exothermic nature of oxidation reactions results in a temperature rise, promoting the tendency of nanoparticles to agglomerate and sinter together[67]. Combustion of particles within the size range of 30-100 μm typically follows the d^2-law (diffusion-limited burning). As the size reduces to ~10 μm, the combustion of particles transitions to follow the d-law (kinetics-limited burning). However, the burn time of nanoscale particles is nearly independent of the particle size ($\sim d^{0.3}$), significantly deviating from the kinetically controlled mechanism[35,67]. In-situ TEM heating studies on nanoscale aluminum at high

heat rates (~10^6 K/s) revealed the loss of nearly 80% of the nanoparticle surface area due to sintering[67,68]. These studies also demonstrated that the sintering time of nanoscale aluminum (~50 ns) is lower than the reaction time (~10 μs), which indicates that aluminum nanoparticles sinter before the main combustion event[5,67–69]. Consequently, the advantages of having a high surface to volume ratio of nanoparticles are negated by sintering and agglomeration.

Sintering and agglomeration are also frequently observed with in-situ imaging techniques during the propagation of energetic composites. For instance, as displayed in Figure 1-4 (a), agglomerates with sizes ranging in the hundreds of microns are noticeable during the combustion of aluminum-based solid propellant with ammonia perchlorate (AP) as the oxidizer[36]. More recently, Wang et al have observed the sintering process using high-speed microscopic imaging during the propagation of nanothermite (Al/CuO) composite[61].

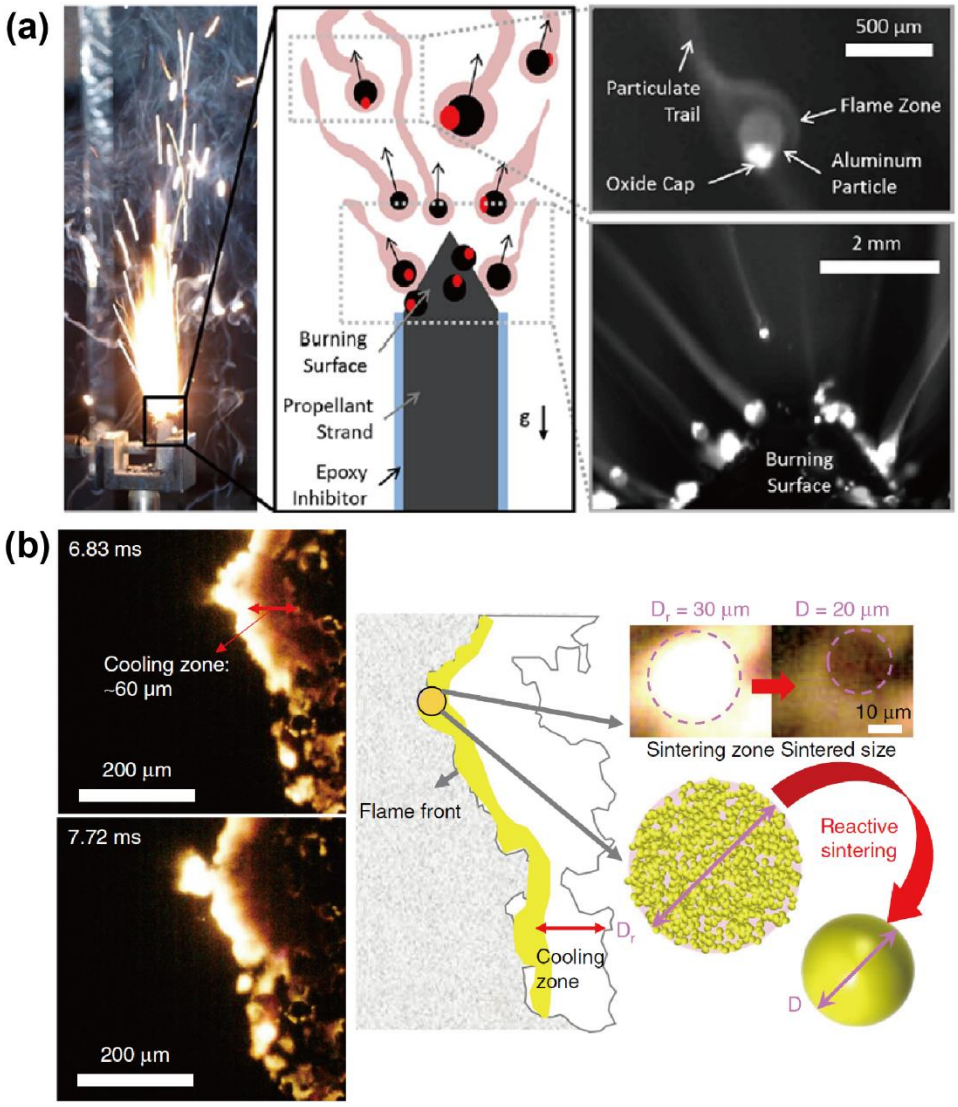

Figure 1-4 Aluminum particle combustion and agglomeration of a propellant strand (a)[36]. Snapshots of burning flame front showing sintering (left) and schematic showing sintering (right) (b) [61]. (*Reproduced with permission from Elsevier and Springer Nature*)

Various methods have been explored to mitigate the sintering and agglomeration of nanoparticles during combustion. One effective approach involves assembling nanothermites into mesoparticles with a gas generating polymer binder (e.g. nitrocellulose, NC), which has been shown to enhance reactivity by reducing the sintering of aluminum nanoparticles[56,57,70]. The significant gas generation from NC at relatively low temperatures

contributes to the disintegration of soft agglomerates before or during the combustion events. Similarly, Wang et al employed an unzipping polymer capable of generating substantial gas at low temperatures to mitigate the sintering of 3D printed energetic composites. Their findings revealed a nearly tenfold increase in burn rate compared to the composite containing binders with minimal gas generation[71]. Additionally, Sippel et al observed that substituting aluminum particles with mechanically activated composite particles (aluminum/polytetrafluoroethylene, Al/PTFE) in solid propellants results in smaller burning metal particles[33].

1.4 Role of heat feedback on the propagation of energetic materials

Heat transfer plays a critical role on the combustion performance of an energetic material. For steady propagation, sufficient heat transferred from the flame back to the nearby unreacted material is essential[72–76]. Higher amounts of heat feedback have been shown to enhance burn rate and energy release rate of energetic systems[33,77,78]. Thermal theories regarding pre-mixed laminar flames argue that the primary mechanism governing flame propagation is the heat transfer through layers of gas. This involves the conduction of heat from the reaction zone, which is required to elevate the unburned gas temperature to the ignition temperature[79]. It is deduced that the velocity of steady-state propagation can be expressed as Equation (1).

$$v \sim \sqrt{\alpha \cdot \dot{\omega}} \tag{1}$$

where v is the propagation rate, α is the thermal diffusivity, and $\dot{\omega}$ is the reaction rate[79]. This implies that the propagation rate depends on the rate at which heat is released from

the reaction ($\dot{\omega}$), and how rapidly this heat can be transferred to the unburned gas (α). Although Equation (1) was originally formulated for gas phase combustion, prior research has shown that this theory can be extended to the solid-state composites[80–82]. The incorporation of materials possessing high thermal diffusivity into solid propellants to regulate combustion performance has a lengthy historical precedent[83]. Caveny et al. documented a notable enhancement in the burn rate of a solid propellant upon the introduction of a wire with high thermal diffusivity[80]. Subsequently, wires have been extensively employed to customize the burn rate of solid propellants[84–86].

Other strategies for enhancing heat feedback in solid-state composites have been explored beyond manipulating thermal diffusivity. For instance, the incorporation of carbon fibers into solid composites serves to intercept detached hot agglomerates near the burning surface, thereby promoting heat feedback. This inclusion of carbon fibers has been shown to significantly increase burn rates[77,78]. In a separate study, Sippel et al. found that the prompt ignition of agglomerates at the burning surface enhances heat feedback and pressure sensitivity[33]. Additionally, Kline et al. demonstrated that the addition of an oxidizer with significant metal condensation provides a pathway for improved heat feedback and promotes the steady propagation of a composite with minimal metal condensation[75].

Recent investigations, however, present a contrasting phenomenon that the inclusion of materials with low thermal diffusivity can enhance the burn rate of solid-state energetic composites[83,87,88]. Additionally, modeling studies on solid-solid combustion indicate that a lower thermal diffusivity in a composite results in a higher burn rate[89,90].

This can be attributed to the improved concentration of heat generated during the reaction in the adjacent unreacted layer. Thus, more of the energy is used for igniting the adjacent reactants rather than diffusing far ahead into the unreacted zone[89]. These studies suggest that the thermal theories of pre-mixed laminar flame may not be applicable to the solid energetic composites.

1.5 Development of energetic biocidal agents

Throughout history, humanity has faced threats from viruses and bacteria, with the emergence of biological weapons presenting new challenges to global security. Therefore, the development of effective biocidal agents is imperative to safeguard human health. Halogen-containing fungicides, including chlorine-based compounds and HF, have demonstrated high efficacy in neutralizing bacteria[91]. However, their application is limited due to potential instability and toxicity concerns. Unlike other elements, iodine possesses unique properties, as it can eradicate microorganisms without harming the environment[91]. Iodine can penetrate the cell walls of microorganisms and interact with cellular nucleic acids and react with thiol groups in enzymes and proteins, disrupting their structure and rendering them inactive[92]. Iodine has proven to be exceptionally effective as a biocidal agent, achieving a 99.999% kill rate for certain viruses and bacteria in just 10 minutes at 25 °C with concentrations below 15 ppm[93]. Nevertheless, the direct application of molecular iodine as a biocidal agent poses challenges due to its sublimation at room temperature, driven by its high vapor pressure. Furthermore, traditional biocidal agents containing halogen-based disinfectants often face inefficiencies in large-scale microorganism deactivation within short timeframes[91].

An alternative approach to deactivate microorganism involves applying a thermal pulse, often utilizing energetic materials[92]. However, this approach may lead to incomplete deactivation due to the transient nature of the thermal pulse as well as the potential non-uniform delivery of heat across the target area[92,94]. Taking into consideration the pros and cons of using halogen-containing fungicides and thermal pulses, the concept of agent defeat weapons (ADWs) has been proposed[93,95]. ADWs deliver a thermal pulse and remain active for an extended period of time afterward from the release of large amounts of strong biocides. Therefore, there is a focus on energetic materials with both high energy density and high iodine content.

Nanothermites offer significant advantages for use in ADWs, owing to their high energy density and high tunability. Incorporating molecular iodine into energetic materials is a direct and effective strategy in the development of ADWs. Recent studies have investigated the combustion behavior and biocidal efficacy of composites containing molecular iodine, prepared through mechanical milling[96–100]. However, these composites exhibit instability during long-term storage and require the incorporation of an additional oxidizer for combustion to occur, which means the overall energy density is compromised by adding molecular iodine to the composites. I_2O_5 emerges as a promising candidate due to its high oxygen and iodine content, as well as its strong oxidizing properties. Several studies have explored the energy release of energetic composites containing I_2O_5, along with their effectiveness in deactivating spore-forming bacteria[101–103]. Nonetheless, the hygroscopic nature of I_2O_5 poses significant challenges to its practical application, prompting further exploration of iodine-containing oxidizers suitable for use in ADWs.

Ideally, the sought-after material would engage in a highly exothermic redox reaction, possess a high iodine content, release molecular iodine, be easy to handle, and exhibit long-term stability for storage[92].

1.6 Motivation and research outline

1.6.1 Effect of physical properties on ignition behavior and combustion characteristic

Nanoscale metal and metalloid particles, such as aluminum, boron, silicon, titanium, magnesium, and zirconium, attract significant attention in the field of energetic materials due to their high energy density[18,27,29,50,71,104]. Boron has the highest high gravimetric and volumetric energy content among these fuels, as shown in Figure 1-1. However, boron suffers from slow oxidation kinetics due to the low melting point (723 K) and high boiling point (2130 K) of its oxide shell (B_2O_3). At relatively low temperatures during combustion, the B_2O_3 melts into a liquid shell that lacks physical voids. The diffusion of reacting species is significantly limited by this liquid barrier, which leads to the low reactivity and long ignition delays[24,40,43,105].

Various methods have been explored to improve the reactivity of boron and lower the ignition temperature and ignition delays. One straightforward method is to remove the surface oxide layer by dissolving it away. Chintersingh et al found that washing with acetonitrile can effectively remove the surface oxide of boron powders and shorten the ignition delays[106]. However, this approach only removes the initial oxide shell of boron particles and lacks control over newly formed oxide from the oxidation of boron. Another

effective approach to improve oxidation of boron is to coat the boron surface with compound that can potentially interact with B_2O_3 or produce heat to boil off B_2O_3[107]. This approach involves coating or mixing boron particles with metal such as magnesium and lithium[108–111], metal hydrides[112], metal fluorides[50], metal oxides[51], and polymers[54,113]. Alternative methods to enhance the ignition and combustion performance of boron include the utilization of various solid-state oxidizers, such as binary metal oxides[42,114], metal oxides with oxygen vacancy[115,116], and fluorinated compounds[41,117–119]. However, the effect of physical properties of these oxidizers on the boron ignition and combustion is not well understood. In addition, the aforementioned approaches to improve boron ignition or combustion often result in the reduction in energy density, making it challenging to improve boron combustion without compromising energy density. Hence, there is motivation to study the ignition mechanism of boron with oxidizers that have high oxygen content.

In Chapter 3 of this dissertation, a systematic study of the ignition mechanism of nanoscale boron with alkali metal perchlorates ($LiClO_4$, $NaClO_4$, and $KClO_4$) and iodates ($LiIO_3$, $NaIO_3$, and KIO_3) is described. Boron combined with perchlorates and iodates demonstrates higher energy density compared to boron combined with other commonly used oxidizers like CuO and Fe_2O_3. Significant differences in ignition behavior are observed among boron combined with different alkali metal perchlorates, although the chemical reaction between boron and these oxidizers are very similar. Specifically, B/$LiClO_4$, B/$NaClO_4$ ignite, whereas B/$KClO_4$ does not, as shown in Figure 1-5 (a). The heat generated from the reaction between boron and $LiClO_4$ and $NaClO_4$ promotes further

decomposition of $LiClO_4$ and $NaClO_4$, whereas this effect is absent for B/$KClO_4$. Similarly, for boron with alkali metal iodates, B/$LiIO_3$ and B/$NaIO_3$ ignite while B/KIO_3 does not (Figure 1-5 (a)). Additionally, there is a notable increase in decomposition observed for $LiIO_3$ and $NaIO_3$ resulting from the reaction between B and $LiIO_3$ and $NaIO_3$, whereas there is minimal promotion for further decomposition of KIO_3 from B/KIO_3.

Analysis of the decomposition process of the alkali metal perchlorates and iodates reveals the presence of temperature gap between melting and decomposition onset of $LiClO_4$, $NaClO_4$, $LiIO_3$, and $NaIO_3$, respectively, while $KClO_4$ and KIO_3 melt and decompose concurrently. I have found that the larger interval between melting and decomposition provides more time for the oxidizer to melt and envelop the boron nanoparticles, facilitating better contact. Consequently, boron nanoparticles have immediate access to oxygen once the oxidizer decomposes, results in vigorous ignition (Figure 1-5(b)). Whereas for oxidizers that melt and decompose concurrently, there is little time for the oxidizer to envelop the boron nanoparticles before decomposition. This implies that although oxygen release occurs near the boron particles, only boron nanoparticles with intimate contact with the initial oxidizer particles have instant access to oxygen, resulting in a small ignition event (Figure 1-5(b)). These findings reveal the significance of physical properties of oxidizers in the ignition of metal fuels.

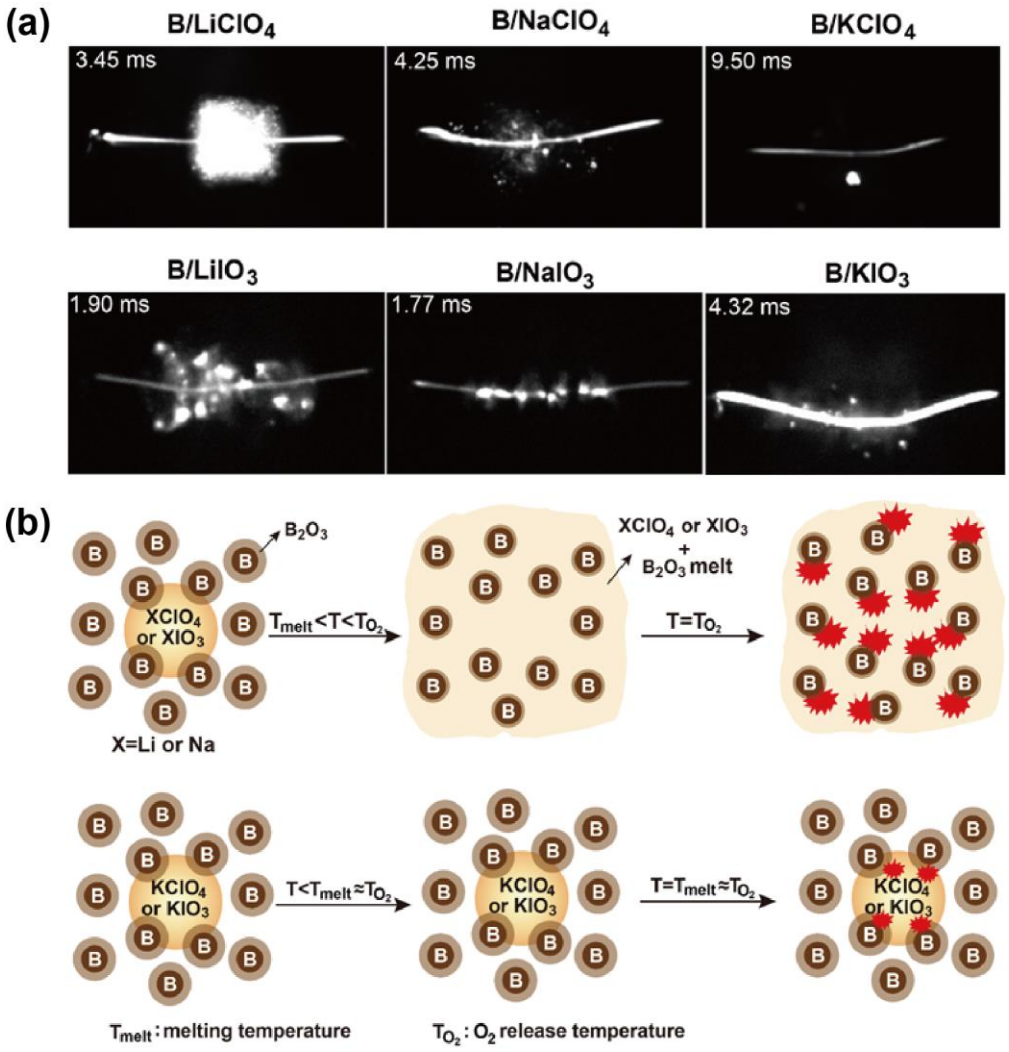

Figure 1-5 Ignition snapshots of B with different alkali metal perchlorates and iodates (a). Proposed mechanism explaining the relationship of ignition behavior and temperature difference between melting and decomposition (b)[23]. (*Reproduced with permission from Elsevier*)

Sintering and agglomeration are commonly observed prior to or during combustion and negate the advantages of using nanoscale particles, as discussed earlier. Aluminum is commonly employed as the primary fuel in solid propellants, while boron, with its high energy content, and titanium serve as alternative fuel sources[24,29]. Chapter 4 investigates the combustion characteristics of high loading composites with nanoscale aluminum, boron,

and titanium as the fuel and $KClO_4$ as the oxidizer. $KClO_4$ is selected as the oxidizer due to its potential for minimal interaction with the fuel agglomerates during combustion, as its decomposition products are gaseous at the temperature of interest. I have found that the combustion characteristics are heavily dependent on the fuel type. For instance, mobile droplets with dark caps form on the burning surface of composite with aluminum as the fuel. These droplets coalesce and grow before departing the burning surface. While for the composites of boron and titanium as the fuel, fractal-shaped agglomerates form on the burning surface (Figure 1-6 (a))[28]. The difference in combustion characteristics between boron and titanium lies in the higher tendency of the fractal-shaped agglomerates to transition to a more spherical shape for titanium compared to boron. The agglomerates observed in composites containing all three fuels are notably larger than the initial nanoscale particles used in their preparation, indicating substantial sintering and agglomeration during combustion.

The combustion characteristic of these composites are attributed to the physical properties, e.g. melting and boiling points, of the fuels and their corresponding oxides. For aluminum, the temperature of the droplets exceeds both the melting point of aluminum and aluminum oxide, leading to the formation of molten droplets. In contrast, for boron, the temperature of the agglomerates falls between the melting and boiling points of B_2O_3, while remaining lower than the melting point of boron itself. Consequently, although boron oxide exists in a liquid state, the boron core remains solid, resulting in the formation of fractal-shaped agglomerates. Regarding titanium, the measured temperature of the agglomerates is slightly above the melting point of both titanium and TiO_2, indicating a

potential transition into molten droplets. However, the agglomerate temperature remains below the melting point of Ti_2O_3, which forms at the interface of titanium and TiO_2, thereby explaining the retention of the fractal-shaped morphology. I have also observed that the agglomerates remain on the burning surface for a certain duration before detaching, and their surface residence times vary from ~1.5 ms to ~4 ms. Interestingly, these surface residence times are shorter than their theoretical burn times, indicating that the agglomerates continue to burn after separating from the burning surface. This observation aligns with the experimental findings depicted in Figure 1-6 (b)[28]. In summary, Chapters 3 and 4 provide mechanistic insights into how the physical properties—such as melting and boiling temperatures—of both fuel and oxides influence the ignition and combustion behavior of energetic materials.

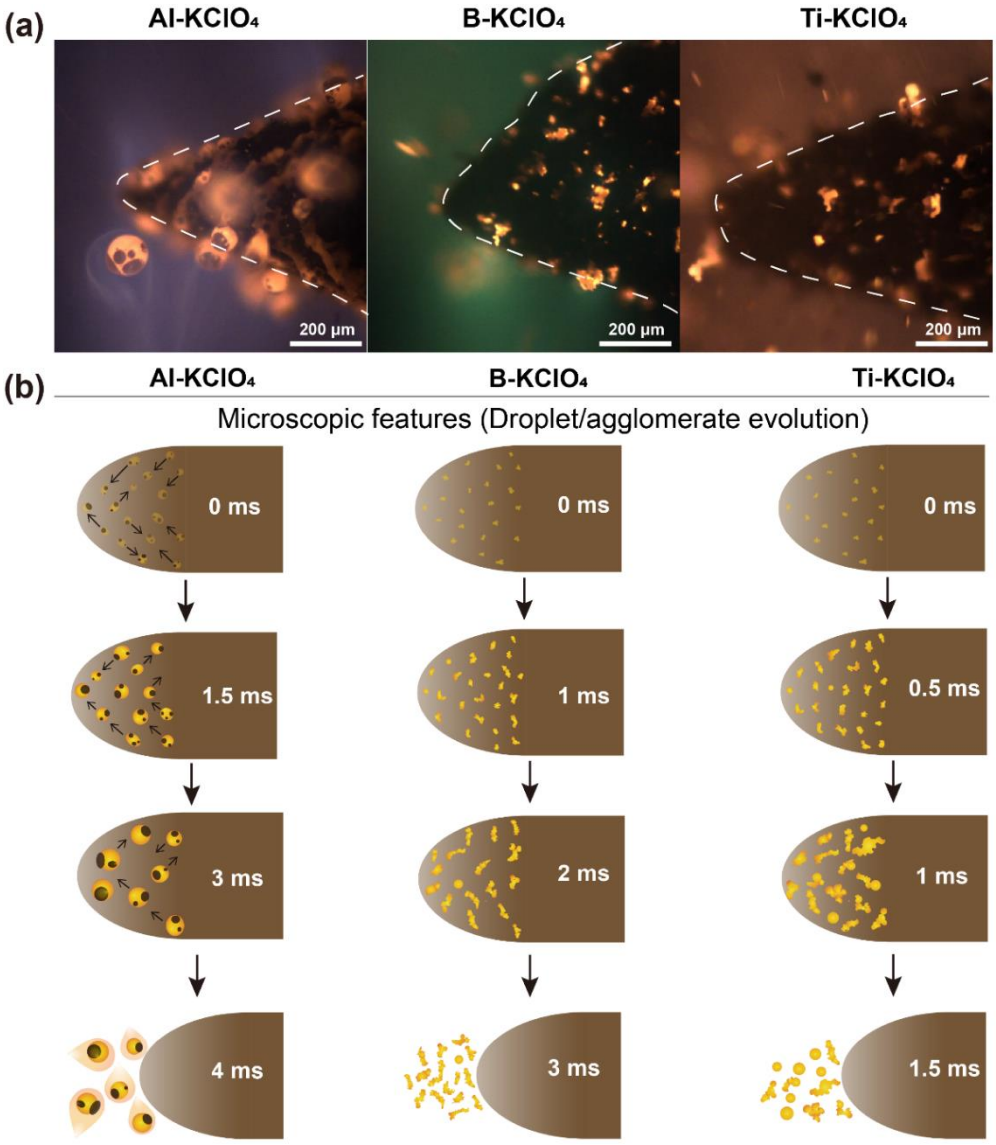

Figure 1-6 Microscopic imaging snapshot of combustion characteristics (a) and illustration of combustion characteristics (b) of Al-$KClO_4$, B-$KClO_4$, and Ti-$KClO_4$[28]. (*Reproduced with permission from Elsevier*)

1.6.2 Tuning the energy release rate of energetic composites by manipulating heat feedback

Sufficient feedback from the flame or reaction front to the unreacted materials is essential for the steady propagation of an energetic material[72–76] and it has been

demonstrated that higher amounts of heat feedback can increase the energy release rate of energetic materials[33,77,78]. These findings prompt a fundamental question: How can heat feedback be manipulated to adjust the energy release rate of an energetic system? The research conducted in this dissertation has addressed this question by presenting three distinct approaches (Chapters 5-7) for manipulating heat feedback to tune the burn rate and energy release rate of energetic composites.

Convection, conduction, and radiation constitute the three primary mechanisms of heat transfer. For the research conducted in this dissertation for manipulating heat feedback (Chapters 5-7), the combustion tests of all the energetic composites are performed within a vented chamber maintained at approximately the atmospheric pressure. Prior research has shown that radiative heat feedback is insignificant for a propellant propagating under atmospheric pressure conditions. Therefore the effect of radiative heat feedback can be disregarded[73,74,76,120].

Convective heat transfer can be subdivided into two categories: convection of gases and convection resulting from the movement of condensed phase material[73,121–123]. A previous study by Egan et al. found that convective heat transfer alone was inadequate to maintain combustion for a thermite (Al/CuO) propagating within a narrow channel[73]. It was further inferred that convective heat transfer should be proportionate or even diminished for other thermite systems, considering that Al/CuO is among the thermite compositions with the highest amount of gas generation[73]. Moreover, the combustion experiments conducted in this dissertation take place within a chamber with a cross-sectional area that is several orders of magnitude larger than that of the composites.

Consequently, convective heat transfer is significantly lower compared to the study by Egan et al.[73] due to the lack of confinement. Therefore, the convection of gases can be neglected for the composites investigated in this dissertation. A significant contribution to the overall heat feedback to sustain propagation of Al/CuO in the study by Egan et al. was the movement of hot solid and molten material[73], which was also suggested by other studies[122,123]. However, I have not observed the movement of burning particles back to the unburnt materials after their departure from the burning surface for the research conducted in this dissertation (Chapters 5-7). This is likely attributed to the lack of confinement in the chamber used for testing the composites. Therefore, it is improbable that convective heat feedback plays a dominant role in the propagation of these composites.

The remaining heat transfer mechanism is conduction, the significance of which has been suggested previously. For instance, a study by Brewster et al. reported that more efficient heat transfer from the agglomerates during their residence on or near the propellant surface leads to an enhanced burn rate of solid propellant[72]. Chapters 5-7 of this dissertation provide three distinct approaches for manipulating conductive heat feedback to tune the energy release rate of energetic composites.

Chapter 5 introduces one of the approaches to manipulate conductive heat feedback, which involves tuning the equivalence ratio between the fuel and oxidizer of the composite. I have prepared aluminum/ammonium perchlorate (AP) composites with different equivalence ratios (φ=0.5, 1, and 2). All three composites propagate in an inert environment, with the formation of molten droplets occurring on the burning surface. The

droplet size from composites with an equivalence ratio of 0.5 and 1 are similar, whereas the droplet size is significantly larger for the composite with an equivalence ratio of 2.

One would anticipate that the composite with an equivalence ratio of 1 should exhibit the highest burn rate based on energy density considerations. Indeed, the composite with an equivalence ratio of 1 demonstrates a higher burn rate compared to that of an equivalence ratio of 0.5, aligning with expectations. However, the measured burn rate of the composites increases as the equivalence ratio increases from 1 to 2, contrary to initial expectations, as illustrated in Figure 1-7 (a). This unexpected trend in burn rate between the composites with equivalence ratios of 1 and 2 is attributed to differences in agglomerate residence time. The composite with an equivalence ratio of 2 exhibits significantly longer agglomerate surface residence time than that of an equivalence ratio of 1, resulting in considerably more conductive heat feedback to unburnt materials. This notably higher heat feedback offsets the burn rate decrease resulting from lower energy density, ultimately leading to a higher burn rate.

Chapter 6 explores another method for manipulating heat feedback, focusing on tuning agglomerate surface tension. Aluminum/potassium perchlorate ($KClO_4$) composites with varying silicon contents were fabricated for this purpose. Silicon is selected as the additive to manipulate the agglomerate surface tension due to the similar energy density between Si/$KClO_4$ and Al/$KClO_4$, miscibility of Al and Si at the relevant temperature, and the lower surface tension of molten Si compared to Al at the same temperature[124]. I have found that the addition of Si slightly increases the agglomerate size with minimal impact on the agglomerate temperature. However, the lower surface tension of Si leads to the

decreased surface tension of the agglomerate, resulting in a reduced droplet growth rate. Consequently, the inclusion of Si extended the agglomerate residence time on the burning surface, as depicted in Figure 1-7 (b), thereby enhancing conductive heat feedback and ultimately resulting in higher burn rates and energy release rates.

Chapter 7 demonstrates the third approach for manipulating heat feedback, which involves utilizing carbon fiber (C.F.) as an additive to intercept agglomerates near the burning surface, thereby increasing the heat feedback. The loss of nanostructure prior to or during the combustion diminishes the benefits of using nanoscale particles, as mention earlier. Mesoparticles containing nanoscale fuel and oxidizer particles, along with a low-temperature gas generating polymer binder, have demonstrated superior combustion performance compared to the physically mixed fuel and oxidizer nanoparticles[56,57,70]. This improved reactivity is attributed to the reduced sintering from the breakup of agglomerates before or during the combustion due to gas generation from the polymer binder. However, the mesoparticles are in the powder form and cannot be directly utilized in practical applications such as propellants. An essential advancement for practical application of these mesoparticles is the fabrication of free-standing composites containing them. I have successfully prepared free-standing composites with 90% loading of mesoparticles via 3D printing without compromising the integrity of the mesoparticles.

However, the printed composite exhibits noncontinuous propagation behavior, attributed to the lack of sufficient heat feedback from the flame to the unburnt composite. Carbon fiber is introduced to the composite to enhance heat feedback by trapping and retaining the hot agglomerates near the burning surface (Figure 1-7 (c)). The inclusion of

carbon fiber results in steady propagation. Agglomerate residence time and characteristic heat transfer time near the burning surface are estimated and compared for the composites with and without carbon fiber. I have found that the composite without carbon fiber has an agglomerate residence time comparable to the characteristic heat transfer time, whereas the composite with carbon fiber experiences a notably prolonged agglomerate residence time compared to the characteristic heat transfer duration (Figure 1-7 (c)). This analysis confirms the enhanced heat feedback achieved through carbon fiber incorporation.

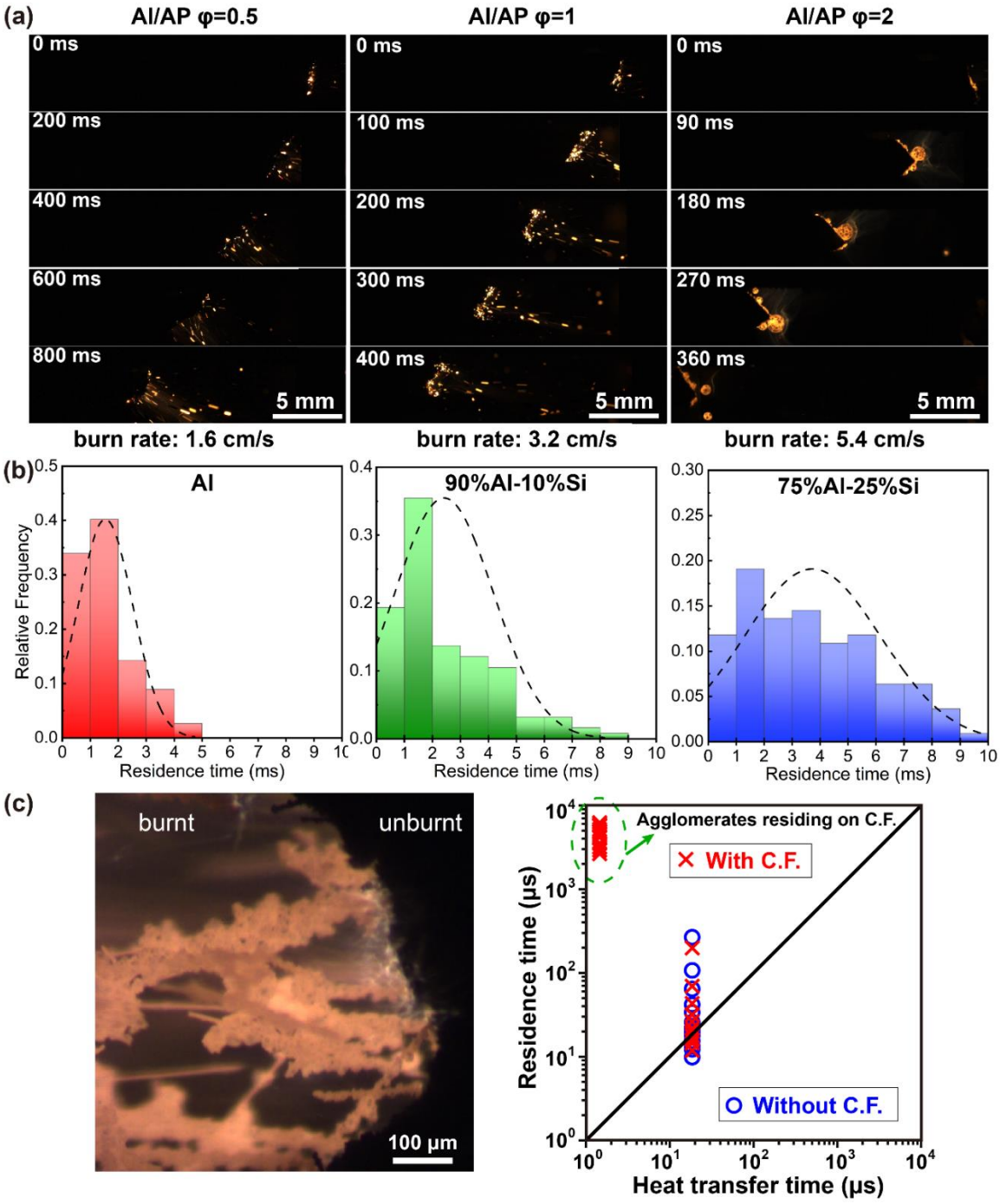
(a)
Al/AP φ=0.5
Al/AP φ=1
Al/AP φ=2
0 ms
200 ms
400 ms
600 ms
800 ms
0 ms
100 ms
200 ms
300 ms
400 ms
0 ms
90 ms
180 ms
270 ms
360 ms
5 mm
5 mm
5 mm
burn rate: 1.6 cm/s
burn rate: 3.2 cm/s
burn rate: 5.4 cm/s
(b)
Al
90%Al-10%Si
75%Al-25%Si
Relative Frequency
Residence time (ms)
Residence time (ms)
Residence time (ms)
(c)
burnt
unburnt
100 μm
Agglomerates residing on C.F.
With C.F.
Without C.F.
Residence time (μs)
Heat transfer time (μs)

Figure 1-7 Time-resolved images with corresponding burn rate for aluminum and AP composites with different equivalence ratios (a). The measured agglomerate surface residence time distribution for the composites of aluminum and silicon as the fuel and $KClO_4$ as the oxidizer with varying aluminum-to-silicon content (b). An image showing agglomerates residing on carbon fibers for the composites with mesoparticles (left) and estimated agglomerate residence time and characteristic heat transfer time for the composites with and without C.F. (right) (c).

1.6.3 Developing energetic biocidal agents with metal iodates

Interest in the development of agent defeat weapons (ADWs) has facilitated studies on iodine-containing compounds for the application as oxidizers in energetic composites with high energy density. As mentioned earlier, although having high iodine content and high oxidizing capability, I_2O_5 suffers from moisture sensitivity that limits its practical application[101]. Metal iodates are promising alternative candidates due to their high iodine content and strong oxidizing property[92,94,125]. Combustion characteristics and iodine release have been investigated for energetic composites containing a variety of metal iodates, such as $AgIO_3$, $Bi(IO_3)_2$, $Ca(IO_3)_2$, $Fe(IO_3)_2$, $Ti(IO_3)_4$, and $Cu(IO_3)_2$, with iodine content ranging from 44.9% to 67.9%[92,94,125–127]. Interestingly, the studies revealed that not all of these iodates can produce molecular iodine as the final decomposition product. For instance, $AgIO_3$ decomposes into condensed phase AgI instead of releasing gaseous molecular iodine, which means that iodine is kinetically trapped in the form of metal iodide[127]. While AgI is also known to act as a biocide, it is less effective than iodine[92]. However, the underlying decomposition mechanism of metal iodates and fundamental factors governing the decomposition pathway remain not well understood.

The research performed for this dissertation has been able to provide a systematic study on the decomposition mechanism of alkali and alkaline metal iodates ($LiIO_3$, $NaIO_3$, KIO_3, $Mg(IO_3)_2$, and $Ca(IO_3)_2$) with high iodine and oxygen content (Chapter 8). It is found that all of these metal iodates produce O_2, confirming their potential utilization as oxidizers. However, only $Mg(IO_3)_2$, $Ca(IO_3)_2$, and $LiIO_3$ release significant amount of I_2 while $NaIO_3$ and KIO_3 have minimal I_2 release (Figure 1-8 (a) and (b)). Analysis of the condensed phase species reveals the presence of two distinct decomposition processes among these metal iodates. $Mg(IO_3)_2$, $Ca(IO_3)_2$, and $LiIO_3$ follow a two-step decomposition, while $NaIO_3$ and KIO_3 follow a one-step decomposition. Two decompositions pathways are proposed based on these observations as well as previous studies[128–130]. One pathway undergoes two decomposition steps: (1) Decomposition of metal iodate (MIO_3) into metal orthoperiodate ($M_x(IO_6)_y$) accompanied by I_2 and O_2 release, and (2) decomposition from metal orthoperiodate to metal oxide (MO) accompanied by I_2 and O_2 release. $LiIO_3$, $Mg(IO_3)_2$, and $Ca(IO_3)_2$ follow this pathway. The other pathway undergoes one decomposition step that produces metal iodide and O_2. $NaIO_3$ and KIO_3 follow this decomposition pathway. In this scenario, iodine becomes trapped as metal iodide rather than being released as molecular iodine, rendering these iodates less suitable candidates for applications in biocidal agents. Thermodynamic data is employed to forecast which decomposition pathway is more advantageous for a specific metal iodate, and these predictions are broadly aligned with the experimental findings obtained from the examined alkali and alkaline metal iodates. These results suggest that not all metal iodates are potential candidates for

the application in ADWs, and a simple thermodynamic calculation can predict whether a metal iodate is a promising biocidal agent by estimating its decomposition pathway[131].

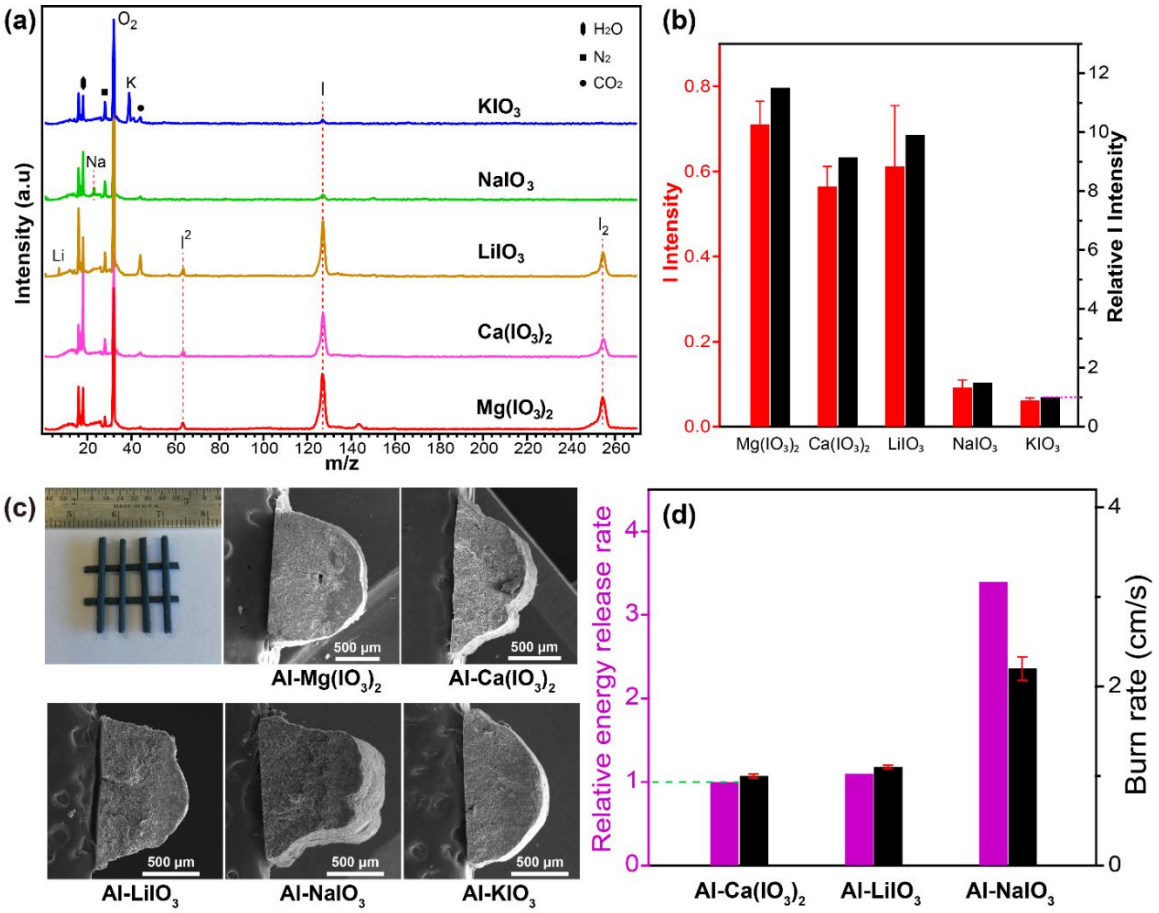

Figure 1-8 Mass spectrum of heated alkali and alkaline metal iodates (a). The measured I release of these iodates and their relative intensity to KIO_3 (b)[131]. SEM cross-section of the assembled 90% loading composites of aluminum and metal iodates (c). Burn rate and relative energy release rate of Al-$Ca(IO_3)_2$, Al-$LiIO_3$, and Al-$NaIO_3$ (d)[132]. (*Reproduced with permission from Elsevier*).

To further determine if a metal iodate is suitable to be used in ADWs, its reactivity with a fuel as well as the iodine release rate need to be investigated. Furthermore, a significant step forward to the real-world application of the metal iodates in ADWs is their incorporation into composites with mechanical integrity, high energy density, and iodine

content as well as the investigation of combustion characteristics of the composites. To achieve high energy density and iodine content, high loading of fuel particles and metal iodate particles is desirable. Chapter 9 in this dissertation investigates the ignition, iodine release, and reactivity of alkali and alkaline metal iodates ($LiIO_3$, $NaIO_3$, KIO_3, $Mg(IO_3)_2$, and $Ca(IO_3)_2$) with nanoscale aluminum, which is the mostly commonly used fuel, as mentioned earlier. Consistent with the observation for bare metal iodates in Chapter 8, Al-$Mg(IO_3)_2$, Al-$Ca(IO_3)_2$, and Al-$LiIO_3$ release a significant amount of iodine at roughly the same temperature, while Al-$NaIO_3$ and Al-KIO_3 have minimal iodine release. However, the reactivity of Al-$NaIO_3$ and Al-KIO_3 is much higher than that of Al-$Mg(IO_3)_2$, Al-$Ca(IO_3)_2$, and Al-$LiIO_3$. This indicates that there is trade-off between iodine release and reactivity among aluminized metal iodates. The estimation of iodine release rates is conducted for thermites containing metal iodates with significant iodine release. The findings suggest that Al-$Mg(IO_3)_2$ and Al-$Ca(IO_3)_2$ have considerably higher iodine release rates than Al-$LiIO_3$.

Free-standing composites of 90% loading of aluminum and metal iodates are also successfully fabricated via 3D printing (Figure 1-8 (c)). A high iodine content within an energetic composite is desirable for its application in ADWs. These fabricated composites boast iodine contents reaching nearly 50 wt%, and their combustion characteristics are studied with high-speed videography and pyrometry. It has been observed that only Al-$Ca(IO_3)_2$, Al-$LiIO_3$, and Al-$NaIO_3$ exhibit complete propagation in an inert environment, with their microscopic combustion behaviors showing similar characteristics. Comparatively, Al-$NaIO_3$ has higher propagation rate and flame temperature than Al-

$Ca(IO_3)_2$ and Al-$LiIO_3$, resulting in a higher energy release rate for Al-$NaIO_3$ than for Al-$Ca(IO_3)_2$ and Al-$LiIO_3$ (Figure 1-8 (d)). This indicates a trade-off between iodine release and energy release rate. These results demonstrate that not all aluminized metal iodate composites have potentials in the biocidal applications, Al-$Ca(IO_3)_2$ and Al-$LiIO_3$ composites are promising biocidal agents due to both heat and iodine release[132].

1.7 References

(1) Pang, W.; De Luca, L. T.; Wang, K.; Fu, X.; Li, J.; Xu, H.; Fan, X.; Li, H. Chapter 7 - Performance of Composite Solid Propellant Containing Nanosized Metal Particles. In *Nanomaterials in Rocket Propulsion Systems*; Yan, Q.-L., He, G.-Q., Liu, P.-J., Gozin, M., Eds.; Micro and Nano Technologies; Elsevier, 2019; pp 263–298. https://doi.org/10.1016/B978-0-12-813908-0.00007-1.

(2) Huang, S.; Hong, S.; Su, Y.; Jiang, Y.; Fukushima, S.; Gill, T. M.; Yilmaz, N. E. D.; Tiwari, S.; Nomura, K.; Kalia, R. K.; Nakano, A.; Shimojo, F.; Vashishta, P.; Chen, M.; Zheng, X. Enhancing Combustion Performance of Nano-Al/PVDF Composites with β-PVDF. *Combust. Flame* **2020**, *219*, 467–477. https://doi.org/10.1016/j.combustflame.2020.06.011.

(3) Hendel, F. J. Review of Solid Propellants for Space Exploration.

(4) Mason, B. P.; Roland, C. M. SOLID PROPELLANTS. *Rubber Chem. Technol.* **2019**, *92* (1), 1–24. https://doi.org/10.5254/rct.19.80456.

(5) Chowdhury, S.; Sullivan, K.; Piekiel, N.; Zhou, L.; Zachariah, M. R. Diffusive vs Explosive Reaction at the Nanoscale. *J. Phys. Chem. C* **2010**, *114* (20), 9191–9195. https://doi.org/10.1021/jp906613p.

(6) Ma, X.; Li, Y.; Hussain, I.; Shen, R.; Yang, G.; Zhang, K. Core–Shell Structured Nanoenergetic Materials: Preparation and Fundamental Properties. *Adv. Mater.* **2020**, *32* (30), 2001291. https://doi.org/10.1002/adma.202001291.

(7) Hobosyan, M.; Lyshevski, S. E.; Martirosyan, K. S. Chapter 11 - Integrated Micropropulsion Systems With Nanoenergetic Propellants. In *Nanomaterials in Rocket Propulsion Systems*; Yan, Q.-L., He, G.-Q., Liu, P.-J., Gozin, M., Eds.; Micro and Nano Technologies; Elsevier, 2019; pp 403–420. https://doi.org/10.1016/B978-0-12-813908-0.00011-3.

(8) Rehwoldt, M. C.; Wang, H.; Kline, D. J.; Wu, T.; Eckman, N.; Wang, P.; Agrawal, N. R.; Zachariah, M. R. Ignition and Combustion Analysis of Direct Write Fabricated Aluminum/Metal Oxide/PVDF Films. *Combust. Flame* **2020**, *211*, 260–269. https://doi.org/10.1016/j.combustflame.2019.08.023.

(9) Sundaram, D.; Yang, V.; Yetter, R. A. Metal-Based Nanoenergetic Materials: Synthesis, Properties, and Applications. *Prog. Energy Combust. Sci.* **2017**, *61*, 293–365. https://doi.org/10.1016/j.pecs.2017.02.002.

(10) Comet, M.; Martin, C.; Schnell, F.; Spitzer, D. Nanothermites: A Short Review. Factsheet for Experimenters, Present and Future Challenges. *Propellants Explos. Pyrotech.* **2019**, *44* (1), 18–36. https://doi.org/10.1002/prep.201800095.

(11) Zohari, N.; Keshavarz, M. H.; Seyedsadjadi, S. A. The Advantages and Shortcomings of Using Nano-Sized Energetic Materials. *Cent. Eur. J. Energ. Mater.* **2013**, *Vol. 10* (1).

(12) Jian, G.; Chowdhury, S.; Sullivan, K.; Zachariah, M. R. Nanothermite Reactions: Is Gas Phase Oxygen Generation from the Oxygen Carrier an Essential Prerequisite to Ignition? *Combust. Flame* **2013**, *160* (2), 432–437. https://doi.org/10.1016/j.combustflame.2012.09.009.

(13) Rai, A.; Park, K.; Zhou, L.; Zachariah, M. R. Understanding the Mechanism of Aluminium Nanoparticle Oxidation. *Combust. Theory Model.* **2006**, *10* (5), 843–859. https://doi.org/10.1080/13647830600800686.
(14) Yetter, R. A.; Risha, G. A.; Son, S. F. Metal Particle Combustion and Nanotechnology. *Proc. Combust. Inst.* **2009**, *32* (2), 1819–1838. https://doi.org/10.1016/j.proci.2008.08.013.
(15) Bockmon, B. S.; Pantoya, M. L.; Son, S. F.; Asay, B. W.; Mang, J. T. Combustion Velocities and Propagation Mechanisms of Metastable Interstitial Composites. *J. Appl. Phys.* **2005**, *98* (6), 064903. https://doi.org/10.1063/1.2058175.
(16) Asay, B. W.; Son, S. F.; Busse, J. R.; Oschwald, D. M. Ignition Characteristics of Metastable Intermolecular Composites. *Propellants Explos. Pyrotech.* **2004**, *29* (4), 216–219. https://doi.org/10.1002/prep.200400049.
(17) Sullivan, K.; Young, G.; Zachariah, M. R. Enhanced Reactivity of Nano-B/Al/CuO MIC's. *Combust. Flame* **2009**, *156* (2), 302–309. https://doi.org/10.1016/j.combustflame.2008.09.011.
(18) Ghildiyal, P.; Biswas, P.; Herrera, S.; Xu, F.; Alibay, Z.; Wang, Y.; Wang, H.; Abbaschian, R.; Zachariah, M. R. Vaporization-Controlled Energy Release Mechanisms Underlying the Exceptional Reactivity of Magnesium Nanoparticles. *ACS Appl. Mater. Interfaces* **2022**. https://doi.org/10.1021/acsami.1c22685.
(19) Karasev, V. V.; Onischuk, A. A.; Glotov, O. G.; Baklanov, A. M.; Maryasov, A. G.; Zarko, V. E.; Panfilov, V. N.; Levykin, A. I.; Sabelfeld, K. K. Formation of Charged Aggregates of Al2O3 Nanoparticles by Combustion of Aluminum Droplets in Air. *Combust. Flame* **2004**, *138* (1), 40–54. https://doi.org/10.1016/j.combustflame.2004.04.001.
(20) Emelyanov, V. N.; Teterina, I. V.; Volkov, K. N. Dynamics and Combustion of Single Aluminium Agglomerate in Solid Propellant Environment. *Acta Astronaut.* **2020**, *176*, 682–694. https://doi.org/10.1016/j.actaastro.2020.03.046.
(21) Harrison, J.; Brewster, M. Q. Analysis of Thermal Radiation from Burning Aluminium in Solid Propellants. *Combust. Theory Model.* **2009**, *13* (3), 389–411. https://doi.org/10.1080/13647830802684318.
(22) Beckstead, M. W. A Summary of Aluminum Combustion. 47.
(23) Wang, Y.; Wang, H.; Xu, F.; Ghildiyal, P.; Zachariah, M. R. Effect of Alkali Metal Perchlorate and Iodate Type on Boron Ignition: The Role of Oxidizer Phase Change. *Chem. Eng. J.* **2022**, *446*, 136786. https://doi.org/10.1016/j.cej.2022.136786.
(24) Yeh, C. L.; Kuo, K. K. Ignition and Combustion of Boron Particles. *Prog. Energy Combust. Sci.* **1996**, *22* (6), 511–541. https://doi.org/10.1016/S0360-1285(96)00012-3.
(25) Spalding, M. J.; Krier, H.; Burton, R. L. Boron Suboxides Measured during Ignition and Combustion of Boron in Shocked Ar/F/O2 and Ar/N2/O2 Mixtures. *Combust. Flame* **2000**, *120* (1), 200–210. https://doi.org/10.1016/S0010-2180(99)00082-6.
(26) Ghildiyal, P.; Ke, X.; Biswas, P.; Nava, G.; Schwan, J.; Xu, F.; Kline, D. J.; Wang, H.; Mangolini, L.; Zachariah, M. R. Silicon Nanoparticles for the Reactivity and Energetic Density Enhancement of Energetic-Biocidal Mesoparticle Composites.

ACS Appl. Mater. Interfaces **2021**, *13* (1), 458–467. https://doi.org/10.1021/acsami.0c17159.
(27) Xu, F.; Nava, G.; Biswas, P.; Dulalia, I.; Wang, H.; Alibay, Z.; Gale, M.; Kline, D. J.; Wagner, B.; Mangolini, L.; Zachariah, M. R. Energetic Characteristics of Hydrogenated Amorphous Silicon Nanoparticles. *Chem. Eng. J.* **2021**, 133140. https://doi.org/10.1016/j.cej.2021.133140.
(28) Wang, Y.; Hagen, E.; Biswas, P.; Wang, H.; Zachariah, M. R. Imaging the Combustion Characteristics of Al, B, and Ti Composites. *Combust. Flame* **2023**, *252*, 112747. https://doi.org/10.1016/j.combustflame.2023.112747.
(29) Rehwoldt, M. C.; Yang, Y.; Wang, H.; Holdren, S.; Zachariah, M. R. Ignition of Nanoscale Titanium/Potassium Perchlorate Pyrotechnic Powder: Reaction Mechanism Study. *J. Phys. Chem. C* **2018**, *122* (20), 10792–10800. https://doi.org/10.1021/acs.jpcc.8b03164.
(30) Shafirovich, E.; Teoh, S. K.; Varma, A. Combustion of Levitated Titanium Particles in Air. *Combust. Flame* **2008**, *152* (1), 262–271. https://doi.org/10.1016/j.combustflame.2007.05.008.
(31) Glotov, O. G. Ignition and Combustion of Titanium Particles: Experimental Methods and Results. *Phys.-Uspekhi* **2019**, *62* (2), 131. https://doi.org/10.3367/UFNe.2018.04.038349.
(32) Badiola, C.; Dreizin, E. L. Combustion of Micron-Sized Particles of Titanium and Zirconium. *Proc. Combust. Inst.* **2013**, *34* (2), 2237–2243. https://doi.org/10.1016/j.proci.2012.05.089.
(33) Sippel, T. R.; Son, S. F.; Groven, L. J. Aluminum Agglomeration Reduction in a Composite Propellant Using Tailored Al/PTFE Particles. *Combust. Flame* **2014**, *161* (1), 311–321. https://doi.org/10.1016/j.combustflame.2013.08.009.
(34) DeLuca, L. T.; Galfetti, L.; Colombo, G.; Maggi, F.; Bandera, A.; Babuk, V. A.; Sinditskii, V. P. Microstructure Effects in Aluminized Solid Rocket Propellants. *J. Propuls. Power* **2010**, *26* (4), 724–732. https://doi.org/10.2514/1.45262.
(35) Jacob, R. J.; Wei, B.; Zachariah, M. R. Quantifying the Enhanced Combustion Characteristics of Electrospray Assembled Aluminum Mesoparticles. *Combust. Flame* **2016**, *167*, 472–480. https://doi.org/10.1016/j.combustflame.2015.09.032.
(36) Chen, Y.; Guildenbecher, D. R.; Hoffmeister, K. N. G.; Cooper, M. A.; Stauffacher, H. L.; Oliver, M. S.; Washburn, E. B. Study of Aluminum Particle Combustion in Solid Propellant Plumes Using Digital In-Line Holography and Imaging Pyrometry. *Combust. Flame* **2017**, *182*, 225–237. https://doi.org/10.1016/j.combustflame.2017.04.016.
(37) Dreizin, E. L. Experimental Study of Stages in Aluminium Particle Combustion in Air. *Combust. Flame* **1996**, *105* (4), 541–556. https://doi.org/10.1016/0010-2180(95)00224-3.
(38) Trunov, M. A.; Schoenitz, M.; Dreizin, E. L. Effect of Polymorphic Phase Transformations in Alumina Layer on Ignition of Aluminium Particles. *Combust. Theory Model.* **2006**, *10* (4), 603–623. https://doi.org/10.1080/13647830600578506.

(39) Henz, B. J.; Hawa, T.; Zachariah, M. R. On the Role of Built-in Electric Fields on the Ignition of Oxide Coated Nanoaluminum: Ion Mobility versus Fickian Diffusion. *J. Appl. Phys.* **2010**, *107* (2), 024901. https://doi.org/10.1063/1.3247579.
(40) King, M. K. Ignition and Combustion of Boron Particles and Clouds. *J. Spacecr. Rockets* **1982**, *19* (4), 294–306. https://doi.org/10.2514/3.62256.
(41) Ulas, A.; Kuo, K. K.; Gotzmer, C. Ignition and Combustion of Boron Particles in Fluorine-Containing Environments. *Combust. Flame* **2001**, *127* (1), 1935–1957. https://doi.org/10.1016/S0010-2180(01)00299-1.
(42) Huang, S.; Deng, S.; Jiang, Y.; Zheng, X. Experimental Effective Metal Oxides to Enhance Boron Combustion. *Combust. Flame* **2019**, *205*, 278–285. https://doi.org/10.1016/j.combustflame.2019.04.018.
(43) Ao, W.; Wang, Y.; Li, H.; Xi, J.; Liu, J.; Zhou, J. Effect of Initial Oxide Layer on Ignition and Combustion of Boron Powder. *Propellants Explos. Pyrotech.* **2014**, *39* (2), 185–191. https://doi.org/10.1002/prep.201300079.
(44) Krier, H.; Burton, R. L.; Spalding, M. J.; Rood, T. J. Ignition Dynamics of Boron Particles in a Shock Tube. *J. Propuls. Power* **1998**, *14* (2), 166–172. https://doi.org/10.2514/2.5282.
(45) Gottfried, J. L.; Wainwright, E. R.; Huang, S.; Jiang, Y.; Zheng, X. Probing Boron Thermite Energy Release at Rapid Heating Rates. *Combust. Flame* **2021**, *231*, 111491. https://doi.org/10.1016/j.combustflame.2021.111491.
(46) Li, S. C.; Williams, F. A.; Takahashi, F. An Investigation of Combustion of Boron Suspensions. *Symp. Int. Combust.* **1989**, *22* (1), 1951–1960. https://doi.org/10.1016/S0082-0784(89)80210-3.
(47) Young, G.; Sullivan, K.; Zachariah, M. R.; Yu, K. Combustion Characteristics of Boron Nanoparticles. *Combust. Flame* **2009**, *156* (2), 322–333. https://doi.org/10.1016/j.combustflame.2008.10.007.
(48) Yetter, R. A.; Rabitz, H.; Dryer, F. L.; Brown, R. C.; Kolb, C. E. Kinetics of High-Temperature B/O/H/C Chemistry. *Combust. Flame* **1991**, *83* (1), 43–62. https://doi.org/10.1016/0010-2180(91)90202-M.
(49) Paidi, V. K.; Lee, B.-H.; Ahn, D.; Kim, K.-J.; Kim, Y.; Hyeon, T.; Lee, K.-S. Oxygen-Vacancy-Driven Orbital Reconstruction at the Surface of TiO2 Core–Shell Nanostructures. *Nano Lett.* **2021**, *21* (19), 7953–7959. https://doi.org/10.1021/acs.nanolett.1c01995.
(50) Valluri, S. K.; Schoenitz, M.; Dreizin, E. Bismuth Fluoride-Coated Boron Powders as Enhanced Fuels. *Combust. Flame* **2020**, *221*, 1–10. https://doi.org/10.1016/j.combustflame.2020.07.023.
(51) Deshmukh, P. R.; Lee, H.; Kim, Y.; Shin, W. G. Ignition and Oxidation Performance of SnO2 Coated Boron Particles: A Solid Fuel for Energetic Applications. *J. Alloys Compd.* **2021**, 161123. https://doi.org/10.1016/j.jallcom.2021.161123.
(52) Jiang, Y.; Dincer Yilmaz, N. E.; Barker, K. P.; Baek, J.; Xia, Y.; Zheng, X. Enhancing Mechanical and Combustion Performance of Boron/Polymer Composites via Boron Particle Functionalization. *ACS Appl. Mater. Interfaces* **2021**. https://doi.org/10.1021/acsami.1c06727.

(53) Liu, T.-K.; Luh, S.-P.; Perng, H.-C. Effect of Boron Particle Surface Coating on Combustion of Solid Propellants for Ducted Rockets. *Propellants Explos. Pyrotech.* **1991**, *16* (4), 156–166. https://doi.org/10.1002/prep.19910160403.
(54) Shyu, I.-M.; Liu, T.-K. Combustion Characteristics of GAP-Coated Boron Particles and the Fuel-Rich Solid Propellant. *Combust. Flame* **1995**, *100* (4), 634–644. https://doi.org/10.1016/0010-2180(94)00032-N.
(55) Jacob, R. J.; Hill, K. J.; Yang, Y.; Pantoya, M. L.; Zachariah, M. R. Pre-Stressing Aluminum Nanoparticles as a Strategy to Enhance Reactivity of Nanothermite Composites. *Combust. Flame* **2019**, *205*, 33–40. https://doi.org/10.1016/j.combustflame.2019.03.024.
(56) Wang, H.; Jian, G.; Egan, G. C.; Zachariah, M. R. Assembly and Reactive Properties of Al/CuO Based Nanothermite Microparticles. *Combust. Flame* **2014**, *161* (8), 2203–2208. https://doi.org/10.1016/j.combustflame.2014.02.003.
(57) Wang, H.; Jacob, R. J.; DeLisio, J. B.; Zachariah, M. R. Assembly and Encapsulation of Aluminum NP's within AP/NC Matrix and Their Reactive Properties. *Combust. Flame* **2017**, *180*, 175–183. https://doi.org/10.1016/j.combustflame.2017.02.036.
(58) Wang, H.; Kline, D. J.; Rehwoldt, M.; Wu, T.; Zhao, W.; Wang, X.; Zachariah, M. R. Architecture Can Significantly Alter the Energy Release Rate from Nanocomposite Energetics. *ACS Appl. Polym. Mater.* **2019**, *1* (5), 982–989. https://doi.org/10.1021/acsapm.9b00016.
(59) Wang, H.; Shen, J.; Kline, D. J.; Eckman, N.; Agrawal, N. R.; Wu, T.; Wang, P.; Zachariah, M. R. Direct Writing of a 90 Wt% Particle Loading Nanothermite. *Adv. Mater.* **2019**, *31* (23), 1806575. https://doi.org/10.1002/adma.201806575.
(60) Shen, J.; Wang, H.; Kline, D. J.; Yang, Y.; Wang, X.; Rehwoldt, M.; Wu, T.; Holdren, S.; Zachariah, M. R. Combustion of 3D Printed 90 Wt% Loading Reinforced Nanothermite. *Combust. Flame* **2020**, *215*, 86–92. https://doi.org/10.1016/j.combustflame.2020.01.021.
(61) Wang, H.; Kline, D. J.; Zachariah, M. R. In-Operando High-Speed Microscopy and Thermometry of Reaction Propagation and Sintering in a Nanocomposite. *Nat. Commun.* **2019**, *10* (1), 3032. https://doi.org/10.1038/s41467-019-10843-4.
(62) Muravyev, N. V.; Monogarov, K. A.; Schaller, U.; Fomenkov, I. V.; Pivkina, A. N. Progress in Additive Manufacturing of Energetic Materials: Creating the Reactive Microstructures with High Potential of Applications. *Propellants Explos. Pyrotech.* **2019**, *44* (8), 941–969. https://doi.org/10.1002/prep.201900060.
(63) Elder, B.; Neupane, R.; Tokita, E.; Ghosh, U.; Hales, S.; Kong, Y. L. Nanomaterial Patterning in 3D Printing. *Adv. Mater.* **2020**, *32* (17), 1907142. https://doi.org/10.1002/adma.201907142.
(64) Durban, M. M.; Golobic, A. M.; Bukovsky, E. V.; Gash, A. E.; Sullivan, K. T. Development and Characterization of 3D Printable Thermite Component Materials. *Adv. Mater. Technol.* **2018**, *3* (12), 1800120. https://doi.org/10.1002/admt.201800120.

(65) Wainwright, E. R.; Sullivan, K. T.; Grapes, M. D. Designer Direct Ink Write 3D-Printed Thermites with Tunable Energy Release Rates. *Adv. Eng. Mater.* **2020**, *22* (6), 1901196. https://doi.org/10.1002/adem.201901196.
(66) Ligon, S. C.; Liska, R.; Stampfl, J.; Gurr, M.; Mülhaupt, R. Polymers for 3D Printing and Customized Additive Manufacturing. *Chem. Rev.* **2017**, *117* (15), 10212–10290. https://doi.org/10.1021/acs.chemrev.7b00074.
(67) Chakraborty, P.; Zachariah, M. R. Do Nanoenergetic Particles Remain Nano-Sized during Combustion? *Combust. Flame* **2014**, *161* (5), 1408–1416. https://doi.org/10.1016/j.combustflame.2013.10.017.
(68) Egan, G. C.; Sullivan, K. T.; LaGrange, T.; Reed, B. W.; Zachariah, M. R. In Situ Imaging of Ultra-Fast Loss of Nanostructure in Nanoparticle Aggregates. *J. Appl. Phys.* **2014**, *115* (8), 084903. https://doi.org/10.1063/1.4867116.
(69) Sullivan, K. T.; Piekiel, N. W.; Wu, C.; Chowdhury, S.; Kelly, S. T.; Hufnagel, T. C.; Fezzaa, K.; Zachariah, M. R. Reactive Sintering: An Important Component in the Combustion of Nanocomposite Thermites. *Combust. Flame* **2012**, *159* (1), 2–15. https://doi.org/10.1016/j.combustflame.2011.07.015.
(70) Chowdhury, M.; Ghildiyal, P.; Rojas, A.; Wang, Y.; Wang, H.; Zachariah, M. R. High-Yield Spray Drying Assembly and Reactive Properties of Nanoenergetic Mesoparticle Composites. *Adv. Powder Technol.* **2023**, *34* (7), 104075. https://doi.org/10.1016/j.apt.2023.104075.
(71) Wang, H.; Wang, Y.; Garg, M.; Moore, J. S.; Zachariah, M. R. Unzipping Polymers Significantly Enhance Energy Flux of Aluminized Composites. *Combust. Flame* **2022**, *244*, 112242. https://doi.org/10.1016/j.combustflame.2022.112242.
(72) Brewster, M. Q.; Hardt, B. E. Influence of Metal Agglomeration and Heat Feedback on Composite Propellant Burning Rate. *J. Propuls. Power* **1991**, *7* (6), 1076–1078. https://doi.org/10.2514/3.23431.
(73) Egan, G. C.; Zachariah, M. R. Commentary on the Heat Transfer Mechanisms Controlling Propagation in Nanothermites. *Combust. Flame* **2015**, *162* (7), 2959–2961. https://doi.org/10.1016/j.combustflame.2015.04.013.
(74) Summerfield, M. *Solid Propellant Rocket Research*; Elsevier, 2013.
(75) Kline, D. J.; Alibay, Z.; Rehwoldt, M. C.; Idrogo-Lam, A.; Hamilton, S. G.; Biswas, P.; Xu, F.; Zachariah, M. R. Experimental Observation of the Heat Transfer Mechanisms That Drive Propagation in Additively Manufactured Energetic Materials. *Combust. Flame* **2020**, *215*, 417–424. https://doi.org/10.1016/j.combustflame.2020.01.020.
(76) Ishihara, A.; Brewster, M. Q.; Sheridan, T. A.; Krier, H. The Influence of Radiative Heat Feedback on Burning Rate in Aluminized Propellants. *Combust. Flame* **1991**, *84* (1), 141–153. https://doi.org/10.1016/0010-2180(91)90043-B.
(77) Wang, H.; Kline, D. J.; Rehwoldt, M. C.; Zachariah, M. R. Carbon Fibers Enhance the Propagation of High Loading Nanothermites: In Situ Observation of Microscopic Combustion. *ACS Appl. Mater. Interfaces* **2021**. https://doi.org/10.1021/acsami.1c02911.

(78) Wang, H.; Hagen, E.; Shi, K.; Herrera, S.; Xu, F.; Zachariah, M. R. Carbon Fibers as Additives to Engineer Agglomeration and Propagation of Aluminized Propellants. *Chem. Eng. J.* **2023**, 141653. https://doi.org/10.1016/j.cej.2023.141653.
(79) Glassman, I.; Yetter, R. A. *Combustion*, 4th ed.; Academic Press: Amsterdam ; Boston, 2008.
(80) CAVENY, L. H.; GLICK, R. L. Influence of Embedded Metal Fibers on Solid-Propellant Burning Rate. *J. Spacecr. Rockets* **1967**, *4* (1), 79–85. https://doi.org/10.2514/3.28813.
(81) KANURY, A. M.; HERNANDEZ-GUERRERO, A. Steady Planar Propagation of the Gasless SHS Reaction Producing Titanium Carbide. *Combust. Sci. Technol.* **1994**, *102* (1–6), 1–19. https://doi.org/10.1080/00102209408935467.
(82) Mukasyan, A. S.; Shuck, C. E. Kinetics of SHS Reactions: A Review. *Int. J. Self-Propagating High-Temp. Synth.* **2017**, *26* (3), 145–165. https://doi.org/10.3103/S1061386217030049.
(83) Kline, D. J.; Rehwoldt, M. C.; Wang, H.; Eckman, N. E.; Zachariah, M. R. Why Does Adding a Poor Thermal Conductor Increase Propagation Rate in Solid Propellants? *Appl. Phys. Lett.* **2019**, *115* (11), 114101. https://doi.org/10.1063/1.5113612.
(84) Shuling, C.; Fengsheng, L. Influence of Long Metal Wires on Combustion of Double-Base Propellants. *Combust. Flame* **1982**, *45*, 213–218. https://doi.org/10.1016/0010-2180(82)90047-5.
(85) Isert, S.; Lane, C. D.; Gunduz, I. E.; Son, S. F. Tailoring Burning Rates Using Reactive Wires in Composite Solid Rocket Propellants. *Proc. Combust. Inst.* **2017**, *36* (2), 2283–2290. https://doi.org/10.1016/j.proci.2016.06.141.
(86) Kubota, N.; Ichida, M.; Fujisawa, T. Combustion Processes of Propellants with Embedded Metal Wires. *AIAA J.* **1982**, *20* (1), 116–121. https://doi.org/10.2514/3.51056.
(87) Shioya, S.; Kohga, M.; Naya, T. Burning Characteristics of Ammonium Perchlorate-Based Composite Propellant Supplemented with Diatomaceous Earth. *Combust. Flame* **2014**, *161* (2), 620–630. https://doi.org/10.1016/j.combustflame.2013.09.019.
(88) Wang, H.; DeLisio, J. B.; Holdren, S.; Wu, T.; Yang, Y.; Hu, J.; Zachariah, M. R. Mesoporous Silica Spheres Incorporated Aluminum/Poly (Vinylidene Fluoride) for Enhanced Burning Propellants. *Adv. Eng. Mater.* **2018**, *20* (2), 1700547. https://doi.org/10.1002/adem.201700547.
(89) Ballas, M.; Song, H.; Ilegbusi, O. J. Effect of Thermal Conductivity on Reaction Front Propagation during Combustion Synthesis of Intermetalics. *J. Mater. Sci.* **2006**, *41* (13), 4169–4177. https://doi.org/10.1007/s10853-006-6751-0.
(90) Viljoen, H. J.; Hlavacek, V. Deflagration and Detonation in Solid-Solid Combustion. *AIChE J.* **1997**, *43* (11), 3085–3094. https://doi.org/10.1002/aic.690431119.
(91) Chang, J.; Zhao, G.; Zhao, X.; He, C.; Pang, S.; Shreeve, J. M. New Promises from an Old Friend: Iodine-Rich Compounds as Prospective Energetic Biocidal

Agents. *Acc. Chem. Res.* **2021**, *54* (2), 332–343. https://doi.org/10.1021/acs.accounts.0c00623.
(92) Hu, X.; DeLisio, J. B.; Li, X.; Zhou, W.; Zachariah, M. R. Direct Deposit of Highly Reactive Bi(IO3)3- Polyvinylidene Fluoride Biocidal Energetic Composite and Its Reactive Properties. *Adv. Eng. Mater.* **2017**, *19* (1), 1500532. https://doi.org/10.1002/adem.201500532.
(93) Kaiho, T. *Iodine Chemistry and Applications*; John Wiley & Sons, 2014.
(94) Wang, H.; Jian, G.; Zhou, W.; DeLisio, J. B.; Lee, V. T.; Zachariah, M. R. Metal Iodate-Based Energetic Composites and Their Combustion and Biocidal Performance. *ACS Appl. Mater. Interfaces* **2015**, *7* (31), 17363–17370. https://doi.org/10.1021/acsami.5b04589.
(95) Wheelis, M. *Deadly Cultures: Biological Weapons Since 1945*; Harvard University Press, 2006.
(96) Aly, Y.; Zhang, S.; Schoenitz, M.; Hoffmann, V. K.; Dreizin, E. L.; Yermakov, M.; Indugula, R.; Grinshpun, S. A. Iodine-Containing Aluminum-Based Fuels for Inactivation of Bioaerosols. *Combust. Flame* **2014**, *161* (1), 303–310. https://doi.org/10.1016/j.combustflame.2013.07.017.
(97) Wang, S.; Abraham, A.; Zhong, Z.; Schoenitz, M.; Dreizin, E. L. Ignition and Combustion of Boron-Based Al·B·I2 and Mg·B·I2 Composites. *Chem. Eng. J.* **2016**, *293*, 112–117. https://doi.org/10.1016/j.cej.2016.02.071.
(98) Zhang, S.; Schoenitz, M.; Dreizin, E. L. Iodine Release, Oxidation, and Ignition of Mechanically Alloyed Al−I Composites. *J. Phys. Chem. C* **2010**, *114* (46), 19653–19659. https://doi.org/10.1021/jp108171k.
(99) Grinshpun, S. A.; Adhikari, A.; Yermakov, M.; Reponen, T.; Dreizin, E.; Schoenitz, M.; Hoffmann, V.; Zhang, S. Inactivation of Aerosolized Bacillus Atrophaeus (BG) Endospores and MS2 Viruses by Combustion of Reactive Materials. *Environ. Sci. Technol.* **2012**, *46* (13), 7334–7341. https://doi.org/10.1021/es300537f.
(100) Zhang, S.; Badiola, C.; Schoenitz, M.; Dreizin, E. L. Oxidation, Ignition, and Combustion of Al·I2 Composite Powders. *Combust. Flame* **2012**, *159* (5), 1980–1986. https://doi.org/10.1016/j.combustflame.2012.01.004.
(101) Xu, F.; Biswas, P.; Nava, G.; Schwan, J.; Kline, D. J.; Rehwoldt, M. C.; Mangolini, L.; Zachariah, M. R. Tuning the Reactivity and Energy Release Rate of I2O5 Based Ternary Thermite Systems. *Combust. Flame* **2021**, *228*, 210–217. https://doi.org/10.1016/j.combustflame.2020.12.047.
(102) R. Clark, B.; L. Pantoya, M. The Aluminium and Iodine Pentoxide Reaction for the Destruction of Spore Forming Bacteria. *Phys. Chem. Chem. Phys.* **2010**, *12* (39), 12653–12657. https://doi.org/10.1039/C0CP00473A.
(103) Martirosyan, K. S.; Wang, L.; Luss, D. Novel Nanoenergetic System Based on Iodine Pentoxide. *Chem. Phys. Lett.* **2009**, *483* (1), 107–110. https://doi.org/10.1016/j.cplett.2009.10.038.
(104) Lempert, D. B.; Nechiporenko, G. N.; Manelis, G. B. Energetic Capabilities of High-Density Composite Solid Propellants Containing Zirconium or Its Hydride.

Combust. Explos. Shock Waves **2011**, *47* (1), 45–54. https://doi.org/10.1134/S0010508211010060.
(105) Chintersingh, K.-L.; Sun, Y.; Schoenitz, M.; Dreizin, E. L. Heterogeneous Reaction Kinetics for Oxidation and Combustion of Boron. *Thermochim. Acta* **2019**, *682*, 178415. https://doi.org/10.1016/j.tca.2019.178415.
(106) Chintersingh, K.-L.; Schoenitz, M.; Dreizin, E. L. Oxidation Kinetics and Combustion of Boron Particles with Modified Surface. *Combust. Flame* **2016**, *173*, 288–295. https://doi.org/10.1016/j.combustflame.2016.08.027.
(107) Chintersingh, K. A. Improving Boron for Combustion Applications. Ph.D., New Jersey Institute of Technology, United States -- New Jersey, 2019. https://www.proquest.com/docview/2299127991/abstract/70FA10D73C524002PQ/1 (accessed 2024-04-01).
(108) Liu, J.; Xi, J.; Yang, W.; Hu, Y.; Zhang, Y.; Wang, Y.; Zhou, J. Effect of Magnesium on the Burning Characteristics of Boron Particles. *Acta Astronaut.* **2014**, *96*, 89–96. https://doi.org/10.1016/j.actaastro.2013.11.039.
(109) Liu, X.; Chintersingh, K.-L.; Schoenitz, M.; Dreizin, E. L. Reactive Composite Boron–Magnesium Powders Prepared by Mechanical Milling. *J. Propuls. Power* **2018**, *34* (3), 787–794. https://doi.org/10.2514/1.B36315.
(110) Liu, L.; Liu, P.; He, G. Ignition and Combustion Characteristics of Compound of Magnesium and Boron. *J. Therm. Anal. Calorim.* **2015**, *121* (3), 1205–1212. https://doi.org/10.1007/s10973-015-4653-6.
(111) Mestwerdt, R.; Selzer, H. Experimental Investigation of Boron/Lithium Combustion. *AIAA J.* **1976**, *14* (1), 100–102. https://doi.org/10.2514/3.60665.
(112) Xi, J.; Liu, J.; Wang, Y.; Liang, D.; Zhou, J. Effect of Metal Hydrides on the Burning Characteristics of Boron. *Thermochim. Acta* **2014**, *597*, 58–64. https://doi.org/10.1016/j.tca.2014.10.017.
(113) Keerthi, V.; Nie, H.; Pisharath, S.; Hng, H. H. Combustion Characteristics of Fluoropolymer Coated Boron Powders. *Combust. Sci. Technol.* **2020**, *0* (0), 1–16. https://doi.org/10.1080/00102202.2020.1804885.
(114) Liu, T.; Chen, X.; Xu, H.; Han, A.; Ye, M.; Pan, G. Preparation and Properties of Boron-Based Nano-B/NiO Thermite. *Propellants Explos. Pyrotech.* **2015**, *40* (6), 873–879. https://doi.org/10.1002/prep.201400308.
(115) Wang, X.; Wu, T.; Wang, H.; DeLisio, J. B.; Yang, Y.; Zachariah, M. R. Boron Ignition and Combustion with Doped δ-Bi2O3: Bond Energy/Oxygen Vacancy Relationships. *Combust. Flame* **2018**, *197*, 127–133. https://doi.org/10.1016/j.combustflame.2018.07.015.
(116) Wang, H.; Ren, H.; Yin, L.; Li, Y.; Wu, X. High Energy Release Boron-Based Material with Oxygen Vacancies Promoting Combustion. *Chem. Eng. J.* **2022**, *430*, 133027. https://doi.org/10.1016/j.cej.2021.133027.
(117) Connell, T. L.; Risha, G. A.; Yetter, R. A.; Roberts, C. W.; Young, G. Boron and Polytetrafluoroethylene as a Fuel Composition for Hybrid Rocket Applications. *J. Propuls. Power* **2015**, *31* (1), 373–385. https://doi.org/10.2514/1.B35200.

(118) Young, G.; Roberts, C. W.; Stoltz, C. A. Ignition and Combustion Enhancement of Boron with Polytetrafluoroethylene. *J. Propuls. Power* **2015**, *31* (1), 386–392. https://doi.org/10.2514/1.B35390.
(119) Liu, T.-K.; Shyu, I.-M.; Hsia, Y.-S. Effect of Fluorinated Graphite on Combustion of Boron and Boron-Based Fuel-Rich Propellants. *J. Propuls. Power* **2012**. https://doi.org/10.2514/3.23986.
(120) HORTON, M. D.; YOUNGBER, L. Z. Effect of Radiant Energy on the Burning Rate of a Composite Solid Propellant. *AIAA J.* **1970**, *8* (10), 1738–1741. https://doi.org/10.2514/3.5983.
(121) Sanders, V. E.; Asay, B. W.; Foley, T. J.; Tappan, B. C.; Pacheco, A. N.; Son, S. F. Reaction Propagation of Four Nanoscale Energetic Composites (Al/MoO3, Al/WO3, Al/CuO, and B12O3). *J. Propuls. Power* **2007**, *23* (4), 707–714. https://doi.org/10.2514/1.26089.
(122) Son, S. F.; Asay, B. W.; Foley, T. J.; Yetter, R. A.; Wu, M. H.; Risha, G. A. Combustion of Nanoscale Al/MoO3 Thermite in Microchannels. *J. Propuls. Power* **2007**, *23* (4), 715–721. https://doi.org/10.2514/1.26090.
(123) Sullivan, K. T.; Kuntz, J. D.; Gash, A. E. Electrophoretic Deposition and Mechanistic Studies of Nano-Al/CuO Thermites. *J. Appl. Phys.* **2012**, *112* (2), 024316. https://doi.org/10.1063/1.4737464.
(124) Egry, I.; Ricci, E.; Novakovic, R.; Ozawa, S. Surface Tension of Liquid Metals and Alloys — Recent Developments. *Adv. Colloid Interface Sci.* **2010**, *159* (2), 198–212. https://doi.org/10.1016/j.cis.2010.06.009.
(125) Johnson, C. E.; Higa, K. T. Iodine-Rich Biocidal Reactive Materials. *MRS Online Proc. Libr.* **2013**, *1521* (1), 307. https://doi.org/10.1557/opl.2013.46.
(126) Wang, H.; Kline, D. J.; Rehwoldt, M.; Zachariah, M. R. Ignition and Combustion Characterization of Ca(IO3)2-Based Pyrotechnic Composites with B, Al, and Ti. *Propellants Explos. Pyrotech.* **2018**, *43* (10), 977–985. https://doi.org/10.1002/prep.201800041.
(127) Sullivan, K. T.; Piekiel, N. W.; Chowdhury, S.; Wu, C.; Zachariah, M. R.; Johnson, C. E. Ignition and Combustion Characteristics of Nanoscale Al/AgIO3: A Potential Energetic Biocidal System. *Combust. Sci. Technol.* **2010**, *183* (3), 285–302. https://doi.org/10.1080/00102202.2010.496378.
(128) Stern, K. H. *High Temperature Properties and Thermal Decomposition of Inorganic Salts with Oxyanions*; CRC Press, 2000.
(129) Ito, N.; Obata, K.; Shindo, Y.; Hakuta, T.; Yoshitome, H. Catalytic Thermal Decomposition of Magnesium Iodate in the Presence of Metal Oxides or Carbon. *Thermochim. Acta* **1984**, *73* (1), 33–40. https://doi.org/10.1016/0040-6031(84)85174-6.
(130) Morton, R. C. B.; McKelvey, V. E. UNITED STATES DEPARTMENT OF THE INTERIOR.
(131) Wang, Y.; Shi, K.; Paul, G. I.; Biswas, P.; Zachariah, M. R. Combustion Behavior of Aluminized Metal Iodate Composites. Part 1: Decomposition Mechanism of Metal Iodates. *Combust. Flame* **2024**, *262*, 113372. https://doi.org/10.1016/j.combustflame.2024.113372.

(132) Wang, Y.; Paul, G. I.; Hagen, E.; Wang, H.; Zachariah, M. R. Combustion Behavior of Aluminized Metal Iodate Composites. Part 2: Iodine and Energy Release Rate. *Combust. Flame* **2024**, *262*, 113373. https://doi.org/10.1016/j.combustflame.2024.113373.

2 Experimental Methods

2.1 Temperature-jump time-of-flight mass spectrometry (T-Jump TOFMS)

Studying the behavior of materials under rapid heating conditions is vital for investigating energetic materials. Temperature-Jump Time-of-Flight Mass Spectrometry (T-Jump/TOFMS) is an analytical tool that combines linear time-of-flight mass spectrometry with rapid heating techniques to detect chemical species. The core principle of this experimental approach is to replicate the heating rate typically provided by a flame front by initiating the reaction at a characteristic heating rate ranging between 10^5 and 10^6 K/s. This high heating rate is crucial for triggering ignition and combustion reactions effectively. The T-Jump setup involves a wire flash heating technique that utilizes a 76 μm diameter platinum wire. This wire is prepared by soldering a segment of 8−12 mm wire between two electrical copper leads. Condensed phase samples can be drop-casted onto the platinum wire to form a thin layer. It is important to ensure that the sample layer is sufficiently thin, as one key assumption of this technique is that the coated sample has a similar temperature to the wire during heating. Rapid heating of the wire is achieved by delivering a single voltage pulse with a predetermined pulse time, typically around 3 ms. Temperature readings with a resolution of 0.1 ms are obtained using the calibrated relationship between the temperature of the platinum wire, derived from its measured resistance, and the current passing through the wire, following the Callendar−Van Dusen equation[1]. The platinum wire can reach temperatures of approximately ~1400 K from room temperature within 3 ms, resulting in a heating rate of approximately ~$4x10^5$ K/s.

The basic schematic of the time-of-flight mass spectrometer is illustrated in Figure 2-1. It is noteworthy that the chamber needs to maintain at high vacuum as the time-of-flight mass spectrometry replies on an environment that the species have essentially no interaction with other gas molecules. The sample on the sample probe undergoes vaporization or gasification through the rapid heating of a platinum wire, after which the vapor or gas is ionized by an electron gun source typically operated at 70 eV. It is worth noting that this electron energy level is adequate to fragment certain species. Ionization occurs between two plates, A1 and A2, initially grounded. For a typical time-resolved measurement, following an electron ionization dwell time of approximately 3 μs, a voltage pulse of -200 V is applied to A2. Consequently, positively charged ions are extracted into the accelerating area between A2 and A3. A constant voltage of -1500 V is maintained for A3, serving as the accelerator and exerting force on the ions to traverse through the time-of-flight tube. A liner, also held at -1500 V within the time-of-flight tube, creates a field-free region to confine the divergence of the ion beam. Additionally, two steering plates currently maintained at a bias of -1600 V perpendicular to A3 optimize the signal by ensuring the ion beam follows the path towards the detector. Initially in the same packet, ions are accelerated differently based on their masses, with lighter ions reaching a higher velocity than heavier ones. Consequently, these ions separate as they travel through the time-of-flight tube, with lighter ions arriving at the detector earlier than heavier ones. Raw data from the detector, presented as a function of time, are output to a Teledyne Lecroy high-frequency oscilloscope for further processing. The electron gun and extraction plates are triggered at intervals of 0.1 ms, typically 100 times (10 ms), resulting in the collection

of 100 spectra for one measurement. This sampling time period can be adjusted according to the intended time scale for the event of interest by altering the sequence number. Tracking the evolution of a single species with a resolution of 0.1 ms is feasible. Coupling time-resolved temperatures of the platinum wire with time-of-flight mass spectrometry provides both time- and temperature-resolved characterization of a reaction.

The raw data obtained from the oscilloscope undergoes processing through a mass-time calibration procedure to generate mass spectra, where the signal intensity is plotted as a function of mass-to-charge ratio (m/z). This calibration involves conducting measurements for various species with known masses across a wide range, typically from m/z=1 to m/z=260. Species that are normally used for calibration include argon, air, SF_6, CuO, $LiIO_3$. The calibration curve follows a general form represented by the equation $\frac{m}{z} = at^2 + bt + c$, where t denotes the time of flight, and a, b, and c are constants. These constants are determined by fitting the time of flight data obtained from ions with known m/z values.

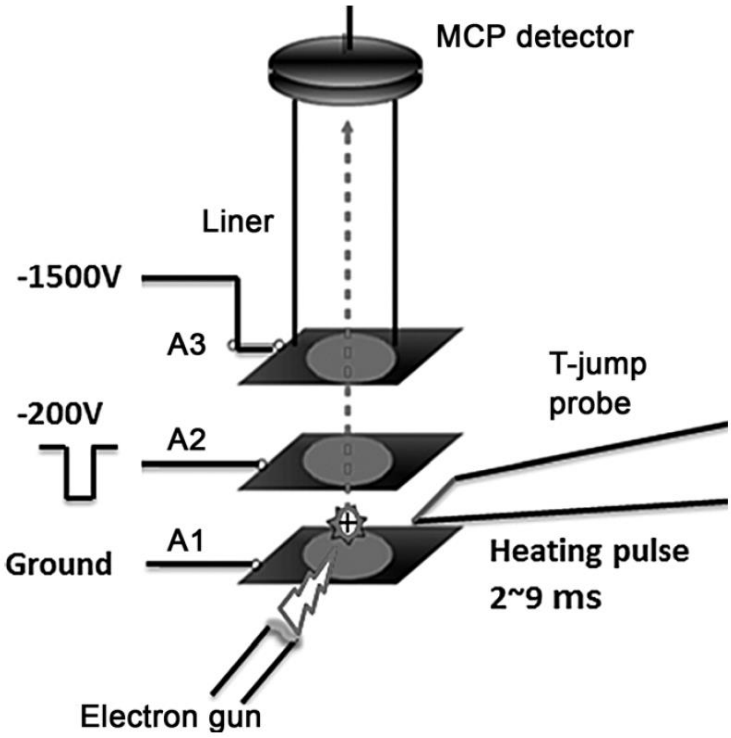

Figure 2-1 Schematic of T-Jump TOFMS system[1]. (*Reproduced with permission from John Wiley and Sons*).

2.2 Temperature-jump ignition

Ignition occurs only at high heating rates, as thermal runaway involves reaction rates and the generation of kinetic energy within the system significantly exceeding the rate at which kinetic energy dissipates from it. Therefore, ignition characterization is conducted using the same heating setup as temperature-jump time-of-flight mass spectrometry to achieve high heating rates. The basic schematic of the temperature-jump (T-Jump) ignition setup is illustrated in Figure 2-2. The chamber primarily consists of a quartz window, a pressure gauge, an inlet for vacuum, and an inlet for gas. Unlike the mass spectrometer chamber, which operates under high vacuum, the T-Jump ignition chamber

can provide various environments, including atmospheric pressure, vacuum, and pressures higher than atmospheric pressure. When testing thermites with solid-state oxidizers, argon is typically used to create an inert environment. In the absence of a solid-state oxidizer, air or oxygen is employed. A high-speed black and white camera is focused on the sample coated on the platinum wire and is triggered simultaneously with the start of heating for the platinum wire. This setup enables direct visualization of an ignition event and facilitates the analysis of the ignition event's timing relative to the start of heating.

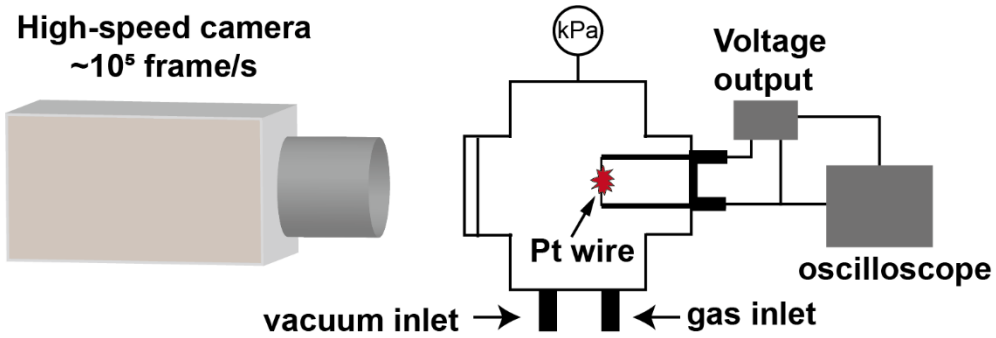

Figure 2-2 Illustration of T-Jump ignition setup.

The ignition time is identified as the time when a sudden increase in light intensity occurs at one or more locations after the trigger event, as depicted in Figure 2-3 (a). Voltage and current data from the platinum wire, with a resolution of 0.1 ms, are processed to generate a plot of wire temperature versus time. The ignition temperature of a sample is determined by comparing the ignition time observed in the video to the temperature of the wire at that moment, as illustrated in Figure 2-3 (b). It is assumed that the temperature of the platinum wire increases continuously, enabling the estimation of the ignition temperature with a resolution of approximately 0.01 ms.

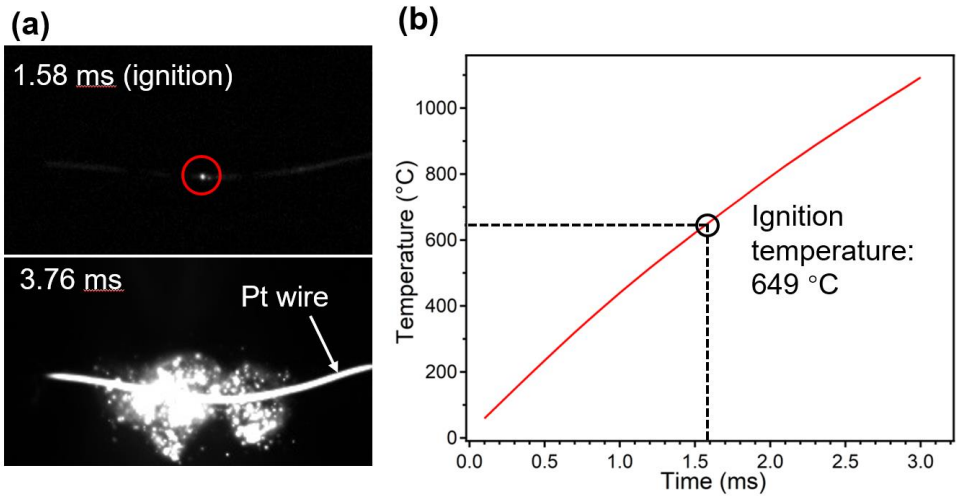

Figure 2-3 Snapshots of an example T-Jump ignition video showing the ignition point by frame-by-frame analysis of the video (a) and the corresponding ignition temperature obtained from the heating profile of the platinum wire.

2.3 3D printing

3D printing plays a crucial role in additive manufacturing, particularly for assembling nanothermites into free-standing composites. In the research conducted for this dissertation, the printing process begins with the preparation of an ink consisting of nanoparticles suspended in a polymer binder solution. Typically, the nanoparticles contain both fuels and oxidizers, with a loading of 90 wt%, while the polymer binder content is maintained at 10 wt%. For the standard printing procedure, a binder solution comprising 4 wt% polyvinylidene fluoride (PVDF) and 6 wt% hydroxypropyl methylcellulose (HPMC) is utilized due to its optimal viscosity. N,N-dimethylformamide (DMF) serves as the solvent because of its ability to dissolve various polymer binders and evaporate at moderately elevated temperatures. Once PVDF and HPMC are completely dissolved,

oxidizer particles are introduced into the viscous solution and then subjected to 30 minutes of sonication. For oxidizers that dissolve in DMF, such as potassium perchlorate, the sample is magnetically stirred until full dissolution instead of being sonicated. Subsequently, fuel particles are added to the suspension, which is then sonicated for an additional 30 minutes before being magnetically stirred overnight. It is imperative to ensure that all oxidizer and fuel powders are fully immersed before sonicating the suspension.

Before printing, the glass substrate of the printer is preheated to approximately 75°C, and the ink is sonicated for about 15 minutes. Typically, an 18-gauge needle is used for printing. During the printing process, it is essential to ensure that each layer is dried adequately before depositing another layer, and the distance between the tip of the needle and the printed layer is maintained at an appropriate distance. After printing, the films are subjected to continuous heating at around 75°C for 30 minutes to remove any remaining DMF. Subsequently, the obtained films are cut into approximately 2 cm sticks for further characterizations.

When printing samples containing much larger particles, such as micron-sized particles, replacing the 18-gauge needle with a 16-gauge or 14-gauge needle has been found to improve printing quality. Additionally, when printing samples with carbon fiber, increasing the viscosity of the ink prolongs the time needed for carbon fiber precipitation, resulting in smoother printing. When using solvents other than DMF, the temperature of the glass substrate needs to be adjusted accordingly. For instance, when a mixture of ethanol and dichloromethane is used as the solvent, room temperature is sufficient for printing.

2.4 Microscopic and macroscopic imaging

High-speed microscopic and macroscopic imaging allow for direct observation of the combustion process of energetic composites *in operando*. The schematic of the basic setup for both microscopic and macroscopic imaging is illustrated in Figure 2-4. For microscopic imaging, a high-speed color camera (Vision Research Phantom VEO710L) is combined with a microscope (Infinity Photo-Optical Model K2 DistaMax). Conversely, macroscopic imaging employs a high-speed color camera (Vision Research Phantom Miro M110). The microscopic imaging setup provides a resolution of 1.7-2.2 μm/pixel, while the macroscopic setup typically offers a resolution around 30 μm/pixel. During a typical measurement, a printed stick is secured on a holder inside a chamber positioned between the two imaging setups. The chamber is usually filled with argon and maintained at atmospheric pressure for a sample with oxidizer. For samples without oxidizer, air is typically employed instead. A nichrome wire, placed adjacent to one side of the stick, is Joule-heated to ignite the stick. The heating of the wire is triggered simultaneously with the two cameras, and the ensuing combustion events are recorded.

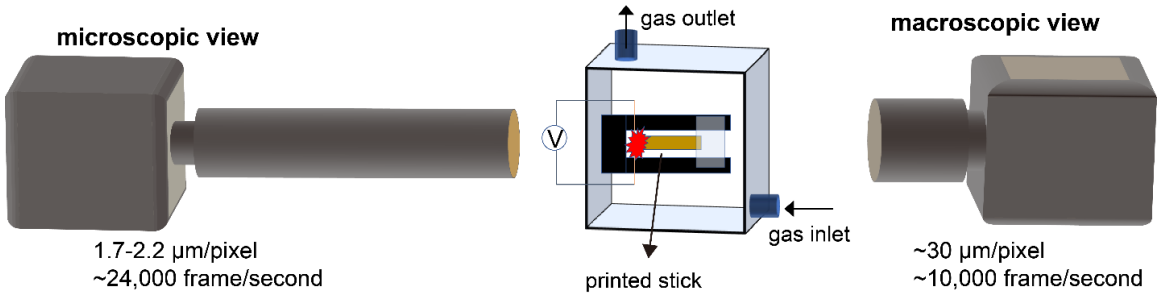

Figure 2-4 Illustration of microscopic and macroscopic imaging setup.

2.5 References

(1) Jian, G.; Zhou, L.; Piekiel, N. W.; Zachariah, M. R. Low Effective Activation Energies for Oxygen Release from Metal Oxides: Evidence for Mass-Transfer Limits at High Heating Rates. *ChemPhysChem* **2014**, *15* (8), 1666–1672. https://doi.org/10.1002/CPHC.201301148.

3 Effect of Alkali Metal Perchlorate and Iodate Type on Boron Ignition: The Role of Oxidizer Phase Change

3.1 Summary

Boron often demonstrates low reactivity despite having high gravimetric and volumetric energy density. Here I explore a family of oxidizers with very similar chemistries to understand controlling mechanisms in boron ignition. Boron nanoparticles with alkali metal perchlorates as well as iodates ($LiClO_4$, $NaClO_4$, $KClO_4$, $LiIO_3$, $NaIO_3$ and KIO_3) were investigated under rapid heating conditions ($\sim 10^5$ K/s) by temperature-jump (T-Jump) ignition and time-of-flight mass spectrometry (TOFMS). T-Jump ignition tests in atmospheric pressure argon show that B/$LiClO_4$, B/$NaClO_4$, B/$LiIO_3$, and B/$NaIO_3$ ignite while B/$KClO_4$ and B/KIO_3 do not, despite the nearly identical chemistries. T-Jump TOFMS results demonstrate a dramatic increase of Cl and I containing species for Li and Na systems relative to K when B is added. Thermogravimetry/differential scanning calorimetry (TGA/DSC) analysis reveals that there is a temperature gap between melting and decomposition onset of $LiClO_4$, $NaClO_4$, $LiIO_3$, and $NaIO_3$, respectively, whereas $KClO_4$ and KIO_3 melt and decompose concurrently. I find that the larger interval between melting and decomposition renders more time for the oxidizer to melt and surround/wet the nanoscale B before decomposing, providing instant access to oxygen for B nanoparticles that results in vigorous ignition. This study of a set of equivalent oxidizers illustrates the important role of transport phenomena and physical properties have on ignition.

3.2 Introduction

Nanoscale particles including boron, aluminum, titanium, silicon, magnesium, and zirconium have been the focus of research for energetic materials including propellants and pyrotechnics due to their potential as high energy density fuels [1–6]. Of these boron has always been ranked as the most attractive due to its very high gravimetric and volumetric energy content [7–9]. However it is well known that boron suffers from slow oxidation kinetics since its native oxide shell boron oxide (B_2O_3) has a low melting point (723 K) and a high boiling point (2130 K) [10], leading to a liquid barrier that retards the reactivity [7–9,11–14]. Another limiting factor is the lowered energy release from combustion of boron in hydrogen containing gases due to the thermodynamically favored formation of HOBO, which "traps" boron and prevents it from forming gaseous B_2O_3 and releasing all its potential energy [9,15]. To overcome the challenge from the low reactivity of boron, various approaches have been investigated, including washing to dissolve the oxide layer [16], using metal carbides for accelerating energy release [17], mixing boron with metal or metal hydride additives [18–25], decreasing the size of boron particles to the nanoscale [26,27], coating boron particles with oxidants, metal fluorides, organics or polymers [3,28–36]. In addition to modifying boron particles, other studies have investigated tuning the ignition and combustion performance of boron using different solid-state oxidizers including metal oxides [10,37], binary metal oxides [10,38], metal oxides with oxygen vacancy [39,40], mixture of graphene oxide and graphite fluoride [41], as well as gaseous fluorine-based oxidizers [9,42]. Alkali metal perchlorates are attractive oxidizers for boron because of their higher oxygen content compared to commonly utilized metal oxides. Moreover, B/$MClO_4$ (M=Li, Na and

K) reactions have much higher combustion enthalpies on both gravimetric and volumetric basis than many common B/metal oxide systems (Figure 3-1). Similarly, B with alkali metal iodates also have higher combustion enthalpies compared to B with these common metal oxide systems. However, the ignition mechanism of boron with these metal perchlorates and iodates as oxidizers have not been widely explored [43].

This chapter systematically investigates the ignition mechanism of boron nanoparticles with alkali metal perchlorates ($LiClO_4$, $NaClO_4$, and $KClO_4$) and iodates ($LiIO_3$, $NaIO_3$, and KIO_3). Temperature-jump ignition (T-Jump ignition) tests and temperature-jump time of flight mass spectrometry (T-Jump/TOFMS) under rapid heating ($\sim 10^5$ K/s) conditions were utilized to analyze ignition and reaction characteristics. Thermal decomposition of alkali metal perchlorates and iodates under slow heating (10 K/min) conditions were conducted with thermogravimetry-differential scanning calorimetry (TGA-DSC) to support the observations from T-Jump measurements. A mechanism explaining the observed ignition behavior difference among the $B/MClO_4$ as well as B/MIO_3 (M=Li, Na, K) composites is proposed.

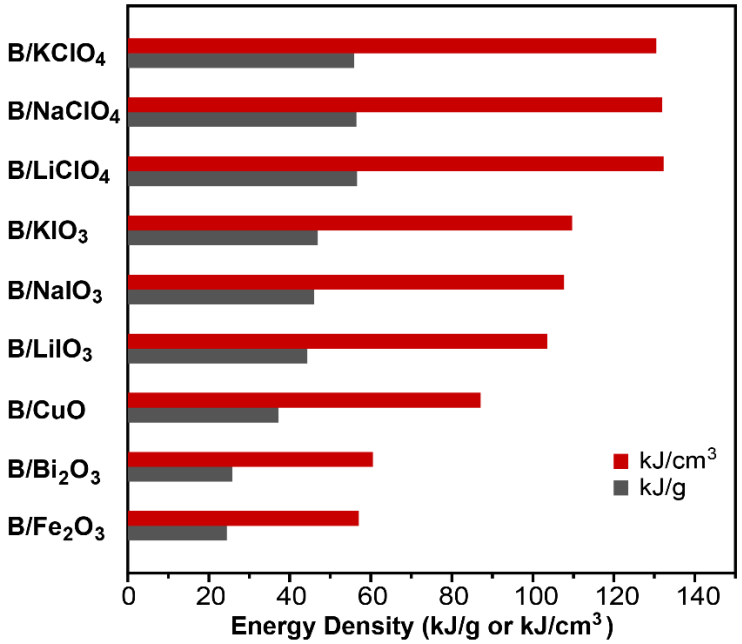

Figure 3-1 Combustion enthalpies of boron with different oxidizers (Φ=1) per g or cm^3 of boron[44].

3.3 Methods

3.3.1 Materials/Sample Preparation

Nanoscale boron (≈100nm, ~85% active) was purchased from US Research Nanomaterials, Inc. $LiClO_4$ (99%), $NaClO_4$ (>98.0%), $KClO_4$ (99%), $NaIO_3$ (99%) were purchased from Alfa Aesar. $LiIO_3$ (97%) and KIO_3 (≥98%) were purchased from Sigma Aldrich (Millipore Sigma). Micron-sized alkali metal perchlorates and iodates particles were synthesized via an aerosol spray pyrolysis (ASP) approach [45,46]. Generally, 1 g of as-purchased larger particles were dissolved into 100 mL of deionized water and the obtained solution was sprayed into small droplets with an atomizer that operated at ~35 psi using compressed air. The droplets passed through a silica-gel diffusion drier to remove water and sequentially passed through a tube furnace that operated at 350 °C for $LiClO_4$ and

$NaClO_4$, 150 °C for $KClO_4$, $LiIO_3$, $NaIO_3$ and KIO_3. The final product was collected on a filter paper.

3.3.2 Characterization

Particles sizes and morphologies of micron-sized alkali metal perchlorates and iodates particles from ASP were characterized by Scanning Electron Microscopy (SEM, FEI NNS450) operating at 20 kV. Active content of B nanopowder was determined with thermogravimetry and differential scanning calorimetry (TGA−DSC) using a Netsch STA449 F3 Jupiter thermal analyzer. Boron powder was loaded into an alumina crucible inside the instrument and heated to 1200 °C at a heating rate of 10 K/min under an oxygen flow of 50 mL/min with an additional isotherm at 1200 °C for 2 h. TGA−DSC tests for thermal decomposition of synthesized alkali metal perchlorates and iodates particles from ASP were conducted using a SDT Q600 from TA Instruments. Generally, the powders were placed into alumina crucibles inside the instrument and heated to 600 or 700 °C under an argon flow of 100 mL/min. X-ray diffraction crystallography (XRD, PANanalytical Empyrean Series 2 diffractometer) was used to characterize the alkali metal perchlorates and iodates particles from ASP with Cu Kα radiation. As shown in Figure S3, the alkali metal perchlorate particles synthesized from ASP were $LiClO_4 \cdot 3H_2O$, a mixture of $NaClO_4 \cdot H_2O$ and $NaClO_4$, $KClO_4$, respectively. H_2O in $LiClO_4 \cdot 3H_2O$ was considered as an oxidizer for boron oxidation when calculating the equivalence ratio according to the following reaction equation (Equation (1)) due to its high content (≈34% of total mass) [7,8]. For simplicity, $LiClO_4 \cdot 3H_2O$ will be referred to as $LiClO_4$.

$$LiClO_4 \cdot 3H_2O + 4B \rightarrow B_2O_3 + 2HOBO + 2H_2 + LiCl \quad (1)$$

H_2O in the mixture of $NaClO_4 \cdot H_2O$ and $NaClO_4$ from ASP was not considered due to its low content (≈3% of the total mass), as shown in Figure 3-5. Equation (2) was used when calculating the equivalence ratio for boron with $NaClO_4$ and $KClO_4$.

$$3ACl O_4 + 8B = 4B_2O_3 + 3ACl \quad (2)$$

Where A=Na and K. Two equivalence ratios mainly, Φ=1 and 1.5, were studied for the three boron/ alkali metal perchlorate systems. Higher equivalence ratios were also studied for B/$LiClO_4$.

XRD results showed the alkali metal iodate particles from ASP were $LiIO_3$, a mixture of $NaIO_3 \cdot H_2O$ and $NaIO_3$, KIO_3, respectively, as show in Figure S5. H_2O in the mixture of $NaIO_3 \cdot H_2O$ and $NaIO_3$ was not considered for calculating the equivalence ratio due to the low content (<3%). Equation (3) was used to determine the equivalence ratio for boron and alkali metal iodates.

$$MIO_3 + 2B = B_2O_3 + MI \quad (3)$$

Where M=Li, Na and K. One equivalence ratio, Φ=1.5, was studied for boron/alkali metal iodate systems.

3.3.3 T-Jump Ignition and T-Jump/TOFMS

The details of T-Jump ignition and T-Jump/TOFMS experiments and the operational settings can be found in previous publications from our group [45,47–51]. The composites were prepared by a physical mixing method. Generally, boron powder and corresponding amounts of oxidizers synthesized from ASP were suspended in hexane in a vial. After 30 mins of sonication, a small amount of the suspension was deposited on the Pt wire (diameter=76 μm, 0.8-1.1 cm length, OMEGA Engineering Inc.) that was soldered

between two copper leads of a T-Jump probe. The Pt wire was resistively heated by a direct current voltage supply that delivers a 3 ms pulsed square wave signal. Fast response thermometry of the Pt wire was acquired and temperature readings were obtained through the calibration relationship between the temperature of the Pt wire and its corresponding resistance from the Callendar-Van Dusen equation. The temperature of the thin coating on Pt wire was approximately the temperature of the wire. The measurements were repeated at least three times for one sample.

For T-Jump/TOFMS, mass spectrometry was obtained by using a trigger signal that communicates wire heating and collection of mass spectra simultaneously. A 70 eV electron gun ionization source was used to ionize gas phase species produced by sample heating. A Teledyne LeCroy 600 MHz oscilloscope was utilized to collect the raw data of mass spectra, current and voltage readings over a 10 ms collection period with 0.1 ms interval. For T-Jump ignition tests, the Pt wire was soldered on a different sample holder that is inserted into a chamber with inlets and outlets for flowing gases and vacuum, a pressure gauge as well as a glass window for imaging of the sample inside the chamber, as described with details in our previous studies [52,53]. The ignition delay time was determined from the video captured with high-speed camera (Vision Research Phantom V12.1). The ignition temperature was estimated by correlating the video and the measured wire temperature. The ignition tests were conducted under 1 atm argon.

3.4 Results and discussion

3.4.1 Ignition under rapid heating rate (~10^5 K/s)

Ignition studies of boron with alkali metal perchlorates and iodates were conducted in 1 atm argon. The representative snapshots of ignition with Φ=1.5 are shown in Figure 3-2 and the progression of ignition with different equivalence ratios are shown in Figure S1 and S2. These results reveal that with Φ=1.5, B/$LiClO_4$ and B/$NaClO_4$, ignite although B/$NaClO_4$ has a less vigorous flame, while B/$KClO_4$ barely ignites, even though some glowing particles are present. Similarly, B/$LiIO_3$ and B/$NaIO_3$ ignite while B/KIO_3 does not. This demonstrates a reactivity difference among these perchlorates as well as iodates acting as oxidizer for boron. I will explore the reasons for these differences in subsequent sections of this chapter.

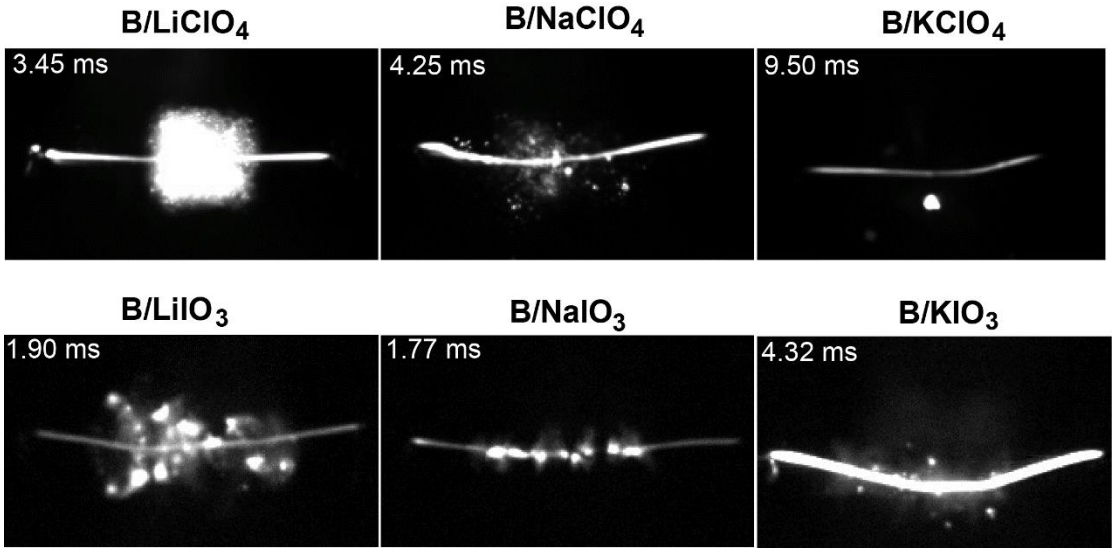

Figure 3-2 T-Jump ignition snapshots of B with $LiClO_4$ (top left), $NaClO_4$ (top middle), $KClO_4$ (top right), $LiIO_3$ (bottom left), $NaIO_3$ (bottom middle) and KIO_3 (bottom right) with peak flame size in 1 atm argon, Φ=1.5. The inserted time in every snapshot is the time after triggering. Note: B/perchlorate (top) snapshots have sensitivity of 1, B/iodate (bottom) snapshots have sensitivity of 16.

Figure S1 shows that B/$NaClO_4$ and B/$KClO_4$ maintain their ignition behavior as equivalence ratio changes from 1 to 1.5, however, B/$LiClO_4$ does not ignite at equivalence ratio of 1 although it ignites vigorously at equivalence ratio of 1.5 and higher equivalence ratios (Figure S7). As mentioned previously, XRD results (Figure S3) show that the particles synthesized from ASP of $LiClO_4$ is actually $LiClO_4 \cdot 3H_2O$, and I was unable to prepare a stable anhydrous sample. Therefore, H_2O is considered as an oxidizer in the equivalence ratio calculation as shown in Equation (1), although the exact reaction mechanism between B and H_2O is not well understood [7–9,54–56]. The fact that B/$LiClO_4$ only ignites when fuel-rich (ignition snapshots of Φ=2 and 3 are shown in Figure S7) suggests a different role of H_2O than what is shown in Equation (1), but details about the role of H_2O are out of the scope of this study, therefore will not be discussed further.

One may surmise the ignition difference simply arises from the thermochemical property difference. But as shown in Figure 3-1, there is no significant difference in reaction enthalpies among B/perchlorates as well as in B/iodates. Therefore, the ignition behavior difference cannot be explained by the thermochemical property of the reactions.

3.4.2 Reaction products under rapid heating rate (~10^5 K/s)

T-Jump/TOFMS was utilized to analyze reaction intermediates and products of metal perchlorates as well as iodates with and without the presence of B under high heating rates (~10^5 K/s). The resulting mass spectra summed over a collection period time of 10 ms at a 0.1 ms interval are displayed in Figure 3-3 (a) and (b) as well as

Figure **3-4** (a) and (b).

The bare metal perchlorates have similar decomposition patterns, releasing the corresponding metal (Li, Na, K), O_2, as well as small amounts of Cl-containing species including Cl, ClO, ClO_2 and Cl_2. When B is introduced, the metal perchlorates behave differently, where the intensity of the Cl-containing species dramatically increases for $LiClO_4$ and $NaClO_4$, however it only increases slightly for $KClO_4$. Semiquantitative analysis of the release behavior of Cl, a representative of the Cl-containing species, was conducted by measuring its peak intensity (m/z=35) of B-$LiClO_4$ and B-$NaClO_4$ upon release relative to B-$KClO_4$ over the 10 ms of collection time. The results displayed in Figure 3-3 (c).

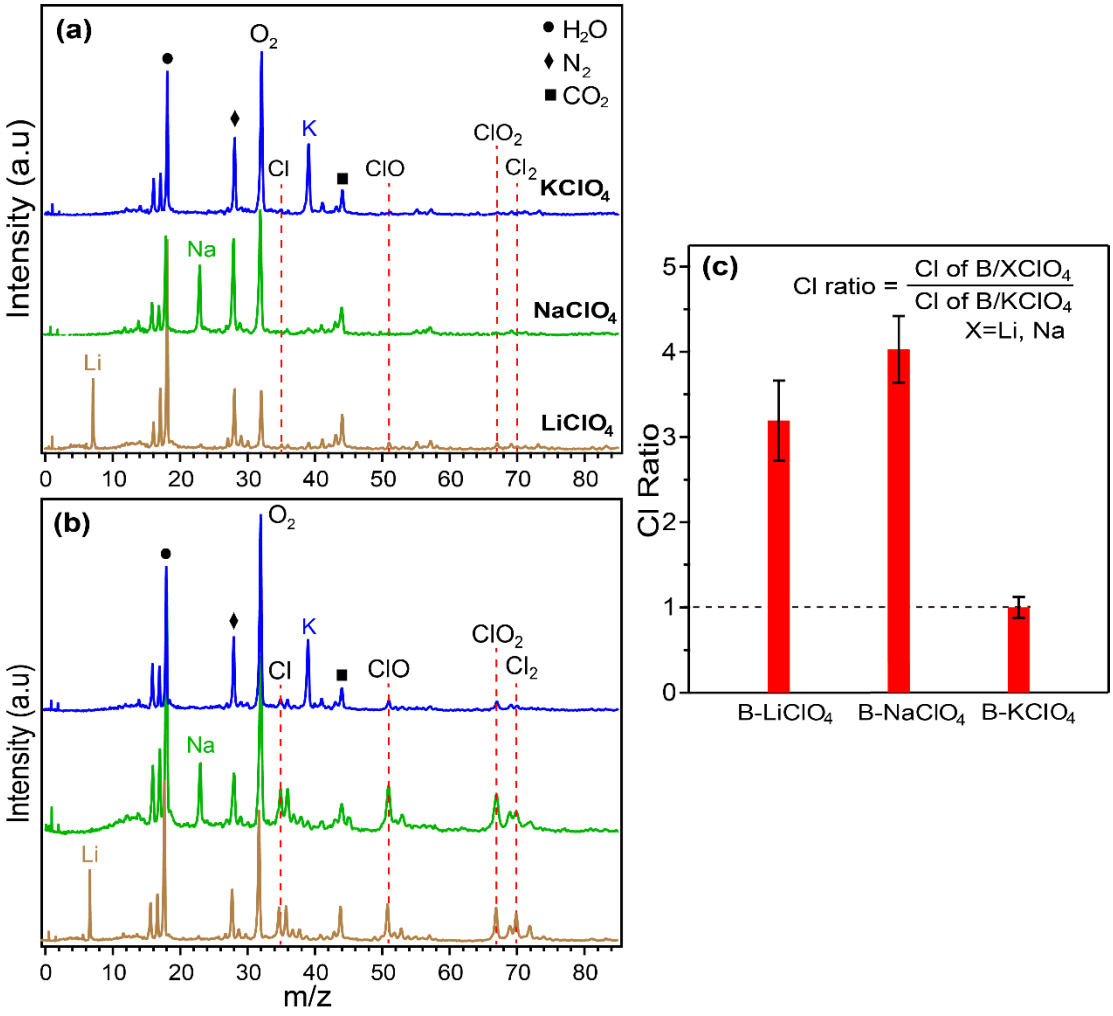

Figure 3-3 Mass spectrum of rapidly heated $LiClO_4$ (bottom), $NaClO_4$ (middle), and $KClO_4$ (top) in (a), and the corresponding composites with B with Φ=1.5 in (b). The spectra are normalized to the corresponding metal ion, and most notable mass species are labeled. (c) the measured relative Cl release of B-$XClO_4$ to the B-$KClO_4$, where X=Li, Na.

A higher intensity of a particular species in the spectra indicates that the average release rate of that species over the collection period is higher. Figure 3-3(c) clearly illuminates that the average rates of release of Cl from B/$LiClO_4$ and B/$NaClO_4$ reactions are much higher (~3X) compared to B/$KClO_4$ reaction. During combustion, a higher energy release rate causes rapid increase in temperature, which in turn leads to an increase

in the reaction rate. As shown in Figure 3-2, B/$LiClO_4$ and B/$NaClO_4$ ignite while B/$KClO_4$ does not, indicating more energy is released from B/$LiClO_4$ and B/$NaClO_4$ than B/$KClO_4$. For B/$LiClO_4$ and B/$NaClO_4$, the significant amount of energy released from the combustion promotes the decomposition of $LiClO_4$ and $NaClO_4$, respectively. Therefore, much more Cl-containing species are released compared to B/$KClO_4$ because decomposition of $KClO_4$ is not enhanced.

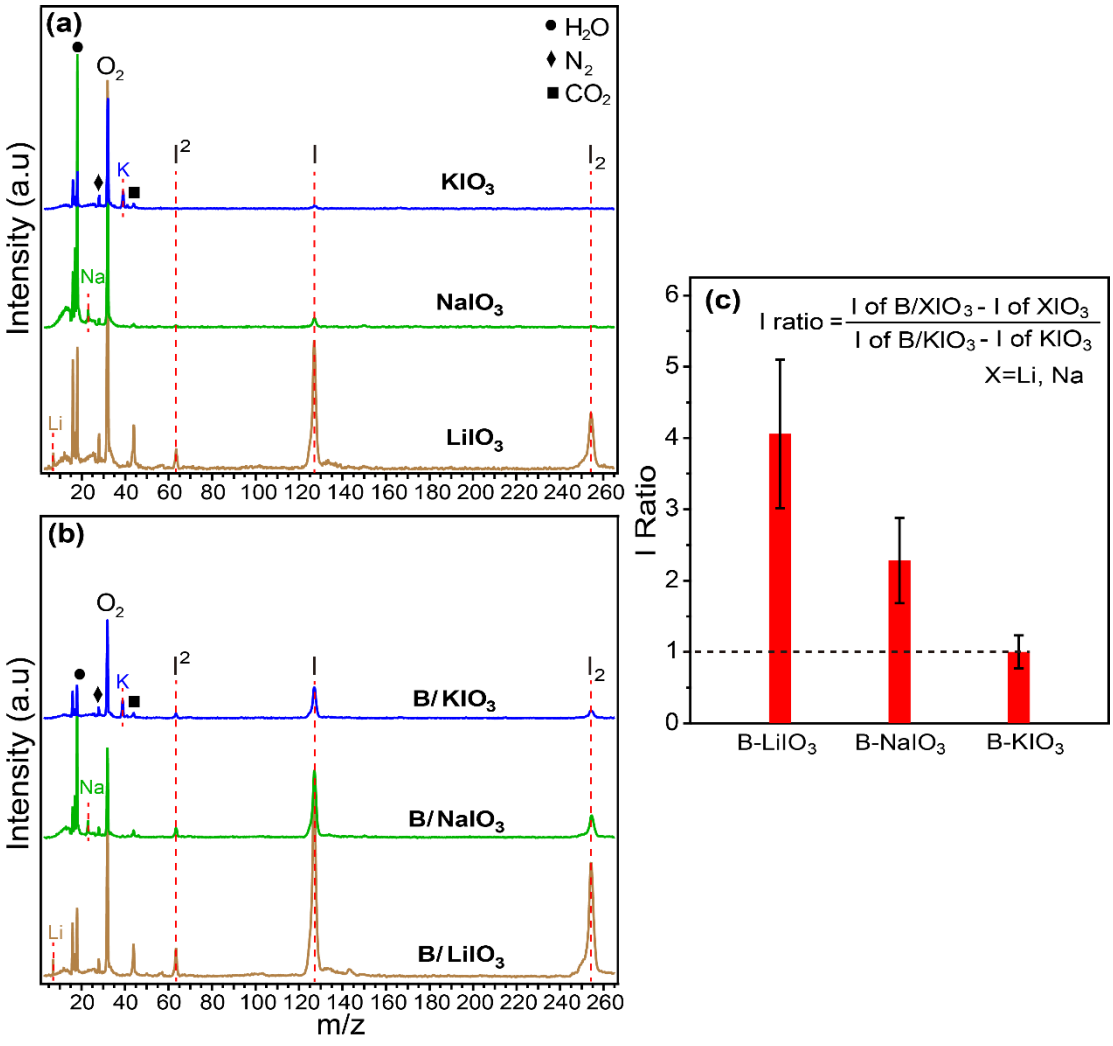

Figure 3-4 Mass spectrum of rapidly heated $LiIO_3$ (bottom), $NaIO_3$ (middle), and KIO_3 (top) in (a), and the corresponding composites with B with Φ=1.5 in (b). The spectra are normalized to the corresponding metal ion, and most notable mass species are labeled. (c) the measured relative Cl release difference between B-$XClO_4$ and XIO_3 to the difference between B-KIO_3 and KIO_3, where X=Li, Na.

Figure **3-4** (a) and (b) display the mass spectra of bare metal iodates and B/iodate composites upon rapid heating. The bare metal iodates share the same decomposition behavior, where they mainly release corresponding metal, O_2, I^2, I and I_2, and the intensity of I-containing species from $LiIO_3$ is much higher than $NaIO_3$ and KIO_3, as shown in

Figure **3-4**. Intensity of I-containing species increases for all three iodates when B is introduced, however, the extent of the increase is different. Semiquantitative analysis displayed in

Figure **3-4** (c) shows that the increase of I release from $LiIO_3$ and $NaIO_3$ is more significant than that of KIO_3 when B is added (>2X). As discussed above, a more significant increase in intensity of the species from decomposition of the oxidizer indicates more energy is released from the combustion reaction. Therefore, the mass spectra result suggests B/$LiIO_3$ and B/$NaIO_3$ release more energy than B/KIO_3. This is consistent with the ignition test results, where B/$LiIO_3$ and B/$NaIO_3$ ignite while B/KIO_3 does not in 1 atm argon.

3.4.3 Thermal behavior under slow heating rate (10 K/min)

This still leaves on the question as to why $KClO_4$ and KIO_3 behave differently compared to their Li and Na counterparts in boron ignition. To explore this difference, thermolysis of the metal perchlorates and iodates were carried out with slow heating rate

(10 K/min) thermogravimetric-differential scanning calorimetry (TGA-DSC) in an argon environment. The results are shown in Figure 3-5 and Figure 3-6.

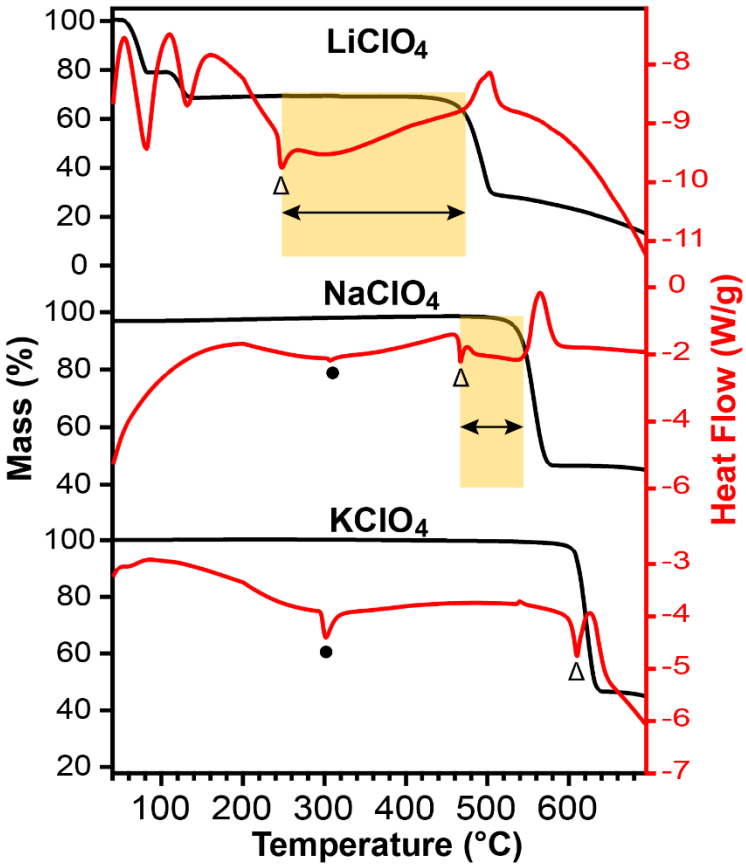

Figure 3-5 TGA-DSC of $LiClO_4$ (top), $NaClO_4$ (middle) and $KClO_4$ (bottom) under argon environment. ● indicates phase transition and Δ indicates melting. The orange area indicates the temperature range from melting to decomposition onset.

$LiClO_4$ shows previously documented multiple-stepped mass loss that results from dehydration up to 150 °C, a melting endotherm at 248 °C and exothermic decomposition onset at 473 °C [57,58]. $NaClO_4$ shows an endotherm at 306 °C that corresponds to a phase transition from orthorhombic to cubic, a melting endotherm at 467 °C, followed by an

exothermic decomposition onset at 542 °C [59,60]. Similarly, $KClO_4$ demonstrates a phase change from rhombic to cubic at 302 °C, a melting process at 610 °C and a decomposition onset at 610 °C [61]. One think that became clear from these results is that there is a temperature gap between the melting and decomposition temperature which I have shown as the shaded area. As the shaded areas indicate, the temperature intervals between melting and decomposition onset are ∼225 °C, ∼75 °C and ∼0 °C for $LiClO_4$, $NaClO_4$ and $KClO_4$, respectively. I believe it is this temperature gap that provides a key to understanding our observations.

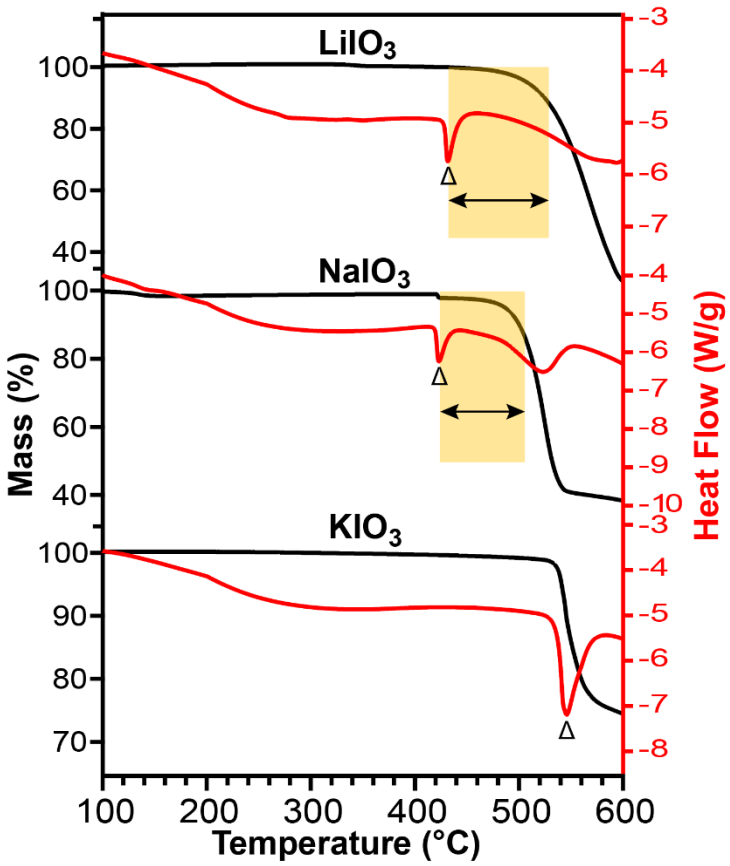

Figure 3-6 TGA/DSC of $LiIO_3$ (top), $NaIO_3$ (middle) and KIO_3 (bottom) under argon environment. Δ indicates melting. The orange area indicates the temperature range from melting to decomposition onset.

Thermolysis results of iodates further support this hypothesis. Iodates demonstrate similar decomposition behaviors to perchlorates, where $LiIO_3$ and $NaIO_3$ decompose about 95 °C and 80 °C above the melting point, respectively, while KIO_3 melts and decomposes at about the same temperature, as shown in Figure 3-6 [62]. From the proposed hypothesis, as the intervals between melting and decomposition of $LiIO_3$ and $NaIO_3$ are much larger than that of KIO_3, it is expected B/$LiIO_3$ and B/$NaIO_3$ to have more violent ignition than

B/KIO_3. T-Jump ignition test result matches this expectation and validates the hypothesis (Figure 3-2).

3.4.4 Proposed mechanism

As a general rule, all things being equal, one should expect that the more mobile the reactants are, the more facile should be the chemistry, assuming all other variables are invariant. As such one might expect then that a reactant that releases an oxidizer fragment would most efficiently react with fuel if it is in intimate contact prior to release of the oxidant. In particular I see from Figure 3-5 that $LiClO_4$ particles melt well before decomposing and thus one might expect wetting of the B nanoparticles to occur before $LiClO_4$ decomposes. Therefore, B nanoparticles have instant access to oxidant upon $LiClO_4$ decomposition, leading to violent ignition. $NaClO_4$ behaves similarly to $LiClO_4$, but its particles are much larger (as shown in Figure S4) and its melting-decomposition temperature difference is smaller than $LiClO_4$, thus there is less time for melted $NaClO_4$ to surround/wet B nanoparticles before decomposition, resulting in less vigorous ignition. $KClO_4$ is significantly different than either $LiClO_4$ or $NaClO_4$, as its decomposition and melting are concurrent, which means that most of oxidant release occurs in the proximity of B but not necessarily in intimate contact with B and only B nanoparticles with intimate contact with $KClO_4$ initially are oxidized efficiently, leading to a barely visible ignition event. This likely is the reason why $KClO_4$ appears to be a poor oxidizer for B. Ignition behavior difference among B/iodates can be explained in the same manner, where $LiIO_3$ and $NaIO_3$ melt and wet the B nanoparticles before decomposing and result in more violent ignition than KIO_3, which melts and decomposes concurrently. Although the particles

synthesized from ASP for KIO_3 are slightly larger than $LiIO_3$ and $NaIO_3$, as shown in Figure S6, the ignition behaviors with B are far too different to be explained by the particle size difference.

Ignition of B/$XClO_4$ and B/XIO_3 (X=Li or Na) may also be further facilitated by the added complexity of the interaction between melted B_2O_3 and $XClO_4$ or XIO_3. Nanoscale B has native B_2O_3 shell that melts at 450 °C [10], a temperature that is above the melting temperature, but below the decomposition temperature of $XClO_4$ and XIO_3, suggesting that both the oxide shell and $XClO_4$ or XIO_3 are melted before the oxidizer decomposition. It is likely that the liquid perchlorates or iodates are partially miscible with melted B_2O_3, so the liquid B_2O_3 is partially dissolved into the liquid perchlorates or iodates before the decomposition of these oxidizers. This means that the thickness of liquid barrier that retards the B oxidation is reduced and diffusion of oxygen to the boron core or boron to the oxide surface is enhanced, leading to a more violent ignition. While for B/$KClO_4$ and B/KIO_3, this effect is negligible since $KClO_4$ and KIO_3 have a minimum window between melting and decomposing. These effects are summarized in Figure 3-7.

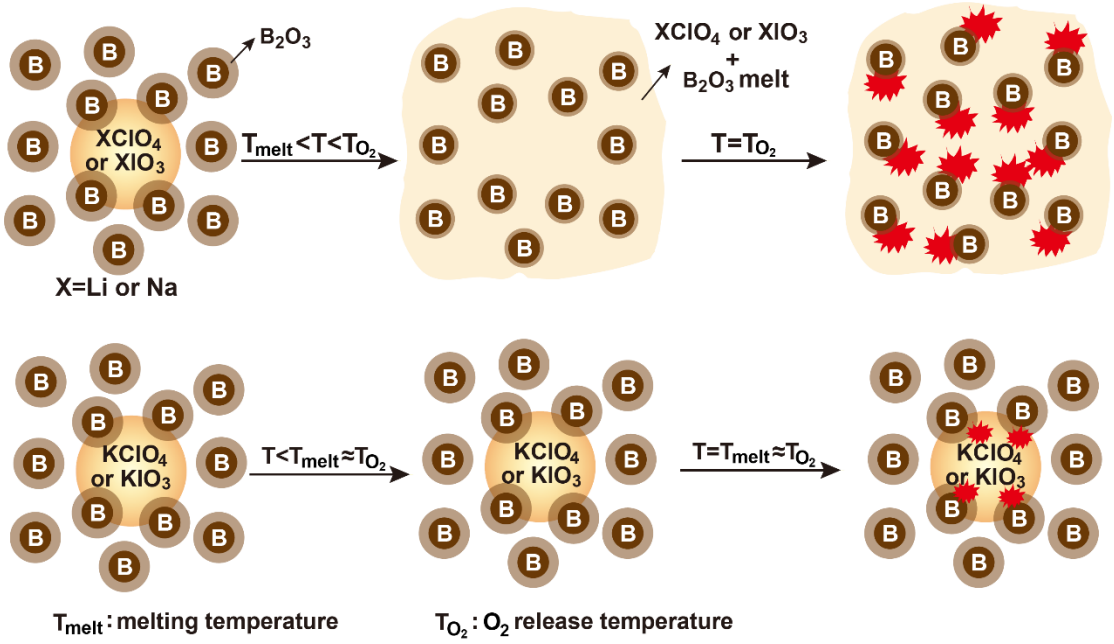

Figure 3-7 Proposed mechanism for the correlation of the ignition behavior and the difference between melting and decomposition temperatures.

3.5 Conclusions

This study investigates the role of alkali metal perchlorate and iodate type on the ignition behavior of nanoscale B. B/$XClO_4$ and B/XIO_3 (X=Li or Na) composites ignite in atmospheric pressure argon while B/$KClO_4$ and B/KIO_3 do not. T-Jump TOFMS demonstrates that when B is added, there is a dramatic increase of Cl-containing and I-containing species from $XClO_4$ and XIO_3 than $KClO_4$ and KIO_3, respectively, which is attributed to the higher amount of heat released from the ignition reaction. TGA/DSC analysis reveals that there is an interval of ~225 °C and ~75 °C between the melting point and decomposition onset of $LiClO_4$ and $NaClO_4$ respectively, whereas $KClO_4$ melts and decomposes concurrently. Similarly, $LiIO_3$ and $NaIO_3$ decompose ~95 °C and ~80 °C after melting, respectively, while KIO_3 melts and decomposes at about the same temperature, A

mechanism emphasizing the difference between melting and decomposition of the oxidizers is proposed to explain the difference in ignition behavior among the B/metal salt-based oxidizer composites. For B/$XClO_4$ and B/XIO_3, the larger interval between melting and decomposition renders more time for the oxidizer to melt and surround/wet the nanoscale B before decomposing, providing instant access to oxidant for B nanoparticles that results in vigorous ignition. While for B/$KClO_4$ and B/KIO_3, only B nanoparticles that are in intimate contact with $KClO_4$ or KIO_3 particles have access to oxygen upon the oxidizer decomposition, resulting in a less likely ignition event.

3.6 References

(1) Rehwoldt, M. C.; Yang, Y.; Wang, H.; Holdren, S.; Zachariah, M. R. Ignition of Nanoscale Titanium/Potassium Perchlorate Pyrotechnic Powder: Reaction Mechanism Study. *J. Phys. Chem. C* **2018**, *122* (20), 10792–10800. https://doi.org/10.1021/acs.jpcc.8b03164.

(2) Egan, G. C.; Sullivan, K. T.; Olson, T. Y.; Han, T. Y.-J.; Worsley, M. A.; Zachariah, M. R. Ignition and Combustion Characteristics of Nanoaluminum with Copper Oxide Nanoparticles of Differing Oxidation State. *J. Phys. Chem. C* **2016**, *120* (51), 29023–29029. https://doi.org/10.1021/acs.jpcc.6b11081.

(3) Valluri, S. K.; Schoenitz, M.; Dreizin, E. Bismuth Fluoride-Coated Boron Powders as Enhanced Fuels. *Combust. Flame* **2020**, *221*, 1–10. https://doi.org/10.1016/j.combustflame.2020.07.023.

(4) Lempert, D. B.; Nechiporenko, G. N.; Manelis, G. B. Energetic Capabilities of High-Density Composite Solid Propellants Containing Zirconium or Its Hydride. *Combust. Explos. Shock Waves* **2011**, *47* (1), 45–54. https://doi.org/10.1134/S0010508211010060.

(5) Xu, F.; Nava, G.; Biswas, P.; Dulalia, I.; Wang, H.; Alibay, Z.; Gale, M.; Kline, D. J.; Wagner, B.; Mangolini, L.; Zachariah, M. R. Energetic Characteristics of Hydrogenated Amorphous Silicon Nanoparticles. *Chem. Eng. J.* **2021**, 133140. https://doi.org/10.1016/j.cej.2021.133140.

(6) Ghildiyal, P.; Biswas, P.; Herrera, S.; Xu, F.; Alibay, Z.; Wang, Y.; Wang, H.; Abbaschian, R.; Zachariah, M. R. Vaporization-Controlled Energy Release Mechanisms Underlying the Exceptional Reactivity of Magnesium Nanoparticles. *ACS Appl. Mater. Interfaces* **2022**. https://doi.org/10.1021/acsami.1c22685.

(7) King, M. K. Ignition and Combustion of Boron Particles and Clouds. *J. Spacecr. Rockets* **1982**, *19* (4), 294–306. https://doi.org/10.2514/3.62256.

(8) Yeh, C. L.; Kuo, K. K. Ignition and Combustion of Boron Particles. *Prog. Energy Combust. Sci.* **1996**, *22* (6), 511–541. https://doi.org/10.1016/S0360-1285(96)00012-3.

(9) Ulas, A.; Kuo, K. K.; Gotzmer, C. Ignition and Combustion of Boron Particles in Fluorine-Containing Environments. *Combust. Flame* **2001**, *127* (1), 1935–1957. https://doi.org/10.1016/S0010-2180(01)00299-1.

(10) Huang, S.; Deng, S.; Jiang, Y.; Zheng, X. Experimental Effective Metal Oxides to Enhance Boron Combustion. *Combust. Flame* **2019**, *205*, 278–285. https://doi.org/10.1016/j.combustflame.2019.04.018.

(11) Ao, W.; Wang, Y.; Li, H.; Xi, J.; Liu, J.; Zhou, J. Effect of Initial Oxide Layer on Ignition and Combustion of Boron Powder. *Propellants Explos. Pyrotech.* **2014**, *39* (2), 185–191. https://doi.org/10.1002/prep.201300079.

(12) Chintersingh, K.-L.; Sun, Y.; Schoenitz, M.; Dreizin, E. L. Heterogeneous Reaction Kinetics for Oxidation and Combustion of Boron. *Thermochim. Acta* **2019**, *682*, 178415. https://doi.org/10.1016/j.tca.2019.178415.

(13) Krier, H.; Burton, R. L.; Spalding, M. J.; Rood, T. J. Ignition Dynamics of Boron Particles in a Shock Tube. *J. Propuls. Power* **1998**, *14* (2), 166–172. https://doi.org/10.2514/2.5282.
(14) Gottfried, J. L.; Wainwright, E. R.; Huang, S.; Jiang, Y.; Zheng, X. Probing Boron Thermite Energy Release at Rapid Heating Rates. *Combust. Flame* **2021**, *231*, 111491. https://doi.org/10.1016/j.combustflame.2021.111491.
(15) Yetter, R. A.; Rabitz, H.; Dryer, F. L.; Brown, R. C.; Kolb, C. E. Kinetics of High-Temperature B/O/H/C Chemistry. *Combust. Flame* **1991**, *83* (1), 43–62. https://doi.org/10.1016/0010-2180(91)90202-M.
(16) Chintersingh, K.-L.; Schoenitz, M.; Dreizin, E. L. Oxidation Kinetics and Combustion of Boron Particles with Modified Surface. *Combust. Flame* **2016**, *173*, 288–295. https://doi.org/10.1016/j.combustflame.2016.08.027.
(17) Liang, D.; Liu, J.; Qiu, Q. Nano Carbides-Mediated Acceleration of Energy Release Behavior of Amorphous Boron during Ignition and Combustion. *Energy Rep.* **2020**, *6*, 1160–1169. https://doi.org/10.1016/j.egyr.2020.05.002.
(18) Xi, J.; Liu, J.; Wang, Y.; Liang, D.; Zhou, J. Effect of Metal Hydrides on the Burning Characteristics of Boron. *Thermochim. Acta* **2014**, *597*, 58–64. https://doi.org/10.1016/j.tca.2014.10.017.
(19) Liu, J.; Xi, J.; Yang, W.; Hu, Y.; Zhang, Y.; Wang, Y.; Zhou, J. Effect of Magnesium on the Burning Characteristics of Boron Particles. *Acta Astronaut.* **2014**, *96*, 89–96. https://doi.org/10.1016/j.actaastro.2013.11.039.
(20) Korotkikh, A. G.; Sorokin, I. V. Effect of Me/B-Powder on the Ignition of High-Energy Materials. *Propellants Explos. Pyrotech. n/a* (n/a). https://doi.org/10.1002/prep.202100180.
(21) Chintersingh, K.-L.; Schoenitz, M.; Dreizin, E. L. Effect of Purity, Surface Modification and Iron Coating on Ignition and Combustion of Boron in Air. *Combust. Sci. Technol.* **2019**, *0* (0), 1–20. https://doi.org/10.1080/00102202.2019.1702649.
(22) Chintersingh, K.-L.; Schoenitz, M.; Dreizin, E. L. Transition Metal Catalysts for Boron Combustion. *Combust. Sci. Technol.* **2019**, *0* (0), 1–25. https://doi.org/10.1080/00102202.2019.1696317.
(23) Liang, D.; Liu, J.; Xiao, J.; Xi, J.; Wang, Y.; Zhou, J. Effect of Metal Additives on the Composition and Combustion Characteristics of Primary Combustion Products of B-Based Propellants. *J. Therm. Anal. Calorim.* **2015**, *122* (1), 497–508. https://doi.org/10.1007/s10973-015-4750-6.
(24) Ma, M.; Liu, G.; Qin, Z.; Zhang, R.; Ying, Y.; Xu, L.; Liu, D. Effects of Aluminum Addition on Flash Ignition and Combustion of Boron Nanoparticles. *Combust. Flame* **2022**, *236*, 111762. https://doi.org/10.1016/j.combustflame.2021.111762.
(25) Hashim, S. A.; Karmakar, S.; Roy, A. Effects of Ti and Mg Particles on Combustion Characteristics of Boron–HTPB-Based Solid Fuels for Hybrid Gas Generator in Ducted Rocket Applications. *Acta Astronaut.* **2019**, *160*, 125–137. https://doi.org/10.1016/j.actaastro.2019.04.002.

(26) Young, G.; Sullivan, K.; Zachariah, M. R.; Yu, K. Combustion Characteristics of Boron Nanoparticles. *Combust. Flame* **2009**, *156* (2), 322–333. https://doi.org/10.1016/j.combustflame.2008.10.007.
(27) Song, Q.; Cao, W.; Wei, X.; Liu, J.; Yuan, J.; Li, X.; Guo, X.; Gao, D. Laser Ignition and Combustion Characteristics of Micro- and Nano-Sized Boron under Different Atmospheres and Pressures. *Combust. Flame* **2021**, *230*, 111420. https://doi.org/10.1016/j.combustflame.2021.111420.
(28) Liu, T.-K.; Luh, S.-P.; Perng, H.-C. Effect of Boron Particle Surface Coating on Combustion of Solid Propellants for Ducted Rockets. *Propellants Explos. Pyrotech.* **1991**, *16* (4), 156–166. https://doi.org/10.1002/prep.19910160403.
(29) Deshmukh, P. R.; Lee, H.; Kim, Y.; Shin, W. G. Ignition and Oxidation Performance of SnO2 Coated Boron Particles: A Solid Fuel for Energetic Applications. *J. Alloys Compd.* **2021**, 161123. https://doi.org/10.1016/j.jallcom.2021.161123.
(30) Keerthi, V.; Nie, H.; Pisharath, S.; Hng, H. H. Combustion Characteristics of Fluoropolymer Coated Boron Powders. *Combust. Sci. Technol.* **2020**, *0* (0), 1–16. https://doi.org/10.1080/00102202.2020.1804885.
(31) Shyu, I.-M.; Liu, T.-K. Combustion Characteristics of GAP-Coated Boron Particles and the Fuel-Rich Solid Propellant. *Combust. Flame* **1995**, *100* (4), 634–644. https://doi.org/10.1016/0010-2180(94)00032-N.
(32) Jiang, Y.; Dincer Yilmaz, N. E.; Barker, K. P.; Baek, J.; Xia, Y.; Zheng, X. Enhancing Mechanical and Combustion Performance of Boron/Polymer Composites via Boron Particle Functionalization. *ACS Appl. Mater. Interfaces* **2021**. https://doi.org/10.1021/acsami.1c06727.
(33) Xi, J.; Liu, J.; Wang, Y.; Liang, D.; Li, H.; Zhou, J. Role of Oxalic Acid in Promoting Ignition and Combustion of Boron: An Experimental and Theoretical Study. *Propellants Explos. Pyrotech.* **2014**, *39* (6), 844–851. https://doi.org/10.1002/prep.201400048.
(34) Van Devener, B.; Perez, J. P. L.; Jankovich, J.; Anderson, S. L. Oxide-Free, Catalyst-Coated, Fuel-Soluble, Air-Stable Boron Nanopowder as Combined Combustion Catalyst and High Energy Density Fuel. *Energy Fuels* **2009**, *23* (12), 6111–6120. https://doi.org/10.1021/ef900765h.
(35) Hu, Y.; Wang, X.; Zhang, J.; Zhu, Z.; Ren, X.; Yang, Y.; Lin, K.; Pang, A.; Shuai, Y. Encapsulated Boron-Based Energetic Spherical Composites with Improved Reaction Efficiency and Combustion Performance. *Chem. Eng. J.* **2022**, 134478. https://doi.org/10.1016/j.cej.2021.134478.
(36) Piao, J.; Deng, L.; Mao, Y.; Wang, J.; Zhang, L. Promoting the Combustion Properties of Boron Powder through In-Situ Coating. *Nano Sel. n/a* (n/a). https://doi.org/10.1002/nano.202100344.
(37) Liu, T.; Chen, X.; Xu, H.; Han, A.; Ye, M.; Pan, G. Preparation and Properties of Boron-Based Nano-B/NiO Thermite. *Propellants Explos. Pyrotech.* **2015**, *40* (6), 873–879. https://doi.org/10.1002/prep.201400308.

(38) Valluri, S. K.; Gandhi, P. M.; Schoenitz, M.; Dreizin, E. L. Boron-Rich Composite Thermite Powders with Binary Bi2O3·CuO Oxidizers. *Energy Fuels* **2021**. https://doi.org/10.1021/acs.energyfuels.1c01052.
(39) Wang, X.; Wu, T.; Wang, H.; DeLisio, J. B.; Yang, Y.; Zachariah, M. R. Boron Ignition and Combustion with Doped δ-Bi2O3: Bond Energy/Oxygen Vacancy Relationships. *Combust. Flame* **2018**, *197*, 127–133. https://doi.org/10.1016/j.combustflame.2018.07.015.
(40) Wang, H.; Ren, H.; Yin, L.; Li, Y.; Wu, X. High Energy Release Boron-Based Material with Oxygen Vacancies Promoting Combustion. *Chem. Eng. J.* **2022**, *430*, 133027. https://doi.org/10.1016/j.cej.2021.133027.
(41) Jiang, Y.; Demko, A. R.; Baek, J.; Shi, X.; Vallez, L.; Ning, R.; Zheng, X. Facilitating Laser Ignition and Combustion of Boron with a Mixture of Graphene Oxide and Graphite Fluoride. *Appl. Energy Combust. Sci.* **2020**, *1–4*, 100013. https://doi.org/10.1016/j.jaecs.2020.100013.
(42) Spalding, M. J.; Krier, H.; Burton, R. L. Boron Suboxides Measured during Ignition and Combustion of Boron in Shocked Ar/F/O2 and Ar/N2/O2 Mixtures. *Combust. Flame* **2000**, *120* (1), 200–210. https://doi.org/10.1016/S0010-2180(99)00082-6.
(43) Liu, P.; Liu, L.; He, G. Effect of Solid Oxidizers on the Thermal Oxidation and Combustion Performance of Amorphous Boron. *J. Therm. Anal. Calorim.* **2016**, *124* (3), 1587–1593. https://doi.org/10.1007/s10973-016-5252-x.
(44) *Materials Project*. https://materialsproject.org/ (accessed 2021-12-09).
(45) Zhou, W.; DeLisio, J. B.; Wang, X.; Zachariah, M. R. Reaction Mechanisms of Potassium Oxysalts Based Energetic Composites. *Combust. Flame* **2017**, *177*, 1–9. https://doi.org/10.1016/j.combustflame.2016.05.024.
(46) Wu, T.; SyBing, A.; Wang, X.; Zachariah, M. R. Aerosol Synthesis of Phase Pure Iodine/Iodic Biocide Microparticles. *J. Mater. Res.* **2017**, *32* (4), 890–896. https://doi.org/10.1557/jmr.2017.6.
(47) Jian, G.; Piekiel, N. W.; Zachariah, M. R. Time-Resolved Mass Spectrometry of Nano-Al and Nano-Al/CuO Thermite under Rapid Heating: A Mechanistic Study. *J. Phys. Chem. C* **2012**, *116* (51), 26881–26887. https://doi.org/10.1021/jp306717m.
(48) Jian, G.; Chowdhury, S.; Sullivan, K.; Zachariah, M. R. Nanothermite Reactions: Is Gas Phase Oxygen Generation from the Oxygen Carrier an Essential Prerequisite to Ignition? *Combust. Flame* **2013**, *160* (2), 432–437. https://doi.org/10.1016/j.combustflame.2012.09.009.
(49) DeLisio, J. B.; Hu, X.; Wu, T.; Egan, G. C.; Young, G.; Zachariah, M. R. Probing the Reaction Mechanism of Aluminum/Poly(Vinylidene Fluoride) Composites. *J. Phys. Chem. B* **2016**, *120* (24), 5534–5542. https://doi.org/10.1021/acs.jpcb.6b01100.
(50) Rehwoldt, M. C.; Wang, Y.; Xu, F.; Ghildiyal, P.; Zachariah, M. R. High-Temperature Interactions of Metal Oxides and a PVDF Binder. *ACS Appl. Mater. Interfaces* **2022**. https://doi.org/10.1021/acsami.1c20938.
(51) Biswas, P.; Ghildiyal, P.; Kwon, H.; Wang, H.; Alibay, Z.; Xu, F.; Wang, Y.; Wong, B. M.; Zachariah, M. R. Rerouting Pathways of Solid-State Ammonia Borane Energy Release. *J. Phys. Chem. C* **2021**. https://doi.org/10.1021/acs.jpcc.1c08985.

(52) Zhou, W.; DeLisio, J. B.; Wang, X.; Egan, G. C.; Zachariah, M. R. Evaluating Free vs Bound Oxygen on Ignition of Nano-Aluminum Based Energetics Leads to a Critical Reaction Rate Criterion. *J. Appl. Phys.* **2015**, *118* (11), 114303. https://doi.org/10.1063/1.4930889.
(53) Xu, F.; Biswas, P.; Nava, G.; Schwan, J.; Kline, D. J.; Rehwoldt, M. C.; Mangolini, L.; Zachariah, M. R. Tuning the Reactivity and Energy Release Rate of I2O5 Based Ternary Thermite Systems. *Combust. Flame* **2021**, *228*, 210–217. https://doi.org/10.1016/j.combustflame.2020.12.047.
(54) Ao, W.; Wang, Y.; Wu, S. Ignition Kinetics of Boron in Primary Combustion Products of Propellant Based on Its Unique Characteristics. *Acta Astronaut.* **2017**, *136*, 450–458. https://doi.org/10.1016/j.actaastro.2017.03.002.
(55) Vovchuk, Ya. I.; Zolotko, A. N.; Klyachko, L. A.; Polishchuk, D. I.; Shevchuk, V. G. Gasification of Boron Oxide. *Combust. Explos. Shock Waves* **1974**, *10* (4), 538–540. https://doi.org/10.1007/BF01465287.
(56) Yoshida, T.; Yuasa, S. Effect of Water Vapor on Ignition and Combustion of Boron Lumps in an Oxygen Stream. *Proc. Combust. Inst.* **2000**, *28* (2), 2735–2741. https://doi.org/10.1016/S0082-0784(00)80694-3.
(57) Application and Research on the Generation of Oxygen from the Decomposition of Lithium Perchlorate--*Ship Electronic Engineering* **2012** 08 https://en.cnki.com.cn/Article_en/CJFDTotal-JCGC201208046.htm (accessed 2021-04-26).
(58) Non-isothermal Decomposition Mechanism and Kinetics of LiClO_4 in Nitrogen--*Chemical Research in Chinese Universities* **2010** 02. https://www.cnki.com.cn/Article/CJFDTotal-GHYJ201002033.htm (accessed 2021-04-26).
(59) Becker, C. R.; Currano, L. J.; Churaman, W. A.; Stoldt, C. R. Thermal Analysis of the Exothermic Reaction between Galvanic Porous Silicon and Sodium Perchlorate. *ACS Appl. Mater. Interfaces* **2010**, *2* (11), 2998–3003. https://doi.org/10.1021/am100975u.
(60) Devlin, D. J.; Herley, P. J. Thermal Decomposition and Dehydration of Sodium Perchlorate Monohydrate. *React. Solids* **1987**, *3* (1), 75–84. https://doi.org/10.1016/0168-7336(87)80019-0.
(61) Pourmortazavi, S. M.; Fathollahi, M.; Hajimirsadeghi, S. S.; Hosseini, S. G. Thermal Behavior of Aluminum Powder and Potassium Perchlorate Mixtures by DTA and TG. *Thermochim. Acta* **2006**, *443* (1), 129–131. https://doi.org/10.1016/j.tca.2005.11.045.
(62) Haynes, W. M. *CRC Handbook of Chemistry and Physics*; CRC Press, 2014.

3.7 Supporting information

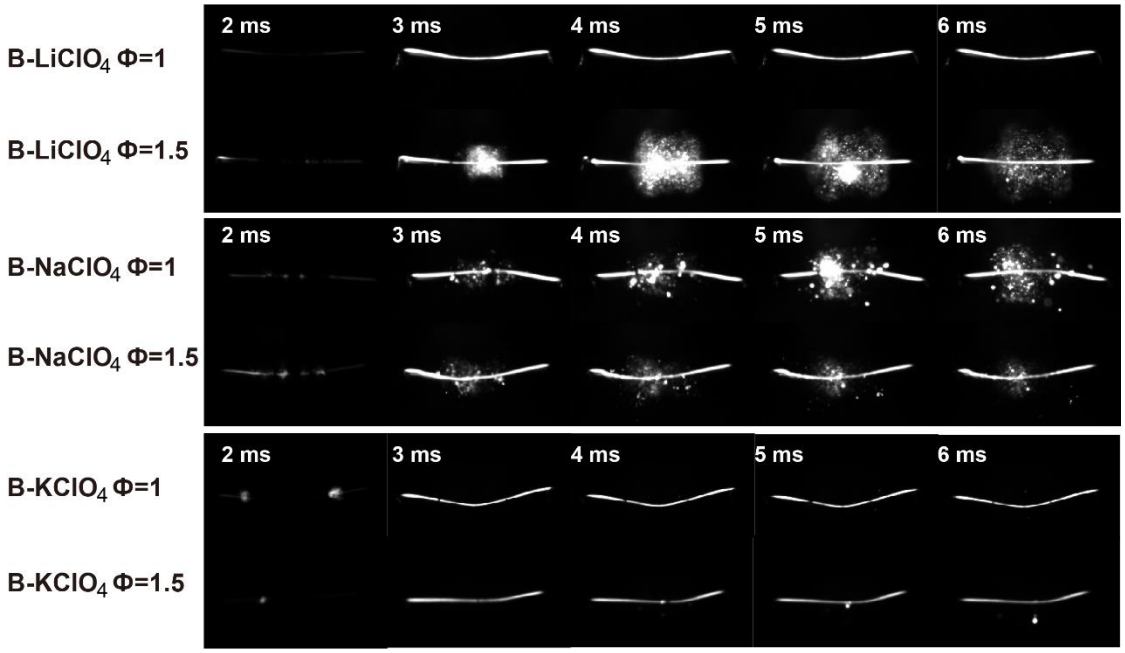

Figure S1 T-Jump ignition snapshots of B-$LiClO_4$ (top), B-$NaClO_4$ (middle) and B-$KClO_4$ (bottom) with Φ=1 and 1.5 in 1atm argon. Sensitivity: 1.

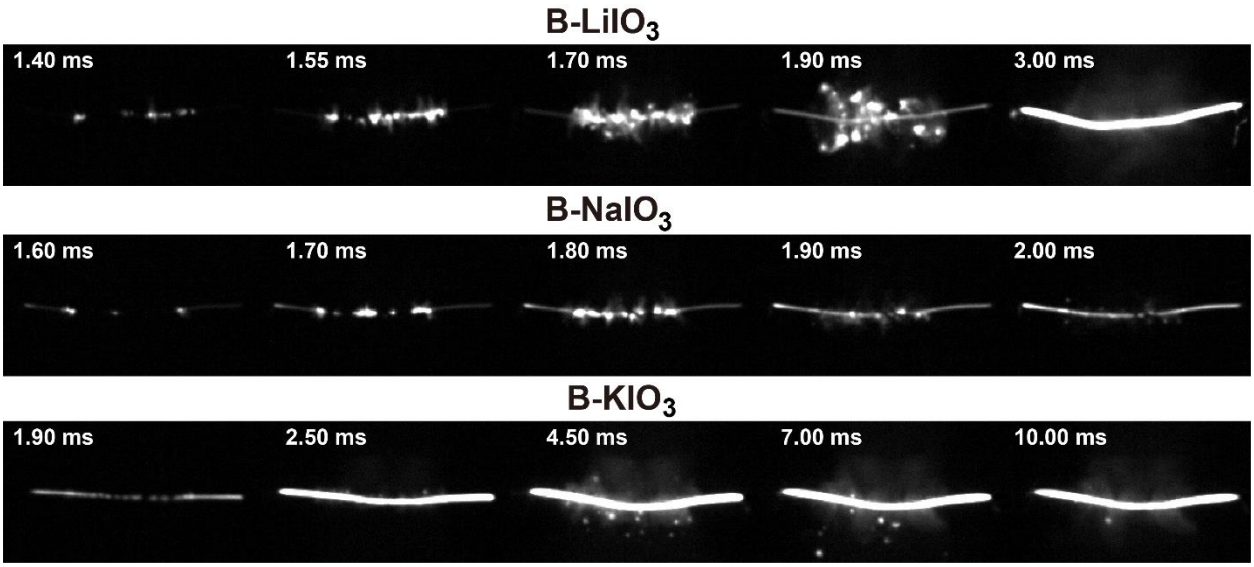

Figure S2 T-Jump ignition snapshots of B-LiIO3 (top), B-NaIO3 (middle) and B-KIO3 (bottom) in 1 atm argon, Φ=1.5. Sensitivity:16

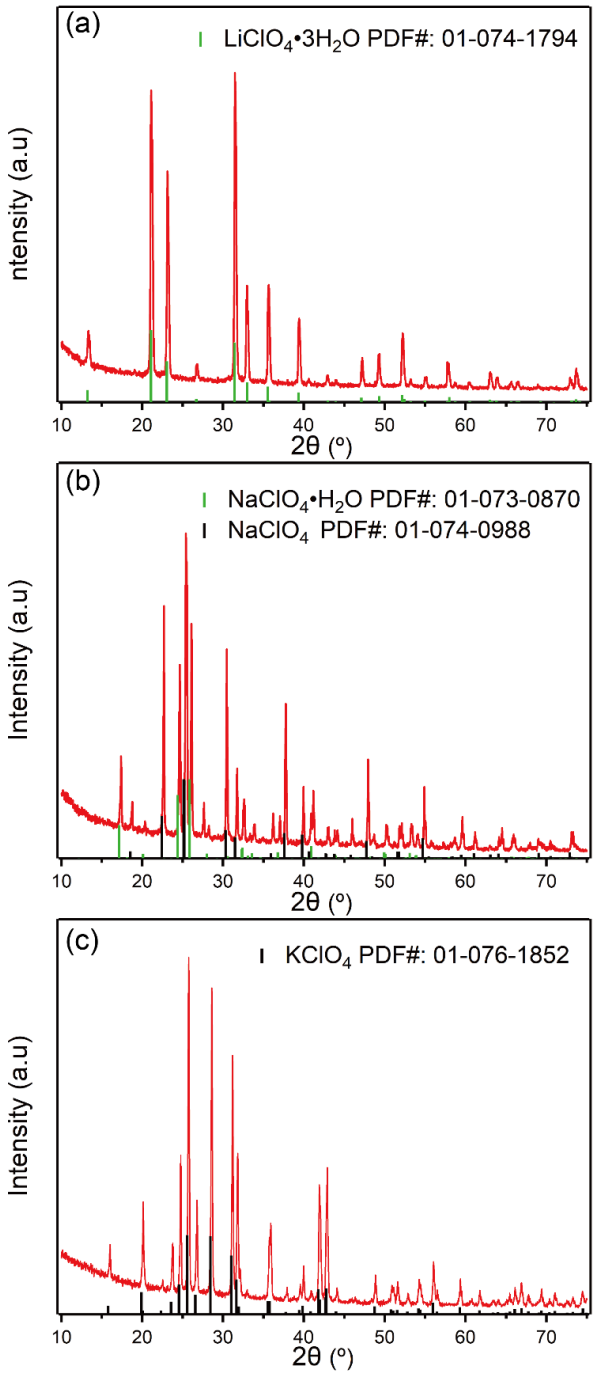

Figure S3 XRD analysis of particles synthesized from ASP for $LiClO_4$ (top), $NaClO_4$ (middle) and $KClO_4$ (bottom).

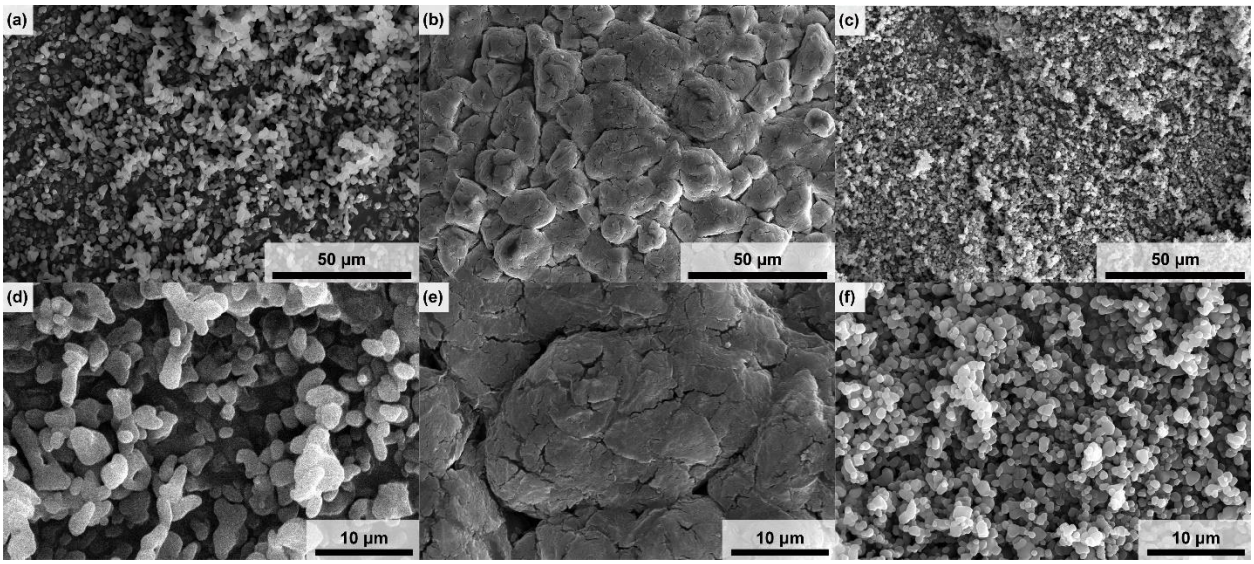

Figure S4 SEM of particles synthesized from ASP for $LiClO_4$ (a) and (d), $NaClO_4$ (b) and (e), and $KClO_4$ (c) and (f).

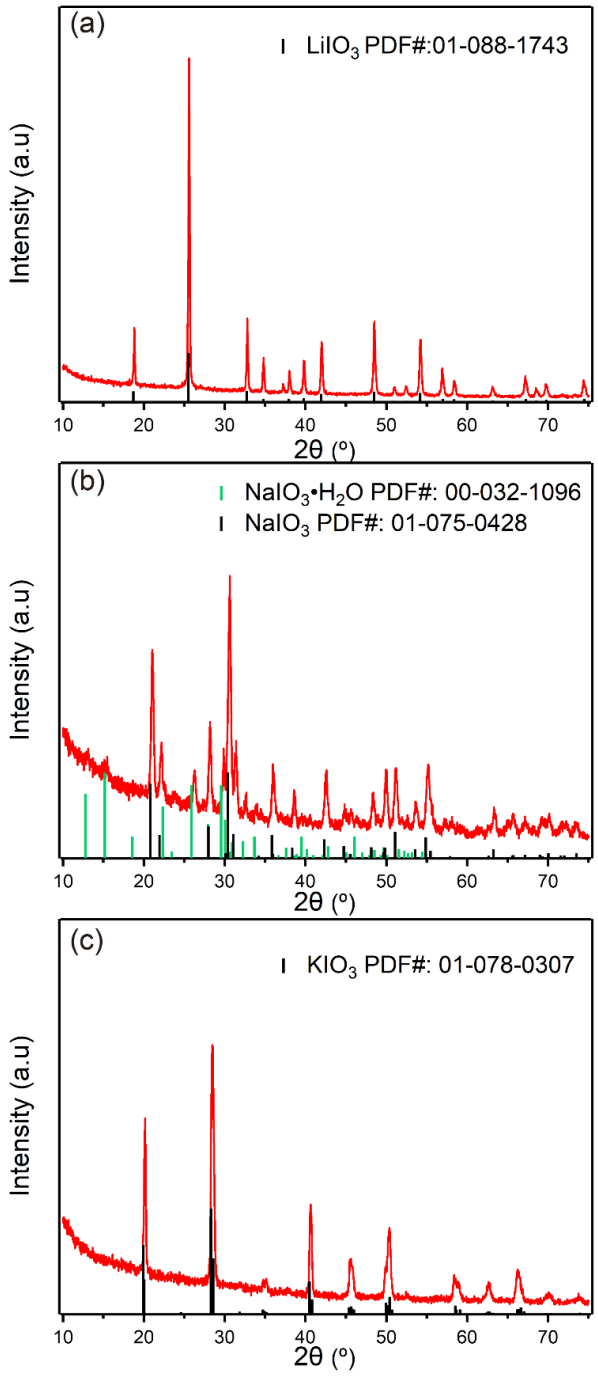

Figure S5 XRD analysis of particles synthesized from ASP for $LiIO_3$ (top), $NaIO_3$ (middle) and KIO_3 (bottom).

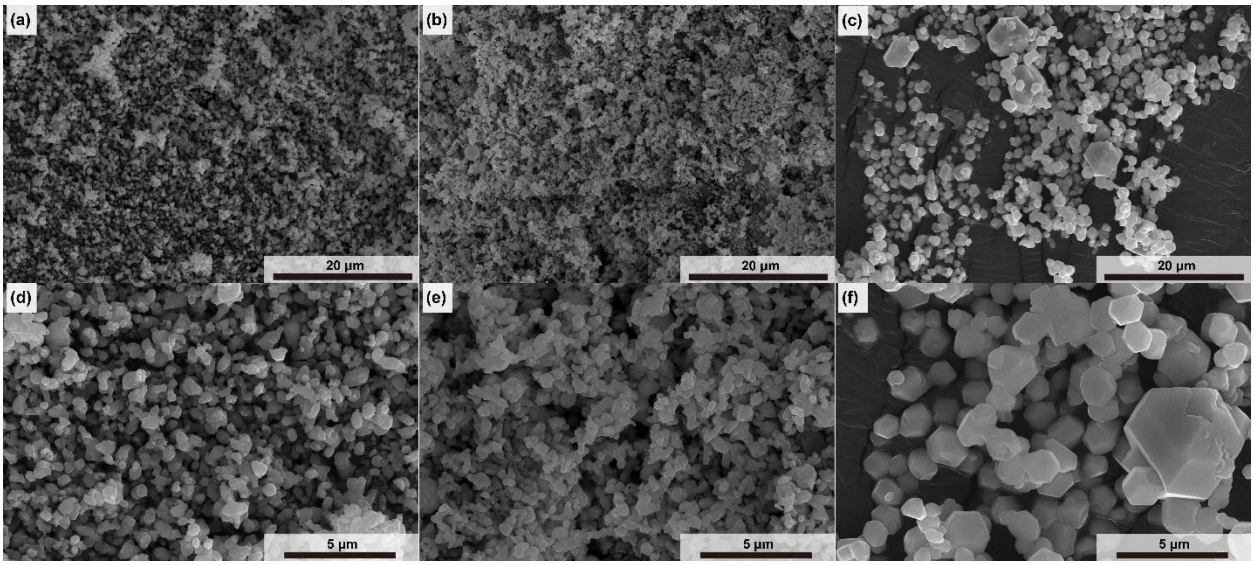

Figure S6 SEM of particles synthesized from ASP for $LiIO_3$ (a) and (d), $NaIO_3$ (b) and (e), and KIO_3 (c) and (f).

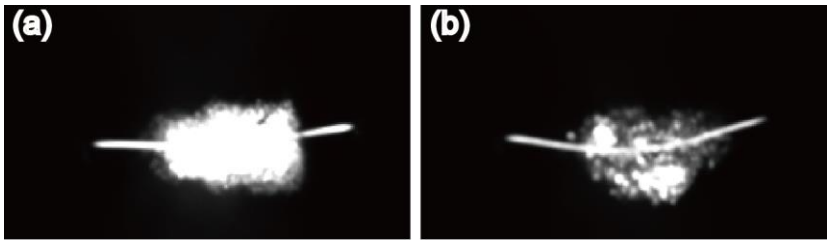

Figure S7 T-Jump ignition snapshot of B-$LiClO_4$ with Φ=2 (a) and Φ=3 (b) in 1atm argon.

4 Imaging the Combustion Characteristics of Al, B, and Ti Composites

4.1 Summary

In this study, I prepare 90 wt% loading composites of Al, B, and Ti with $KClO_4$ by 3D printing and study their combustion characteristics with high-speed videography and pyrometry. Combustion characteristics are found to be strongly dependent on the fuel type. For Al, Al droplets with Al_2O_3 caps form and coalesce before departing the burning surface, while for B and Ti, fractal-shaped agglomerates form. Temperatures of the burning particles (droplet/agglomerates) are determined with color imaging-pyrometry. The combustion characteristics are attributed to the physical properties, e.g. melting and boiling points, of these fuels and their corresponding oxides. I can observe particles residing and burning on the propellant surface for times on the order of ~1-5 ms. This is significantly lower than the theoretical particle burn time, suggesting particles undergo incomplete combustion on the burning surface, consistent with the experimental observation that particles continue to burn after departing the surface. The estimated particle downstream burning distance is significantly larger than the observed luminous zone, implying it does not represent the complete flame zone. Since Al undergoes vapor phase combustion while B and Ti combust in the condense phase, burn rate of Al should be drastically higher than B and Ti, However, the differences are not as significant as expected. This is attributed to the formation of much larger droplets for Al that results in dramatically longer particle burn times.

4.2 Introduction

Energetic nanocomposites, such as nanothermites typically consist of nanoscale fuels and oxidizers, offer higher energy release rates compared to their micron counterparts due to significantly increased interfacial area and reduced diffusion distance between fuel and oxidizer[1–3]. Nevertheless the enhanced combustion rates are not as high as they should be based on simple theoretical arguments. One contributing factor is the loss of nanostructure during a reaction, which may be responsible for the lower than expected energy release rate[4–8]. The loss of nanostructure from reactive sintering has a significant impact on the combustion behavior of the composite[7]. Nanoscale aluminum, boron, and titanium are attractive in nanothermites based on their potential as high energy density fuels and possess very different physical properties such as metal and metal oxide melting points, which can impact sintering rates[9–12]. Aluminum has been used as the primary fuel in solid rocket propellant and other propulsive systems due to its ready availability and high enthalpy[13–15]. Boron has very high gravimetric and volumetric energy content and titanium is a viable alternative fuel source[11,16–18]. Therefore probing and understanding the combustion dynamics of these nanoscale fuels are essential for their practical application.

Previous studies have demonstrated that imaging techniques are particularly useful in probing spatial and temporal combustion dynamics[19–21]. Studies investigating aluminum particle combustion have utilized imaging techniques coupled with holography and pyrometry for quantifying position, size, and velocity of aluminum particles as well as estimating particle temperatures[22,23]. Although titanium and boron combustion has been investigated with videography and pyrometry[18,24–26], these studies are far less prevalent as

compared to aluminum, and a systematic study focusing on combustion behavior differences among different metal fuels is still lacking.

In this chapter, I prepare free-standing $KClO_4$/nanoscale Al, B, and Ti composites at 90% loading by 3D printing, and investigate their combustion characteristics systematically. $KClO_4$ is used as the oxidizer since its decomposition products, O_2 and KCl (boiling point of 1412 °C)[27,28], are gaseous at the temperature of interest, thus presumably there is little condensed-phase residue interacting with fuel agglomerates during combustion. High-speed (μs) videos at high resolution (μm) are obtained for visualizing the combustion processes and physical properties of the as-formed agglomerates in-operando. Color imaging pyrometry is utilized to estimate the temperature profile of the reacting zone and provide information about the particle combustion of these metals. Scanning Electron Microscopy (SEM) with energy-dispersive spectrometry (EDS) is employed to analyze the post-combustion product and provide insight into combustion process. Burn rate of these composites are measured and relative energy release rate are calculated.

4.3 Materials and Methods

4.3.1 Materials

Aluminum nanoparticles (Al NPs, ~50 nm, 67 wt% active) were obtained from Argonide Corporation. Titanium nanoparticles (Ti NPs, ~50 nm, 70 wt% active) and boron nanoparticles (B NPs, ~100 nm, 85 wt% active) were purchased from US Research Nanomaterials. The active content of these fuels was determined with thermogravimetry

and differential scanning calorimetry (TGA−DSC) using a Netsch STA449 F3 Jupiter thermal analyzer. Potassium perchlorate ($KClO_4$, 99%) was purchased from Alfa Aesar. Polyvinylidene Fluoride (PVDF, average molecular weight: ~534,000) was purchased from Sigma-Aldrich and METHOCEL™ F4M Hydroxypropyl Methylcellulose (HPMC) was obtained from Dow Chemical Company. Poly(propylene carbonate) (PPC) pellets (Mw196 kDa) were gifted by Novomer. N, N dimethylformamide (DMF, 99.8%) was purchased from Fisher Scientific and used as a solvent to dissolve the above polymers as well as $KClO_4$.

4.3.2 Preparation of ink and direct ink writing of 90 wt% loading M/$KClO_4$ composites

The details on ink preparation and printing with 90 wt% nanoparticle loading composites can be found in our previous study[29]. Generally, the inks were prepared by firstly dissolving 4 wt% of PVDF and 6 wt% of HPMC or 10 wt% PPC in DMF (all composites use PVDF/HPMC as binders unless otherwise noted). The effect of binder (4 wt% of PVDF and 6 wt% of HPMC) on combustion of the agglomerates is believed to be insignificant due to the low content, low gas generation, and miminal chemical reactions between the fuels and the decomposition product of the polymers[30]. $KClO_4$ was then dissolved in this solution and fuel nanoparticles were added to the obtained solution. The mixture was then ultrasonicated for 30 mins and magnetically stirred overnight. The amount of fuel and $KClO_4$ was determined with the following equations to prescribe the stoichiometric ratio.

$$8Al + 3KClO_4 = 4Al_2O_3 + 3KCl \quad (1)$$

$$8B + 3KClO_4 = 4B_2O_3 + 3KCl \quad (2)$$

$$2Ti + KClO_4 = 2TiO_2 + KCl \quad (3)$$

For printing, an ink was extruded through an 18-gauge nozzle and directly written in a pre-designed pattern on a preheated (~75 °C) glass substrate. During printing, I ensured that every layer was dry before the deposition of the next layer. After printing, the obtained films were heated at ~75 °C for 30 mins to remove the remaining solvent. Then the films were cut into ~2 cm long sticks for combustion characterizations.

4.3.3 SEM/EDS

The morphology and composition of the 3D-printed samples and combustion residues were characterized by scanning electron microscope (SEM, Thermo-Fisher Scientific NNS450) coupled with energy dispersive X-ray spectroscopy (EDS). SEM images of the as-received fuel nanoparticles and cross section of the printed sticks are displayed in Figure S1 and Figure S2, respectively. The post-combustion product was collected by placing a piece of carbon tape ~1.5 cm away from a printed composite before combustion tests. For Al-$KClO_4$, the larger particles did not attach on the tape probably because of the deposition of KCl and aluminum oxide nanoparticles (as shown in Figure S3). To resolve this issue and visualize larger agglomerates in SEM, post-combustion product of Al-$KClO_4$ was collected on glass at the same distance from the composite (~1.5 cm), then the product was washed with water briefly to dissolve KCl nanoparticles. To minimize oxidation of the particles from water, the washing process was performed by

adding water to the post-combustion product and followed by immediate vortexing for ~20 s. Then the suspension was centrifuged immediately, and precipitate was collected and dried under vacuum in a desiccator before SEM.

4.3.4 Microscopic and macroscopic imaging

The details of the imaging process can be found in previous publications from our group[31]. Generally, two imaging systems were used for capturing the combustion process of the composites. One of them was the microscopic imaging system with high-speed camera (Vision Research Phantom VEO710L) coupled with Infinity Photo-Optical Model K2 DistaMax, and the other one was the macroscopic imaging system with high-speed camera (Vision Research Phantom Miro M110). Printed sticks (~2 cm long) were mounted on a stage inside a chamber filled with argon that was placed between the two imaging systems and settings were adjusted so that the surfaces of the sticks were in focus in two imaging systems. The sticks were then ignited with a Joule-heated nichrome wire. The burning process was recorded at a sample rate of 24 000 frame/s (512 x 512 pixels, 1.7 μm/pixel) with a microscopic imaging system and 10 000 frame/s with the macroscopic imaging system.

Size measurement was performed with ImageJ. Only particles that were about to depart from the burning surface or already departed were measured. For B-$KClO_4$ and Ti-$KClO_4$, agglomerates we observed, so an area equivalent diameter is reported. To obtain reasonable statistics at least 120 particles were measured for each composite.

4.3.5 Three-color imaging pyrometry

Details about three-color imaging pyrometry can be found in our previous studies[1,32,33]. Briefly, channel intensities of three colors (red, green, and blue) from the Bayer filter and their ratios were used for estimating the temperature of the sample with a custom MATLAB routine assuming graybody emission behavior of the sample. Calibration factors were obtained by the response to a blackbody source (Mikron M390). Temperature uncertainty was estimated to be nominally 200-300 K[32,34].

It is worth noting that I use the entire spectral range for the temperature measurement, the issues with which as McNesby *et al* pointed out[35], is the possibility of atomic/molecular interference which leads to error in temperature calculation. Our research group has estimated the error being less than 300 K based on black body calibration and wire emission for this study[32,34]. When the error exceeds this threshold, the data is removed. For this study interference from atomic/molecular emission BO_2 has characteristic green emission that results in error in temperature calculation. To circumvent this problem, two-color pyrometry is used for measuring the agglomerate temperature of B-$KClO_4$, the details of which can be found in 4.3.6.

4.3.6 Two-color imaging pyrometry

For the sample of B-$KClO_4$, imaging data was also processed as two-color pyrometry similarly to the three-color process, using a short pass filter (Edmunds Optics, 625 nm 50 mm Diameter, OD 4.0 Shortpass Filter #84-724) placed between the camera and the sample to cut-off wavelengths above 625 nm. The theoretical curves were generated using Planck's law and the response spectrum of the CMOS sensor of the camera

after removing wavelengths above 625 nm from the response spectrum. These curves were then fitted to a polynomial. The usage of the short pass filter resulted in a different calibration curve compared to the previous calibration result without the filter, therefore calibration was performed with a short pass filter. Calibration data obtained with a black body source (Mikron M390) at known temperatures were compared with the theoretical curves and was fit to a linear correction function with the corrected estimated error being 2-4%. A custom MATLAB script demosaiced the videos and used the polynomial fit from the theoretical curves and linear correction function to estimate the temperature of the burning particles. Two-color (red and blue) pyrometry was used by neglecting the green channel when analyzing the B-$KClO_4$ composite, as the green molecular emission from BO_2 corrupts the temperature estimation.

4.3.7 CHEETAH calculation

CHEETAH was performed with constant pressure (1 atm) where only the fuel (including native oxide) and the oxidizer of the composites were considered.

4.4 Results and discussion

4.4.1 Combustion behavior at the microscopic scale

High-speed microscopic video enables direct observation of events near the flame front and adds insight into the combustion behavior of a thermite reaction. Figure 4-1 displays the representative snapshots taken from the high-speed microscopic videos for different composites. All the three composites show cone-shaped flame front that is

attributed to the porosity difference arising from printing, where the edge of the stick has a higher solvent evaporation rate that results in a higher porosity.

As shown in Figure 4-1 (a), molten droplets form on the burning surface of Al-$KClO_4$. Prior to departing from the burning surface, the moving droplets coalesce into larger droplets with sizes typically below 150 μm (Figure 4-2). The molten droplets, particularly those leaving the burning surface, are surrounded by smoke which are presumably dispersed aluminum oxide particles nucleated from the oxidation of aluminum vapor[20,22]. The dark lobes on the molten droplets are Al_2O_3 caps, which may form from three sources: 1) phase separation of the native oxide shell (33 wt%) of Al nanoparticles along sintering/coalescence, 2) condensation of oxide smoke, and 3) Al droplet oxidation (mostly happens before departing from the burning surface)[20,36,37]. For the latter, oxygen penetrates into an Al droplet and Al-O solution forms, which then phase separates into liquid Al and Al_2O_3 when the dissolved oxygen reaches the solubility limit[20]. Following phase separation, the oxide retracts into a distinct cap through surface tension forces[37]. Rotation is observed on most of the departed droplets, although the rotation frequency varies significantly, for example ~4800 Hz vs ~400 Hz as shown in Figure S4 and Figure S5 and is due to asymmetric burning of the particle, leading to asymmetric gas generation[23,36,38]. Bubbling and bursting of droplets are also observed, as shown in Figure S6.

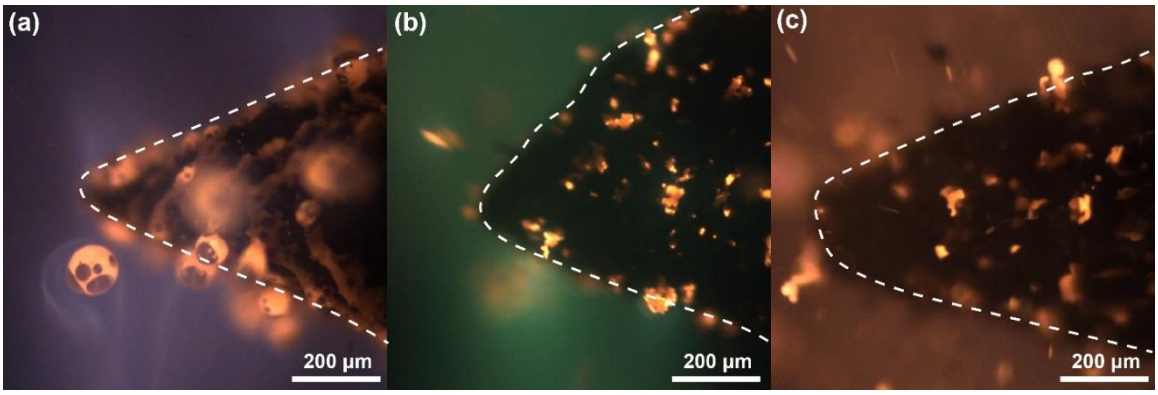

Figure 4-1 Images from high-speed microscopy videos for (a) Al-$KClO_4$, (b) B-$KClO_4$, and (c) Ti-$KClO_4$. The dashed lines represent boundaries of the burning surfaces.

B-$KClO_4$ and Ti-$KClO_4$ burn similarly to each other but dramatically differently as compared to Al-$KClO_4$. As illustrated in Figure 4-1 (b) and (c), burning particles agglomerate and form fractal-shaped structures before leaving the burning surface. The size distribution of the burning particles is displayed in Figure 4-2. Some agglomerates melt and shrink to be spheres, as shown in Figure S7 and Figure S8, and the agglomerates from Ti-$KClO_4$ have a higher tendency to become spheres than B-$KClO_4$, the reasons for which will be discussed in 3.3. Around the burning surface of B-$KClO_4$, a characteristic green color arising from the emission of BO_2 is observed[39,40]. As for Ti-$KClO_4$, emission from TiO is responsible for the red-orange glow around the burning surface[41].

SEM images and corresponding size distributions of the as-received nanoparticles show that the size is generally below 150 nm for Al, 600 nm for B, and 200 nm for Ti (Figure S1). Size comparison between these initial fuel nanoparticles and the microdroplets/particles formed during combustion reveals extensive

sintering/agglomeration of these fuels, as the size increases ~800 times for Al, ~150 times for B, and ~550 times for Ti.

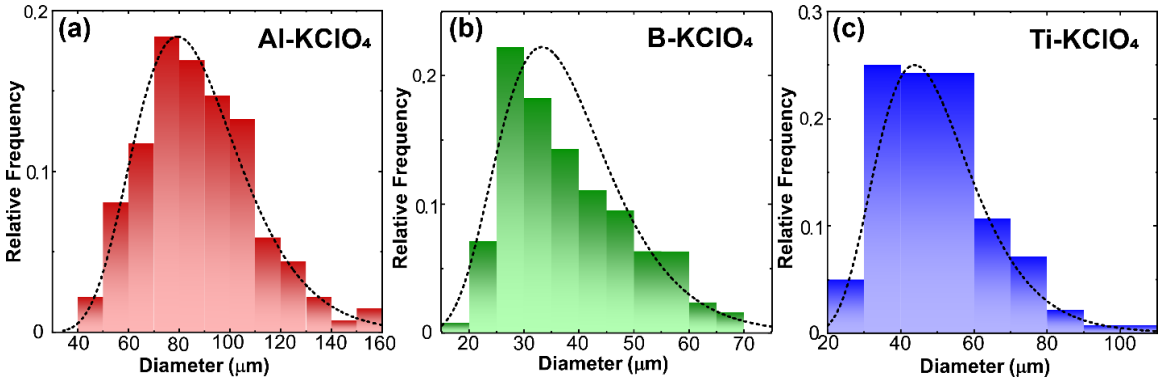

Figure 4-2 Size distribution of agglomerates for Al-$KClO_4$ (a), B-$KClO_4$ (b) and Ti-$KClO_4$ (c). Note: only agglomerates that are about to depart from the burning surface or already departed. For B-$KClO_4$ and Ti-$KClO_4$, area equivalent diameter is displayed.

4.4.2 Temperature measurement from imaging-pyrometry

Three-color (RGB) imaging-pyrometry is employed for temperature estimation of Al-$KClO_4$. Smoke present around Al/Al_2O_3 droplets can bias droplet temperature estimation when the smoke is optically thick. To evaluate the effect of the smoke on temperature estimation (details can be found in Section S3), the optical thickness is estimated based on Equation S1, and demonstrates that the smoke is optically thin (optical thickness less than 0.1 as shown in Figure S9)[42–44]. Figure 4-3 displays the demosaiced image and the temperature map for the Al-$KClO_4$ composite. As mentioned above, molten droplets are composed of aluminum as the main body and aluminum oxide as the cap. The estimated temperature for the Al body of the droplets around 2500 K is higher than the melting point at 930 K while lower than the boiling point of Al at 2743 K (Table 4-1). The estimated oxide cap temperature at ~3100 K is higher than the Al body temperature as well

as the melting point of Al_2O_3 (Table 4-1). Chen et al has seen similar observations where the oxide caps were hotter than Al bodies in molten droplets[22]. One may suppose that the difference in the measured temperature of the Al body and Al_2O_3 cap arises from the difference in their emissivity. Indeed, Al and Al_2O_3 have drastically different emissivity at high temperatures[37]. However, since we determine temperature based on the gray body emission assumption (emissivity remains constant when wavelength changes), the absolute value of emissivity cancels out[33].

Molten Al droplets are known to burn with vapor-phase combustion with the formation of a detached and diffusion-flame envelope away from the surface of the droplets where Al vaporizes, as shown in Figure 4-3[37,45]. Under vapor-phase combustion, nanometric smoke formed via homogeneous nucleation primarily consists of Al_2O_3[37] SEM/EDS images for post-combustion product confirm the presence of nanoparticles of Al_2O_3 (~100 nm, Figure S11) along with the aluminum oxide microparticles as the final product (Figure 4-7).

The temperature of these nanoparticles, which presumably represents the surrounding gas temperature due to their small size, is estimated to be ~3500 K, which is close to the adiabatic flame temperature of Al-$KClO_4$ at 3800 K as calculated with CHEETAH.

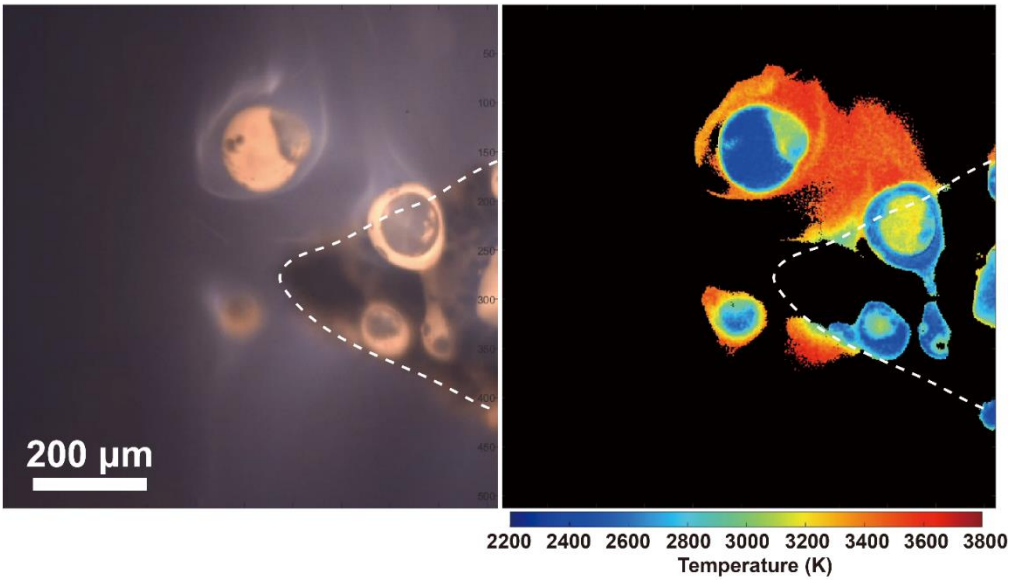

Figure 4-3 Temperature map (right) from three-color (RGB) pyrometry for an image (left) from high-speed microscopy video of Al-$KClO_4$. High error points and low-intensity points were excluded from the calculation. The dashed line represents the boundary of the burning surface.

Table 4-1 Melting and boiling point of Al, Al_2O_3, B, B_2O_3, Ti, TiO_2, Ti_2O_3 with references, and measured temperature of burning agglomerates.

	Melting Point (K)	Boiling Point (K)	References		Measured Temperature of Burning Agglomerates (K)
Al	930	2743	[22]	Al-$KClO_4$	2500
Al_2O_3	2345	3240	[22]		
B	2349	4200	[46]	B-$KClO_4$	1950
B_2O_3	723	2130	[46]		
Ti	1941	3560	[47]	Ti-$KClO_4$	2350
TiO_2	2116	3245	[41]		
Ti_2O_3	2400	3300	[41]		

Boron has a characteristic green flame emission (between 450 and 600 nm) from BO_2 as an intermediate during combustion[40,48,49]. This emission (since it is non-graybody) can significantly affect the green-color channel, and lead to inaccuracy in temperature estimation from three-color (RGB) pyrometry, under the gray-body assumption. To circumvent this problem, two-color (BR) pyrometry was employed (details can be found in Section 2.6) and the resultant temperature map is displayed in Figure 4-4, which shows the burning particles are at ~1950 K. Figure S10 shows temperature of the burning particles of B-$KClO_4$ measured with three-color (RGB) pyrometry is ~2250 K, which suggests a 300 K discrepancy caused by the molecular emission from BO_2.

It is generally accepted that the combustion of boron particles has two stages, the first stage is the burning of boron particles coated with a liquid B_2O_3 layer, and the second stage is combustion of bare boron after the removal of B_2O_3[16,17,50,51]. The estimated temperature for agglomerates on the burning surface of B-$KClO_4$ is ~1950 K with two-color pyrometry, it is slightly lower than the boiling point of B_2O_3 (2130 K), therefore we conclude that the B_2O_3 is not completely removed and the combustion of agglomerates we observe is in the first stage boron combustion. Also, the estimated temperature is lower than the melting point of boron at 2349 K, shape of the which is consistent with the observation that the particles are still agglomerates.

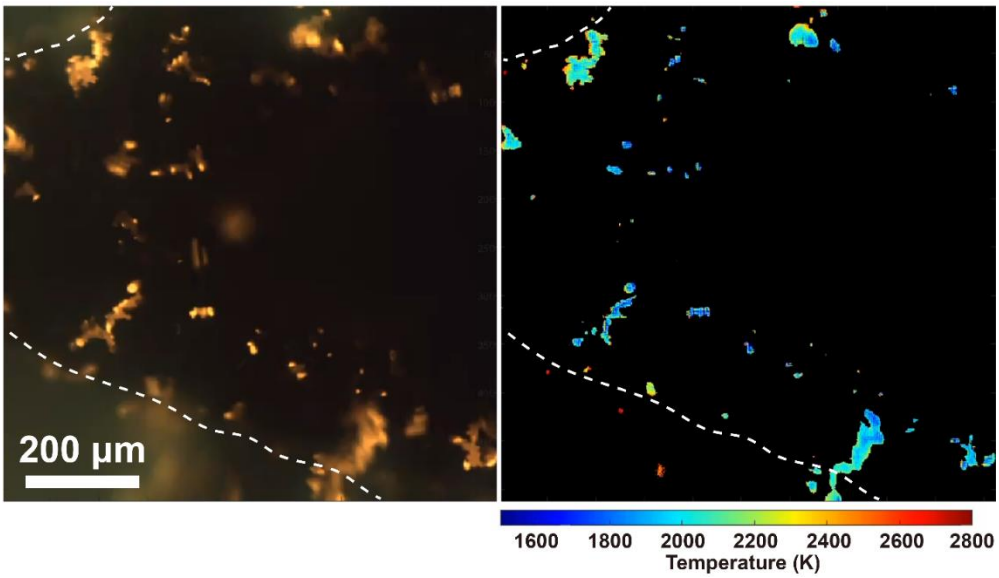

Figure 4-4 Temperature map (right) from two-color (RB) pyrometry for an image (left) from high-speed microscopy video of B-$KClO_4$. High error points and low-intensity points were excluded from the calculation. The dashed lines represent boundaries of the burning surface.

Ti-$KClO_4$ presents a more complex situation than B-$KClO_4$. The obtained temperature from three-color pyrometry for agglomerates on the Ti-$KClO_4$ burning surface is ~2350 K (Figure 4-5), which is higher than the melting point of both Ti and TiO_2 (Table 4-1). The non-spherical shape of the agglomerates suggests the presence of other oxides with a higher melting point. Previous studies on titanium particle oxidation demonstrate that the oxidation process consists of different 'stages', one of which is the building-up of Ti_2O_3 beneath the TiO_2 outer surface[41,52]. Ti_2O_3 with a melting point of 2400 K, forms at a temperature of 2023 K, and the estimated temperature for agglomerates lies between these two temperatures[25,41]. Thus it is likely the agglomerates on the burning surface are mostly composed of Ti, Ti_2O_3, and TiO_2, with Ti_2O_3 being dominant in contributing to the shape, although other oxides including TiO and Ti_3O_5 may also be present[41]. Fragmentation,

probably caused by the release of gas within the particle from the composition phase change, is an important characteristic during the combustion of Ti particles[24,25,53,54]. A previous study observed that the minimum particle size below which Ti particles no longer fragments is ~ 30 μm[53]. Minimal fragmentation is observed during Ti-$KClO_4$ composite burning, probably because the size of the agglomerates (at least in one dimension) is generally below the minimum particle size of ~30 μm for fragmentation[41,53].

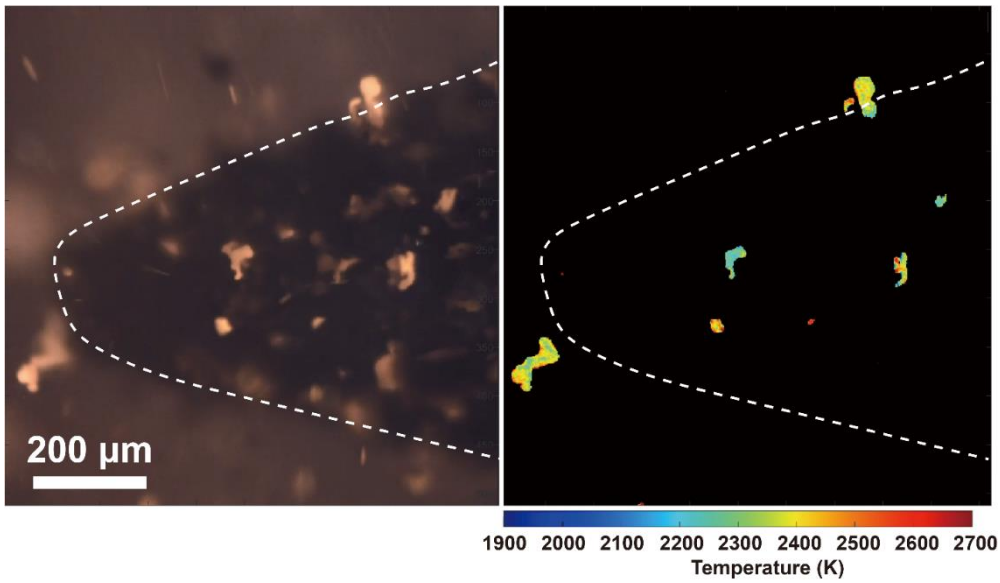

Figure 4-5 Temperature map (right) from three-color (RGB) pyrometry for an image (left) from high-speed microscopy video of Ti-$KClO_4$. High error points and low-intensity points were excluded from the calculation. The dashed line represents boundary of the burning surface.

4.4.3 Combustion performance

Al is known to combust in the vapor phase [34] while B and Ti in the condensed-phase[16,17,55], which implies that the combustion rate of Al should be significantly higher than B and Ti, whose combustion is limited by O_2 diffusion in the condensed-phase. However, we observe only moderate differences, as the burn rate of Al-$KClO_4$ (~10 cm/s)

is about 4 times of B-$KClO_4$ (~2.5cm/s) and about 2 times of Ti-$KClO_4$ (~5 cm/s), as shown in Figure 4-6 (b), and the resultant energy release rate of Al-$KClO_4$ is not dramatically higher than B-$KClO_4$ and Ti-$KClO_4$ (Figure S12). A primary question now arises: Why does Al-$KClO_4$ burns only moderately faster than B-$KClO_4$ and Ti-$KClO_4$?

Combustion of Al droplets is limited by the availability of Al vapor that depends on the evaporation rate of Al, therefore the combustion rate of Al decreases dramatically when droplet size increases since the evaporation rate of Al is significantly reduced due to the decreased overall surface/volume ratio. Typically this scaling is: Burn rate ~ $1/D^2$. The average size of Al droplets (~ 90 μm, Figure 4-6(b)) is significantly larger than the starting Al nanoparticle (~100 nm, Figure S1). The correlations between burn-times and sizes (Figure 4-6 (c)) of Al droplets and Ti particles (agglomerates) have been theoretically evaluated through application of a droplet evaporation model[36] and kinetic shrinking core model[55] (surface reaction controlled), respectively (details can be found in Section S5). A similar evaluation is not conducted for B particle combustion due to the lack of data and a well-accepted oxidation mechanism. These correlations suggest that although the calculated burn time of a 100 nm Al particle should be 4 orders of magnitude smaller than a 100 nm Ti particle (initial particles are both about 100 nm, as displayed in Figure S1), the calculated burn time of a 100 μm Al droplet (~0.05 s) is only slightly lower than the burn time of a 50 μm Ti particle (~0.1 s), as shown in Figure 4-6 (c). This means the experimentally observed Al droplets burn only moderately faster than the Ti particles, since the size of Al droplets is large.

Visualization under microscopic conditions as seen in Figure 4-6 (a) shows that particles are not immediately ejected from the surface but ignite and subsequently burn for some time. A series of snapshots of a representative droplet/agglomerate forming, growing, and departing from the burning surface for Al, B, and Ti are displayed in Figure 4-6 (a), and the extracted surface residence times are estimated based on the time from the emergence of the droplets/agglomerates to their departure, and are tabulated in Figure 4-6(d). It is noteworthy that the theoretical burn times of Al droplets and Ti particles are both much larger than their corresponding residence times on the burning surface, suggesting both Al droplets and Ti particles should have incomplete combustion before departing from the burning surface. This is consistent with the experimental observation that the burning droplet/agglomerate continues burning after departure. As Al droplets and Ti agglomerates have similar temperatures (2500 K vs 2350 K), a higher surface residence time should result in more heat feedback to the unburnt solid composite that leads to a higher burn rate [56]. This also contributes to the observed higher burn rate of Al than Ti in addition to the aforementioned lower burn time of Al droplets compared to Ti particles.

It is clear from the images that luminous zones are indicative of significant burning away from the surface, the sharp edges of which terminate immediately near the burning surfaces (~0 mm, ~0.02 mm, and ~0.03 mm for Al-$KClO_4$, B-$KClO_4$, and Ti-$KClO_4$, respectively). Droplet/agglomerate velocity after departing from the burning surface is measured by tracking the location and the corresponding time. The result of this analysis is displayed in Figure 4-6 (e), which shows there is no significant droplet/agglomerate velocity difference between Al-$KClO_4$ and Ti-$KClO_4$. The expected burning distances of

the dispersed Al droplets and Ti agglomerates are shown in Figure 4-6 (e) and are estimated based on their velocities and calculated burn times after departing from the burn surface (Figure 4-6 (d)). The result shows that the Al droplet would need to travel ~11 mm and Ti agglomerate ~16 mm for complete oxidation. These distances are significantly longer than the sharp edge of the luminous zone. This implies that the luminous zone cannot represent the complete flame zone.

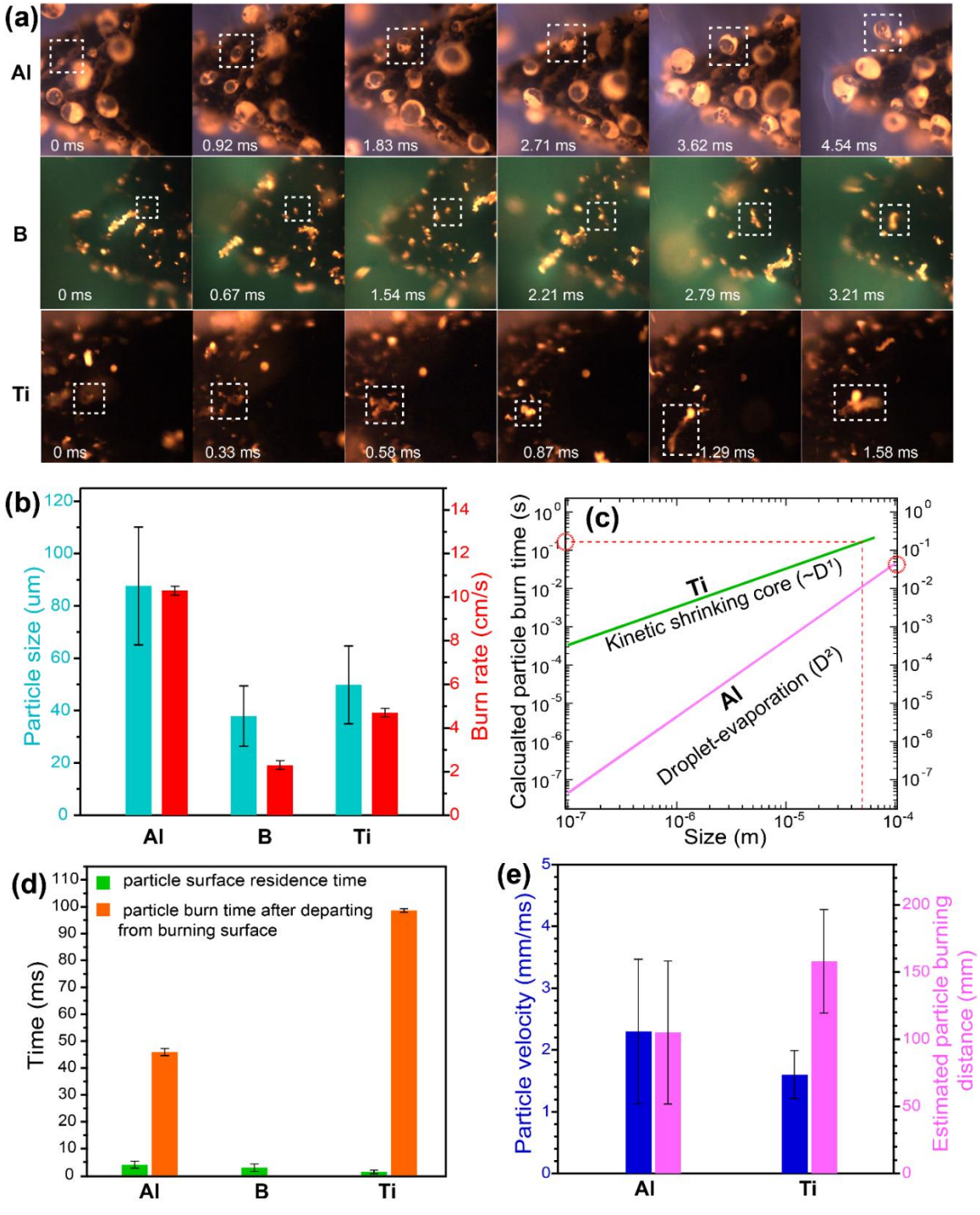
(a)
Al
0 ms
0.92 ms
1.83 ms
2.71 ms
3.62 ms
4.54 ms
B
0 ms
0.67 ms
1.54 ms
2.21 ms
2.79 ms
3.21 ms
Ti
0 ms
0.33 ms
0.58 ms
0.87 ms
1.29 ms
1.58 ms
(b)
Particle size (um)
Burn rate (cm/s)
Al
B
Ti
(c)
Calcualted particle burn time (s)
Ti
Kinetic shrinking core (~D¹)
Al
Droplet-evaporation (D²)
Size (m)
(d)
particle surface residence time
particle burn time after departing from burning surface
Time (ms)
Al
B
Ti
(e)
Particle velocity (mm/ms)
Estimated particle burning distance (mm)
Al
Ti

Figure 4-6 Time-resolved snapshots of the particles (droplets/agglomerates) evolving before departing from burning surface (a), particle size and burn rate of different composites (b), correlations between burn-times and sizes of Al droplet and Ti agglomerate based on droplet-evaporation model and kinetic shrinking core model, respectively (c), particle surface residence time on the burning surface and particle burn time of the observed size (100 μm for Al and 50 μm for Ti) after departing from the burning surface (d), and measured particle velocity and estimated particle burning distance for complete oxidation (e).

4.4.4 Post combustion products

Further insight can be gained when microimaging observations are analyzed in tandem with SEM images of post-combustion products of these composites (Figure 4-7 and Figure S11). Micron-sized particles from Al-$KClO_4$ and B-$KClO_4$ are mostly spherical and fractal-shaped, respectively, consistent with morphology of the burning particles observed in microimaging (Figure 4-7 (a) and (b), Figure 4-1 (a) and (b)). However, different from the dominating fractal-shaped burning particles observed in microimaging, particles of post-combustion products from Ti-$KClO_4$ are spherical (Figure 4-7 (c)). This morphology change is attributed to the aforementioned transition of Ti_2O_3 to TiO_2 during oxidation after agglomerates depart from the burning surface.

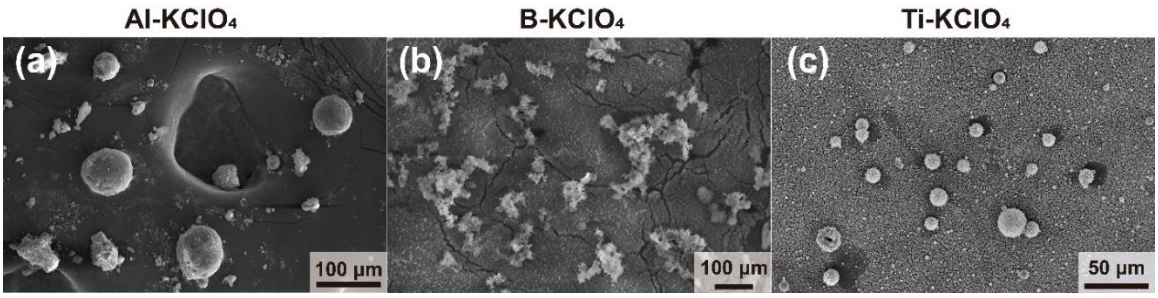

Figure 4-7 SEM images of microparticles for post-combustion products of Al-$KClO_4$ (a), B-$KClO_4$ (b), and Ti-$KClO_4$ (c). *Note: For Al-$KClO_4$, the product was water-washed briefly to remove KCl so that large agglomerates can stay on the carbon tap for SEM. More details can be found in 4.2.3.*

SEM/EDS images of the sub-micron particles of post-combustion products of Al/B/Ti-$KClO_4$ composites also demonstrate the difference and similarity in combustion behaviors. As shown in Figure S11, KCl nanoparticles are produced for all three systems, from the condensation of KCl vapor as the product of decomposition of $KClO_4$. Both Al and B systems show significant aluminum oxide and boron oxide nanoparticles, respectively, but oxide nanoparticles are barely observed for the Ti system. The presence of aluminum oxide nanoparticles confirms the vapor phase reaction of Al. Boron oxide nanoparticles arise from the condensation of evaporated boron oxide as the measured temperature of the burning particles is close to the boiling point of B_2O_3 (Table 4-1). For Ti, both vapor phase combustion and oxide evaporation are negligible as the temperature is not sufficiently high. Unlike boron agglomerates being at the temperature close to the boiling point of B_2O_3 (difference is ~180 K), temperature of titanium agglomerates is much lower (~1000 K) than the boiling point of titanium oxides (TiO_2 and Ti_2O_3), therefore evaporated titanium oxides are less significant (Table 4-1).

4.4.5 Discussion on combustion characteristics

The combustion process of the three composites are summarized and represented in the illustration shown in Figure 4-8. $KClO_4$ melts and decomposes concurrently at 610 °C, and the decomposition product KCl has a boiling point of 1412 °C[27,28], therefore presumably no $KClO_4$ or KCl is present in solid state during burning. The combustion behavior differences between Al-$KClO_4$ and B-$KClO_4$ or Ti-$KClO_4$ as well as the similarity between B-$KClO_4$ and Ti-$KClO_4$ are attributed to the physical property (e.g. melting and boiling point) of their corresponding metal and metal oxide, as shown in Table 4-1. Although the Al_2O_3 shell has a relatively high melting point, the phase transition from amorphous to γ-Al_2O_3 below 900 K introduces voids in the oxide shell, enabling the molten Al core to leak through the oxide shell when the temperature reaches its melting point at 930 K[57] . As oxidation of Al continues, and sintering/coalescence occurs below the melting point of Al_2O_3 because the high mobility of Al within Al_2O_3 likely softens it[58]. Molten Al on the surface merge to form larger droplets before they depart the surface. Based on analysis of the images this this process takes on the order of ~ 4 ms.

B and Ti have much higher melting points compared to Al, and thus are relatively less mobile with considerably smaller atomic diffusivities. This explains why B and Ti primarily form fractal-like structures rather than spherical droplets (Figure 4-8). As mentioned in 3.1, some of these fractal-shaped agglomerates may ball up into spheres during burning, and agglomerates of Ti-$KClO_4$ have a higher tendency for becoming spheres than those of B-$KClO_4$. The measured temperature of agglomerates on B-$KClO_4$ burning surface is ~400 K lower than the melting point of B, thus it is less likely for the

agglomerates to melt and become spheres without a temperature increase. As for Ti-$KClO_4$, the fractal-shaped agglomerates are in the combustion stage where Ti_2O_3 dominates the structure. As agglomerates continue burning, the amount of TiO_2 increases while Ti_2O_3 and other lower oxides diminish. The newly-formed TiO_2 melts upon formation, which means that the agglomerates transition into spheres even if the temperature remains invariant. There is minimal temperature change observed along the burning of agglomerates on the burning surface of both B-$KClO_4$ and Ti-$KClO_4$, explaining why agglomerates of Ti-$KClO_4$ are more likely to become spheres than those of B-$KClO_4$. The time spans from emergence to departure of B and Ti agglomerates are ~3 ms and ~ 1.5 ms, respectively, both are slightly lower than the Al droplets, contributing to lower heat feedback to the composite and thus lower burn rates, as discussed in 4.3.3.

Macroscopic combustion features of the three composites are also displayed in Figure 4-8. As discussed in 4.3.3, the luminous zone ends immediately after the burning surface although the droplets/agglomerates are not completely combusted in that region, indicating a temperature drop downstream.

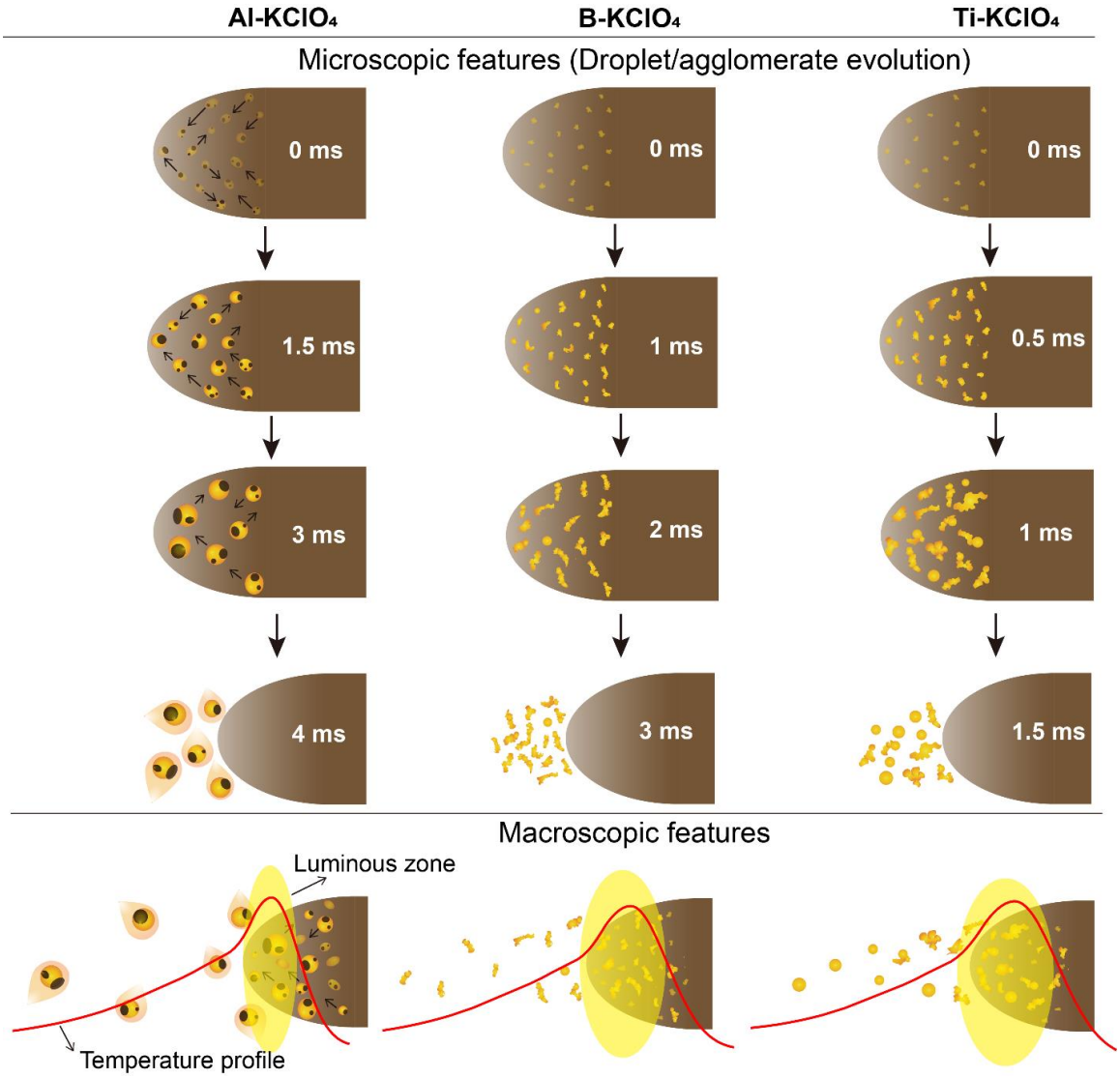

Figure 4-8 Illustration of the microscopic features (droplet/agglomerate evolution) with corresponding time stamps as well as the macroscopic features of Al-$KClO_4$ (left) and B-$KClO_4$ (middle) and Ti-$KClO_4$ (right).

4.5 Conclusions

In this chapter, I study the combustion characteristics of high-loading Al-$KClO_4$, B-$KClO_4$, and Ti-$KClO_4$ composites with high-speed microscopy and pyrometry and find that combustion characteristics of these composites are strongly dependent on the fuel type. Mobile Al droplets with Al_2O_3 caps form on the burning surface of Al-$KClO_4$, then

coalesce into larger droplets before departing from the burning surface. As for B-$KClO_4$ and Ti-$KClO_4$, fractal-shaped agglomerates form. Temperatures of the burning particles are determined with color imaging-pyrometry. The combustion behavior difference between Al-$KClO_4$ and B/Ti-$KClO_4$ as well as the similarity between B-$KClO_4$ and Ti-$KClO_4$ are attributed to the physical properties, e.g. melting and boiling points, of these fuels and their corresponding oxides. Particles reside and burn on the propellant surface with the residence time on the order of ~1-5 ms. This is significantly lower than the theoretical particle burn time, implying incomplete particle combustion on the burning surface. This is consistent with the experimental observation that particles continue to burn after departing the burning surface. The estimated particle downstream burning distance is drastically larger than the observed luminous zone, suggesting the luminous zone does not represent the complete flame zone. Since Al combusts in the vapor phase while B and Ti combust in the condense phase, the burn rate of Al should be significantly higher than B and Ti, However, the differences are not as drastic as expected because the formation of much larger droplets of Al results in dramatically longer particle burn times.

4.6 References

(1) Wang, H.; Kline, D. J.; Zachariah, M. R. In-Operando High-Speed Microscopy and Thermometry of Reaction Propagation and Sintering in a Nanocomposite. *Nat. Commun.* **2019**, *10* (1), 3032. https://doi.org/10.1038/s41467-019-10843-4.

(2) Shin, D. J.; Kim, W. D.; Lee, S.; Lee, D. C. Nanothermite of Al Nanoparticles and Three-Dimensionally Ordered Macroporous CuO: Mechanistic Insight into Oxidation during Thermite Reaction. *Combust. Flame* **2018**, *189*, 87–91. https://doi.org/10.1016/j.combustflame.2017.10.018.

(3) He, W.; Liu, P.-J.; He, G.-Q.; Gozin, M.; Yan, Q.-L. Highly Reactive Metastable Intermixed Composites (MICs): Preparation and Characterization. *Adv. Mater.* **2018**, *30* (41), 1706293. https://doi.org/10.1002/adma.201706293.

(4) Baijot, V.; Mehdi, D.-R.; Rossi, C.; Estève, A. A Multi-Phase Micro-Kinetic Model for Simulating Aluminum Based Thermite Reactions. *Combust. Flame* **2017**, *180*, 10–19. https://doi.org/10.1016/j.combustflame.2017.02.031.

(5) Chiang, Y.-C.; Wu, M.-H. Assembly and Reaction Characterization of a Novel Thermite Consisting Aluminum Nanoparticles and CuO Nanowires. *Proc. Combust. Inst.* **2017**, *36* (3), 4201–4208. https://doi.org/10.1016/j.proci.2016.06.176.

(6) Sullivan, K. T.; Kuntz, J. D.; Gash, A. E. The Role of Fuel Particle Size on Flame Propagation Velocity in Thermites with a Nanoscale Oxidizer. *Propellants Explos. Pyrotech.* **2014**, *39* (3), 407–415. https://doi.org/10.1002/prep.201400020.

(7) Zohari, N.; Keshavarz, M. H.; Seyedsadjadi, S. A. The Advantages and Shortcomings of Using Nano-Sized Energetic Materials. *Cent. Eur. J. Energ. Mater.* **2013**, *Vol. 10* (1).

(8) Sullivan, K. T.; Piekiel, N. W.; Wu, C.; Chowdhury, S.; Kelly, S. T.; Hufnagel, T. C.; Fezzaa, K.; Zachariah, M. R. Reactive Sintering: An Important Component in the Combustion of Nanocomposite Thermites. *Combust. Flame* **2012**, *159* (1), 2–15. https://doi.org/10.1016/j.combustflame.2011.07.015.

(9) Egan, G. C.; Sullivan, K. T.; Olson, T. Y.; Han, T. Y.-J.; Worsley, M. A.; Zachariah, M. R. Ignition and Combustion Characteristics of Nanoaluminum with Copper Oxide Nanoparticles of Differing Oxidation State. *J. Phys. Chem. C* **2016**, *120* (51), 29023–29029. https://doi.org/10.1021/acs.jpcc.6b11081.

(10) Valluri, S. K.; Schoenitz, M.; Dreizin, E. Bismuth Fluoride-Coated Boron Powders as Enhanced Fuels. *Combust. Flame* **2020**, *221*, 1–10. https://doi.org/10.1016/j.combustflame.2020.07.023.

(11) Rehwoldt, M. C.; Yang, Y.; Wang, H.; Holdren, S.; Zachariah, M. R. Ignition of Nanoscale Titanium/Potassium Perchlorate Pyrotechnic Powder: Reaction Mechanism Study. *J. Phys. Chem. C* **2018**, *122* (20), 10792–10800. https://doi.org/10.1021/acs.jpcc.8b03164.

(12) Sippel, T. R.; Son, S. F.; Groven, L. J. Aluminum Agglomeration Reduction in a Composite Propellant Using Tailored Al/PTFE Particles. *Combust. Flame* **2014**, *161* (1), 311–321. https://doi.org/10.1016/j.combustflame.2013.08.009.

(13) Young, G.; Wang, H.; Zachariah, M. R. Application of Nano-Aluminum/Nitrocellulose Mesoparticles in Composite Solid Rocket Propellants.

Propellants Explos. Pyrotech. **2015**, *40* (3), 413–418. https://doi.org/10.1002/prep.201500020.
(14) Meda, L.; Marra, G.; Galfetti, L.; Severini, F.; De Luca, L. Nano-Aluminum as Energetic Material for Rocket Propellants. *Mater. Sci. Eng. C* **2007**, *27* (5), 1393–1396. https://doi.org/10.1016/j.msec.2006.09.030.
(15) Wang, H.; DeLisio, J. B.; Jian, G.; Zhou, W.; Zachariah, M. R. Electrospray Formation and Combustion Characteristics of Iodine-Containing Al/CuO Nanothermite Microparticles. *Combust. Flame* **2015**, *162* (7), 2823–2829. https://doi.org/10.1016/j.combustflame.2015.04.005.
(16) Yeh, C. L.; Kuo, K. K. Ignition and Combustion of Boron Particles. *Prog. Energy Combust. Sci.* **1996**, *22* (6), 511–541. https://doi.org/10.1016/S0360-1285(96)00012-3.
(17) Ulas, A.; Kuo, K. K.; Gotzmer, C. Ignition and Combustion of Boron Particles in Fluorine-Containing Environments. *Combust. Flame* **2001**, *127* (1), 1935–1957. https://doi.org/10.1016/S0010-2180(01)00299-1.
(18) *Study of Titanium Potassium Perchlorate Combustion using Electric Field Holography and Imaging Pyrometry | AIAA SCITECH 2022 Forum*. AIAA SciTech Forum. https://arc.aiaa.org/doi/abs/10.2514/6.2022-1522 (accessed 2022-01-03).
(19) Melcher, J. C.; Krier, H.; Burton, R. L. Burning Aluminum Particles Inside a Laboratory-Scale Solid Rocket Motor. *J. Propuls. Power* **2012**. https://doi.org/10.2514/2.5977.
(20) Dreizin, E. L. Experimental Study of Stages in Aluminium Particle Combustion in Air. *Combust. Flame* **1996**, *105* (4), 541–556. https://doi.org/10.1016/0010-2180(95)00224-3.
(21) Karasev, V. V.; Onischuk, A. A.; Glotov, O. G.; Baklanov, A. M.; Maryasov, A. G.; Zarko, V. E.; Panfilov, V. N.; Levykin, A. I.; Sabelfeld, K. K. Formation of Charged Aggregates of Al2O3 Nanoparticles by Combustion of Aluminum Droplets in Air. *Combust. Flame* **2004**, *138* (1), 40–54. https://doi.org/10.1016/j.combustflame.2004.04.001.
(22) Chen, Y.; Guildenbecher, D. R.; Hoffmeister, K. N. G.; Cooper, M. A.; Stauffacher, H. L.; Oliver, M. S.; Washburn, E. B. Study of Aluminum Particle Combustion in Solid Propellant Plumes Using Digital In-Line Holography and Imaging Pyrometry. *Combust. Flame* **2017**, *182*, 225–237. https://doi.org/10.1016/j.combustflame.2017.04.016.
(23) Marsh, A. W.; Wang, G. T.; Heyborne, J. D.; Guildenbecher, D. R.; Mazumdar, Y. C. Time-Resolved Size, Velocity, and Temperature Statistics of Aluminum Combustion in Solid Rocket Propellants. *Proc. Combust. Inst.* **2021**, *38* (3), 4417–4424. https://doi.org/10.1016/j.proci.2020.08.010.
(24) Shafirovich, E.; Teoh, S. K.; Varma, A. Combustion of Levitated Titanium Particles in Air. *Combust. Flame* **2008**, *152* (1), 262–271. https://doi.org/10.1016/j.combustflame.2007.05.008.
(25) Molodetsky, I. E.; Vicenzi, E. P.; Dreizin, E. L.; Law, C. K. Phases of Titanium Combustion in Air. *Combust. Flame* **1998**, *112* (4), 522–532. https://doi.org/10.1016/S0010-2180(97)00146-6.

(26) Liu, D.; Xia, Z.; Huang, L.; Hu, J. Boron Particle Combustion in Solid Rocket Ramjets. *J. Aerosp. Eng.* **2015**, *28* (4), 04014112. https://doi.org/10.1061/(ASCE)AS.1943-5525.0000443.
(27) Wang, Y.; Wang, H.; Xu, F.; Ghildiyal, P.; Zachariah, M. R. Effect of Alkali Metal Perchlorate and Iodate Type on Boron Ignition: The Role of Oxidizer Phase Change. *Chem. Eng. J.* **2022**, *446*, 136786. https://doi.org/10.1016/j.cej.2022.136786.
(28) Xu, X.; Wang, X.; Li, P.; Li, Y.; Hao, Q.; Xiao, B.; Elsentriecy, H.; Gervasio, D. Experimental Test of Properties of KCl–MgCl2 Eutectic Molten Salt for Heat Transfer and Thermal Storage Fluid in Concentrated Solar Power Systems. *J. Sol. Energy Eng.* **2018**, *140* (5). https://doi.org/10.1115/1.4040065.
(29) Wang, H.; Shen, J.; Kline, D. J.; Eckman, N.; Agrawal, N. R.; Wu, T.; Wang, P.; Zachariah, M. R. Direct Writing of a 90 Wt% Particle Loading Nanothermite. *Adv. Mater.* **2019**, *31* (23), 1806575. https://doi.org/10.1002/adma.201806575.
(30) Wang, H.; Wang, Y.; Garg, M.; Moore, J. S.; Zachariah, M. R. Unzipping Polymers Significantly Enhance Energy Flux of Aluminized Composites. *Combust. Flame* **2022**, *244*, 112242. https://doi.org/10.1016/j.combustflame.2022.112242.
(31) Wang, H.; Julien, B.; Kline, D.; Alibay, Z.; Rehwoldt, M.; Rossi, C.; Zachariah, M. Probing the Reaction Zone of Nanolaminates at ∼μs Time and ∼μm Spatial Resolution. *J. Phys. Chem. C* **2020**, *124* (25), 13679–13687. https://doi.org/10.1021/acs.jpcc.0c01647.
(32) Kline, D. J.; Alibay, Z.; Rehwoldt, M. C.; Idrogo-Lam, A.; Hamilton, S. G.; Biswas, P.; Xu, F.; Zachariah, M. R. Experimental Observation of the Heat Transfer Mechanisms That Drive Propagation in Additively Manufactured Energetic Materials. *Combust. Flame* **2020**, *215*, 417–424. https://doi.org/10.1016/j.combustflame.2020.01.020.
(33) Jacob, R. J.; Kline, D. J.; Zachariah, M. R. High Speed 2-Dimensional Temperature Measurements of Nanothermite Composites: Probing Thermal vs. Gas Generation Effects. *J. Appl. Phys.* **2018**, *123* (11), 115902. https://doi.org/10.1063/1.5021890.
(34) Wang, H.; Kline, D. J.; Rehwoldt, M. C.; Zachariah, M. R. Carbon Fibers Enhance the Propagation of High Loading Nanothermites: In Situ Observation of Microscopic Combustion. *ACS Appl. Mater. Interfaces* **2021**. https://doi.org/10.1021/acsami.1c02911.
(35) McNesby, K.; Dean, S.; Benjamin, R.; Grant, J.; Anderson, J.; Densmore, J. Imaging Pyrometry for Most Color Cameras Using a Triple Pass Filter. *Rev. Sci. Instrum.* **2021**, *92* (6). https://doi.org/10.1063/5.0037230.
(36) Emelyanov, V. N.; Teterina, I. V.; Volkov, K. N. Dynamics and Combustion of Single Aluminium Agglomerate in Solid Propellant Environment. *Acta Astronaut.* **2020**, *176*, 682–694. https://doi.org/10.1016/j.actaastro.2020.03.046.
(37) Harrison, J.; Brewster, M. Q. Analysis of Thermal Radiation from Burning Aluminium in Solid Propellants. *Combust. Theory Model.* **2009**, *13* (3), 389–411. https://doi.org/10.1080/13647830802684318.

(38) Dreizin, E. L. Experimental Study of Aluminum Particle Flame Evolution in Normal and Micro-Gravity. *Combust. Flame* **1999**, *116* (3), 323–333. https://doi.org/10.1016/S0010-2180(97)00331-3.
(39) Spalding, M.; Krier, H.; Burton, R.; Spalding, M.; Krier, H.; Burton, R. Emission Spectroscopy during Ignition of Boron Particles at High Pressure. In *35th Aerospace Sciences Meeting and Exhibit*; American Institute of Aeronautics and Astronautics. https://doi.org/10.2514/6.1997-119.
(40) Spalding, M. J.; Krier, H.; Burton, R. L. Boron Suboxides Measured during Ignition and Combustion of Boron in Shocked Ar/F/O2 and Ar/N2/O2 Mixtures. *Combust. Flame* **2000**, *120* (1), 200–210. https://doi.org/10.1016/S0010-2180(99)00082-6.
(41) Glotov, O. G. Ignition and Combustion of Titanium Particles: Experimental Methods and Results. *Phys.-Uspekhi* **2019**, *62* (2), 131. https://doi.org/10.3367/UFNe.2018.04.038349.
(42) Biswas, P.; Mulholland, G. W.; Rehwoldt, M. C.; Kline, D. J.; Zachariah, M. R. Microwave Absorption by Small Dielectric and Semi-Conductor Coated Metal Particles. *J. Quant. Spectrosc. Radiat. Transf.* **2020**, *247*, 106938. https://doi.org/10.1016/j.jqsrt.2020.106938.
(43) Biswas, P.; Ghildiyal, P.; Mulholland, G. W.; Zachariah, M. R. Modelling and Simulation of Field Directed Linear Assembly of Aerosol Particles. *J. Colloid Interface Sci.* **2021**, *592*, 195–204. https://doi.org/10.1016/j.jcis.2021.02.050.
(44) Bohren, C. F.; Huffman, D. R. *Absorption and Scattering of Light by Small Particles*; John Wiley & Sons, 2008.
(45) Beckstead, M. W. A Summary of Aluminum Combustion. 47.
(46) Huang, S.; Deng, S.; Jiang, Y.; Zheng, X. Experimental Effective Metal Oxides to Enhance Boron Combustion. *Combust. Flame* **2019**, *205*, 278–285. https://doi.org/10.1016/j.combustflame.2019.04.018.
(47) Haynes, W. M. *CRC Handbook of Chemistry and Physics, 95th Edition.*; CRC Press: Hoboken, 2014.
(48) Liang, D.; Liu, J.; Xiao, J.; Xi, J.; Wang, Y.; Zhang, Y.; Zhou, J. Energy Release Properties of Amorphous Boron and Boron-Based Propellant Primary Combustion Products. *Acta Astronaut.* **2015**, *112*, 182–191. https://doi.org/10.1016/j.actaastro.2015.03.019.
(49) Xi, J.; Liu, J.; Wang, Y.; Liang, D.; Zhou, J. Effect of Metal Hydrides on the Burning Characteristics of Boron. *Thermochim. Acta* **2014**, *597*, 58–64. https://doi.org/10.1016/j.tca.2014.10.017.
(50) Li, S. C.; Williams, F. A.; Takahashi, F. An Investigation of Combustion of Boron Suspensions. *Symp. Int. Combust.* **1989**, *22* (1), 1951–1960. https://doi.org/10.1016/S0082-0784(89)80210-3.
(51) Young, G.; Sullivan, K.; Zachariah, M. R.; Yu, K. Combustion Characteristics of Boron Nanoparticles. *Combust. Flame* **2009**, *156* (2), 322–333. https://doi.org/10.1016/j.combustflame.2008.10.007.
(52) Kubaschewski, O. G. V. Samsonov (Ed.): The Oxide Handbook, 2nd Edition. IFI/Plenum, New York and London 1982. 463 Seiten, Preis: $75,-. *Berichte*

Bunsenges. Für Phys. Chem. **1982**, *86* (8), 761–762. https://doi.org/10.1002/bbpc.19820860820.
(53) Glotov, O. G. Combustion of Spherical Agglomerates of Titanium in Air. II. Results of Experiments. *Combust. Explos. Shock Waves* **2013**, *49* (3), 307–319. https://doi.org/10.1134/S0010508213030076.
(54) Badiola, C.; Dreizin, E. L. Combustion of Micron-Sized Particles of Titanium and Zirconium. *Proc. Combust. Inst.* **2013**, *34* (2), 2237–2243. https://doi.org/10.1016/j.proci.2012.05.089.
(55) Zong, Y.; Jacob, R. J.; Li, S.; Zachariah, M. R. Size Resolved High Temperature Oxidation Kinetics of Nano-Sized Titanium and Zirconium Particles. *J. Phys. Chem. A* **2015**, *119* (24), 6171–6178. https://doi.org/10.1021/acs.jpca.5b02590.
(56) Survey of Rocket Propellants and Their Combustion Characteristics. In *Fundamentals of Solid-Propellant Combustion*; Progress in Astronautics and Aeronautics; American Institute of Aeronautics and Astronautics, 1984; pp 1–52. https://doi.org/10.2514/5.9781600865671.0001.0052.
(57) Trunov, M. A.; Schoenitz, M.; Dreizin, E. L. Effect of Polymorphic Phase Transformations in Alumina Layer on Ignition of Aluminium Particles. *Combust. Theory Model.* **2006**, *10* (4), 603–623. https://doi.org/10.1080/13647830600578506.
(58) Chakraborty, P.; Zachariah, M. R. Do Nanoenergetic Particles Remain Nano-Sized during Combustion? *Combust. Flame* **2014**, *161* (5), 1408–1416. https://doi.org/10.1016/j.combustflame.2013.10.017.

4.7 Supporting information

S.1 SEM

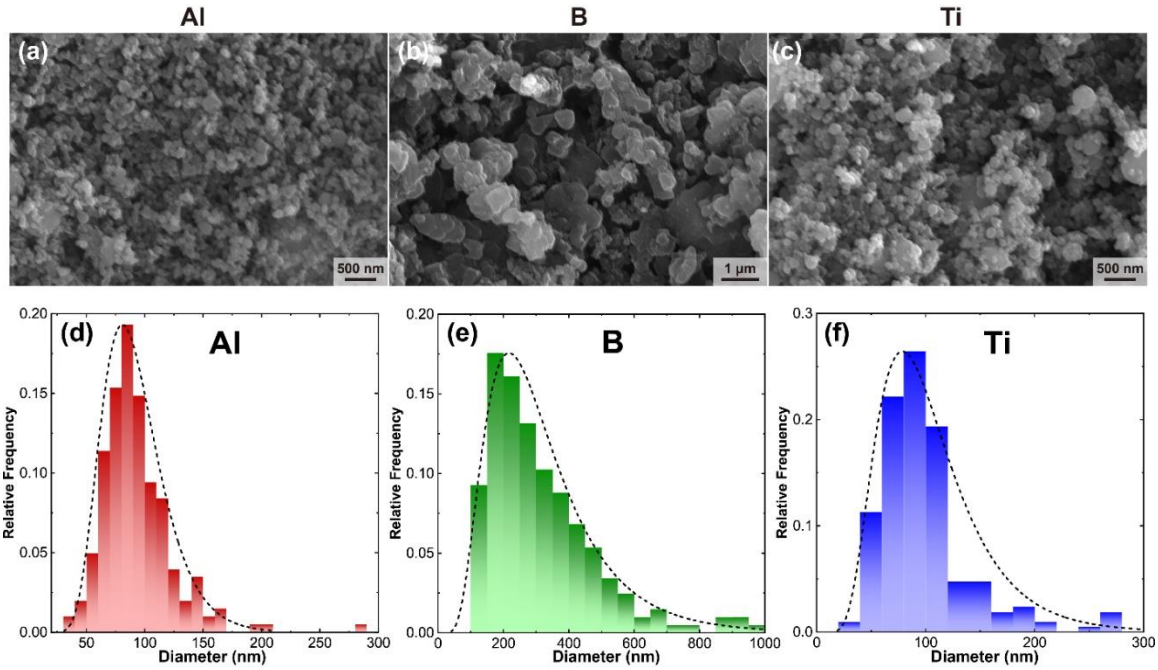

Figure S 1. SEM images of the initial nanoparticles of Al (a), B (b), and Ti (c) as well as their corresponding size distribution of Al (d), B (e), and Ti (f). Note: area equivalent diameter is displayed for B.

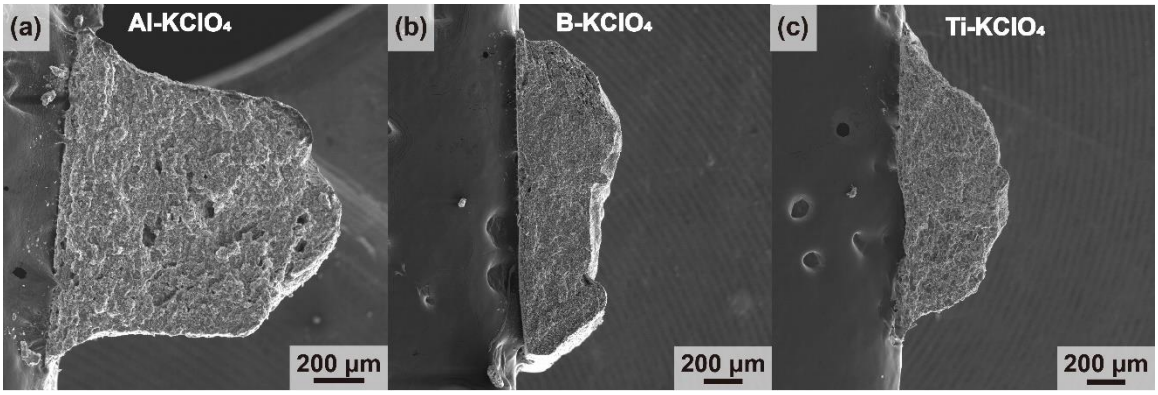

Figure S 2. SEM images of the cross section of the printed sticks of Al-$KClO_4$ (a), B-$KClO_4$ (b), Ti-$KClO_4$ (c).

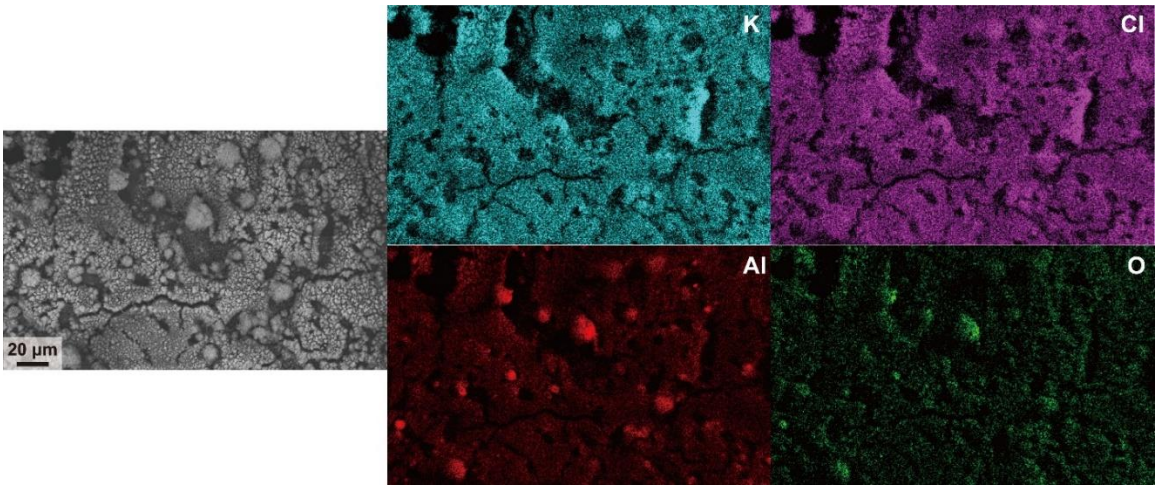

Figure S 3. SEM image and corresponding EDS images containing micro aluminum oxide particles for post-combustion product of Al-$KClO_4$.

S.2. Snapshots from microimaging videos

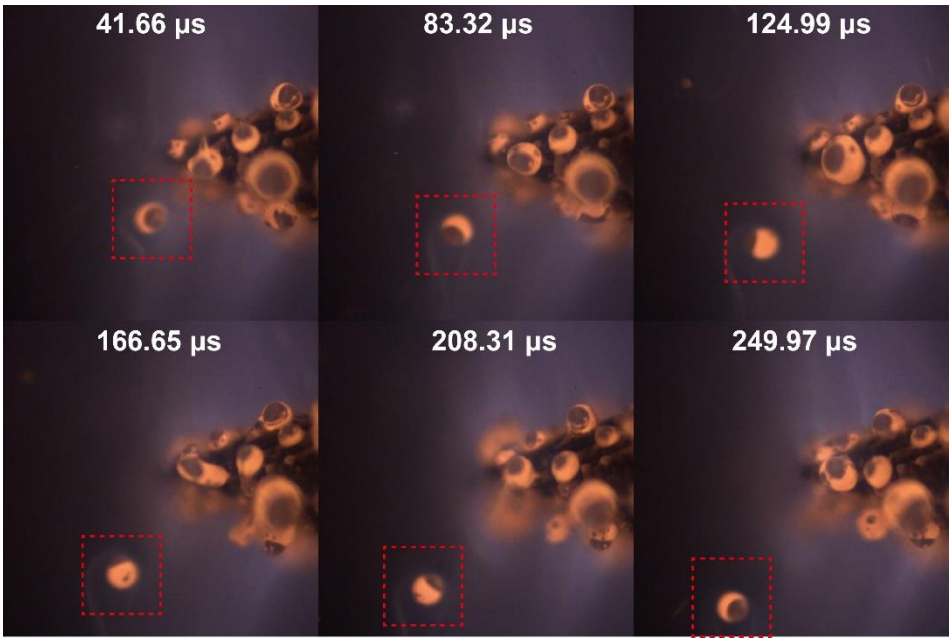

Figure S 4. A series of images with time stamps from Al-$KClO_4$ showing a particle spinning at high frequency. (The particle is enclosed in the dash square)

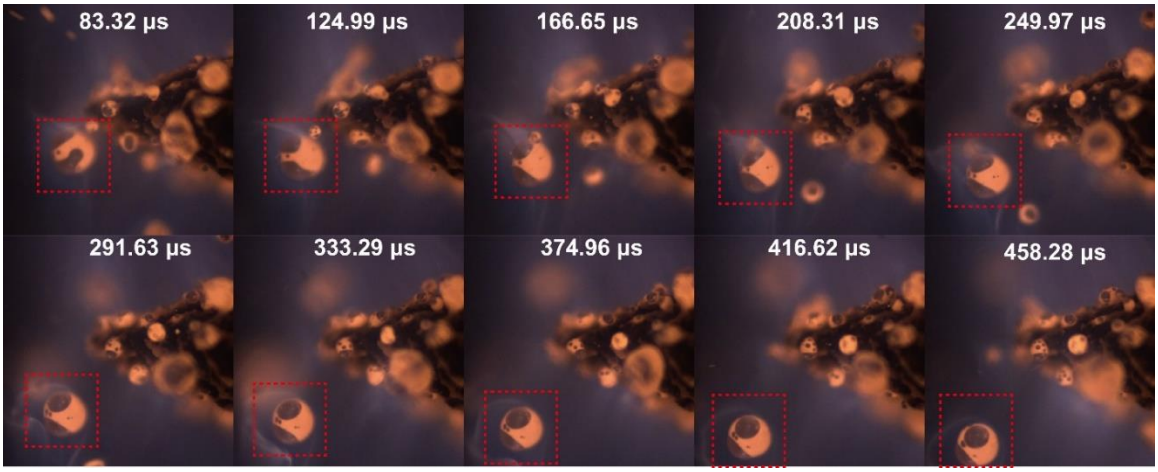

Figure S 5. A series of images with time stamps from Al-$KClO_4$ showing a particle spinning at low frequency. (The particle is enclosed in the dash square)

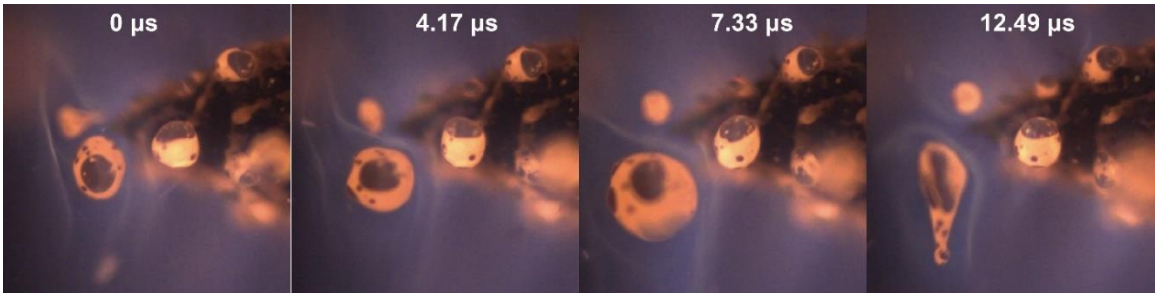

Figure S 6. A series of images from Al-$KClO_4$ showing a particle bubbling and busting.

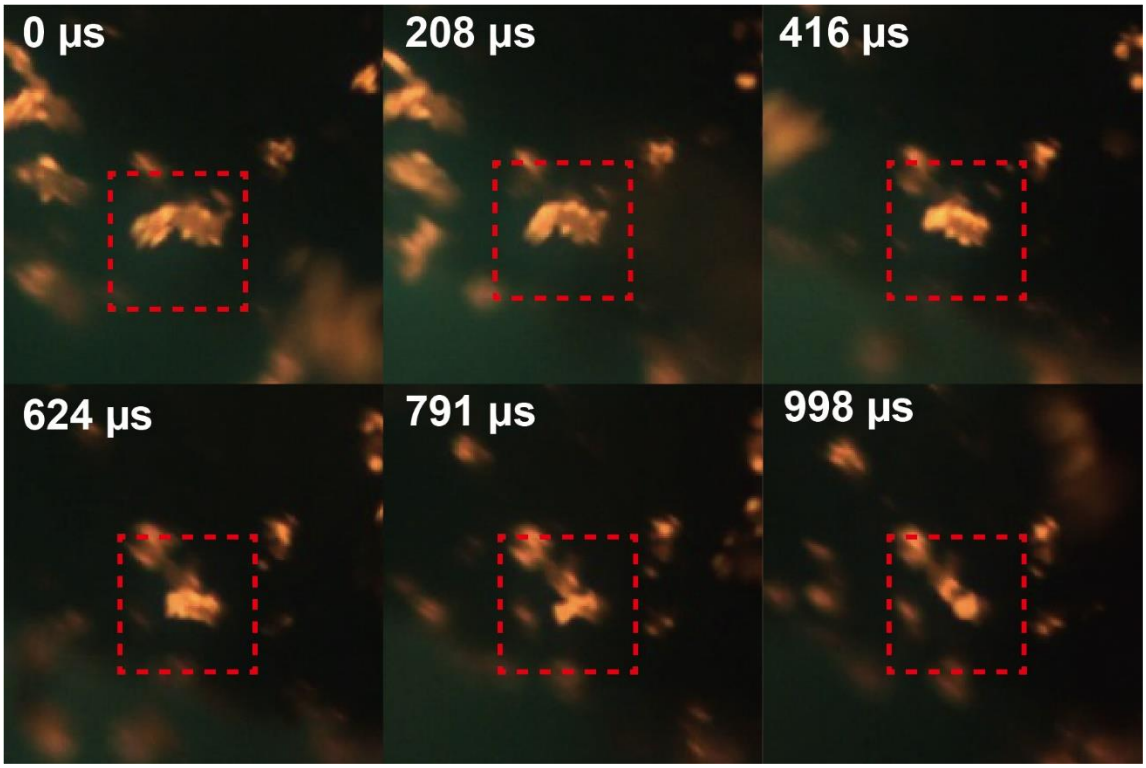

Figure S 7. A series of images from B-$KClO_4$ showing an agglomerate balling up into sphere.

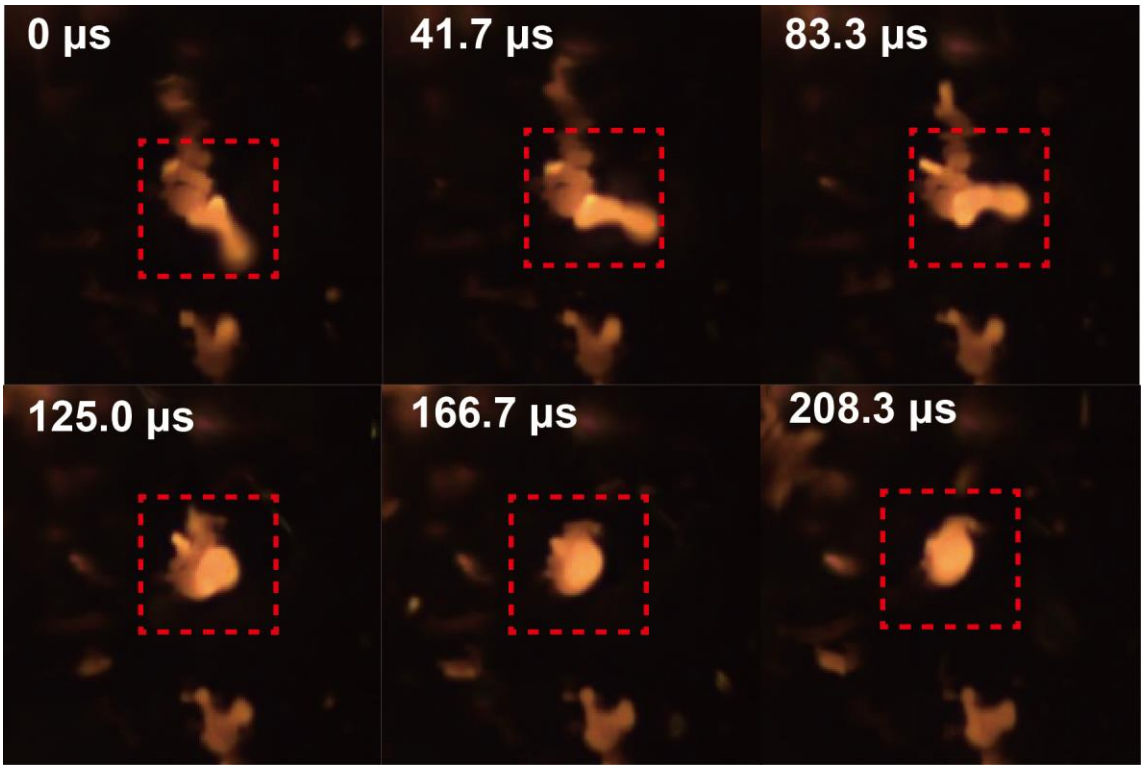

Figure S 8. A series of images from Ti-$KClO_4$ showing an agglomerate balling up into sphere.

S.3 Optical thickness calculation

The optical thickness of the smoke surrounding the Al droplets are estimated with the following equation:

$$\tau = -\ln(10^{\epsilon c L}) \quad \text{(S1)}$$

Where τ is the optical thickness, ϵ is molar absorption coefficient that is calculated with Mie theory (Biswas, P.; Mulholland, G. W.; Rehwoldt, M. C.; Kline, D. J.; Zachariah, M. R. Microwave Absorption by Small Dielectric and Semi-Conductor Coated Metal Particles. *J. Quant. Spectrosc. Radiat. Transf.* **2020**, *247*, 106938.), c is the number concentration of

particles in the smoke that is estimated to be between 10^{14} and $10^{18}/m^3$ and we use $10^{16}/m^3$ for the estimation (Biswas, P.; Ghildiyal, P.; Mulholland, G. W.; Zachariah, M. R. Modelling and Simulation of Field Directed Linear Assembly of Aerosol Particles. *J. Colloid Interface Sci.* **2021**, *592*, 195–204.), and L is the smoke thickness/optical path length, which is assumed to be 100 μm. The complex permittivity of the Al_2O_3 was assumed to be around 9.78+0.001i to perform the Mie theory calculation (Kline, D. J.; Rehwoldt, M. C.; Turner, C. J.; Biswas, P.; Mulholland, G. W.; McDonnell, S. M.; Zachariah, M. R. Spatially Focused Microwave Ignition of Metallized Energetic Materials. *J. Appl. Phys.* **2020**, *127* (5), 055901.

Estimated optical thickness in the range of visible wavelength with different particle sizes is shown in Figure. S10.

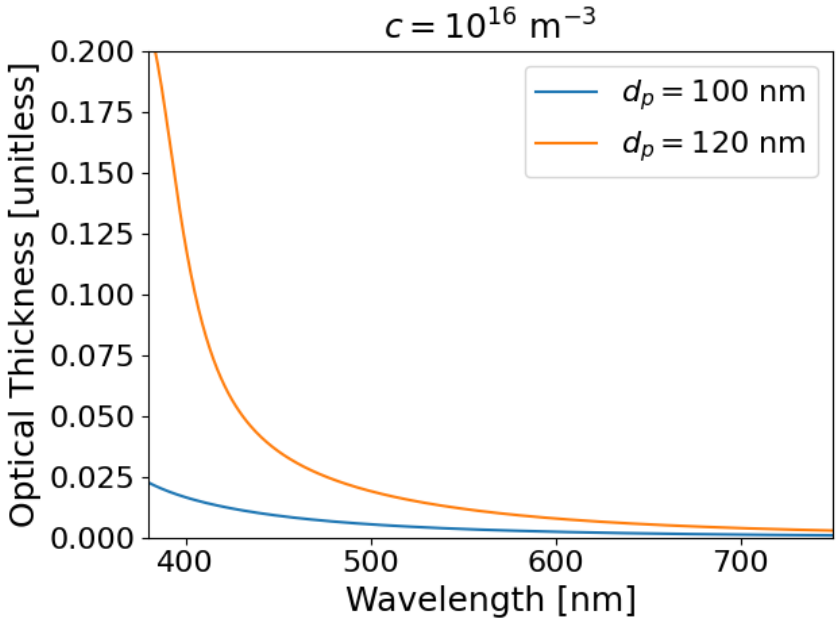

Figure S 9. Estimated optical thickness for different particle sizes in the range of visible light wavelength with number concentration c=10^{16}/m^3.

S.4 Characterization from SEM of the post-combustion products and three-color (RBG) pyrometry for B-$KClO_4$

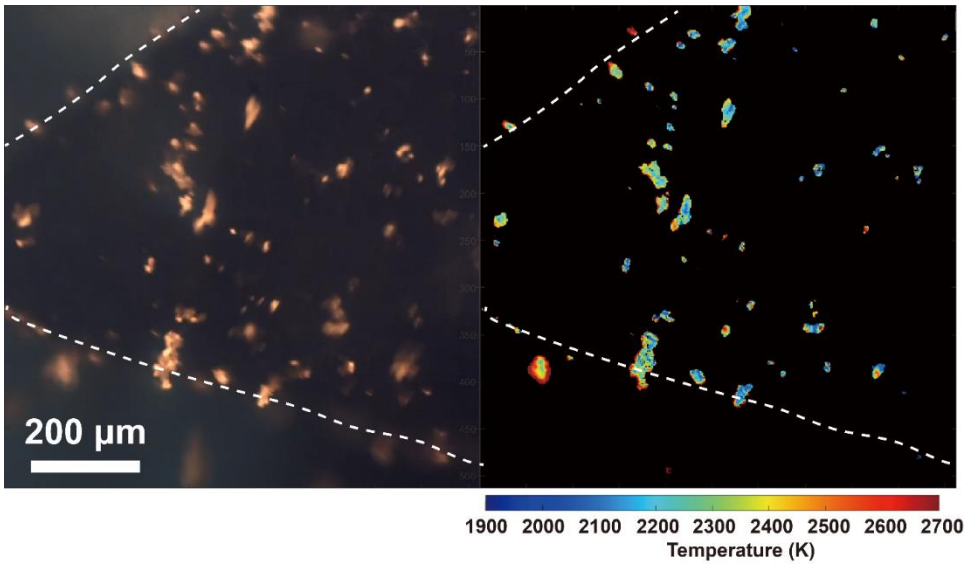

Figure S 10. Temperature map from three-color (RGB) pyrometry for an image from high-speed microscopy video of B-$KClO_4$. High error points and low-intensity points were excluded from the calculation. The dashed line represents boundary of the burning surface.

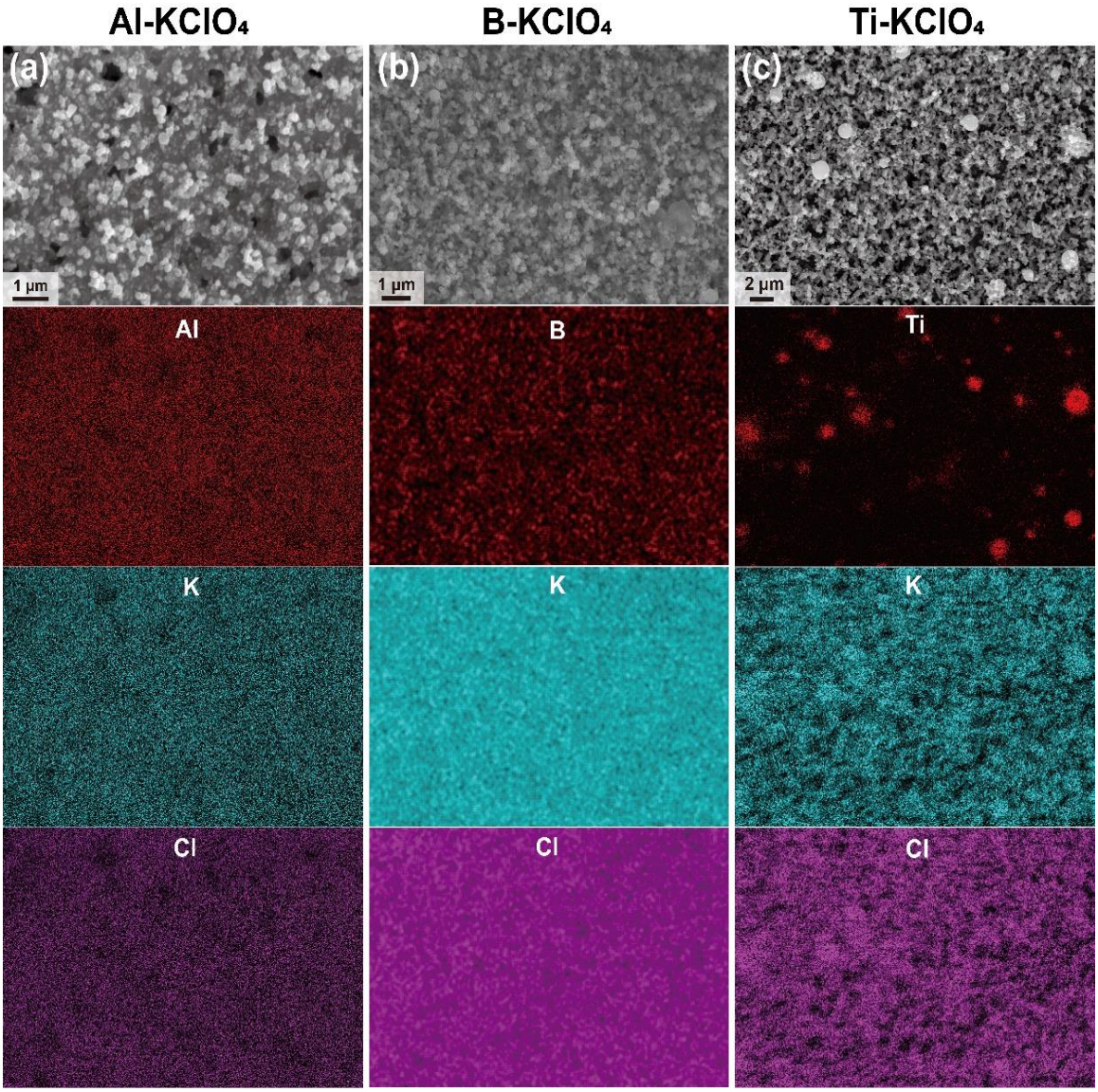

Figure S 11. SEM images and corresponding EDS images focusing on background areas without larger microparticles for post-combustion products of Al-$KClO_4$ (a), B-$KClO_4$ (b), and Ti-$KClO_4$ (c).

S.5 Energy release rate and modeling details

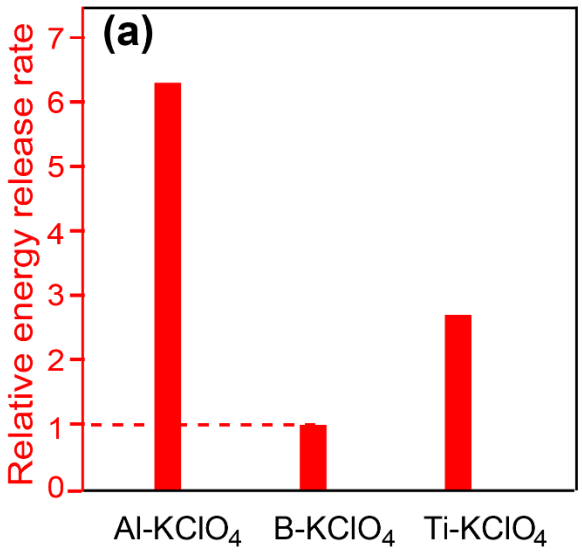

Figure S 12 The relative energy release rate of Al-$KClO_4$, B-$KClO_4$, and Ti-$KClO_4$.

Energy release rate per unit area of a composite is estimated based on the following equation:

$$E = \rho \times v \times A \times Cp \times \Delta T \quad \text{(S2)}$$

Where ρ is the density of the printed composite, v is the burn rate, A is the cross-section area of the composite, C_p is the heat capacity of the composite, and ΔT is the difference between flame temperature and room temperature. C_p is assumed to be the same for all three composites. For all the three systems, estimated temperature of the agglomerates from pyrometry is used.

Model of burn time of Al droplets is based on the following equation

$$\mathrm{t} = \frac{D_0^2}{K}$$

$$\mathrm{K} = \frac{8k_g}{\rho_l c_{pg} \ln(1+B)}$$

$$\mathrm{B} = \frac{\frac{\Delta h_c}{v} + c_{pg}(T_{bulk} - T_s)}{q_{i-l} + h_{fg}}$$

Where D_0 is initial droplet diameter, Δh_c is combustion enthalpy (31kJ/g) [NIST], v is oxygen to fuel mass ratio, ρ_l is the density of liquid Al (2357 kg/m^3), k_g is the thermal conductivity of air (0.024 W/mK), c_{pg} is specific heat of Al (900 J/kgK), T_s is 298 K, T_{bulk} is 2350 K (avg. from experiments), h_{fg} is latent heat of vaporization (293.4 kJ/mol), q_{i-l} is interface to liquid heat transfer, which is 0 as it is assumed that there is no thermal gradient inside the droplet.

Model of burn time of Ti particles are based on the following equation:

$$\mathrm{t} = \frac{\rho}{2k_r C_{Ti}} D_0$$

$$k_r = \frac{2D_e}{D^*}$$

where k_r is surface reaction rate, ρ is the density of Ti (4500 kg/m^3), C_A ($\frac{mol}{m^3}$) is the concentration of Ti atoms in the particle. D_e is effective free-molecular diffusivity of O_2 in air., which is 10^{-5} m^2/s. D^* is the critical diameter from diffusion to surface reaction

transition (~30 μm) (Zong, Y.; Jacob, R. J.; Li, S.; Zachariah, M. R. Size Resolved High Temperature Oxidation Kinetics of Nano-Sized Titanium and Zirconium Particles. *J. Phys. Chem. A* **2015**, *119* (24), 6171–6178.).

5 Investigating the Combustion Behavior of Al/AP Composites with High-Speed Videography

5.1 Summary

In this study, I prepare 90wt% loading composites of aluminum and ammonia perchlorate with different equivalence ratios and study their combustion behavior with high-speed microscopic and macroscopic videography and pyrometry. For all equivalence ratios, microscopic videography reveals the formation of fractal-shaped agglomerates that transform into molten droplets eventually growing into larger droplets before departing the burning surface. Droplet size analysis suggests that droplets of similar sizes evolve from composites with equivalence ratio of 0.5 and 1, while dramatically larger droplets are observed for composite with equivalence ratio of 2. Temperature measurement from three-color pyrometry suggests that there is no difference in temperature among the agglomerates/droplets from difference equivalence ratios. Burn rates obtained from the macroscopic imaging show that burn rate of the composites increases as equivalence ratio increases, although one expects that equivalence ratio of 2 should have a lower burn rate due to its lower energy density. Analysis of droplet residence time on the burning surface shows that while the droplets on the burning surface in the case of composites with equivalence ratio of 0.5 and 1 have similar residence times, droplets at equivalence ratio of 2 have significantly longer residence times on the burning surface, which results in significantly more heat feedback to the unburnt propellant and leads to the unexpected higher burn rate than equivalence ratio of 1.

5.2 Introduction

Aluminum (Al) particles are widely used in solid propellants as additives to increase specific impulse and enhance combustion stability [1]. Al nanoparticles offer a higher energy release rate and lower ignition temperature than traditional Al microparticles [2–5]. Nevertheless, the nanostructure of Al nanoparticles is typically rapidly lost prior to and during combustion due to reactive sintering and in-combustion agglomeration [6–8]. This means that the effective size of Al particles increases during combustion [9–11]. This phenomenon can have a significant impact on the combustion performance of the propellant and is the motivation for imaging studies explored in this work.

The Al particle agglomeration in propellants has been widely observed and a variety of diagnostic techniques have been applied to investigate the particle behavior [12–16]. Ex-situ techniques using electron microscopes for characterizing the captured particles from combustion are commonly used to study agglomerates [12,13,15,17]. Recently, in-situ high-speed imaging techniques have proven to be particularly useful for probing spatial and temporal combustion dynamics as well as estimating particle temperatures, quantifying size, and velocity of Al particles [1,18–21]. Despites these studies, a systematic investigation focusing on characterizing combustion behavior of Al/AP (ammonium perchlorate) composites with various equivalence ratios using high-speed imaging techniques is still lacking.

In this chapter, I prepare free-standing Al/AP composites with 90% loading with different equivalence ratios by 3D printing and investigate their combustion behavior

systematically using high-speed (μs) and high resolution (μm) imaging techniques, which enable direct visualization of Al agglomerates/droplets evolving during combustion process in-operando. Size and residence time of droplets on the burning surface are measured. Temperature of the burning agglomerates/droplets in the reacting zone is estimated with three-color pyrometry. Burn rate of different composites and droplet velocity after departing from the burning surface are obtained from macroscopic imaging.

5.3 Materials and Methods

5.3.1 Materials

Aluminum nanoparticles (Al NPs, ~70nm, 66 wt% active) were purchased from US Research Nanomaterials Inc. The active content of these fuels was determined with thermogravimetry and differential scanning calorimetry (TGA−DSC) using a SDT Q600 from TA Instruments. Ammonia perchlorate microparticles (AP MPs, 90 μm) were obtained from Pyro Chem Source. Ethanol (200 proof) was purchased from Koptec. Dichloromethane (99.9%) was purchased from Fisher Scientific. Polymethyl methacrylate (PMMA) was purchased from Alfa Aesar.

5.3.2 Preparation of ink and direct ink writing of 90 wt% loading Al/AP composites

A typical ink was prepared by firstly dissolving 10 wt% of PMMA in the mixture of ethanol and dichloromethane (volumetric ratio of 1:1). AP was then added to the solution and the obtained suspension was sonicated for 15 mins. Then Al was added, and the obtained suspension was sonicated for 30 mins. After sonication the suspension was stirred

for ~3 h before printing. The amount of Al and AP was determined with the following equation, and different equivalence ratios (φ=0.5, 1, and 2) were considered.

$$10Al + 6NH_4ClO_4 = 5Al_2O_3 + 6HCl + 3N_2 + 9H_2O$$

Details about printing can be found in our previous studies [22]. Generally, for printing, an ink was extruded through an 18-gauge nozzle and written on a glass substrate at room temperature. After printing, the films were cut into ~2 cm long sticks for studying combustion behaviors.

5.3.3 Microscopic and macroscopic imaging

The details of the microscopic and macroscopic imaging process can be found in our previous publications [21]. Briefly, the macroscopic imaging was performed with a high-speed camera (Vision Research Phantom Miro M110) and the microscopic imaging was performed with a high-speed camera (Vision Research Phantom VEO710L) coupled to a long working length objective; Infinity Photo-Optical Model K2 DistaMax. For a typical measurement, a printed stick was mounted on a stage holder within a chamber filled with argon, and the chamber was placed between the two imaging systems. The stick was then ignited with a nichrome wire by Joule-heating. The combustion process was recorded at a sample rate of 10 000 frame/s with the macroscopic imaging system and 24 000 frame/s (512 x 512 pixels, 1.7 μm/pixel) with the microscopic imaging system. The schematic of the setup is shown in Figure 5-1.

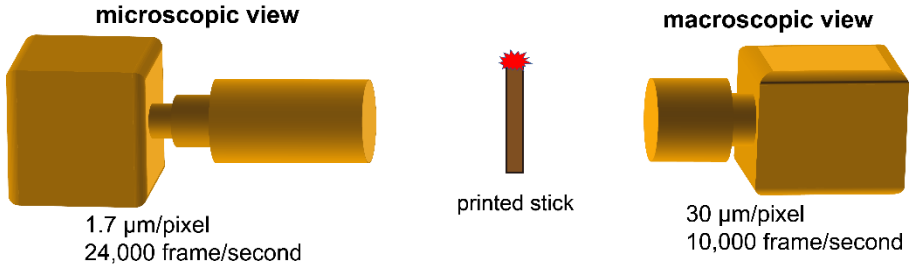

Figure 5-1 Setup of the microscopic and macroscopic imaging systems.

Size measurement was performed only on spherical droplets (fractal-shaped agglomerates were not counted). For φ=0.5 and 1, residence time of droplets were performed in microimaging videos by tracking the starting time of the emergence of the fractal-shaped agglomerates, to the time when the droplets leave the burning surface 1. For φ=2, in addition to the aforementioned tracking method in microimaging videos, residence time of large droplets were also tracked in macroscopic imaging videos due to their much larger size and longer residence time. Particle velocity in the gas phase was measured by tracking the location of the particles and the corresponding time.

5.3.4 Three-color imaging pyrometry

Details about three-color imaging pyrometry can be found in the previous studies from our group [19,23]. Briefly, temperature estimation of a sample was performed with the ratios of channel intensities of three colors (red, green, blue) from the Bayer filter by using a custom MATLAB routine assuming graybody emission behavior of the sample. Calibration parameters were collected by the response to a blackbody source (Mikron M390) and the temperature uncertainty was estimated to be nominally 200-300 K [10,24].

5.3.5 Results and discussion

High-speed microscopic videos enable direct visualization of events on the burning surface that provides key understanding of the combustion characteristics. Figure 5-2 (top) shows the representative snapshots from the high-speed microscopic videos for Al-AP with different equivalence ratios. For all the three equivalence ratios, fractal-shaped agglomerates form and transform into molten droplets with dark Al_2O_3 caps [18], which may coalesce into larger droplets. For equivalence ratio of 0.5 and 1, these droplets depart from the burning surface, and do not coalesce further significantly. While for equivalence ratio of 2, the majority of droplets merge into much larger droplets before leaving the burning surface. Size distribution of the droplets and its impact on the macroscopic combustion behavior will be discussed further in the following section.

Three-color (RGB) pyrometry was used for estimating temperature of the agglomerates/droplets and the obtained representative temperature maps for different equivalence ratios are shown in Figure 5-2 (bottom). For all the three equivalence ratios, fractal-shaped agglomerates have a temperature of ~2100 K. Although this temperature is significantly higher than the melting point of Al at 930 K, it is lower than the melting point of Al_2O_3 at 2345 K [1], therefore Al_2O_3 is in the solid-state and prevents the fractal-shaped agglomerate from becoming droplets. As oxidation continues and temperature increases near the melting point (~2345 K), Al_2O_3 melts and phase separates from Al, and retracts into a distinct cap through surface tension [25]. The measured temperature of droplets is ~2350 K, which is about the melting point of Al_2O_3, explaining the observed nearly spherical morphology. It is noteworthy that although droplets of equivalence ratio of 2 are

significantly larger than equivalence ratio of 0.5 and 1, these droplets have the about same temperature at ~ 2350 K. For equivalence of 2, it is clear than the Al_2O_3 cap is slightly hotter (~150 K) than the Al body, consistent with the observations from previous studies [1,18]. This temperature difference is attributed to the evaporation of Al that removes heat from the Al body.

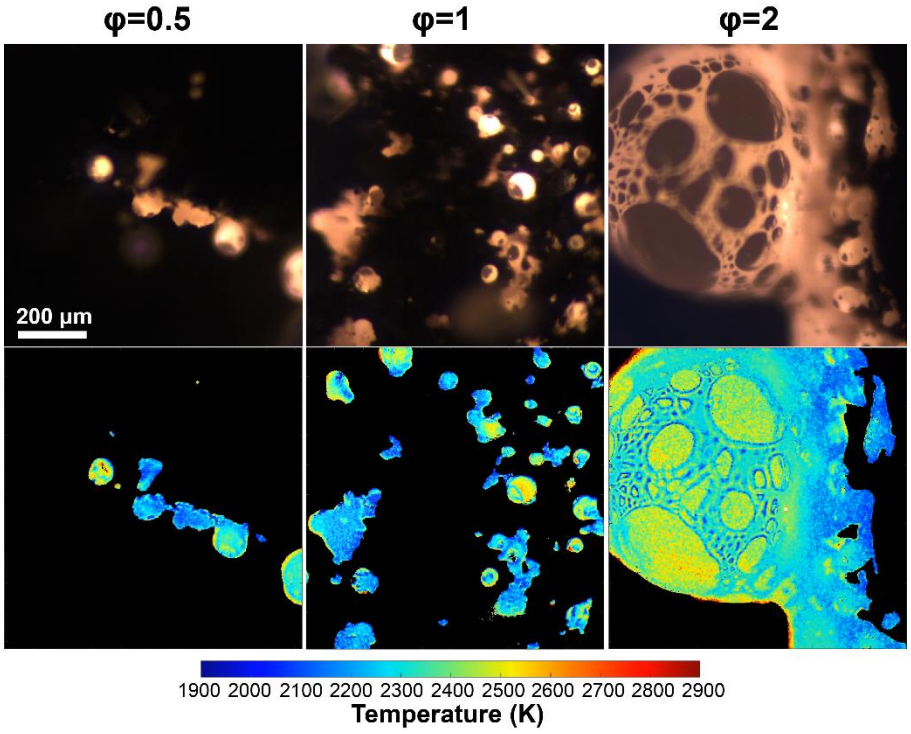

Figure 5-2 Representative images from high-speed microscopy video for Al-AP at different equivalence ratios on the top and their corresponding temperature map from three-color pyrometry on the bottom. High error points and low-intensity points were excluded from the temperature calculation.

Size distributions of droplets observed in microimaging videos for Al-AP with different equivalence ratios are displayed in Figure 5-3 (a). There is minimal difference in size distribution between equivalence of 0.5 and 1, as the majority of the droplets for both equivalence ratios are below 120 µm. While for equivalence ratio of 2, the overall droplet

sizes are dramatically larger with more than half of the droplets being above 200 μm. It is noteworthy that the primary Al particles initially incorporated into the composite is 70 nm, which implies that there is extensive sintering/coalescence and agglomeration of Al during the combustion process and the sintering/agglomeration extent of equivalence of 2 is significantly higher, as the size increases ~1000 times for equivalence ratio of 0.5 and 1, whereas ~ 4500 times in the case of equivalence ratio of 2.

Figure 5-3 (b) displays a series of snapshots of a representative droplet forming from a fractal-shaped agglomerate and growing before departing from the burning surface at equivalence ratio of 1. This visualization shows that the droplets burn for some time on the burning surface rather than departing upon formation. The droplet residence time on the burning surface is estimated based on the time span from the emergence of an agglomerate that evolves into a droplet to the departure of that droplet, and the obtained residence time distribution of different equivalence ratios are shown in Figure 5-3 (c). Similar to the size distribution comparison, there is minimal difference in droplet residence time between equivalence ratio of 0.5 and 1, and majority of the residence times are less than 6 ms. While for equivalence ratio of 2, the overall residence time is significantly higher, with about 40% of the droplets having residence times more than 8 ms.

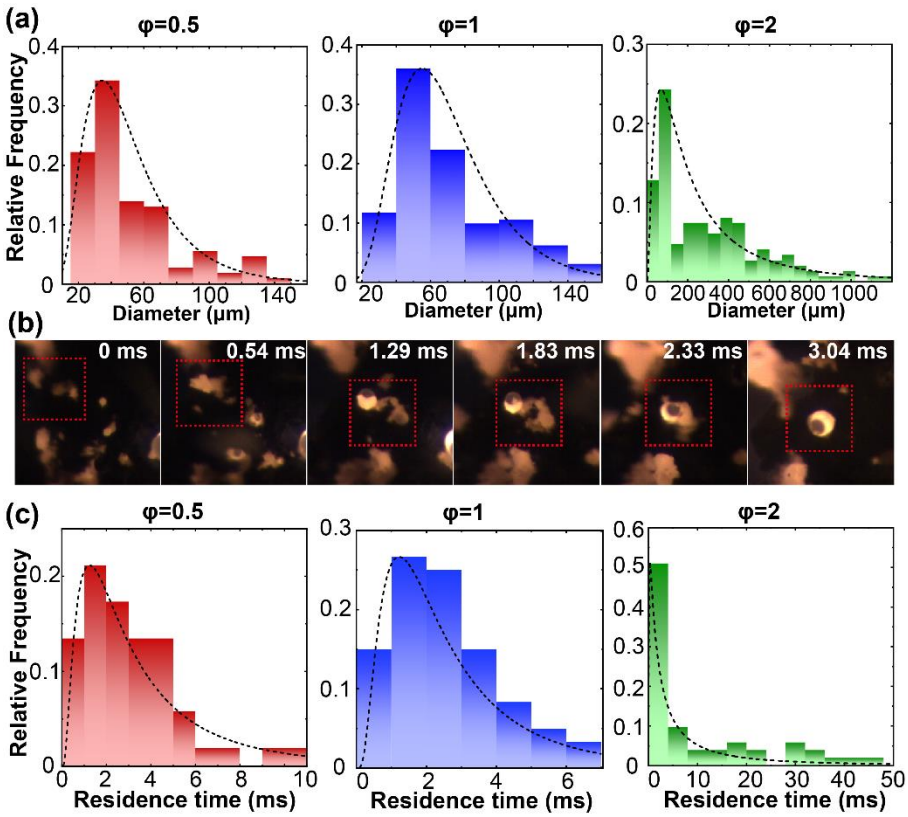

Figure 5-3 Droplet size distribution of Al-AP with different equivalence ratios (a), time-resolved snapshots of a representative droplet evolving before departing from the burning surface for φ=1 (b), and residence time distribution of Al-AP with different equivalence ratios (c).

Burn rate of a composite normally reflects its energy release rate, and provides insight on the overall combustion performance[9,26,27]. Figure 5-4 (a) displays a series of time-resolved snapshots from the macroscopic videos for different equivalence ratios, with their corresponding burn rates. It is worth noting that some droplets are sufficiently large to be resolved in the macroscopic videos for equivalence ratio of 2. Droplet velocity in the gas phase after departing from the burning surface is measured by tracking the travelling distance and the corresponding time. The obtained velocity distribution is shown in Figure 5-4 (b), which reveals that majority of droplets have a velocity above 2 m/s for equivalence

ratio of 0.5 and 1, while for equivalence ratio of 2, the droplet velocity is mostly below 2 m/s. This difference is attributed to the considerably larger droplet size of equivalence ratio of 2 compared to equivalence ratio of 0.5 and 1. It is interesting that although there is only minimal difference between equivalence of 0.5 and 1 for both droplet size and residence time on the burning surface, the droplet velocity in the gas phase of equivalence of 1 is about twice of equivalence ratio of 0.5. As the equivalence ratio changes from 0.5 and 1, the AP content decreases slightly, which means the amount of gas generated cannot explain this difference. Nevertheless, the heat generated from equivalence ratio of 1 is almost twice of equivalence ratio of 0.5. The higher amount of heat generation causes faster gas expansion performing PV work by pushing the droplets apart and thereby results in a higher droplet velocity, which is believed to be the primary reason for a higher droplet velocity of equivalence ratio of 1.

As equivalence ratio increases from 0.5 (fuel lean) to 1, burn rate increases as expected from 1.6 cm/s to 3.2 cm/s. As equivalence ratio increase from 1 to 2 (fuel rich), burn rate is expected to decrease as the overall energy density of the composite is reduced due to the excess content of fuel and the burn tests are performed in an argon environment that provides no extra oxygen. However, I observe that the burn rate increases from 3.2 cm/s to 5.4 cm/s when equivalence ratio increases from 1 to 2. Previous studies have demonstrated that reduction in agglomeration/sintering of aluminum particles effectively promotes the propagation rate [9,10,15,28,29]. A primary question now arises: Why does the composite with equivalence ratio of 2 have a higher burn rate than equivalence ratio of 1

even though it has lower energy density and significantly more severe sintering/agglomeration?

For propagation sufficient heat transferred from the flame back to the unreacted material is essential for steady propagation [24,29–31]. For Al based composites, previous studies have demonstrated through calculation that conduction is not the dominant source for heat feedback to the unburnt material [24,30]. These calculations had the underlying assumption that burning particles depart from the burning surface immediately after reaching a certain temperature. However, in the case of the current study, droplets reside on the burning surface for a significant duration after reaching the maximum temperature. Figure 5-2 shows that droplets from composites with different equivalence ratios have the same temperature, which suggests a higher amount of absolute energy has been provided as conductive heat feedback for a longer residence time if assuming other factors remain invariant. As discussed above, droplet residence time from composite with equivalence ratio of 2 is significantly longer than equivalence of 1, which indicates that a higher amount of total heat is provided back to the unburnt material from the burning droplets for equivalence ratio of 2 than equivalence of 1. This higher heat feedback results in enhanced burn rate, and this enhancement exceeds the reduction effects from lower energy density, and more severe sintering/agglomeration. Therefore, a higher burn rate is observed for the composite with equivalence ratio of 2 than equivalence ratio of 1.

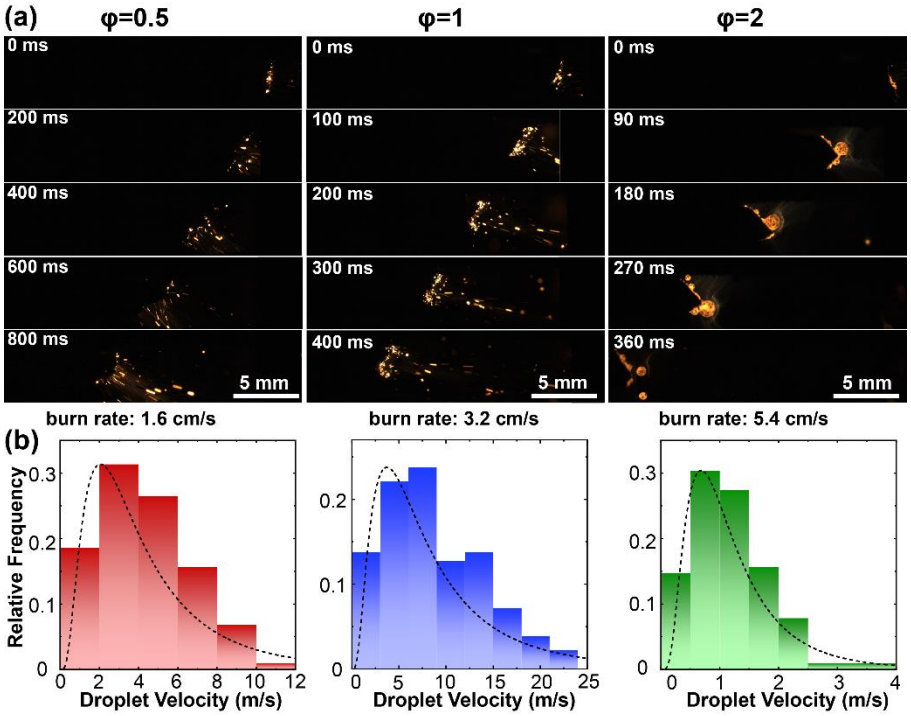

Figure 5-4 Time resolved-snapshots of high-speed macroscopic video with corresponding burn rate (a), and droplet velocity distribution (b) of Al-AP with different equivalence ratios. Note: the videos have the same framerate.

5.4 Conclusions

In this study, high-speed microscopic and macroscopic imaging techniques were used as the primary diagnostic tools for investigating the combustion behavior of 3D printed 90% loading Al-AP propellants with different equivalence ratios (φ=0.5, 1, and 2) in an inert environment. Microscopic imaging shows that for all the three equivalence ratios, fractal-shaped agglomerates transition into spherical droplets that grow into larger droplets before departing the burning surface. While droplets with similar sizes are observed for equivalence ratio 0.5 and 1, significantly larger droplets form for equivalence ratio of 2. Three-color pyrometry employed for measuring agglomerate/droplet temperature shows there is no difference among the agglomerates/droplets from difference equivalence ratios.

Macroscopic imaging reveals that burn rate of the composite increases as equivalence ratio increases. Residence time analysis shows droplet evolving from composite with equivalence ratio of 2 has dramatically longer residence time on the burning surface than equivalence ratio of 0.5 and 1. This significantly longer residence time is believed to result in more heat feedback to the unburnt composite that causes the unexpected higher burn rate than equivalence ratio of 1. This study reveals the dominance of conductive heat feedback on the propagation rate of an aluminized propellant.

5.5 References

(1) Chen, Y.; Guildenbecher, D. R.; Hoffmeister, K. N. G.; Cooper, M. A.; Stauffacher, H. L.; Oliver, M. S.; Washburn, E. B. Study of Aluminum Particle Combustion in Solid Propellant Plumes Using Digital In-Line Holography and Imaging Pyrometry. *Combust. Flame* **2017**, *182*, 225–237. https://doi.org/10.1016/j.combustflame.2017.04.016.

(2) Sundaram, D.; Yang, V.; Yetter, R. A. Metal-Based Nanoenergetic Materials: Synthesis, Properties, and Applications. *Prog. Energy Combust. Sci.* **2017**, *61*, 293–365. https://doi.org/10.1016/j.pecs.2017.02.002.

(3) Comet, M.; Martin, C.; Schnell, F.; Spitzer, D. Nanothermites: A Short Review. Factsheet for Experimenters, Present and Future Challenges. *Propellants Explos. Pyrotech.* **2019**, *44* (1), 18–36. https://doi.org/10.1002/prep.201800095.

(4) Granier, J. J.; Pantoya, M. L. Laser Ignition of Nanocomposite Thermites. *Combust. Flame* **2004**, *138* (4), 373–383. https://doi.org/10.1016/j.combustflame.2004.05.006.

(5) Sundaram, D. S.; Puri, P.; Yang, V. A General Theory of Ignition and Combustion of Nano- and Micron-Sized Aluminum Particles. *Combust. Flame* **2016**, *169*, 94–109. https://doi.org/10.1016/j.combustflame.2016.04.005.

(6) Chakraborty, P.; Zachariah, M. R. Do Nanoenergetic Particles Remain Nano-Sized during Combustion? *Combust. Flame* **2014**, *161* (5), 1408–1416. https://doi.org/10.1016/j.combustflame.2013.10.017.

(7) Galfetti, L.; DeLuca, L. T.; Severini, F.; Colombo, G.; Meda, L.; Marra, G. Pre and Post-Burning Analysis of Nano-Aluminized Solid Rocket Propellants. *Aerosp. Sci. Technol.* **2007**, *11* (1), 26–32. https://doi.org/10.1016/j.ast.2006.08.005.

(8) Melcher, J. C.; Krier, H.; Burton, R. L. Burning Aluminum Particles Inside a Laboratory-Scale Solid Rocket Motor. *J. Propuls. Power* **2012**. https://doi.org/10.2514/2.5977.

(9) Wang, H.; Wang, Y.; Garg, M.; Moore, J. S.; Zachariah, M. R. Unzipping Polymers Significantly Enhance Energy Flux of Aluminized Composites. *Combust. Flame* **2022**, *244*, 112242. https://doi.org/10.1016/j.combustflame.2022.112242.

(10) Wang, H.; Kline, D. J.; Rehwoldt, M. C.; Zachariah, M. R. Carbon Fibers Enhance the Propagation of High Loading Nanothermites: In Situ Observation of Microscopic Combustion. *ACS Appl. Mater. Interfaces* **2021**. https://doi.org/10.1021/acsami.1c02911.

(11) Emelyanov, V. N.; Teterina, I. V.; Volkov, K. N. Dynamics and Combustion of Single Aluminium Agglomerate in Solid Propellant Environment. *Acta Astronaut.* **2020**, *176*, 682–694. https://doi.org/10.1016/j.actaastro.2020.03.046.

(12) Li, L.; Chen, X.; Zhou, C.; Li, W.; Zhu, M. Experimental and Model Investigation on Agglomeration of Aluminized Fuel-Rich Propellant in Solid Fuel Ramjet. *Combust. Flame* **2020**, *219*, 437–448. https://doi.org/10.1016/j.combustflame.2020.06.019.

(13) Ao, W.; Liu, P.; Liu, H.; Wu, S.; Tao, B.; Huang, X.; Li, L. K. B. Tuning the Agglomeration and Combustion Characteristics of Aluminized Propellants via a New

Functionalized Fluoropolymer. *Chem. Eng. J.* **2020**, *382*, 122987. https://doi.org/10.1016/j.cej.2019.122987.
(14) Jin, B.; Wang, Z.; Xu, G.; Ao, W.; Liu, P. Three-Dimensional Spatial Distributions of Agglomerated Particles on and near the Burning Surface of Aluminized Solid Propellant Using Morphological Digital in-Line Holography. *Aerosp. Sci. Technol.* **2020**, *106*, 106066. https://doi.org/10.1016/j.ast.2020.106066.
(15) Sippel, T. R.; Son, S. F.; Groven, L. J. Aluminum Agglomeration Reduction in a Composite Propellant Using Tailored Al/PTFE Particles. *Combust. Flame* **2014**, *161* (1), 311–321. https://doi.org/10.1016/j.combustflame.2013.08.009.
(16) Cohen, O.; Michaels, D.; Yavor, Y. Agglomeration in Composite Propellants Containing Different Nano-Aluminum Powders. *Propellants Explos. Pyrotech.* **2022**, *47* (9), e202100320. https://doi.org/10.1002/prep.202100320.
(17) Tu, C.; Chen, X.; Li, Y.; Zhang, B.; Zhou, C. Experimental Study of Al Agglomeration on Solid Propellant Burning Surface and Condensed Combustion Products. *Def. Technol.* **2022**. https://doi.org/10.1016/j.dt.2022.05.016.
(18) Wang, Y.; Hagen, E.; Biswas, P.; Wang, H.; Zachariah, M. R. Imaging the Combustion Characteristics of Al, B, and Ti Composites. *Combust. Flame* **2023**, *252*, 112747. https://doi.org/10.1016/j.combustflame.2023.112747.
(19) Wang, H.; Kline, D. J.; Zachariah, M. R. In-Operando High-Speed Microscopy and Thermometry of Reaction Propagation and Sintering in a Nanocomposite. *Nat. Commun.* **2019**, *10* (1), 3032. https://doi.org/10.1038/s41467-019-10843-4.
(20) Marsh, A. W.; Wang, G. T.; Heyborne, J. D.; Guildenbecher, D. R.; Mazumdar, Y. C. Time-Resolved Size, Velocity, and Temperature Statistics of Aluminum Combustion in Solid Rocket Propellants. *Proc. Combust. Inst.* **2021**, *38* (3), 4417–4424. https://doi.org/10.1016/j.proci.2020.08.010.
(21) Wang, H.; Julien, B.; Kline, D.; Alibay, Z.; Rehwoldt, M.; Rossi, C.; Zachariah, M. Probing the Reaction Zone of Nanolaminates at ∼μs Time and ∼μm Spatial Resolution. *J. Phys. Chem. C* **2020**, *124* (25), 13679–13687. https://doi.org/10.1021/acs.jpcc.0c01647.
(22) Wang, H.; Shen, J.; Kline, D. J.; Eckman, N.; Agrawal, N. R.; Wu, T.; Wang, P.; Zachariah, M. R. Direct Writing of a 90 Wt% Particle Loading Nanothermite. *Adv. Mater.* **2019**, *31* (23), 1806575. https://doi.org/10.1002/adma.201806575.
(23) Jacob, R. J.; Kline, D. J.; Zachariah, M. R. High Speed 2-Dimensional Temperature Measurements of Nanothermite Composites: Probing Thermal vs. Gas Generation Effects. *J. Appl. Phys.* **2018**, *123* (11), 115902. https://doi.org/10.1063/1.5021890.
(24) Kline, D. J.; Alibay, Z.; Rehwoldt, M. C.; Idrogo-Lam, A.; Hamilton, S. G.; Biswas, P.; Xu, F.; Zachariah, M. R. Experimental Observation of the Heat Transfer Mechanisms That Drive Propagation in Additively Manufactured Energetic Materials. *Combust. Flame* **2020**, *215*, 417–424. https://doi.org/10.1016/j.combustflame.2020.01.020.
(25) Harrison, J.; Brewster, M. Q. Analysis of Thermal Radiation from Burning Aluminium in Solid Propellants. *Combust. Theory Model.* **2009**, *13* (3), 389–411. https://doi.org/10.1080/13647830802684318.

(26) Wang, H.; Kline, D. J.; Rehwoldt, M.; Wu, T.; Zhao, W.; Wang, X.; Zachariah, M. R. Architecture Can Significantly Alter the Energy Release Rate from Nanocomposite Energetics. *ACS Appl. Polym. Mater.* **2019**, *1* (5), 982–989. https://doi.org/10.1021/acsapm.9b00016.
(27) Wang, H.; Jiang, Y.; Wang, Y.; Kline, D. J.; Zheng, X.; Zachariah, M. R. Do We Need Perfect Mixing between Fuel and Oxidizer to Maximize the Energy Release Rate of Energetic Nanocomposites? *Appl. Phys. Lett.* **2023**, *122* (1), 011901. https://doi.org/10.1063/5.0133995.
(28) Wang, H.; Kline, D. J.; Biswas, P.; Zachariah, M. R. Connecting Agglomeration and Burn Rate in a Thermite Reaction: Role of Oxidizer Morphology. *Combust. Flame* **2021**, *231*, 111492. https://doi.org/10.1016/j.combustflame.2021.111492.
(29) Brewster, M. Q.; Hardt, B. E. Influence of Metal Agglomeration and Heat Feedback on Composite Propellant Burning Rate. *J. Propuls. Power* **1991**, *7* (6), 1076–1078. https://doi.org/10.2514/3.23431.
(30) Egan, G. C.; Zachariah, M. R. Commentary on the Heat Transfer Mechanisms Controlling Propagation in Nanothermites. *Combust. Flame* **2015**, *162* (7), 2959–2961. https://doi.org/10.1016/j.combustflame.2015.04.013.
(31) Ishihara, A.; Brewster, M. Q.; Sheridan, T. A.; Krier, H. The Influence of Radiative Heat Feedback on Burning Rate in Aluminized Propellants. *Combust. Flame* **1991**, *84* (1), 141–153. https://doi.org/10.1016/0010-2180(91)90043-B.

6 Role of Surface Tension on Heat Feedback and Power from Energetic Composites

6.1 Summary

Heat feedback to the unburned reaction interface is an important controlling factor on the velocity of the reaction front and power delivery. In this chapter, I investigate the effect of agglomerate surface tension and its relationship to surface residence time and heat feedback on the combustion characteristics by Si addition to an $Al/KClO_4$ composite. Macroscopic imaging demonstrates a significant increase in burn rate with the addition of Si despite the fact that $Si/KClO_4$ has a slightly lower energy density than $Al/KClO_4$. Microscopic imaging coupled with three-color pyrometry reveals that molten liquid forms, and evolves into spherical droplets on the burning surface, which is subsequently ejected from the surface. I find that addition of Si results in a small increase in droplet size and a negligible impact on droplet temperature. However, the droplet formation rate on the surface is slower, leading to a significantly longer surface residence time. This leads to enhanced conductive heat feedback to the unburnt materials, thereby increasing the burn rate and energy release rate. I attribute the decreased droplet growth rate to the lowered surface tension of the liquid mixture with Si addition. This study highlights the crucial role of agglomerate physical property (e.g. surface tension) in influencing the combustion behavior of energetic composites.

6.2 Introduction

The development of solid propellants using metals as high-energy fuel has gained growing interest in the quest for materials capable of achieving higher energy release rates [1]. Metalized energetics has emerged as a promising frontier due to their higher theoretically chemical energy density compared to the traditional CHNO energetics [2–6]. Despite the higher energy density, the relatively long diffusion length between fuel and oxidizer of traditional micron-scale metal energetics results in slow reaction kinetics. Modern formulations that incorporate nanoscale fuels and oxidizers aim to enhance reactivity by increasing the specific surface area and reducing the transport distances [2,5,7–9]. Aluminum (Al) nanoparticles have been widely used for this purpose due to its high gravimetric and volumetric energy density (31.1 $kJ \cdot g^{-1}$ and 83.8 $kJ \cdot cm^{-3}$, respectively) as well as ready availability [10–15]. However, agglomeration becomes prevalent with the replacement of micron scale Al with nanoscale Al [16,17]. This is because of the tendency of Al nanoparticles to aggregate, sinter, and coalesce due to either solid state diffusion or viscous flow [1,18]. The agglomeration mitigates the advantages of utilizing Al nanoparticles and decreases the energy release rate [10,19,20].

Previous studies have explored various methods to improve the combustion performance of Al nanoparticles, such as surface coating [21–23], utilizing an additive [1], employing an unzipping polymer [24], and assembling Al nanoparticles into mesoparticles [19,25,26]. While these studies primarily focus on reducing agglomeration, other factors significantly influence combustion performance, one of which is the heat feedback [1,27–32]. Sufficient heat feedback to the unreacted material is essential for the steady propagation of

an energetic system [31–33], and a higher amount of heat feedback has been proven to enhance the burn rate and energy release rate [27,28,34]. Despite these findings, an investigation focusing on the effect of agglomerate physical properties on the heat feedback and burn rate is still lacking and is the focus of this chapter.

In this chapter, I investigate the effect of agglomerate surface tension and its relationship to heat feedback on the combustion characteristics of 3D printed 90% loading Al/$KClO_4$ composites with Si addition (0 wt%, 10 wt%, and 25 wt%). Si is utilized as Si/$KClO_4$ has a similar energy density to Al/$KClO_4$ (8.7 vs 9.5 kJ/g). In-situ imaging techniques have been demonstrated to be particularly useful to study the combustion behavior of aluminized energetic composites [35–38]. Here I employ high-speed microscopic imaging to study the reaction front and post-flame with high temporal (μs) and spatial (μm) resolution [16,24,39]. This enables us to track agglomerate size and surface residence time to provide information about the evolution process of agglomerates. Three-color imaging pyrometry is used to measure the temperature of the agglomerates. Burn rate of these composites are measured and relative energy release rates are calculated. The different forces affecting a representative agglomerate on the burning surface are estimated and compared to determine the agglomerate detachment mechanism. Scanning Electron Microscopy (SEM) coupled with energy-dispersive spectrometry (EDS) and X-ray diffraction (XRD) are utilized to analyze the post-combustion product and provide insight into the combustion process. In this chapter I will explain why adding a fuel with a slightly lower energy density (Si) to Al can result in an energy release rate increase in power by 2X.

6.3 Materials and Methods

6.3.1 Materials

Aluminum nanoparticles (Al NPs, ~70 nm) were purchased from US Research Nanomaterials. Potassium perchlorate ($KClO_4$, 99%) was obtained from Alfa Aesar. Polyvinylidene Fluoride (PVDF, average molecular weight: ~534,000) obtained from Sigma-Aldrich and METHOCEL™ F4M Hydroxypropyl Methylcellulose (HPMC) purchased from Dow Chemical Company were used as the binder for printing. N, N-dimethylformamide (DMF, 99.8%) was obtained from Fisher Scientific and used as a solvent to dissolve PVDF, HPMC, and $KClO_4$.

6.3.2 Synthesis of silicon nanoparticles

Silicon nanoparticles were synthesized via a nonthermal plasma method [15,40]. Briefly, the reactor is composed of a quartz tube (8 × 1 in.) and two copper ring electrodes. The first electrode was connected to a rf power supply (13.56 MHz) and matching network, and the second electrode was grounded. A butterfly valve was utilized to maintain a constant pressure of 267 Pa, and a baratron (MKS Baratron Capacitance Manometer) was used to monitor the pressure within the reactor. 1.36% SiH_4 and argon mixture was flown as the precursor gas while the rf input power was set at 80 W at to produce Si nanoparticles. The particles were collected downstream of the plasma volume by filtering.

6.3.3 Preparation of ink and direct ink writing of 90 wt% loading Al-Si/$KClO_4$ composites

Three stoichiometric 90 wt% loading composites were prepared with the fuel being Al and Si, and the oxidizer always being $KClO_4$. I will refer to the samples in terms of the mass percentage of Al and Si in the fuel. For example, a 90% Al-10% Si sample means that 90% of the fuel is Al, 10% of is Si, and the corresponding amount of $KClO_4$ is used as the oxidizer to make the overall stoichiometric assuming complete conversion to Al_2O_3 and SiO_2. The details on preparing ink and printing the composites can be found in our previous study [41]. Briefly, 4 wt% of PVDF, 6 wt% of HPMC, and $KClO_4$ were dissolved into DMF. Every ink had a constant 25 mg/ml polymer binder in DMF. Then the fuel nanoparticles were added to the solution, which was ultrasonicated for 30 min and magnetically stirred overnight before printing. For printing with a Hyrel printer (SYSTEM 30 M), the ink was extruded through an 18-gauge needle on a preheated (~75 °C) substrate. The substrate was heated at ~75 °C for another 30 min when the printing was finished to ensure complete removal of DMF. The obtained films were cut into ~2 cm long sticks for combustion investigation. Three composites, Al/$KClO_4$, 90% Al-10% Si/$KClO_4$, and 75% Al-25% Si/$KClO_4$, were prepared by 3D printing. For simplicity, these three composites are referred to Al, 90%Al-10%Si, and 75%Al-25%Si, respectively. Details of the weight percentage of each component of all the composites are displayed in Table S1. SEM images of the cross-section for the three composites are shown in Figure S3.

6.3.4 Microscopic and macroscopic imaging

The details of the imaging process can be found in our previous publications [16,42]. Generally, the combustion process of the composites was studied with two imaging systems, one of which was the microscopic imaging system with high-speed camera (Vision Research Phantom VEO710L) coupled with Infinity Photo-Optical Model K2 DistaMax. The other imaging system was macroscopic imaging system with high-speed camera (Vision Research Phantom Miro M110). For one measurement, a stick was positioned on a stage inside an argon-filled (1 atm) cubic chamber (edge length: 10 cm), which was placed between the two imaging systems. The stick was ignited with a Joule-heated nichrome wire and the combustion process was recorded with both imaging systems. For determining the average burn rate along with standard error, a minimum three tests were conducted on each composite.

For droplet size measurement from the microscopic imaging video, a minimum of 100 droplets were measured for each composite.

6.3.5 Electron microscopy and X-ray diffraction crystallography

X-ray diffraction (XRD) [Empyrean PANalytical Series 2; Cu-Kα source ($\lambda = 1.541$ Å)] was used to characterize the as-synthesized Si nanoparticles (Figure S1) and composition of the post-combustion product of Al/$KClO_4$ and 75%Al-25%Si/$KClO_4$. The size and morphology of Si nanoparticles were characterized by TEM (120-kV accelerating voltage; Thermo Fisher Scientific Talos L120C) (Figure S2). Scanning electron microscope (SEM, Thermo-Fisher Scientific NNS450) coupled with energy dispersive X-ray spectroscopy (EDS) was used to analyze the morphology and composition of the post-

combustion product. Post-combustion product was collected inside a glass tube (ID: 1 inch) filled with argon. For 75%Al-25%Si/$KClO_4$, the obtained product was washed with water briefly to dissolve KCl nanoparticles, which is formed during combustion, to simplify the XRD spectrum [16]. To minimize oxidation of the particles in water, the washing process involved adding water to the post-combustion product and vigorously vortexing it for approximately 20 seconds. Subsequently, the suspension was promptly centrifuged, the precipitate was collected, and it was then dried under vacuum in a desiccator before conducting SEM and XRD analysis.

6.3.6 Three-color imaging pyrometry

Details about three-color imaging pyrometry can be found in previous publications from our group [31,39,43]. In general, temperature measurements of the sample were conducted by analyzing the ratios of channel intensities in three colors (red, green, and blue) captured through the Bayer filter. This analysis was performed using a custom MATLAB routine, assuming that the sample exhibited graybody emission behavior. Calibration factors were determined with a blackbody source (Mikron M390). The estimated temperature uncertainty is typically within the range of 200-300 K [27,31].

6.4 Results and discussion

Combustion behaviors of the Al, 90%Al-10%Si, and 75%Al-25%Si composites were characterized with high-speed macroscopic and microscopic cameras in argon. (For simplicity, $KClO_4$ is excluded in the name of these composites). A series of time-resolved snapshots of these composites from macroscopic video are shown in Figure 6-1 and Figure

S4. All three composites show stable and linear propagation, and the burn rate increases as Si content increases, as displayed in Figure 6-1 (a) and Figure S4. Figure 6-1 (b) shows that the burn rate is 8.6 cm/s, 11.2 cm/s, and 14.3 cm/s for Al, 90%Al-10%Si, and 75%Al-25%Si, respectively. It is noteworthy that while previous studies has demonstrated that the increase in porosity results in a higher burn rate [44], the porosity of the composite was largely unaffected by Si addition in our composites (all composites have porosity near 50%). Therefore, the observed increase in burn rate cannot be explained by porosity increase.

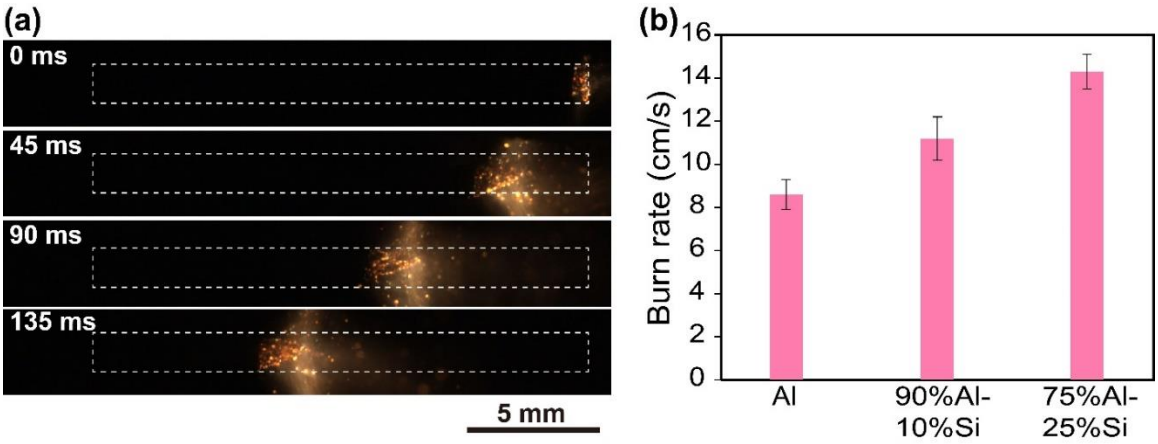

Figure 6-1 Time-resolved snapshots from high-speed macroscopic video of the composite of Al/$KClO_4$, (a). The dashed lines represent the printed composite before ignition. Measured burn rates of different composites (b). Images for the cases with Si addition appear qualitatively similar and can be found in Figure S4 in the supplemental information.

Microscopic videos provide important insight into the combustion characteristics of a composite by enabling direct observation of combustion events on the burning surface. Figure 6-2 (a) shows the snapshots from high-speed microscopic videos of the composites with different Si contents. Cone-shaped flame front is observed for all three composites and is attributed to a higher porosity on the edge of the composites that arises from a higher

solvent evaporation rate during printing [16]. For the composite of bare Al, molten droplets with dark caps form on the burning surface. The main (bright) body of these droplets is almost pure Al while the dark cap consists of Al_2O_3 [16,45]. These mobile droplets coalesce and/or absorb newly formed liquid nearby, growing into larger droplets before departing from the burning surface [46]. The incorporation of 10% and 25% Si has a minimal influence on the morphology of the droplets, as shown in Figure 6-2 (a). Droplet sizes of the three composites are measured, and the distributions are displayed in Figure 6-2 (b), which illustrates that the addition of Si slightly increases the droplet size.

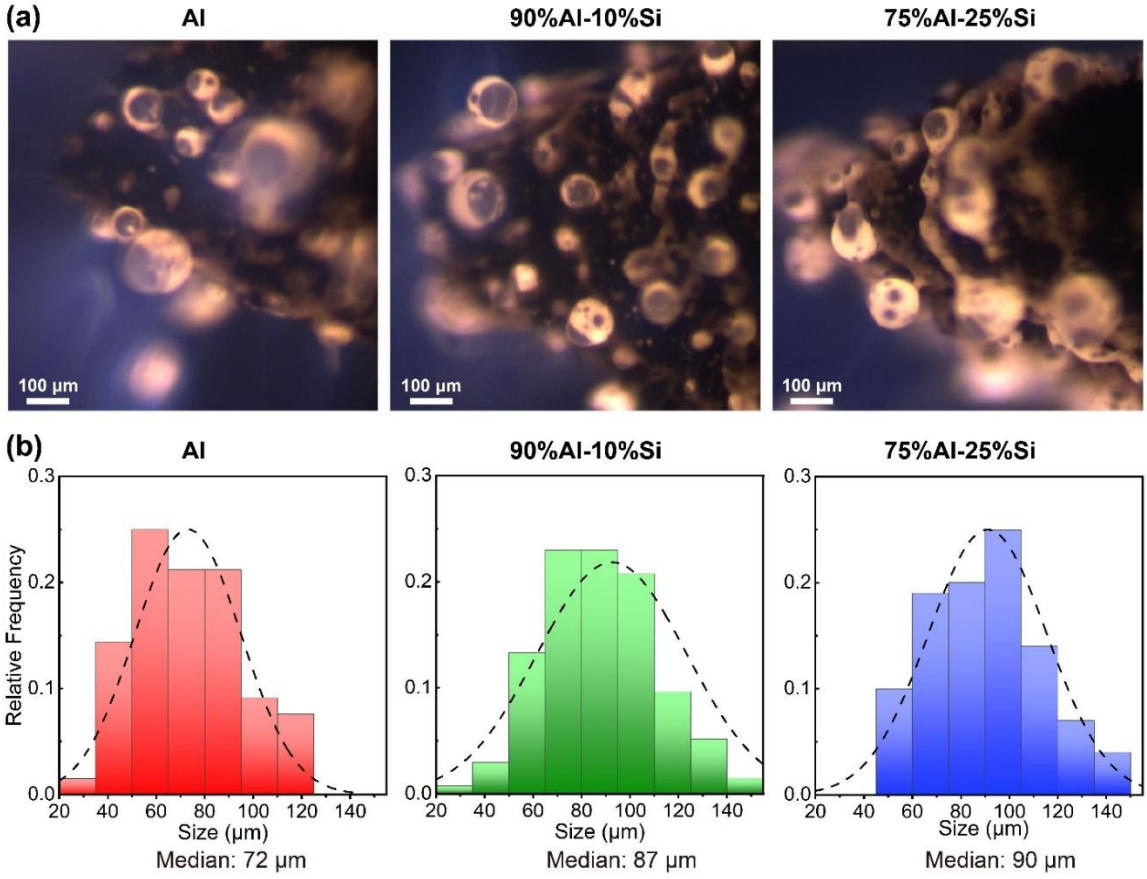

Figure 6-2 Images from high-speed microscopic video (a) and droplet size distribution (b) for the composites of Al, 90%Al-10%Si, and 75%Al-25%Si.

Three-color (RGB) pyrometry is utilized to measure the temperature of the flame front and the representative temperature maps of the composites with different Si content are displayed in Figure 6-3 (a). For the composite with bare Al, main body of the droplets have an average temperature of ~2350 K, which is significantly higher than the melting point of Al at 930 K. It is noteworthy that this measured temperature is approximately equal to the melting point of Al_2O_3 at 2345 K [37]. At this temperature Al_2O_3 melts and retracts, forming a distinct lobe due to surface tension [16,47]. With the introduction of Si to the composite, the average temperature of main body of the droplets is ~2450 K for 90%Al-10%Si and ~2500 K for 75%Al-25%Si, respectively. The droplet temperature difference between bare Al and 75%Al-25%Si is within the uncertainty of the measurement (200-300 K) [27,31], therefore I conclude that the addition of Si has minimal effect on the droplet temperature. For droplets of all three composites, the temperature of Al_2O_3 cap is higher than the main body, consistent with the observations from previous studies [16,37].

Combustion performance of different composites can be evaluated by comparing their energy release rate. Figure 6-3 (b) shows the relative energy release rate of the three composites. It is evident that the energy release rate of the composite increases with the addition of Si. As the Si content increases from 10% to 25%, the relative energy release rate rises from 1.4X to 2.0X that of bare Al. Given that the gravimetric energy density of $Si/KClO_4$ is lower than $Al/KClO_4$ (8.7 vs 9.5 kJ/g), the observed increase in energy release rate cannot be explained by theoretical energy density difference. In addition, previous studies have demonstrated that the smaller agglomeration size favors a higher burn rate [1,24,27,34]. As shown in Figure 6-2 (b), the droplet size of the composite has a slight increase

with Si addition. A primary question now arises: Why does the introduction of Si significantly increase the energy release rate?

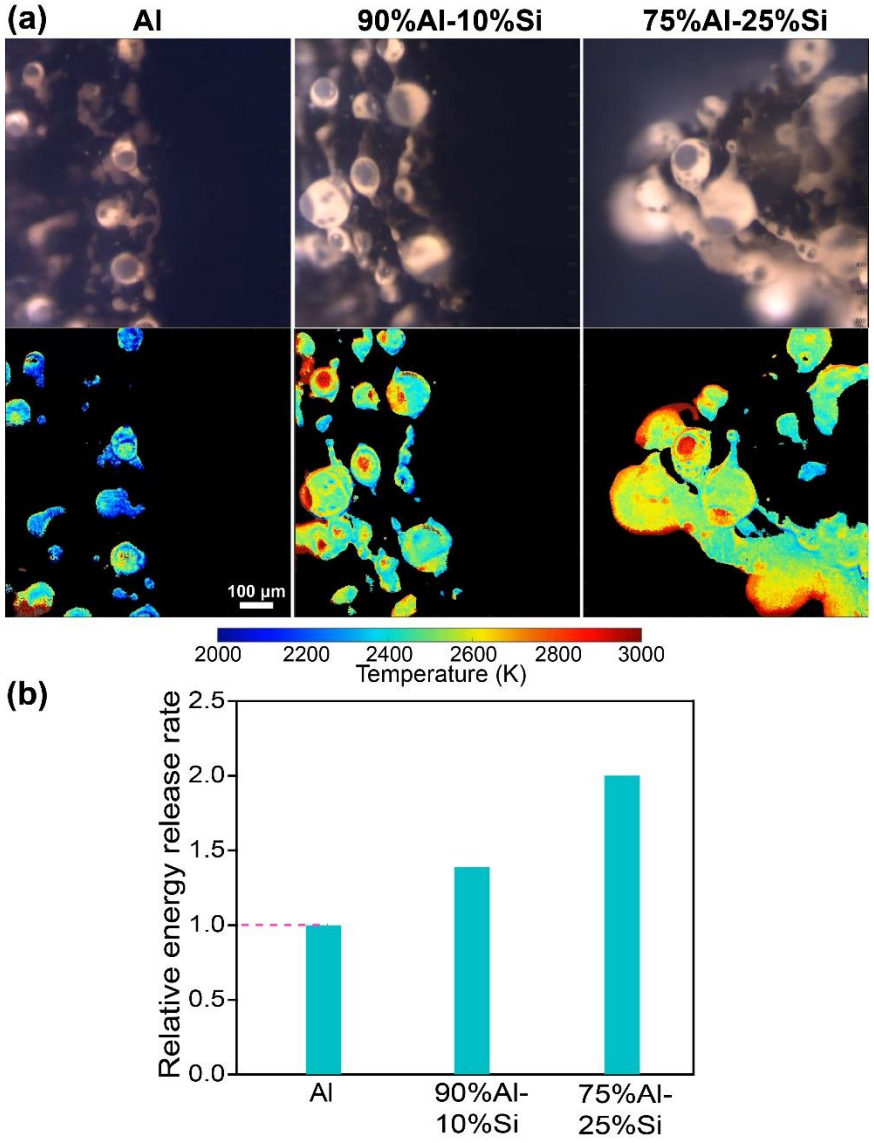

Figure 6-3 Temperature maps from three-color pyrometry (a) and the estimated relative energy release rates (b) for the composites of Al, 90%Al-10%Si, and 75%Al-25%Si. High error points and low-intensity points were excluded from the temperature measurement. Details about relative energy release rate estimation can be found in Supporting Information (Section S2).

Microscopic imaging videos demonstrate that the initial agglomerates require some time to evolve into droplets, which then reside on the burning surface for a period before departure rather than being ejected immediately after formation. Figure 6-4 (a) presents a series of snapshots depicting a representative process from agglomerate emergence, droplet formation, growth, and departure from the burning surface of the bare Al composite. Agglomerate surface residence time is estimated by tracking the time span from emergence of the agglomerate that evolves into a droplet to the departure of that droplet, and the obtained distributions for different composites are shown in Figure 6-4 (b), which shows that the addition of Si clearly increases the agglomerate surface residence time. The vast majority of the agglomerate residence time for bare Al composite is below 3 ms. With 10% Si introduction, the overall agglomerate residence time increases, and approximately 35% of agglomerates have residence time exceeding 3 ms. As the Si content increases from 10% to 25%, the overall agglomerate residence time continues to rise, with more than 60% of agglomerates having a residence time exceeding 3 ms.

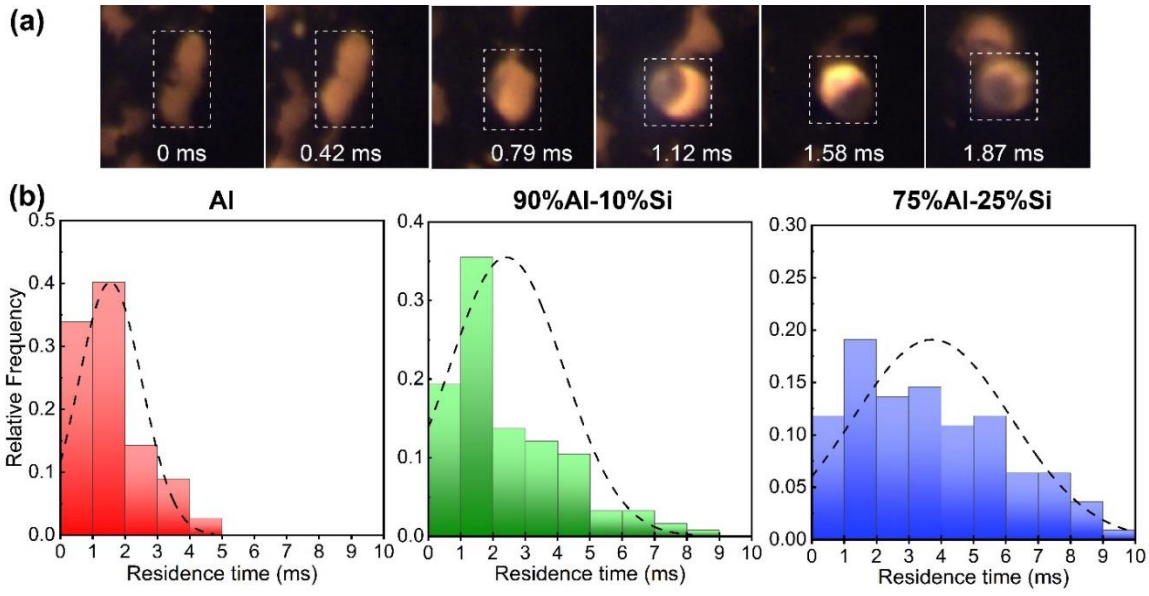

Figure 6-4 Time-resolved snapshots of the evolution of a representative droplet from emergence to departure from the burning surface for the composite of bare Al (a). Measured agglomerate surface residence time distribution of Al, 90%Al-10%Si, and 75%Al-25%Si (b).

Steady propagation requires the transfer of sufficient heat from the flame back to the unreacted material [31–34,48]. Conduction, convection, and radiation are the three primary methods for heat transfer. Previous studies have demonstrated that radiative heat feedback is negligible for a propellant propagating at atmospheric pressure [32,33,48,49]. In the current study, combustion tests of the composites were conducted inside a vented chamber to maintain approximate atmospheric pressure, therefore we disregard the effect of radiative heat feedback. Convective heat transfer can be further divided into convection of gas and convection from the movement of condensed phase material [33,50–52]. Egan et al. investigated gas convection in an Al/CuO system propagating inside a narrow channel and concluded that convective heat transfer was insufficient to sustain combustion [33]. Calculation shows that Al-Si/$KClO_4$ has less gas generation compared to Al/CuO, assuming the oxygen

produced from the oxidizers is completely consumed by Al. While the composite of Al-Si/$KClO_4$ has 10% polymer binder (4% PVDF and 6% HPMC), prior work has demonstrated this polymer mixture has little gas release [24]. It is noteworthy that the combustion test of the composite in the current study was conducted inside a chamber with a cross-section area approximately 4 orders of magnitude higher than that of a composite stick. This indicates that convective heat transfer effect is much lower than the significantly confined Al/CuO system studied by Egan et al. [33], therefore the effect of convective heat transfer of gas is insignificant. As for the effect caused by the movement of condensed phase material, no movement of burning droplet back to the unburnt composite is observed from the microscopic imaging. This can be attributed to the lack of confinement effect from the test chamber, given that its cross-section area is drastically larger than that of the composite stick. Thus, it can be concluded that the convective heat transfer effect is insignificant for the propagation of Al-Si/$KClO_4$ composites.

From the discussion so far, I can conclude that the radiation heat feedback is negligible, and convection is not the dominant mode of energy transport for the propagation of Al-Si/$KClO_4$ composites. The remaining mechanism is conduction heat transfer. The significance of conductive heat transfer has been suggested previously. Brewster et al. concluded that the residence of metal agglomerates on or near the surface of a propellant tended to increase the burn rate of the propellant by transferring heat to the propellant [34]. Our prior work of Wang et al. demonstrated the addition of carbon fiber increased the burn rate of Al/CuO by enhancing conductive heat transfer from hot burned/burning particles to the unburnt materials [27]. In the current study, I have shown that agglomerate residence time

increases with Si addition (Figure 6-4 (b)), suggesting an increase in conductive heat feedback to the unburnt material, which enhances burn rate. A new question now arises: Why does the addition of Si increase the agglomerate residence time? To answer this question, I will primarily compare the composites of bare Al and 75%Al-25%Si.

XRD and SEM/EDS were utilized to analyze the post combustion products. Figure 6-5 (a) displays the XRD results of post-combustion product from the composites of bare Al and 75%Al-25%Si. In the composite of bare Al, KCl resulting from the decomposition of $KClO_4$, unreacted Al, γ-phase Al_2O_3, δ-phase Al_2O_3, and α-phase Al_2O_3 are present. In the composite of 75%Al-25%Si, in addition to the components observed for bare Al composite, SiO and unreacted Si are identified. As discussed in the previous section, for the composite of bare Al, the main body of the droplets during combustion is almost pure Al while the dark cap is Al_2O_3 [16,45]. SEM/EDS images in Figure 6-5 (b) show that for the 75%Al-25%Si composite, aluminum, oxygen, and silicon are homogeneously distributed on the surface of the particles except for a few small spots. Al and Si are miscible at any atomic ratio when the temperature is above the melting point of Si at 1414 °C [53], which is significantly lower than the measured temperature of main body of the droplets (>2100 °C). This suggests that for the composites with Si addition, the main body of the droplets forms a homogeneous mixture of Al and Si, consistent with the EDS analysis that Al and Si are homogeneously distributed on the post-combustion particles. For simplicity in following discussion, I assume Al and Si are in the main body while SiO and Al_2O_3 are in the cap for the burning droplets of composites with Si addition.

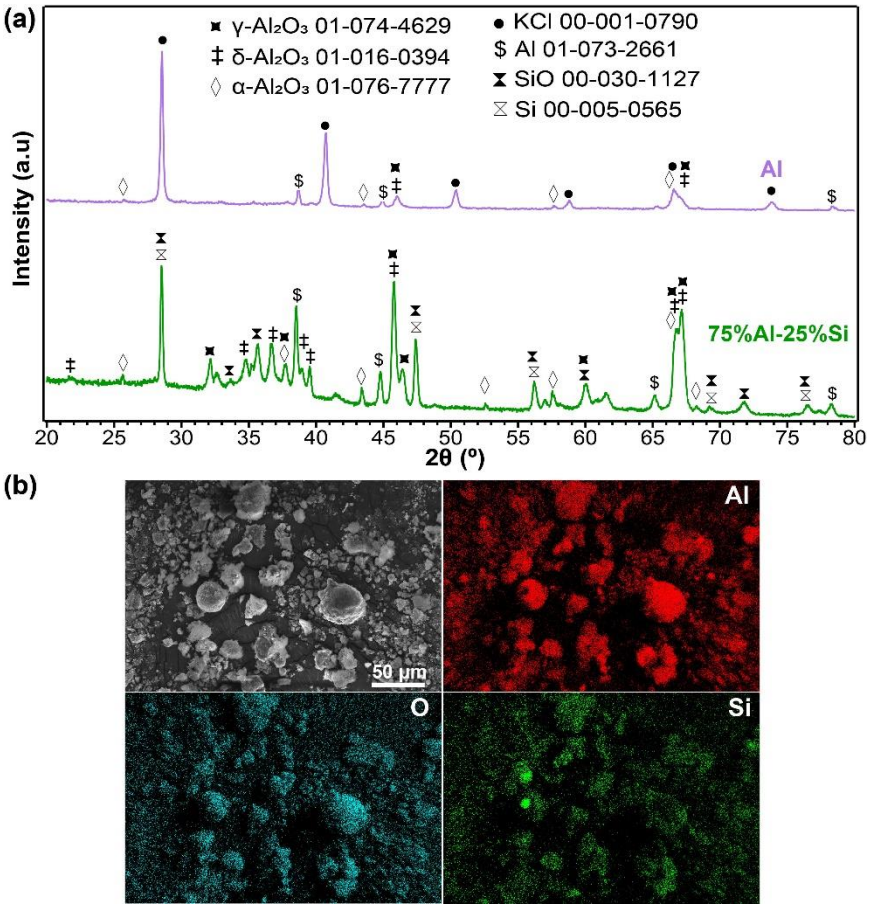

Figure 6-5 XRD spectra of post-combustion products from the composites of bare Al and 75%Al-25%Si (a). SEM image and corresponding EDS images of post-combustion products of the 75%Al-25%Si composite (b). Note: Product of the 75%Al-25%Si composite was water-washed briefly to remove KCl for obtaining a cleaner XRD spectrum and allowing large agglomerates to remain on the carbon tap for SEM.

Now, let me consider the forces that a droplet feels in order to detach from the burning surface. On the burning surface the droplet will experience aerodynamic forces (drag or blowing force) due to gas flow effusing from surface, adhesive forces, and gravity, as shown in Figure 6-6-6 (a) [29,54,55]. Gravity plays an insignificant role in droplet detachment as no consistent downward movement is observed for the departed droplets. I begin by assuming that the surface generates gas (blowing force) which will want to lift the particle from the surface by a drag force. To estimate the drag force, I need to know the

blowing velocity at the surface of attachment. To do this, however, I measure the velocity of the departed particle and assuming it has reached its terminal velocity and assuming it is equivalent to the blowing velocity. I can then calculate the lifting force from Stokes Law (i.e. the drag force; F_{drag}) shown in Equation (1) [56]. Where C_D is drag coefficient, ρ_g is the gas density, d is the diameter of the particle, v is the relative velocity of the gas flow. Counteracting the drag (or detachment) force is the adhesive force (F_{adh}) characterized by Equation (2) [56]. The adhesive force arises from the combination of van der Waals, electrostatic, and surface tension forces, which are represented by the first, second, and third term on the right side of Equation (2), respectively.

$$F_{drag} = C_D \frac{\pi}{8} \rho_g d^2 v^2 \tag{1}$$

$$F_{adh} = \frac{Ad}{12x^2} + \frac{K_\varepsilon q^2}{x_q^2} + 2\pi\gamma d \tag{2}$$

where A is the Hamaker constant, x is the distance between the particle and the plane surface, K_ε is the constant of proportionality, x_q is the separation distance of opposite charges, and γ is the surface tension of the liquid between the particle and the plane surface. For order-of-magnitude estimates I will consider a representative droplet (d=100 μm, temperature=2500 K). Velocity tracking of the droplet leads to an average velocity of ~ 2 m/s, C_D is estimated to be 1 [56], and the gas density (ρ_g) is assumed to be the density of argon (1.6 kg/m^3). A drag force (F_{drag}) from Equation (1) yields a value of 3×10^{-8} N.

In estimating the adhesive force (F_{adh}), I can safely neglect the electrostatic force as the droplet primarily consists of conductive Al, so it is unlikely that charge on the droplet accumulates due to the contact with the burning surface. Given the wetting behavior of these droplets as evidenced by the clear liquid Al bridge (Figure S5), van der Waals force are likely to be much smaller than surface tension forces. In the calculation of surface tension adhesive force, γ_{Al} is estimated to be 0.6 N/m at 2500 K [57], resulting in a surface tension adhesive force of ~4×10^{-4} N. This is orders of magnitude higher than the blowing force (drag force; ~3×10^{-8} N), suggesting that gas generation at the surface is too small to detach the droplet from the burning surface. Previous studies have shown that for the detachment of particles from surfaces, the lifting force usually contributes less than tangential forces acting parallel to the surface, which results in rolling or sliding of particles [58,59]. In the current study, droplet rolling on the burning surface is commonly observed, and I believe it to be the primary cause for droplet detachment. The observed droplet rolling is attributed to the flow dynamics inside the droplet at a high temperature (2500 K), which remain consistent for droplets with different sizes due to the invariant temperature among these droplets [60]. Basu et al. demonstrated that the critical shear rate for the detachment of a partially wetting droplet decreases as the droplet size increases [61]. Thus, a droplet needs to grow to a sufficient size to reach the critical shear rate for detachment. This explains the relatively large droplet size (~100 μm) observed for detachment.

The preceding discussion primarily focused on the droplet detachment mechanism for the composite of bare Al but does not address why the addition of Si results in a higher surface residence time. As discussed above, a critical size must be achieved before a droplet

can detach. To achieve this critical size neighboring droplets must fuse. The fusion occurs through viscous flow, and the characteristic fusion time (τ_F) can be calculated using Frenkel's law [17,62] in Equation (3).

$$\tau_F = \frac{\pi \eta d}{\gamma} \tag{3}$$

where η is the viscosity, γ is the surface tension. For Al at 2500 K, the surface tension is estimated to be 0.6 N/m and the viscosity is estimated to be 0.48 mPa·s [57,63]. For two droplets with diameter of 100 μm, the computed characteristic fusion time is ~2.5×10^{-4} ms. This is a few orders of magnitude smaller than the overall measured droplet surface residence time and can therefore be neglected.

Another contributing factor to the surface residence time is the time needed for the liquid to evolve into a droplet. Microimaging videos show the formation of burning liquid 'pool' before its evolution into a spherical droplet (Figure 6-4 (a) and Figure 6-6-6 (b)). The process for the liquid 'pool' evolving into a droplet can be regarded as dewetting of the burning surface by the liquid fuel [64]. Bertrand et al. demonstrated that growth rate of the droplet for dewetting is related to the surface tension of the liquid, and a higher surface tension results in a higher droplet growth rate [64]. With the introduction of Si, the surface tension of the mixture decreases as $\gamma_{Si} < \gamma_{Al}$ at 2500 K (0.25 N/m vs 0.6 N/m) [57]. Consequently, the droplet growth rate decreases, and more time is required for the liquid to evolve into a droplet. Figure 6-6-6 (b) displays a representative dewetting process for the 75%Al-25%Si composite with a measured dewetting time of ~3.5 ms, which is significantly longer than the total surface residence time for a representative droplet of the

bare Al composite (Figure 6-4(a)). This explains why the introduction of Si increases the agglomerate surface residence time.

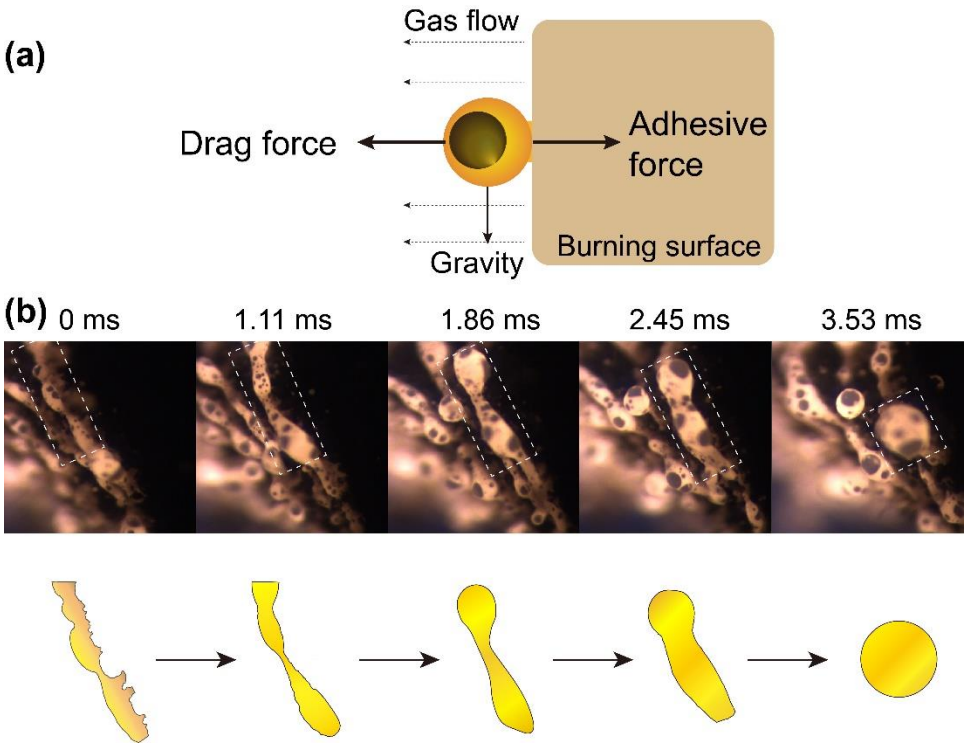

Figure 6-6-6 Schematic of the forces experienced by a droplet on the burning surface (a). A representative dewetting process (top) and the corresponding illustration (bottom) for the composite of 75%Al-25%Si (b).

6.5 Conclusions

This chapter investigates the effect of agglomerate surface tension on heat feedback and burn rate of energetic composites by studying the combustion behavior of Al/$KClO_4$ composites with Si as an additive. The introduction of Si significantly increases the burn rate and energy release rate. Microscopic imaging shows that droplets resulting from the evolution of molten liquid form on the burning surface, and the addition of Si has minimal

impact on the droplet temperature while slightly increases the droplet size. However, the lower surface tension of Si compared to Al decreases the overall liquid surface tension, leading to a lower droplet growth rate and longer time required for the liquid to transform into droplets. This results in a prolonged agglomerate surface residence time and, consequently, enhanced conductive heat feedback to the unburnt materials, ultimately increasing the burn rate and energy release rate. This study illustrates the crucial role of agglomerate surface tension in impacting the combustion behavior of energetic composites.

6.6 References

(1) Sippel, T. R.; Son, S. F.; Groven, L. J. Aluminum Agglomeration Reduction in a Composite Propellant Using Tailored Al/PTFE Particles. *Combust. Flame* **2014**, *161* (1), 311–321. https://doi.org/10.1016/j.combustflame.2013.08.009.

(2) Rehwoldt, M. C.; Wang, H.; Kline, D. J.; Wu, T.; Eckman, N.; Wang, P.; Agrawal, N. R.; Zachariah, M. R. Ignition and Combustion Analysis of Direct Write Fabricated Aluminum/Metal Oxide/PVDF Films. *Combust. Flame* **2020**, *211*, 260–269. https://doi.org/10.1016/j.combustflame.2019.08.023.

(3) Comet, M.; Martin, C.; Klaumünzer, M.; Schnell, F.; Spitzer, D. Energetic Nanocomposites for Detonation Initiation in High Explosives without Primary Explosives. *Appl. Phys. Lett.* **2015**, *107* (24), 243108. https://doi.org/10.1063/1.4938139.

(4) Yen, N. H.; Wang, L. Y. Reactive Metals in Explosives. *Propellants Explos. Pyrotech.* **2012**, *37* (2), 143–155. https://doi.org/10.1002/prep.200900050.

(5) He, W.; Liu, P.-J.; He, G.-Q.; Gozin, M.; Yan, Q.-L. Highly Reactive Metastable Intermixed Composites (MICs): Preparation and Characterization. *Adv. Mater.* **2018**, *30* (41), 1706293. https://doi.org/10.1002/adma.201706293.

(6) Jian, G.; Piekiel, N. W.; Zachariah, M. R. Time-Resolved Mass Spectrometry of Nano-Al and Nano-Al/CuO Thermite under Rapid Heating: A Mechanistic Study. *J. Phys. Chem. C* **2012**, *116* (51), 26881–26887. https://doi.org/10.1021/jp306717m.

(7) Sundaram, D.; Yang, V.; Yetter, R. A. Metal-Based Nanoenergetic Materials: Synthesis, Properties, and Applications. *Prog. Energy Combust. Sci.* **2017**, *61*, 293–365. https://doi.org/10.1016/j.pecs.2017.02.002.

(8) Comet, M.; Martin, C.; Schnell, F.; Spitzer, D. Nanothermites: A Short Review. Factsheet for Experimenters, Present and Future Challenges. *Propellants Explos. Pyrotech.* **2019**, *44* (1), 18–36. https://doi.org/10.1002/prep.201800095.

(9) Granier, J. J.; Pantoya, M. L. Laser Ignition of Nanocomposite Thermites. *Combust. Flame* **2004**, *138* (4), 373–383. https://doi.org/10.1016/j.combustflame.2004.05.006.

(10) Yetter, R. A. Progress towards Nanoengineered Energetic Materials. *Proc. Combust. Inst.* **2021**, *38* (1), 57–81. https://doi.org/10.1016/j.proci.2020.09.008.

(11) Sami, Y.; Richard, N.; Gauchard, D.; Estève, A.; Rossi, C. Selecting Machine Learning Models to Support the Design of Al/CuO Nanothermites. *J. Phys. Chem. A* **2022**, *126* (7), 1245–1254. https://doi.org/10.1021/acs.jpca.1c09520.

(12) Young, G.; Wang, H.; Zachariah, M. R. Application of Nano-Aluminum/Nitrocellulose Mesoparticles in Composite Solid Rocket Propellants. *Propellants Explos. Pyrotech.* **2015**, *40* (3), 413–418. https://doi.org/10.1002/prep.201500020.

(13) DeLuca, L. T.; Galfetti, L.; Colombo, G.; Maggi, F.; Bandera, A.; Babuk, V. A.; Sinditskii, V. P. Microstructure Effects in Aluminized Solid Rocket Propellants. *J. Propuls. Power* **2010**, *26* (4), 724–732. https://doi.org/10.2514/1.45262.

(14) Galfetti, L.; Luca, L. T. D.; Severini, F.; Meda, L.; Marra, G.; Marchetti, M.; Regi, M.; Bellucci, S. Nanoparticles for Solid Rocket Propulsion. *J. Phys. Condens. Matter* **2006**, *18* (33), S1991–S2005. https://doi.org/10.1088/0953-8984/18/33/S15.

(15) Xu, F.; Nava, G.; Biswas, P.; Dulalia, I.; Wang, H.; Alibay, Z.; Gale, M.; Kline, D. J.; Wagner, B.; Mangolini, L.; Zachariah, M. R. Energetic Characteristics of Hydrogenated Amorphous Silicon Nanoparticles. *Chem. Eng. J.* **2021**, 133140. https://doi.org/10.1016/j.cej.2021.133140.
(16) Wang, Y.; Hagen, E.; Biswas, P.; Wang, H.; Zachariah, M. R. Imaging the Combustion Characteristics of Al, B, and Ti Composites. *Combust. Flame* **2023**, *252*, 112747. https://doi.org/10.1016/j.combustflame.2023.112747.
(17) Chakraborty, P.; Zachariah, M. R. Do Nanoenergetic Particles Remain Nano-Sized during Combustion? *Combust. Flame* **2014**, *161* (5), 1408–1416. https://doi.org/10.1016/j.combustflame.2013.10.017.
(18) Zachariah, M. R.; Carrier, M. J. Molecular Dynamics Computation of Gas-Phase Nanoparticle Sintering: A Comparison with Phenomenological Models. *J. Aerosol Sci.* **1999**, *30* (9), 1139–1151. https://doi.org/10.1016/S0021-8502(98)00782-4.
(19) Wang, H.; Jian, G.; Egan, G. C.; Zachariah, M. R. Assembly and Reactive Properties of Al/CuO Based Nanothermite Microparticles. *Combust. Flame* **2014**, *161* (8), 2203–2208. https://doi.org/10.1016/j.combustflame.2014.02.003.
(20) Dreizin, E. L. Metal-Based Reactive Nanomaterials. *Prog. Energy Combust. Sci.* **2009**, *35* (2), 141–167. https://doi.org/10.1016/j.pecs.2008.09.001.
(21) He, W.; Lyu, J.-Y.; Tang, D.-Y.; He, G.-Q.; Liu, P.-J.; Yan, Q.-L. Control the Combustion Behavior of Solid Propellants by Using Core-Shell Al-Based Composites. *Combust. Flame* **2020**, *221*, 441–452. https://doi.org/10.1016/j.combustflame.2020.07.006.
(22) Zhang, J.; Zhao, F.; Li, H.; Yuan, Z.; Zhang, M.; Yang, Y.; Pei, Q.; Wang, Y.; Chen, X.; Qin, Z. Improving Ignition and Combustion Performance of Al@Ni in CMDB Propellants: Effect of Nickel Coating. *Chem. Eng. J.* **2023**, *456*, 141010. https://doi.org/10.1016/j.cej.2022.141010.
(23) Kim, D. W.; Kim, K. T.; Lee, D.-U.; Jung, S.-H.; Yang, D. Y.; Yu, J. Influence of Poly(Vinylidene Fluoride) Coating Layer on Exothermic Reactivity and Stability of Fine Aluminum Particles. *Appl. Surf. Sci.* **2021**, *551*, 149431. https://doi.org/10.1016/j.apsusc.2021.149431.
(24) Wang, H.; Wang, Y.; Garg, M.; Moore, J. S.; Zachariah, M. R. Unzipping Polymers Significantly Enhance Energy Flux of Aluminized Composites. *Combust. Flame* **2022**, *244*, 112242. https://doi.org/10.1016/j.combustflame.2022.112242.
(25) Wang, H.; Jacob, R. J.; DeLisio, J. B.; Zachariah, M. R. Assembly and Encapsulation of Aluminum NP's within AP/NC Matrix and Their Reactive Properties. *Combust. Flame* **2017**, *180*, 175–183. https://doi.org/10.1016/j.combustflame.2017.02.036.
(26) Chowdhury, M.; Ghildiyal, P.; Rojas, A.; Wang, Y.; Wang, H.; Zachariah, M. R. High-Yield Spray Drying Assembly and Reactive Properties of Nanoenergetic Mesoparticle Composites. *Adv. Powder Technol.* **2023**, *34* (7), 104075. https://doi.org/10.1016/j.apt.2023.104075.
(27) Wang, H.; Kline, D. J.; Rehwoldt, M. C.; Zachariah, M. R. Carbon Fibers Enhance the Propagation of High Loading Nanothermites: In Situ Observation of

Microscopic Combustion. *ACS Appl. Mater. Interfaces* **2021**. https://doi.org/10.1021/acsami.1c02911.
(28) Wang, H.; Hagen, E.; Shi, K.; Herrera, S.; Xu, F.; Zachariah, M. R. Carbon Fibers as Additives to Engineer Agglomeration and Propagation of Aluminized Propellants. *Chem. Eng. J.* **2023**, 141653. https://doi.org/10.1016/j.cej.2023.141653.
(29) Ao, W.; Fan, Z.; Liu, L.; An, Y.; Ren, J.; Zhao, M.; Liu, P.; Li, L. K. B. Agglomeration and Combustion Characteristics of Solid Composite Propellants Containing Aluminum-Based Alloys. *Combust. Flame* **2020**, *220*, 288–297. https://doi.org/10.1016/j.combustflame.2020.07.004.
(30) Liu, L.; Sang, L.; Gou, D.; Wen, Z.; Zhang, G.; Liu, P.; He, G.; Ao, W. Controlling the Combustion and Agglomeration Characteristics of Solid Propellants via New Micro-Unit Composite Fuel Al@AP. *Combust. Flame* **2023**, *258*, 113107. https://doi.org/10.1016/j.combustflame.2023.113107.
(31) Kline, D. J.; Alibay, Z.; Rehwoldt, M. C.; Idrogo-Lam, A.; Hamilton, S. G.; Biswas, P.; Xu, F.; Zachariah, M. R. Experimental Observation of the Heat Transfer Mechanisms That Drive Propagation in Additively Manufactured Energetic Materials. *Combust. Flame* **2020**, *215*, 417–424. https://doi.org/10.1016/j.combustflame.2020.01.020.
(32) Summerfield, M. *Solid Propellant Rocket Research*; Elsevier, 2013.
(33) Egan, G. C.; Zachariah, M. R. Commentary on the Heat Transfer Mechanisms Controlling Propagation in Nanothermites. *Combust. Flame* **2015**, *162* (7), 2959–2961. https://doi.org/10.1016/j.combustflame.2015.04.013.
(34) Brewster, M. Q.; Hardt, B. E. Influence of Metal Agglomeration and Heat Feedback on Composite Propellant Burning Rate. *J. Propuls. Power* **1991**, *7* (6), 1076–1078. https://doi.org/10.2514/3.23431.
(35) Melcher, J. C.; Krier, H.; Burton, R. L. Burning Aluminum Particles Inside a Laboratory-Scale Solid Rocket Motor. *J. Propuls. Power* **2002**, *18* (3), 631–640. https://doi.org/10.2514/2.5977.
(36) Karasev, V. V.; Onischuk, A. A.; Glotov, O. G.; Baklanov, A. M.; Maryasov, A. G.; Zarko, V. E.; Panfilov, V. N.; Levykin, A. I.; Sabelfeld, K. K. Formation of Charged Aggregates of Al2O3 Nanoparticles by Combustion of Aluminum Droplets in Air. *Combust. Flame* **2004**, *138* (1), 40–54. https://doi.org/10.1016/j.combustflame.2004.04.001.
(37) Chen, Y.; Guildenbecher, D. R.; Hoffmeister, K. N. G.; Cooper, M. A.; Stauffacher, H. L.; Oliver, M. S.; Washburn, E. B. Study of Aluminum Particle Combustion in Solid Propellant Plumes Using Digital In-Line Holography and Imaging Pyrometry. *Combust. Flame* **2017**, *182*, 225–237. https://doi.org/10.1016/j.combustflame.2017.04.016.
(38) Marsh, A. W.; Wang, G. T.; Heyborne, J. D.; Guildenbecher, D. R.; Mazumdar, Y. C. Time-Resolved Size, Velocity, and Temperature Statistics of Aluminum Combustion in Solid Rocket Propellants. *Proc. Combust. Inst.* **2021**, *38* (3), 4417–4424. https://doi.org/10.1016/j.proci.2020.08.010.

(39) Wang, H.; Kline, D. J.; Zachariah, M. R. In-Operando High-Speed Microscopy and Thermometry of Reaction Propagation and Sintering in a Nanocomposite. *Nat. Commun.* **2019**, *10* (1), 3032. https://doi.org/10.1038/s41467-019-10843-4.
(40) Mangolini, L.; Thimsen, E.; Kortshagen, U. High-Yield Plasma Synthesis of Luminescent Silicon Nanocrystals. *Nano Lett.* **2005**, *5* (4), 655–659. https://doi.org/10.1021/nl050066y.
(41) Wang, H.; Shen, J.; Kline, D. J.; Eckman, N.; Agrawal, N. R.; Wu, T.; Wang, P.; Zachariah, M. R. Direct Writing of a 90 Wt% Particle Loading Nanothermite. *Adv. Mater.* **2019**, *31* (23), 1806575. https://doi.org/10.1002/adma.201806575.
(42) Wang, H.; Julien, B.; Kline, D.; Alibay, Z.; Rehwoldt, M.; Rossi, C.; Zachariah, M. Probing the Reaction Zone of Nanolaminates at ∼μs Time and ∼μm Spatial Resolution. *J. Phys. Chem. C* **2020**, *124* (25), 13679–13687. https://doi.org/10.1021/acs.jpcc.0c01647.
(43) Jacob, R. J.; Kline, D. J.; Zachariah, M. R. High Speed 2-Dimensional Temperature Measurements of Nanothermite Composites: Probing Thermal vs. Gas Generation Effects. *J. Appl. Phys.* **2018**, *123* (11), 115902. https://doi.org/10.1063/1.5021890.
(44) Wu, T.; Julien, B.; Wang, H.; Pelloquin, S.; Esteve, A.; Zachariah, M. R.; Rossi, C. Engineered Porosity-Induced Burn Rate Enhancement in Dense Al/CuO Nanothermites. *ACS Appl. Energy Mater.* **2022**, *5* (3), 3189–3198. https://doi.org/10.1021/acsaem.1c03805.
(45) Dreizin, E. L. Experimental Study of Stages in Aluminium Particle Combustion in Air. *Combust. Flame* **1996**, *105* (4), 541–556. https://doi.org/10.1016/0010-2180(95)00224-3.
(46) Rashkovskii, S. A. Role of the Structure of Heterogeneous Condensed Mixtures in the Formation of Agglomerates. *Combust. Explos. Shock Waves* **2002**, *38* (4), 435–445. https://doi.org/10.1023/A:1016211215981.
(47) Harrison, J.; Brewster, M. Q. Analysis of Thermal Radiation from Burning Aluminium in Solid Propellants. *Combust. Theory Model.* **2009**, *13* (3), 389–411. https://doi.org/10.1080/13647830802684318.
(48) Ishihara, A.; Brewster, M. Q.; Sheridan, T. A.; Krier, H. The Influence of Radiative Heat Feedback on Burning Rate in Aluminized Propellants. *Combust. Flame* **1991**, *84* (1), 141–153. https://doi.org/10.1016/0010-2180(91)90043-B.
(49) HORTON, M. D.; YOUNGBER, L. Z. Effect of Radiant Energy on the Burning Rate of a Composite Solid Propellant. *AIAA J.* **1970**, *8* (10), 1738–1741. https://doi.org/10.2514/3.5983.
(50) Sanders, V. E.; Asay, B. W.; Foley, T. J.; Tappan, B. C.; Pacheco, A. N.; Son, S. F. Reaction Propagation of Four Nanoscale Energetic Composites (Al/MoO3, Al/WO3, Al/CuO, and B12O3). *J. Propuls. Power* **2007**, *23* (4), 707–714. https://doi.org/10.2514/1.26089.
(51) Son, S. F.; Asay, B. W.; Foley, T. J.; Yetter, R. A.; Wu, M. H.; Risha, G. A. Combustion of Nanoscale Al/MoO3 Thermite in Microchannels. *J. Propuls. Power* **2007**, *23* (4), 715–721. https://doi.org/10.2514/1.26090.

(52) Sullivan, K. T.; Kuntz, J. D.; Gash, A. E. Electrophoretic Deposition and Mechanistic Studies of Nano-Al/CuO Thermites. *J. Appl. Phys.* **2012**, *112* (2), 024316. https://doi.org/10.1063/1.4737464.
(53) Du, Y.; Jin, Z.; Huang, B.; Gong, W.; Xu, H.; Yuan, Z.; Schuster, J. C.; Weitzer, F.; Krendelsberger, N. A Thermodynamic Description of the Al-Mn-Si System over the Entire Composition and Temperature Ranges. *Metall. Mater. Trans. A* **2004**, *35* (5), 1613–1628. https://doi.org/10.1007/s11661-004-0267-5.
(54) Tu, C.; Chen, X.; Li, Y.; Zhang, B.; Zhou, C. Experimental Study of Al Agglomeration on Solid Propellant Burning Surface and Condensed Combustion Products. *Def. Technol.* **2023**, *26*, 111–122. https://doi.org/10.1016/j.dt.2022.05.016.
(55) BABUK, V. A.; VASSILIEV, V. A.; SVIRIDOV, V. V. Propellant Formulation Factors and Metal Agglomeration in Combustion of Aluminized Solid Rocket Propellant. *Combust. Sci. Technol.* **2001**, *163* (1), 261–289. https://doi.org/10.1080/00102200108952159.
(56) Hinds, W. C. *Aerosol Technology: Properties, Behavior, and Measurement of Airborne Particles*; Wiley, 1999.
(57) Egry, I.; Ricci, E.; Novakovic, R.; Ozawa, S. Surface Tension of Liquid Metals and Alloys — Recent Developments. *Adv. Colloid Interface Sci.* **2010**, *159* (2), 198–212. https://doi.org/10.1016/j.cis.2010.06.009.
(58) Hubbe, M. A. Theory of Detachment of Colloidal Particles from Flat Surfaces Exposed to Flow. *Colloids Surf.* **1984**, *12*, 151–178. https://doi.org/10.1016/0166-6622(84)80096-7.
(59) Sharma, M. M.; Chamoun, H.; Sarma, D. S. H. S. R.; Schechter, R. S. Factors Controlling the Hydrodynamic Detachment of Particles from Surfaces. *J. Colloid Interface Sci.* **1992**, *149* (1), 121–134. https://doi.org/10.1016/0021-9797(92)90398-6.
(60) Chu, Q.; Chang, X.; Chen, D. A Physiochemical Model for the Combustion of Aluminum Nano-Agglomerates in High-Speed Flows. *Combust. Flame* **2022**, *237*, 111739. https://doi.org/10.1016/j.combustflame.2021.111739.
(61) Basu, S.; Nandakumar, K.; Masliyah, J. H. A Model for Detachment of a Partially Wetting Drop from a Solid Surface by Shear Flow. *J. Colloid Interface Sci.* **1997**, *190* (1), 253–257. https://doi.org/10.1006/jcis.1997.4856.
(62) Friedlander, S. K. *Smoke, Dust and Haze: Fundamentals of Aerosol Behavior*; 1977.
(63) Dinsdale, A. T.; Quested, P. N. The Viscosity of Aluminium and Its Alloys--A Review of Data and Models. *J. Mater. Sci.* **2004**, *39* (24), 7221–7228. https://doi.org/10.1023/B:JMSC.0000048735.50256.96.
(64) Bertrand, E.; Blake, T. D.; De Coninck, J. Dynamics of Dewetting. *Colloids Surf. Physicochem. Eng. Asp.* **2010**, *369* (1), 141–147. https://doi.org/10.1016/j.colsurfa.2010.08.006.

6.7 Supporting information

Section S1

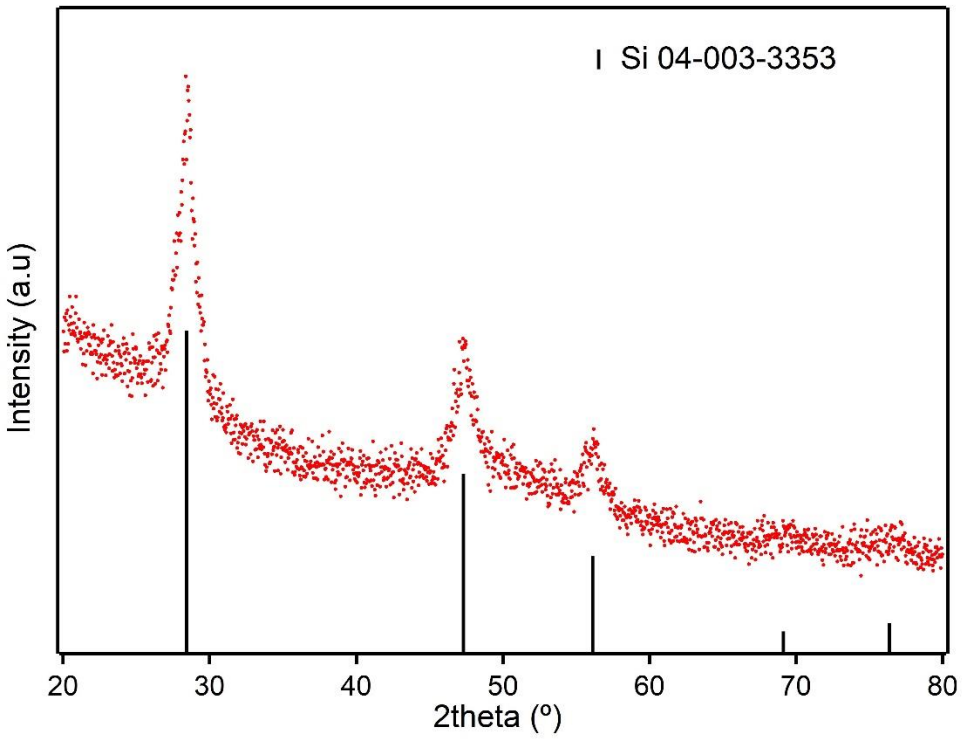

Figure S1 XRD spectrum of Si nanoparticles.

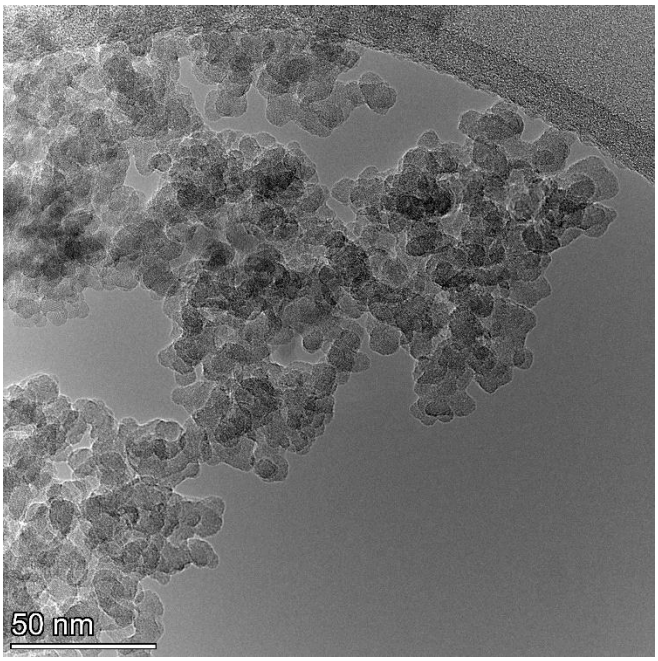

Figure S2 TEM image of the as-synthesized Si nanoparticles.

Table S1. Mass percentage of Al, Si, $KClO_4$, and polymer for different composites.

Sample name	Al (wt%)	Si (wt%)	$KClO_4$ (wt%)	Polymer (wt%)
Al	31.8	0	59.2	10
90%Al-10%Si	27.2	3.1	59.8	10
75%Al-25%Si	22.1	7.4	60.6	10

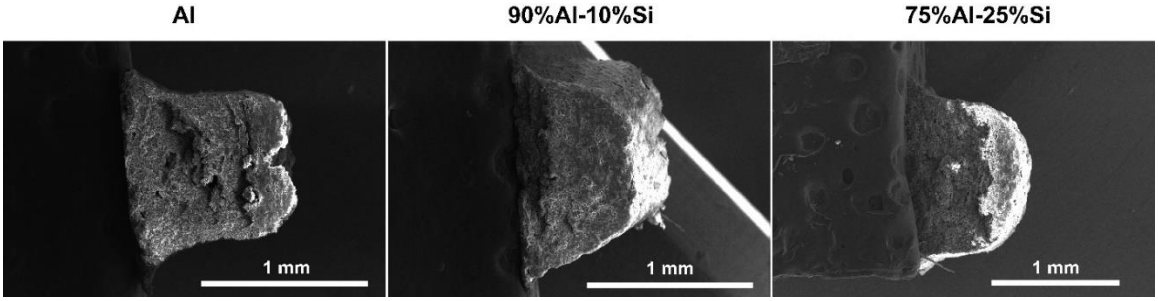

Figure S3 SEM images of cross-section for the printed composites of Al (left), 90%Al-10%Si (middle), and 75%Al-25%Si (right).

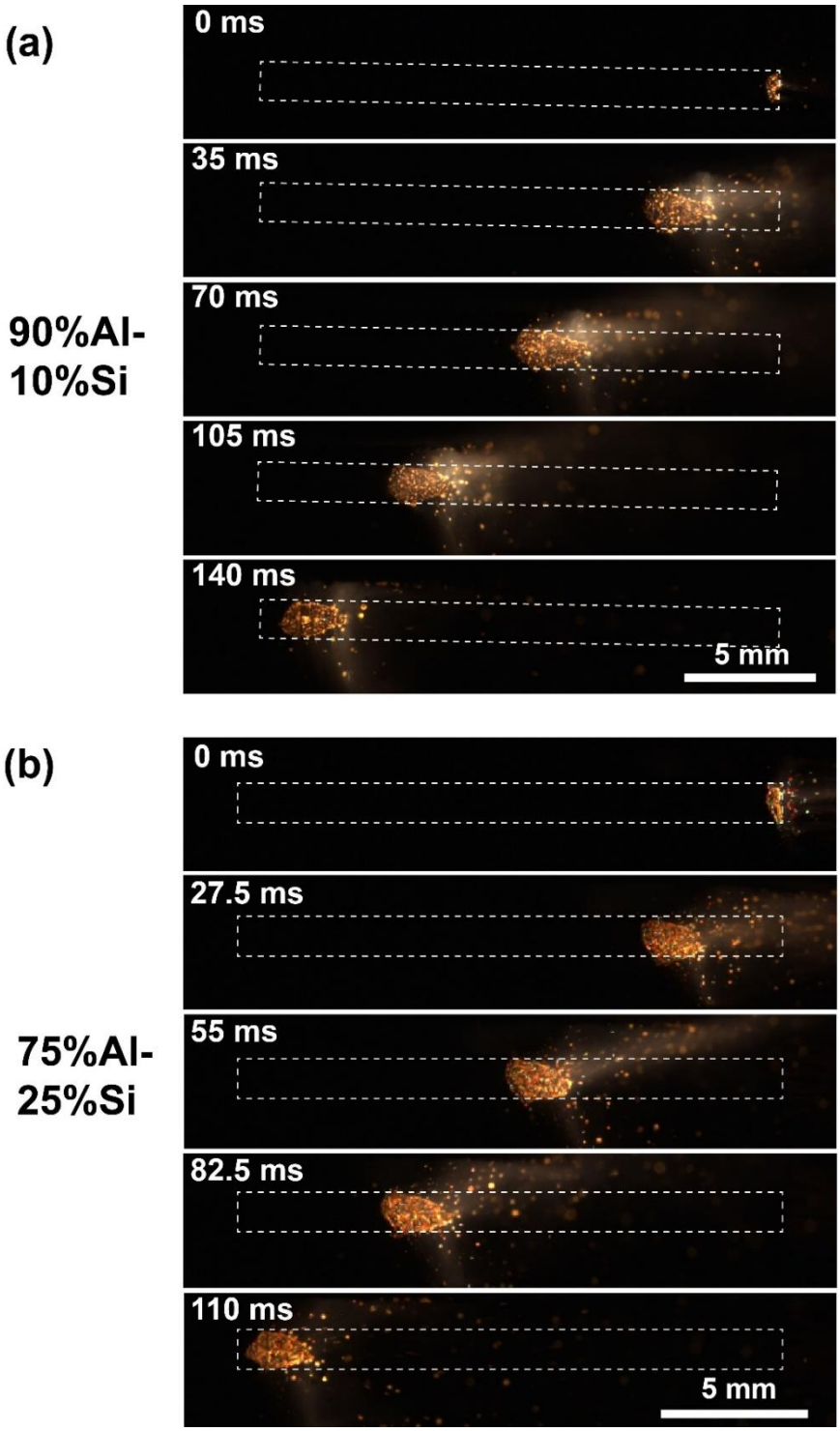

Figure S4 Time resolved-snapshots from high-speed macroscopic video of the composites of 90%Al-10%Si (a), and 75%Al-25%Si (b).

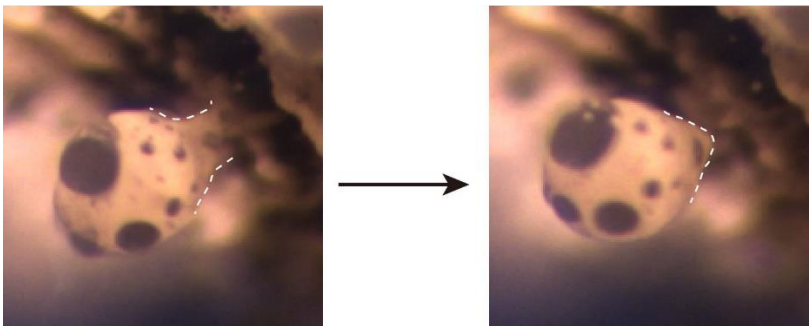

Figure S5 A droplet before and after detachment from the burning surface. The dashed lines represent the interface between the liquid and the gas.

Section S2 Estimation of relative energy release rate

The following equation is used to estimate the energy release rate of a composite:

$$E = \rho \times v \times A \times Cp \times \Delta T$$

Where E is the energy release rate, ρ is the density of the composite, A is the cross-section area of the composite, v is the measured average burn rate, C_p is the heat capacity of the composite, and ΔT is the difference between the measured temperature of the droplets on the burning surface and room temperature. For simplicity, C_p is assumed to remain invariant when Si is introduced. Relative energy release rate is obtained by normalizing the calculated energy release rate relative to the energy release rate of Al.

7 Oscillating-to-Continuous Combustion Transition in Mesoparticle Composites through Manipulation of Heat Feedback

7.1 Summary

Mesoparticles, which include fuel and oxidizer nanoparticles along with a gas-generating binder, have shown superior reactivity compared to physically mixed fuel and oxidizer nanoparticles. A significant step toward practical application of these mesoparticles is the development of composites with both mechanical integrity and high loading. In this study, I fabricate free-standing composites consisting of 90 wt% nanoenergetic mesoparticles using 3D printing and investigate their combustion characteristics. Our findings reveal that the integrity of the mesoparticles remains intact during the printing process and a reduction in sintering is observed for the composite of mesoparticles compared to the physical mixture. However, the composite of mesoparticles exhibits noncontinuous and oscillating propagation behavior at a nominal and steady frequency of ~5 Hz. I attribute this to insufficient heat feedback from the flame to the unburnt material. To address this issue, carbon fiber (C.F.) is introduced into the composite to enhance heat feedback by intercepting hot agglomerates near the burning surface. Incorporating C.F. leads to steady propagation of the composite. Agglomerate residence time and characteristic heat transfer time analysis near the burning surface indicate that while the composite without C.F. has agglomerate residence time on the same order of magnitude as the characteristic heat transfer time, the composite with C.F. has significantly increased overall agglomerate residence time compared to the characteristic heat transfer

time. This confirms the enhanced heat feedback through C.F. inclusion. This study demonstrates the crucial role of heat feedback in the combustion behavior of energetic composites.

7.2 Introduction

The use of nanostructures has significantly increased the research activity into novel classes of energetic materials [1–8]. The reactivity of thermites that typically compose of metals and metal oxides has been increased significantly through the utilization of nanoscale particles [9]. The enhanced reactivity is generally attributed to the increased specific surface area and decreased diffusion length scale of nanoparticles [1]. Aluminum (Al) particles are widely used as additives in energetic materials such as explosives, propellants, and pyrotechnics to improve combustion performance due to its high energy density, availability, and low cost [10–13]. Nevertheless, substituting micron-scale aluminum (nAl) with nanoscale aluminum in energetic materials results in combustion rates that are lower than theoretically expected [4,14], as well as more difficult formulation and processing. This former is attributed to the agglomeration/sintering that results in loss of nanostructure during combustion, as nAl tends to aggregate, sinter, and coalesce [15]. Agglomeration negates the benefits of using nAl and reduces the rate of energy release [11,14,16–22].

Our research group has explored an approach to minimize sintering effects as well as some of the processing constraints in working with nanomaterials in formulations through creation of mesoparticles. A mesoparticle is an assembly of nanometric metal fuels along with an optional oxidizer, and very importantly a low temperature gas

generator/binder. This type of particle system, which assembles nanomaterials into super-micron particles, has been demonstrated to yield considerable improvement in combustion performance on a particle combustion level [13,23–25]. The enhanced reactivity is attributed to the breaking up of soft agglomerates before/during combustion from the low temperature gas generation of NC as well as better mixing between fuel and oxidizer. Another crucial advantage of mesoparticles is their ability to maintain an internal surface area roughly equivalent to the specific surface area of a nanoparticle while providing ease of processing for high loading solid propellant fabrication [23]. High specific surface area of nAl results in severe processing challenges as the integration of nAl into polymer binders leads to dramatically increased viscosity. By assembling nAl into mesoparticles, the overall particle surface area decreases significantly, resulting in easier processing and higher particle loading of solid propellants [26]. Despites the potential advantages of utilizing mesoparticles in energetic materials, an investigation focusing on the combustion characteristics of a solid composite with high mesoparticle loading is still lacking and is the motivation of this chapter.

In this study, I fabricated free-standing composites consisting of mesoparticles at a 90% loading using 3D printing and compared their combustion behaviors with composites made from a physical mixture. Scanning Electron Microscopy (SEM) analysis of the printed composite confirmed that the integrity of the mesoparticles was preserved throughout the printing process. High-speed microscopic and macroscopic imaging techniques were utilized to study the combustion behavior of the printed composites. Microscopic imaging revealed reduced sintering in the composite of mesoparticles

compared to the physical mixture composite during combustion. However, macroscopic imaging showed that while the physical mixture composite propagated steadily, the mesoparticle composite exhibited non-continuous and periodic propagation behavior. This behavior is attributed to insufficient heat feedback from the flame to the unburnt region, hindering steady propagation. To address this issue, carbon fiber was incorporated into the mesoparticle composite to enhance heat feedback[27,28]. Microscopic imaging demonstrated that carbon fiber intercepted agglomerates near the burning surface, while macroscopic imaging revealed that the mesoparticle composite with carbon fiber propagated steadily. Theoretical calculations were performed to compare the residence time of agglomerates and the characteristic heat transfer time near the burning surface. These calculations confirm the critical role of heat feedback in the propagation of the composite of mesoparticles.

7.3 Materials and Methods

7.3.1 Materials

Aluminum nanoparticles (Al NPs, ~70 nm, 66 wt% active) were purchased from US Research Nanomaterials Inc. The active content of was determined with thermogravimetry and differential scanning calorimetry (TGA−DSC, Netsch STA449 F3 Jupiter) [7,29]. Copper oxide nanoparticles (CuO, ~40 nm) were obtained from U.S. Research Nanomaterials. Polymethyl methacrylate (PMMA, MW=550,000) was purchased from Alfa Aesar and METHOCEL™ F4M Hydroxypropyl Methylcellulose (HPMC) was obtained from Dow Chemical Company. The Collodion solution (4-8 wt% in ethanol/diethyl ether) was purchased from Sigma-Aldrich, and nitrocellulose (NC) was

obtained by drying the collodion solution. Carbon fiber (C.F., diameter: 7 μm, length: ~ 3 mm) was purchased from Composite Envisions. Ethanol (200 proof) was purchased from Koptec. Dichloromethane (99.9%), N-dimethylformamide (DMF), 2-propanol (IPA), and acetone (99.5%) were purchased from Fisher Scientific.

7.3.2 Synthesis of Al-CuO-NC mesoparticles

Details about mesoparticle synthesis can be found in our previous publication [25]. Briefly, Al NPs and CuO NPs at stoichiometric ratio were added to an NC solution in the mixture of DMF:IPA:acetone (3:5:2 in volume). The choice of 7.5 wt% NC was based on our prior work which showed an optimal result [25]. The suspension was sonicated for 1 h, followed by a minimum of 24 h of stirring. The obtained suspension was spray dried into mesoparticles with a Büchi B-290 Mini Spray Dryer. Argon preheated at ~110 °C was used as the drying gas throughout the spray drying system.

7.3.3 3D printing

Details about 3D printing of 90 wt% loading composites can be found in previous publications from our group [20,29]. Generally, the inks were prepared by firstly dissolving 10 wt% PMMA or 4 wt% PMMA and 6 wt% HPMC in the mixture of ethanol and dichloromethane (1:1 in volume). Mesoparticles were then added and ultrasonicated for 15 min and magnetically stirred for ~1 h. For preparing the ink for composite with carbon fiber, 2 wt% was added to the PMMA/HPMC solution and gently stirred for ~1 h before the addition of mesoparticles. For printing, an ink was extruded through a 14-gauge nozzle and written directly on a glass substrate kept at room temperature. The obtained films were then cut into ~2 cm long free-standing sticks for further characterizations. It is noteworthy

that while mesoparticles can be printed with both PMMA and PMMA/HPMC as the binder, mesoparticles with carbon fiber can only be printed with PMMA/HPMC. This is because the low viscosity of PMMA solution leads to the rapid settling of carbon fiber, resulting in a failed print. The solution of PMMA/HPMC has significantly higher viscosity that ensures successful printing.

7.3.4 Characterizations

Scanning electron microscope (SEM, Thermo-Fisher Scientific NNS450) was used to characterize the morphology of the as-synthesized mesoparticles, printed composites, and the post-combustion products.

7.3.5 *In operando* microscopic and macroscopic imaging

Details of *in operando* macro and microscopic/pyrometry imaging process can be found in our previous publications [18,30]. Briefly, two color imaging systems were aligned on two opposite sides of a printed stick mounted inside a chamber. One is a macroscopic imaging system with a high-speed camera (Vision Research Phantom Miro M110). The other is a microscopic imaging system with a high-speed camera (Vision Research Phantom VEO710L) coupled with Infinity Photo-Optical Model K2 DistaMax. (The microscopic imaging videos were utilized for measuring temperature with pyrometry, which will be discussed in more details in the following section.) The printed stick was then ignited with a Joule-heated nichrome wire and the combustion process was recorded by both of the imaging systems. It is worth noting that the chamber was filled with air for the composites of physically mixed Al/CuO and mesoparticle with only PMMA as the binder. This was because that the composite containing mesoparticles with PMMA failed

to propagate in an argon environment. In contrast, the chamber was filled with argon for the composites of mesoparticle with PMMA/HPMC as the binder.

7.3.6 Three-color imaging pyrometry

Details of three-color imaging pyrometry can be found in our previous studies [18,27,31]. Briefly, temperature measurements were performed by analyzing the channel intensity ratios of three color (red, green, and blue) captured by the Bayer filter of the camera. A custom MATLAB routine was utilized for this analysis with the assumption that the sample exhibited graybody emission behavior. A blackbody source (Mikron M390) was used to obtain calibration factors. Temperature measurement uncertainty was estimated to be nominally 200-300 K [27,31].

7.3.7 Infrared radiation (IR) camera imaging

IR measurement of the printed mesoparticle with PMMA as the binder was performed with an IR camera (Telops FAST M3K high-speed infrared camera) to capture the infrared radiation signals.

7.4 Results and discussions

The concept of utilizing mesoparticles implies that it is crucial to ensure the mesoparticles maintain their integrity throughout the printing process. As shown in Figure 7-1 (a) and (b), there is no apparent difference in morphology between the mesoparticles (Al-CuO-7.5wt% NC) synthesized through the spray-drying process and those incorporated into the printed composite. This confirms that the mesoparticles remain intact during the printing process.

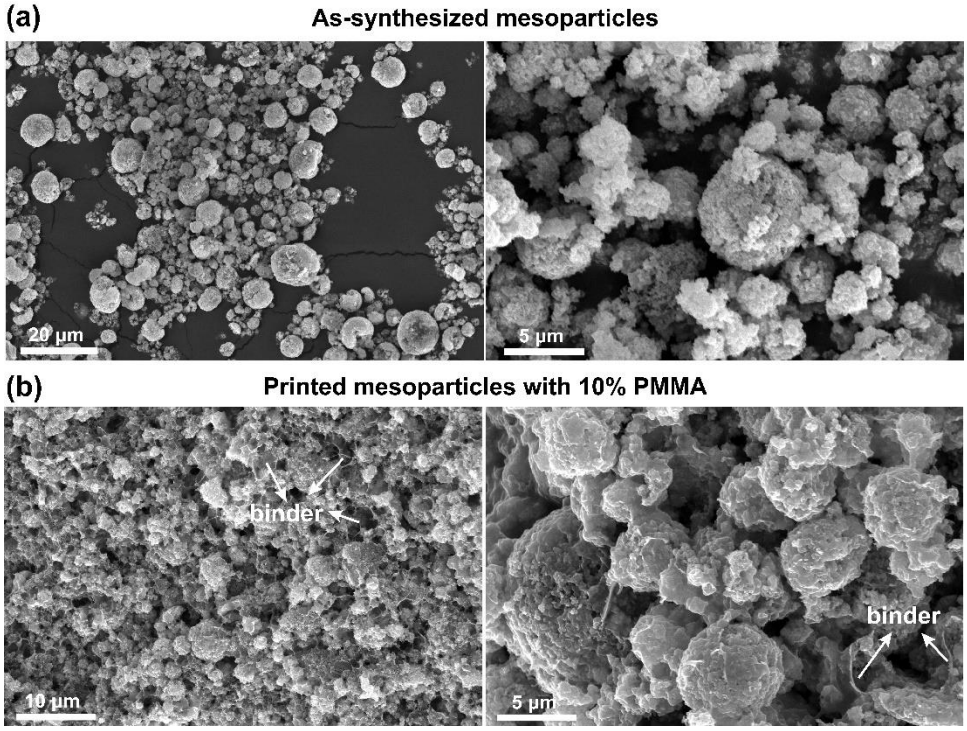

Figure 7-1 SEM images of as-synthesized mesoparticles from the spray-drying process (a) and the mesoparticles incorporated into the printed composite (b). Note: The binder labeled in (b) refers to the binder used for printing (PMMA).

Combustion characteristics of the printed composites of physical mixture and mesoparticles were investigated with high-speed macroscopic imaging. It was expected that the printed composite of mesoparticles has a higher burn rate than that of physical mixture due to the higher intrinsic reactivity of mesoparticles compared to a physical mixture, as previously demonstrated [23,25]. Figure 7-2 (a) displays a series of time-resolved macroscopic snapshots of the physically mixed composite burning. However, the composite of mesoparticles displays non-continuous propagation behavior that reduces the overall burn rate significantly (Figure 7-2 (b)). Furthermore and very curiously, the light intensity extracted from the macroscopic imaging video demonstrates a periodic (but

steady) combustion characteristic (blinking) during propagation of the mesoparticle composite (Figure S1, each peak represents a visible combustion event). The time interval between two adjacent visible (blinking) combustion events is ~200 ms and the burn time of each combustion event is ~15 ms, which appears to be quite consistent.

The fact that the composite of mesoparticles reignites after a combustion event followed by a relatively long period of time without any visible flame suggests the presence of a different ignition source. IR imaging was utilized to measure temperature in-between of the visible combustion events for the composite of mesoparticles and the result is displayed in Figure 7-2 (c). The sharp peaks in Figure 7-2 (c) correspond to the visible thermal events shown in Figure S1. Sample temperature drops to ~450 °C abruptly at the end of a combustion event, and then gradually increases to ~650 °C, which is approximately the ignition temperature of Al/CuO composite measured from our previous study [11]. Once this temperature is reached, the sample is reignited and another combustion event occurs. This behavior will be discussed in more detail in the following section, as well as how to mitigate this behavior.

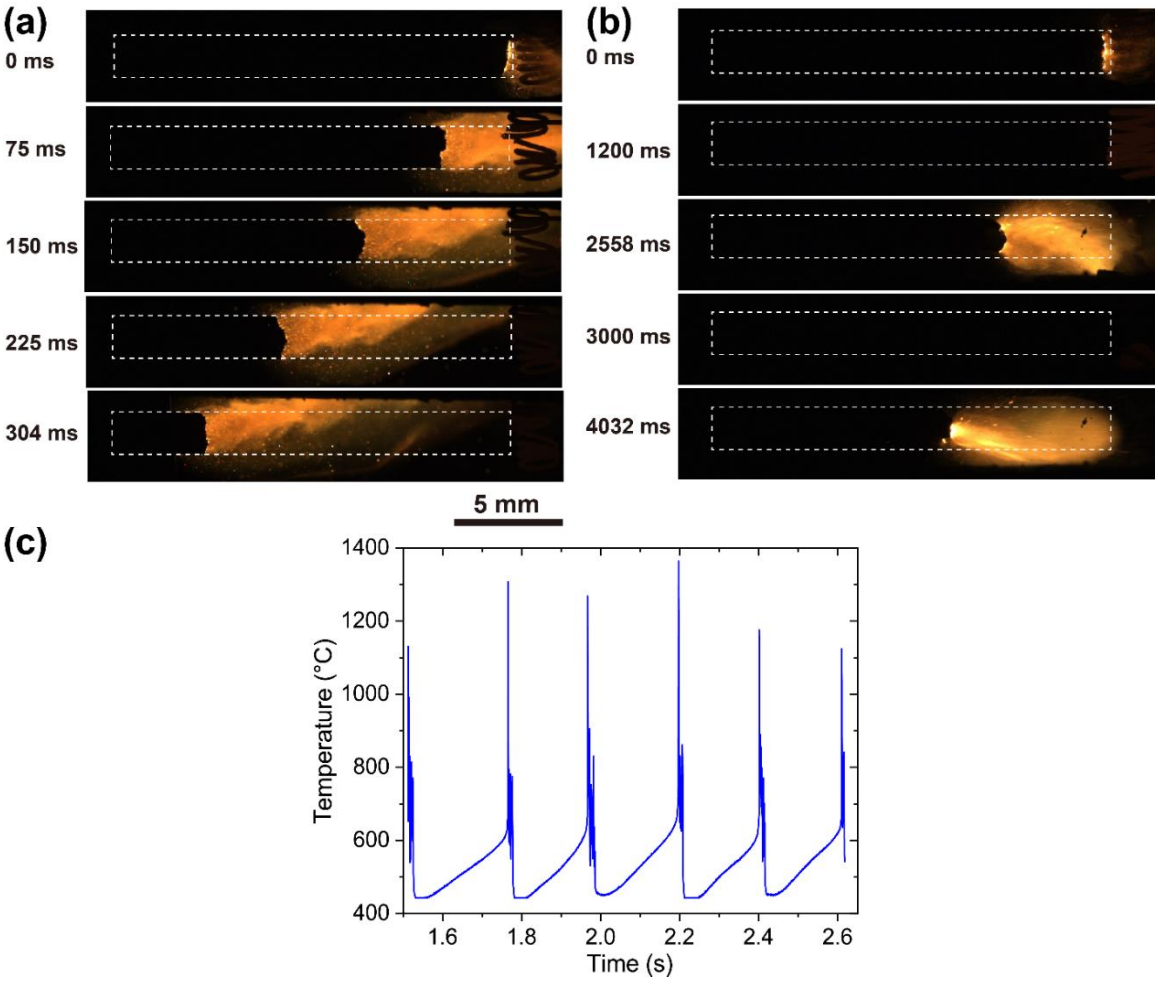

Figure 7-2 Time-resolved snapshots from high-speed macroscopic video of physical mixture composite(a) and mesoparticle composite (b). Note: The dashed lines represent the printed composites before ignition. Time resolved temperature from the IR imaging video for the composite of mesoparticles showing periodic combustion (c).

The preceding analysis primarily focuses on how the non-continuous propagation of the composite of mesoparticles occurs but does not address the reason for why the utilization of mesoparticles results in such a combustion characteristic. High-speed microscopic imaging facilitates direct observation of events occurring near the flame front, providing valuable insights into the combustion behavior of a thermite reaction. Figure 7-3

(a) and (b) display the representative snapshots taken from the high-speed microscopic videos for the composite of physical mixture and the composite of mesoparticles, respectively. While previous studies have used ex-situ techniques to prove the reduction in sintering when assembling Al/CuO into mesoparticles [23,25], the microscopic videos in the current study enable *in-situ* observation of the reduced sintering of mesoparticle over the physical mixture. SEM was utilized to analyze the post-combustion products for the composites with physical mixture and mesoparticles, as displayed in Figure 7-3 (c) and (d), respectively. It is evident that the composite with mesoparticles produces smaller agglomerates during combustion compared to the composite with the physical mixture, consistent with the observation from microscopic imaging.

Steady propagation of an energetic system necessitates sufficient transfer of heat from the reaction front or flame to the unreacted material [31–35]. Previous studies on Al/CuO mesoparticles with NC as the binder have demonstrated that the higher reactivity from mesoparticles arises from the reduced sintering as a result of significant gas generation from NC. However, for the composite with mesoparticles, the large amount of gas generation from NC appears to lead to the rapid departure of agglomerates from the burning surface, resulting in less conductive heat feedback to the unburnt region compared to the composite with physical mixture. This low heat feedback leads to the extinguishment of a combustion event observed from the macroscopic imaging. It is noteworthy that the composite comprises 10% polymer (PMMA) to bind mesoparticles into a free-standing stick through 3D printing, and PMMA undergoes combustion alongside the mesoparticles [36,37]. However, the flame of PMMA is not visible in the color camera with the settings to

observe burning agglomerates, as the combustion products of PMMA (mainly CO_2, CO, H_2O [38,39]) primarily emit in the infrared range [40,41]. After a combustion event, observed from the macroscopic camera, PMMA continues to combust as it forms a continuous network within the composite from 3D printing Figure 7-1 (b). The heat generated from the combustion of PMMA increases the local temperature, igniting nearby mesoparticles when the temperature reaches their ignition point. This is supported by the IR imaging result displayed in Figure 7-2 (c). The ignition of these mesoparticles initiates a new combustion event observed from the macroscopic camera. This series of events repeats, resulting in the non-continuous and cyclic combustion behavior observed in the composite of mesoparticles. To reinforce this point, a composite comprising 20% PMMA and 80% mesoparticles i.e. less mesoparticles also exhibits a non-continuous and cyclic propagation behavior. However, the time interval between two adjacent combustion events is reduced by almost a half to ~110 ms. This discrepancy is attributed to the higher content of PMMA in the composite, leading to a faster accumulation of heat from the PMMA flame and consequently resulting in quicker reignition of the composite. A more extensive investigation into this phenomenon is currently underway in our research group.

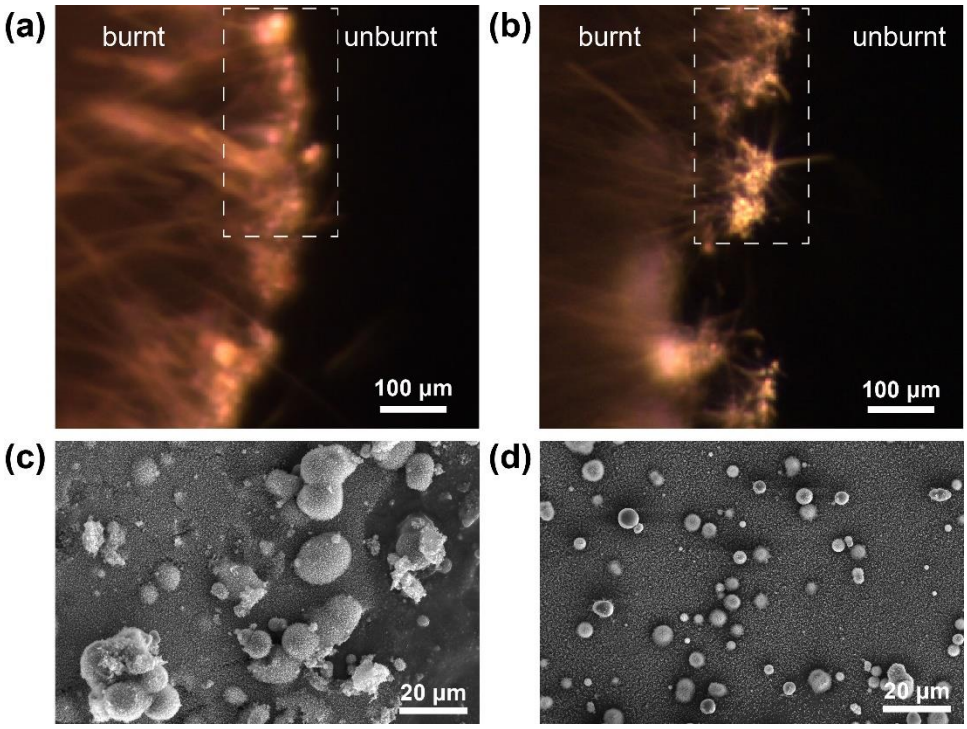

Figure 7-3 Snapshots from high-speed microscopic video for the combustion of the composites of physical mixture (a), and mesoparticles (b). The dashed lines show the representative combustion characteristics on the burning surface. SEM images of the post-combustion product from the composites of physical mixture (c), and mesoparticles (d), i.e. mesoparticle combustion products are smaller.

So far, I have conjectured that insufficient heat feedback causes the non-continuous propagation of the composite of mesoparticles. A primary question now arises: If indeed this is a heat feedback issue, then would increasing heat feedback result in continuous propagation for the composite of mesoparticles? Previous studies have demonstrated that adding carbon fiber (C.F.) increases heat feedback of a solid-state composite by capturing the agglomerates departed from the burning surface [27,28]. Inspired by these studies, I incorporate 2 wt% of C.F. in the 3D printed composite of mesoparticles to increase the heat feedback. For simplicity, this composite will be referred as mesoparticle-2% C.F.

composite in the following discussion. High-speed macroscopic and microscopic imaging reveals that this composite has continuous propagation. Figure 7-4 (a) demonstrates stable and linear propagation of the mesoparticle-2% C.F. composite. Microscopic imaging reveals that carbon fibers intercept burning agglomerates, causing them to remain near the burning surface rather than dispersing to a greater distance, as shown in Figure 7-4 (b). Temperature measurements from three-color pyrometry indicate that the agglomerates on the C.F. maintain a temperature of ~2100 K when they are within a distance of ~1 mm from the burning surface. Agglomerates on the burning surface and those have recently departed from the burning surface without being intercepted by the carbon fibers have a temperature of ~2700 K, which is close to the adiabatic flame temperature of Al/CuO at 2840 K [11]. The lower temperature of agglomerates on the C.F. compared to those not on the C.F. can be attributed to their rapid heat loss to the C.F. with high thermal conductivity. SEM images of post-combustion product of the mesoparticle-2% C.F. composite displayed in Figure 7-4 (c) show the extensive attachment of agglomerates on the carbon fibers, consistent with the observation from microscopic imaging (Figure 7-4 (b)).

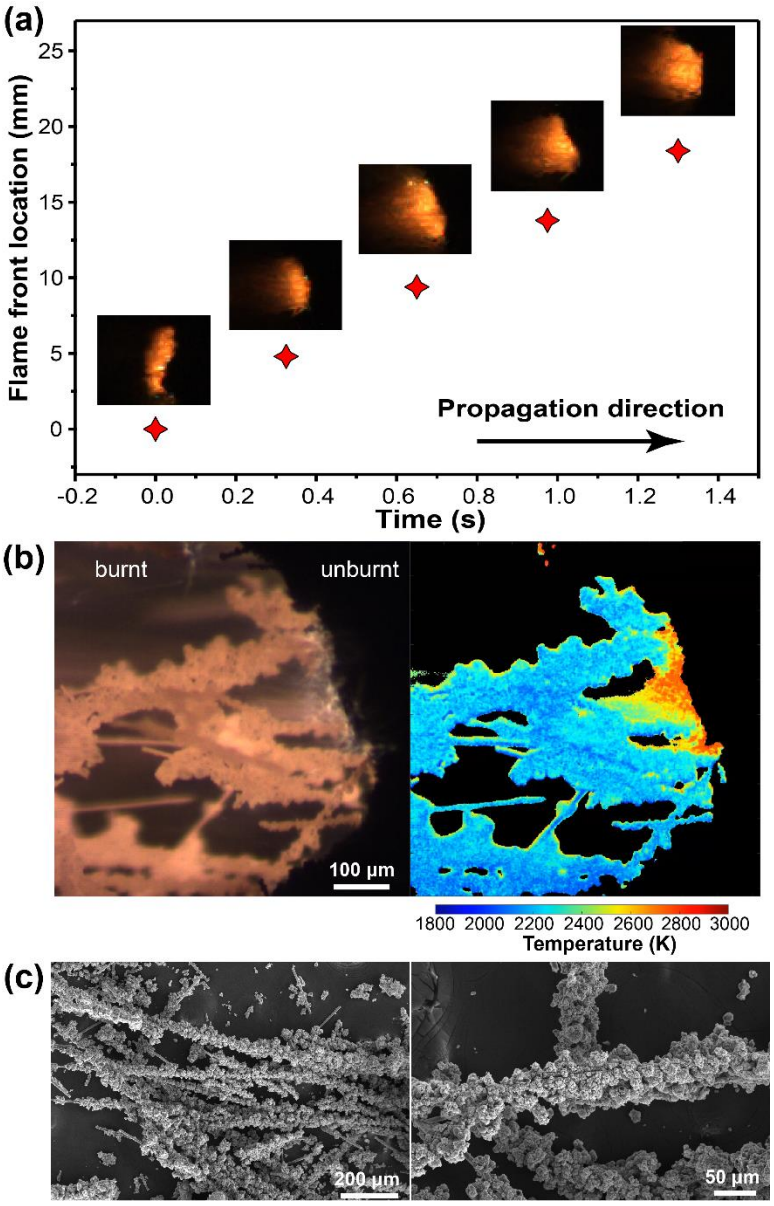

Figure 7-4 Time-resolved flame front position with corresponding snapshot from macroscopic imaging for the composite of mesoparticles with 2% C.F.(a). Representative snapshot from high-speed microscopic video and its corresponding temperature map from three-color pyrometry (b) and SEM images of the post-combustion product (c) for the composite of mesoparticles with 2% C.F.

Previous studies have demonstrated that heat feedback plays a crucial role in the propagation of an energetic material as steady propagation necessities sufficient heat from the flame to the unreacted material[31–34]. The preceding analysis has demonstrated qualitatively that increasing heat feedback of the composite of mesoparticles by incorporating carbon fiber results in a continuous and stable propagation. Now, let us perform a semiquantitative analysis on the change in heat feedback resulted from the incorporation of carbon fiber by comparing the agglomerate residence time (t_{res}) and characteristic heat transfer time ($t_{heat\ transfer}$) in a region near the burning surface. I start by simplifying the system into a one-dimensional model and building a control volume close to the burning surface, within which heat transferred from the agglomerates is considered (Figure 7-5). The length of control volume *L* is assumed to be 100 μm as it is in between the mesoparticle size (~ 3 μm) and the C.F. length (~3 mm). Convective heat feedback is neglected as the combustion test was conducted within an largely unconfined environment (the combustion chamber has a cross-section area 4 orders of magnitude higher than that of the composite) and the hot gas and particles unlikely move backward to the unburn material [34]. Radiative heat transfer is also neglected as the presence of C.F. should have minimal impact on the radiative property of agglomerates. Therefore, heat transfer time ($t_{heat\ transfer}$) is simplified to heat conduction time (t_{cond}) hereafter. Agglomerate residence time for the composite with bare mesoparticles is represented by Equation (1). For the mesoparticle-2% C.F. composite, there are two classes of agglomerates: those that are not intercepted by C.F. (Equation (1)), and those that are intercepted by C.F. (Equation (2)).

$$t_{res1} = \frac{L}{v_x} \quad (1)$$

$$t_{res2} = \frac{L-x}{u} \quad (2)$$

where x is the distance from the agglomerate to the burning surface, v_x is the agglomerate traveling speed within L, u is the macroscopic burn rate of the mesoparticle-2% C.F. composite (1.5 cm/s), t_{res1} is the residence time of the agglomerate that is not intercepted by C.F., and t_{res2} is the residence time of the agglomerate that is intercepted by C.F. The values of x and v_x are obtained from high-speed microscopic imaging by tracking the traveling time and distance after the detachment of the agglomerate from the burning surface.

For an order-of-magnitude estimate of heat conduction time (t_{cond}), I assume that the gas medium near the burning surface is argon and there is no interaction among agglomerates. The heat conduction time is characterized by Equation (3)[42].

$$t_{cond} \sim \frac{L^2}{\alpha} \quad (3)$$

where α is the thermal diffusivity of the medium and is represented by Equation (4).

$$\alpha \sim \frac{k}{\rho c_p} \quad (4)$$

where k is the thermal conductivity, ρ is the density, and c_p is the heat capacity. For the composite without C.F., argon is the only heat conduction medium. Density of argon is calculated based on ideal gas law, and thermal conductivity and heat capacity of argon are calculated with USC Mech II[43] . For the composite with C.F., there are two scenarios for

the agglomerates to conduct heat back to the unburnt composite: those that are not intercepted by C.F., and those that are intercepted by C.F. (Figure 7-5). It is assumed that the agglomerates not intercepted by C.F. conduct heat through argon only and agglomerates intercepted by C.F. conduct heat through C.F. only. The thermal conductivity of C.F. used in the current study is estimated to be 10 $W \cdot m^{-1} \cdot K^{-1}$ and the density and heat capacity of C.F. used are based on a previous study[27].

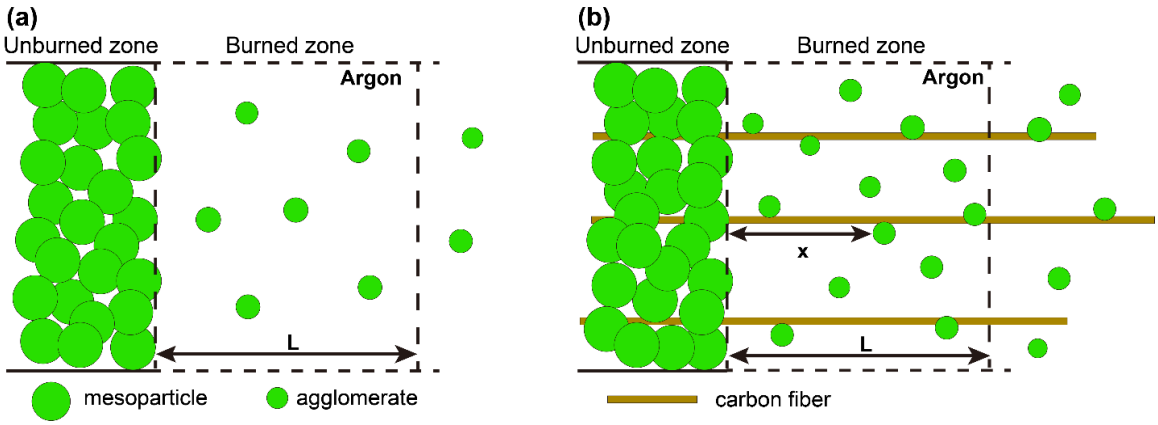

Figure 7-5 Illustration depicting the region near the burning surface for the composite of mesoparticles without C.F. (a) and with C.F. (b).

Figure 7-6 illustrates the estimated agglomerate residence time and characteristic heat transfer time in the region (L) near the burning surface for the composites of mesoparticles with and without C.F. In the case of the composite without C.F., the majority of the estimated residence time is on the same order of magnitude with the heat transfer time. However, for the composite with C.F., in addition to the agglomerates having residence time on the same order of magnitude as the heat transfer time, the agglomerates intercepted by the C.F. demonstrate residence times 3 orders of magnitude higher than the

heat transfer time. This quantitatively confirms the significant increase in heat feedback resulting from the inclusion of C.F. Such enhanced heat feedback is crucial in igniting the nearby unreacted material and sustaining steady propagation. This accounts for the transition from noncontinuous propagation to steady propagation observed upon the incorporation of carbon fiber into the mesoparticle composite.

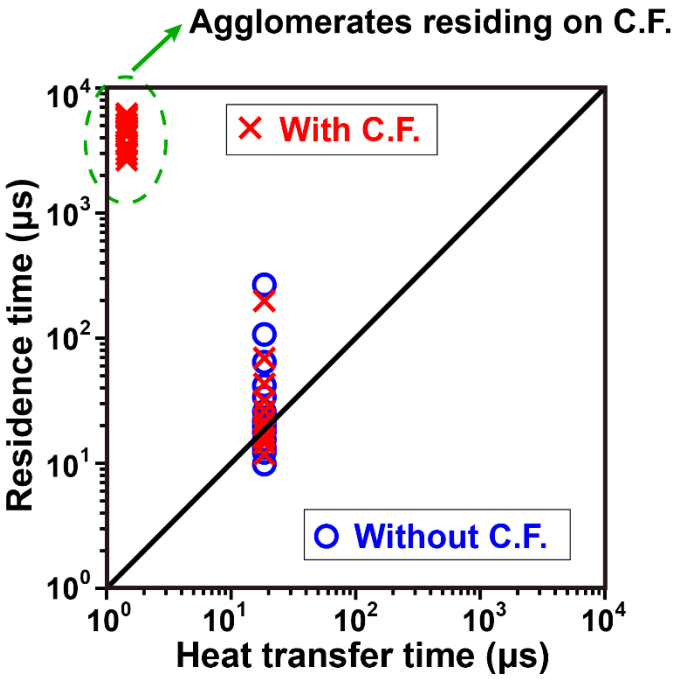

Figure 7-6 Estimated agglomerate residence time and characteristic heat transfer time for the composite of mesoparticles with and without C.F.

7.5 Conclusions

In this chapter, I investigate the combustion characteristics of a free-standing composite consisting of 90 wt% nanoenergetic mesoparticles fabricated via 3D printing. SEM analysis of the printed composite confirms the integrity of the mesoparticles is

maintained during the printing process. High-speed microscopic imaging reveals the expected reduction in sintering for the composite of mesoparticles compared to the physical mixture. However, macroscopic imaging shows noncontinuous and oscillating propagation behavior in the mesoparticle composite, which is attributed to insufficient heat feedback from the flame to the unburnt material. To enhance heat feedback, carbon fiber (C.F.) is incorporated into the composite to intercept agglomerates near the burning surface. With C.F. inclusion, steady propagation of the composite is observed. A theoretical calculation is performed to investigate heat feedback by comparing the residence time and characteristic heat transfer time of agglomerates near the burning surface. The calculation result finds that the overall agglomerate residence time is significantly higher than the heat transfer time for the mesoparticle composite with C.F. compared to the composite without C.F., confirming increased heat feedback. This study underscores the critical role of heat feedback in the combustion behavior of energetic composites.

7.6 References

(1) Egan, G. C.; Sullivan, K. T.; Olson, T. Y.; Han, T. Y.-J.; Worsley, M. A.; Zachariah, M. R. Ignition and Combustion Characteristics of Nanoaluminum with Copper Oxide Nanoparticles of Differing Oxidation State. *J. Phys. Chem. C* **2016**, *120* (51), 29023–29029. https://doi.org/10.1021/acs.jpcc.6b11081.

(2) Sundaram, D.; Yang, V.; Yetter, R. A. Metal-Based Nanoenergetic Materials: Synthesis, Properties, and Applications. *Prog. Energy Combust. Sci.* **2017**, *61*, 293–365. https://doi.org/10.1016/j.pecs.2017.02.002.

(3) Comet, M.; Martin, C.; Schnell, F.; Spitzer, D. Nanothermites: A Short Review. Factsheet for Experimenters, Present and Future Challenges. *Propellants Explos. Pyrotech.* **2019**, *44* (1), 18–36. https://doi.org/10.1002/prep.201800095.

(4) Zohari, N.; Keshavarz, M. H.; Seyedsadjadi, S. A. The Advantages and Shortcomings of Using Nano-Sized Energetic Materials. *Cent. Eur. J. Energ. Mater.* **2013**, *Vol. 10* (1).

(5) Yetter, R. A.; Risha, G. A.; Son, S. F. Metal Particle Combustion and Nanotechnology. *Proc. Combust. Inst.* **2009**, *32* (2), 1819–1838. https://doi.org/10.1016/j.proci.2008.08.013.

(6) Asay, B. W.; Son, S. F.; Busse, J. R.; Oschwald, D. M. Ignition Characteristics of Metastable Intermolecular Composites. *Propellants Explos. Pyrotech.* **2004**, *29* (4), 216–219. https://doi.org/10.1002/prep.200400049.

(7) Sullivan, K.; Young, G.; Zachariah, M. R. Enhanced Reactivity of Nano-B/Al/CuO MIC's. *Combust. Flame* **2009**, *156* (2), 302–309. https://doi.org/10.1016/j.combustflame.2008.09.011.

(8) Sullivan, K. T.; Kuntz, J. D.; Gash, A. E. The Role of Fuel Particle Size on Flame Propagation Velocity in Thermites with a Nanoscale Oxidizer. *Propellants Explos. Pyrotech.* **2014**, *39* (3), 407–415. https://doi.org/10.1002/prep.201400020.

(9) Weismiller, M. R.; Malchi, J. Y.; Lee, J. G.; Yetter, R. A.; Foley, T. J. Effects of Fuel and Oxidizer Particle Dimensions on the Propagation of Aluminum Containing Thermites. *Proc. Combust. Inst.* **2011**, *33* (2), 1989–1996. https://doi.org/10.1016/j.proci.2010.06.104.

(10) Sippel, T. R.; Son, S. F.; Groven, L. J. Aluminum Agglomeration Reduction in a Composite Propellant Using Tailored Al/PTFE Particles. *Combust. Flame* **2014**, *161* (1), 311–321. https://doi.org/10.1016/j.combustflame.2013.08.009.

(11) Wang, H.; Wang, Y.; Garg, M.; Moore, J. S.; Zachariah, M. R. Unzipping Polymers Significantly Enhance Energy Flux of Aluminized Composites. *Combust. Flame* **2022**, *244*, 112242. https://doi.org/10.1016/j.combustflame.2022.112242.

(12) DeLuca, L. T.; Galfetti, L.; Colombo, G.; Maggi, F.; Bandera, A.; Babuk, V. A.; Sinditskii, V. P. Microstructure Effects in Aluminized Solid Rocket Propellants. *J. Propuls. Power* **2010**, *26* (4), 724–732. https://doi.org/10.2514/1.45262.

(13) Jacob, R. J.; Wei, B.; Zachariah, M. R. Quantifying the Enhanced Combustion Characteristics of Electrospray Assembled Aluminum Mesoparticles. *Combust. Flame* **2016**, *167*, 472–480. https://doi.org/10.1016/j.combustflame.2015.09.032.

(14) Chakraborty, P.; Zachariah, M. R. Do Nanoenergetic Particles Remain Nano-Sized during Combustion? *Combust. Flame* **2014**, *161* (5), 1408–1416. https://doi.org/10.1016/j.combustflame.2013.10.017.
(15) Zachariah, M. R.; Carrier, M. J. Molecular Dynamics Computation of Gas-Phase Nanoparticle Sintering: A Comparison with Phenomenological Models. *J. Aerosol Sci.* **1999**, *30* (9), 1139–1151. https://doi.org/10.1016/S0021-8502(98)00782-4.
(16) Yetter, R. A. Progress towards Nanoengineered Energetic Materials. *Proc. Combust. Inst.* **2021**, *38* (1), 57–81. https://doi.org/10.1016/j.proci.2020.09.008.
(17) Dreizin, E. L. Metal-Based Reactive Nanomaterials. *Prog. Energy Combust. Sci.* **2009**, *35* (2), 141–167. https://doi.org/10.1016/j.pecs.2008.09.001.
(18) Wang, H.; Kline, D. J.; Zachariah, M. R. In-Operando High-Speed Microscopy and Thermometry of Reaction Propagation and Sintering in a Nanocomposite. *Nat. Commun.* **2019**, *10* (1), 3032. https://doi.org/10.1038/s41467-019-10843-4.
(19) Wang, Y.; Paul, G. I.; Hagen, E.; Wang, H.; Zachariah, M. R. Combustion Behavior of Aluminized Metal Iodate Composites. Part 2: Iodine and Energy Release Rate. *Combust. Flame* **2024**, *262*, 113373. https://doi.org/10.1016/j.combustflame.2024.113373.
(20) Wang, Y.; Hagen, E.; Biswas, P.; Wang, H.; Zachariah, M. R. Imaging the Combustion Characteristics of Al, B, and Ti Composites. *Combust. Flame* **2023**, *252*, 112747. https://doi.org/10.1016/j.combustflame.2023.112747.
(21) Egan, G. C.; Sullivan, K. T.; LaGrange, T.; Reed, B. W.; Zachariah, M. R. In Situ Imaging of Ultra-Fast Loss of Nanostructure in Nanoparticle Aggregates. *J. Appl. Phys.* **2014**, *115* (8), 084903. https://doi.org/10.1063/1.4867116.
(22) Sullivan, K. T.; Piekiel, N. W.; Wu, C.; Chowdhury, S.; Kelly, S. T.; Hufnagel, T. C.; Fezzaa, K.; Zachariah, M. R. Reactive Sintering: An Important Component in the Combustion of Nanocomposite Thermites. *Combust. Flame* **2012**, *159* (1), 2–15. https://doi.org/10.1016/j.combustflame.2011.07.015.
(23) Wang, H.; Jian, G.; Egan, G. C.; Zachariah, M. R. Assembly and Reactive Properties of Al/CuO Based Nanothermite Microparticles. *Combust. Flame* **2014**, *161* (8), 2203–2208. https://doi.org/10.1016/j.combustflame.2014.02.003.
(24) Wang, H.; Jacob, R. J.; DeLisio, J. B.; Zachariah, M. R. Assembly and Encapsulation of Aluminum NP's within AP/NC Matrix and Their Reactive Properties. *Combust. Flame* **2017**, *180*, 175–183. https://doi.org/10.1016/j.combustflame.2017.02.036.
(25) Chowdhury, M.; Ghildiyal, P.; Rojas, A.; Wang, Y.; Wang, H.; Zachariah, M. R. High-Yield Spray Drying Assembly and Reactive Properties of Nanoenergetic Mesoparticle Composites. *Adv. Powder Technol.* **2023**, *34* (7), 104075. https://doi.org/10.1016/j.apt.2023.104075.
(26) Young, G.; Wang, H.; Zachariah, M. R. Application of Nano-Aluminum/Nitrocellulose Mesoparticles in Composite Solid Rocket Propellants. *Propellants Explos. Pyrotech.* **2015**, *40* (3), 413–418. https://doi.org/10.1002/prep.201500020.
(27) Wang, H.; Kline, D. J.; Rehwoldt, M. C.; Zachariah, M. R. Carbon Fibers Enhance the Propagation of High Loading Nanothermites: In Situ Observation of

Microscopic Combustion. *ACS Appl. Mater. Interfaces* **2021**. https://doi.org/10.1021/acsami.1c02911.
(28) Wang, H.; Hagen, E.; Shi, K.; Herrera, S.; Xu, F.; Zachariah, M. R. Carbon Fibers as Additives to Engineer Agglomeration and Propagation of Aluminized Propellants. *Chem. Eng. J.* **2023**, 141653. https://doi.org/10.1016/j.cej.2023.141653.
(29) Wang, H.; Shen, J.; Kline, D. J.; Eckman, N.; Agrawal, N. R.; Wu, T.; Wang, P.; Zachariah, M. R. Direct Writing of a 90 Wt% Particle Loading Nanothermite. *Adv. Mater.* **2019**, *31* (23), 1806575. https://doi.org/10.1002/adma.201806575.
(30) Wang, H.; Julien, B.; Kline, D.; Alibay, Z.; Rehwoldt, M.; Rossi, C.; Zachariah, M. Probing the Reaction Zone of Nanolaminates at ∼μs Time and ∼μm Spatial Resolution. *J. Phys. Chem. C* **2020**, *124* (25), 13679–13687. https://doi.org/10.1021/acs.jpcc.0c01647.
(31) Kline, D. J.; Alibay, Z.; Rehwoldt, M. C.; Idrogo-Lam, A.; Hamilton, S. G.; Biswas, P.; Xu, F.; Zachariah, M. R. Experimental Observation of the Heat Transfer Mechanisms That Drive Propagation in Additively Manufactured Energetic Materials. *Combust. Flame* **2020**, *215*, 417–424. https://doi.org/10.1016/j.combustflame.2020.01.020.
(32) Ishihara, A.; Brewster, M. Q.; Sheridan, T. A.; Krier, H. The Influence of Radiative Heat Feedback on Burning Rate in Aluminized Propellants. *Combust. Flame* **1991**, *84* (1), 141–153. https://doi.org/10.1016/0010-2180(91)90043-B.
(33) Brewster, M. Q.; Hardt, B. E. Influence of Metal Agglomeration and Heat Feedback on Composite Propellant Burning Rate. *J. Propuls. Power* **1991**, *7* (6), 1076–1078. https://doi.org/10.2514/3.23431.
(34) Egan, G. C.; Zachariah, M. R. Commentary on the Heat Transfer Mechanisms Controlling Propagation in Nanothermites. *Combust. Flame* **2015**, *162* (7), 2959–2961. https://doi.org/10.1016/j.combustflame.2015.04.013.
(35) Summerfield, M. *Solid Propellant Rocket Research*; Elsevier, 2013.
(36) Zarzecki, M.; Quintiere, J. G.; Lyon, R. E.; Rossmann, T.; Diez, F. J. The Effect of Pressure and Oxygen Concentration on the Combustion of PMMA. *Combust. Flame* **2013**, *160* (8), 1519–1530. https://doi.org/10.1016/j.combustflame.2013.02.019.
(37) Van Der Geld, C. W. M.; Korting, P. A. O. G.; Wijchers, T. Combustion of PMMA, PE, and PS in a Ramjet. *Combust. Flame* **1990**, *79* (3), 299–306. https://doi.org/10.1016/0010-2180(90)90141-D.
(38) Kramer, C. A.; Loloee, R.; Wichman, I. S.; Ghosh, R. N. Time Resolved Measurements of Pyrolysis Products From Thermoplastic Poly-Methyl-Methacrylate (PMMA); American Society of Mechanical Engineers Digital Collection, 2010; pp 99–105. https://doi.org/10.1115/IMECE2009-11256.
(39) Ghosh, R. N.; Wichman, I. S.; Kramer, C. A.; Loloee, R. Time-Resolved Measurements of Pyrolysis and Combustion Products of PMMA. *Fire Mater.* **2013**, *37* (4), 280–296. https://doi.org/10.1002/fam.2129.
(40) Cai, T.; Wang, G.; Zhang, W.; Gao, X. Simultaneous Measurement of CO and CO2 at Elevated Temperatures by Diode Laser Wavelength Modulated Spectroscopy.

Measurement **2012**, *45* (8), 2089–2095. https://doi.org/10.1016/j.measurement.2012.05.006.
(41) Fu, G.; Sing, D. K.; Lothringer, J. D.; Deming, D.; Ih, J.; Kempton, E. M.-R.; Malik, M.; Komacek, T. D.; Mansfield, M.; Bean, J. L. Strong H2O and CO Emission Features in the Spectrum of KELT-20b Driven by Stellar UV Irradiation. *Astrophys. J. Lett.* **2022**, *925* (1), L3. https://doi.org/10.3847/2041-8213/ac4968.
(42) Rohsenow, W. M.; Hartnett, J. P.; Ganic, E. N. Handbook of Heat Transfer Fundamentals (2nd Edition). **1985**.
(43) Hai Wang, Xiaoqing You, Ameya V. Joshi, Scott G. Davis, Alexander Laskin, Fokion Egolfopoulos & Chung K. Law, USC Mech Version II. Available at <https://ignis.usc.edu/USC_Mech_II.htm>

7.7 Supporting information

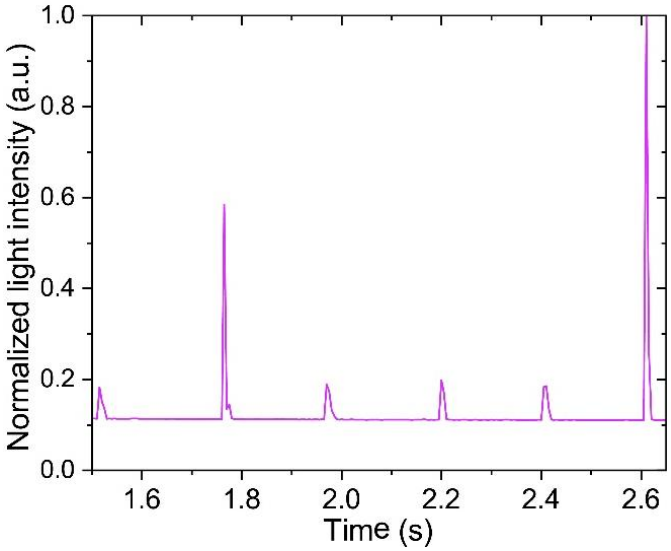

Figure S1 Time-resolved normalized light intensity from the macroscopic video of the combustion process of the composite of mesoparticle with PMMA as the binder.

8 Combustion Behavior of Aluminized Metal Iodate Composites. Part 1: Decomposition Mechanism of Metal Iodates

8.1 Summary

Metal iodates are candidates of high temperature biocidal oxidizing agents owing to their high iodine and oxygen content. Here I explore the high temperature decomposition mechanism of alkali and alkaline metal iodates ($LiIO_3$, $NaIO_3$, KIO_3, $Mg(IO_3)_2$, and $Ca(IO_3)_2$). Temperature-jump/time-of-flight mass spectrometry (T-Jump/TOFMS) measurements reveal that while all of these iodates release O_2, only $Mg(IO_3)_2$, $Ca(IO_3)_2$, and $LiIO_3$ release significant amount of I_2 and there is minimal I_2 release from $NaIO_3$ and KIO_3. Thermogravimetric-differential scanning calorimetry (TGA-DSC) measurement and X-ray diffraction (XRD) analysis of temperature dependent condensed phase species demonstrates the presence of two different decomposition pathways of metal iodates. $LiIO_3$, $Mg(IO_3)_2$, and $Ca(IO_3)_2$, follow a two-step decomposition pathway: (1) Decomposition from metal iodate (MIO_3, M=Mg, Ca, and Li) into metal orthoperiodate ($M_x(IO_6)_y$) accompanied by I_2 and O_2 release, and (2) decomposition from metal orthoperiodate to metal oxide (MO) accompanied by I_2 and O_2 release. $NaIO_3$ and KIO_3 follow a one-step decomposition pathway, where they decompose into NaI and KI, respectively, simultaneously releasing O_2. Decomposition temperatures are estimated from thermodynamic data and compared between different decomposition pathways to predict which pathway is more favorable during decomposition. These estimations predict the decomposition pathway of the investigated metal iodates as they are largely consistent with

the experimental results. This study unveils a simple strategy for predicting whether a metal iodate is a promising biocidal agent by assessing its feasibility of I_2 release.

8.2 Introduction

Biological weapons pose a significant challenge to the global security. Therefore, it is essential to develop a strategy to deactivate or neutralize these highly dangerous bioagents. Halogen-containing fungicides, such as HF and chlorine-containing species, are effective in destroying bacteria[1,2]. However, their application is limited by potential toxicity and causticity. Iodine, while not benign to the environment has at least a significantly diminished footprint while still effective as a biocide. Iodine can react with cellular nucleic acids and thiol groups in enzymes and proteins after penetrating the cell wall of microorganisms, which leads to the structure disorder of microorganisms that eventually results in their inactivation[2]. Iodine has been proven to be an extremely effective biocidal agent as a very low concentration of I_2 (<15 ppm) with a high neutralization of 99.999% for certain bacteria and viruses in 10 min at 25 °C[3]. However, application of molecular iodine as a biocidal agent is inconvenient as it sublimes at room temperature due to its high vapor pressure. Also, these conventional disinfectants with halogen-containing fungicides are often inefficient as they are difficult to be implemented for large-scale microorganism deactivation over a short time.

An alternative strategy for deactivating microorganism is the application of thermal energy over a short period of time, most conventionally though energetic materials[4]. Nevertheless, this strategy is likely insufficient for complete neutralization due to the

transient nature of the thermal event, and the possibility of not homogeneously delivering the thermal pulse over the whole target region[4,5]. Based on the advantages and disadvantages of these two strategies, the development of agent defeat weapons (ADWs) that remain active for an extended period of time post-thermal pulse, has been proposed[3,6]. Therefore, consideration has been given to energetic systems with high energy density and iodine content, and various systems have been explored. Energetic composites containing I_2 have been prepared by mechanical milling and their combustion and biocidal effectiveness investigated[7–11]. However, these composites are unstable over long time storage and an additional oxidizer is required for the combustion to occur. I_2O_5 has received considerable attention due to its high iodine content and strong oxidizing property[12]. Clark et al combined Al with I_2O_5 and investigated the destruction of spore forming bacteria[13]. Our group tuned the reactivity and energy release rate of energetic composites containing I_2O_5 by varying the fuel composition[14]. Nevertheless, the hygroscopic nature of I_2O_5 largely limits its practical application. Ideally, one desires a material which undergoes a highly exothermic redox reaction, contains a high content of iodine, releases molecular iodine, easy to handle, and can be stored over a long period.

Recently, metal iodates have attracted attention for this purpose due to their strong oxidizing property and high iodine content[4,5,15]. Combustion characteristics and iodine release investigations of energetic materials containing various metal iodates, such as $Bi(IO_3)_2$, $Ca(IO_3)_2$, $Fe(IO_3)_2$, $Cu(IO_3)_2$, and $AgIO_3$, have demonstrated that metal iodates are promising candidates in the application of ADWs[4,5,15–17]. Most noteworthy is that these studies show that not all of these iodates produce I_2 as the main iodine-containing species.

Rather iodine can get kinetically trapped via formation of metal iodide[17]. However, a systematic investigation about the decomposition mechanism of metal iodates and the fundamental factors responsible for the decomposition pathway is lacking.

In this chapter, I systematically investigate the decomposition mechanism of alkali and alkaline metal iodates ($LiIO_3$, $NaIO_3$, KIO_3, $Mg(IO_3)_2$, and $Ca(IO_3)_2$), which have high iodine and oxygen content (Figure 8-1). Temperature-jump time of flight mass spectrometry (T-Jump/TOFMS) under rapid heating ($\sim 10^5$ K/s) conditions is utilized to analyze decomposition of metal iodates at high heating rate. Thermogravimetry-differential scanning calorimetry (TGA-DSC) is used to investigate the decomposition of metal iodates under slow heating (10 K/min) conditions to support the observation from T-Jump measurements. X-ray diffraction (XRD) is utilized to characterize the condensed phase species produced at different temperatures of interest with respect to TGA-DSC measurements. Thermodynamic prediction of iodate decomposition pathways is proposed.

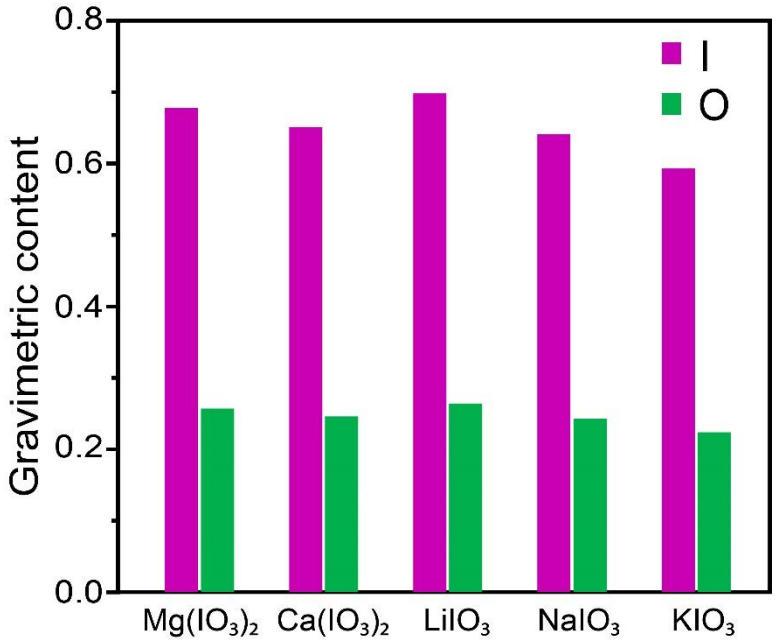

Figure 8-1 Gravimetric iodine and oxygen content in alkali and alkaline metal iodates.

8.3 Materials and Methods

8.3.1 Materials

$NaIO_3$ (99%) was purchased from Alfa Aesar. $LiIO_3$ (97%), KIO_3 (≥98%), $Ca(NO_3)_2 \cdot 4H_2O$ (≥99%), $MgCl_2$ (≥98%), NaI (≥99%), and HIO_3 (≥99.5%) were obtained from Sigma Aldrich. Ethanol (200 proof) was purchased from Koptec. NaOH (≥97%), hexanes (99.9%) and HPLC grade water were obtained from Fisher Scientific.

8.3.2 Size reduction of alkali metal iodates

Size reduction of $LiIO_3$, $NaIO_3$, and KIO_3 was performed via an aerosol spray pyrolysis (ASP) approach and was used for temperature jump time of flight mass spectrometry (T-Jump/TOFMS)[18–20]. Generally, 1 g of the as-received iodates were dissolved into 100 mL water and the resultant solution was sprayed into small droplets with

an atomizer operating at ~35 psi using compressed air. The droplets passed through a silica-gel diffusion drier for removing water of the droplets, and then passed through a tube furnace (Lindberg/Blue) operating at 150 °C. The final product was collected on a filter paper. Sub-micron sized particles were obtained[20].

8.3.3 Synthesis of $Mg(IO_3)_2$ particles

50 mmol $MgCl_2$ was dissolved in 100 mL water and 100 mmol of NaOH was dissolved in 100 mL water. Then the NaOH solution was added to the $MgCl_2$ solution slowly. The obtained suspension was centrifuged at 7000 rpm for 5 min, the supernatant was discarded, and the precipitate was washed three times with 120 mL water each time. Then the precipitate was dried in oven operating at ~ 100 °C. The dried powder was weighed (28.6 mmol) and added to 200 mL water, the resultant cloudy suspension was stirred at ~350 rpm. Separately, HIO_3 (57.2 mmol) was dissolved in 50 mL water. Then the HIO_3 solution was added to the suspension slowly. At the end of HIO_3 solution, the suspension become transparent. The obtained $Mg(IO_3)_2$ solution was filtered before further utilization. $Mg(IO_3)_2$ particles were obtained via ASP with the furnace operating at 300 °C and then dried at 300 °C for 10 min in air. X-ray diffraction crystallography (XRD) confirms the final product is $Mg(IO_3)_2$ (Figure S1).

8.3.4 Synthesis of $Ca(IO_3)_2$ particles

Details of the preparation of $Ca(IO_3)_2$ particles can be found in ref. [21]. Briefly, 1 mmol of $Ca(NO_3)_2 \cdot 4H_2O$, 2 mmol of KIO_3, 0.5 mL ethanol, and three steel balls (7/32″ in diameter, purchased from GlenMills) were loaded into a plastic centrifuge tube (FisherBrand 2 mL), which was then milled with a Retsch CryoMill operated at ambient

conditions for 20 min at a frequency of 25.0 Hz (25/s). The obtained slurry was centrifuged at 7000 rpm for 5 min and the resultant supernatant was discarded. The precipitate was washed three times with 30 mL water each time and the obtained sample was then dried overnight in a vacuum oven to remove free water and then baked in a tube furnace at 350 °C for 40 min in air to remove crystal water[16].

8.3.5 Characterization

Particle sizes were characterized by Scanning Electron Microscopy (SEM, NNS450) operating at 20 kV accelerating voltage. Temperature resolved analysis of as-received alkali metal iodates and synthesized alkaline metal iodates was conducted with a Netzsch STA 449 F3 Jupiter thermogravimetric analysis-differential scanning calorimetry (TGA-DSC) operating in argon with a flow rate of 50 mL/min at a heating rate of 10 K/min. It is noteworthy that the as-received samples of $LiIO_3$, $NaIO_3$, and KIO_3 are used for TGA-DSC, while for $Mg(IO_3)_2$ and $Ca(IO_3)_2$, the synthesized particles are used. Temperatures of interest for iterative analysis of each iodate were pinpointed from TGA-DSC profiles. Iodates were then heated in a tube furnace at these temperatures for 10 min ($LiIO_3$ at 650 °C, $NaIO_3$ at 575 °C, KIO_3 at 585 °C, $Mg(IO_3)_2$ at 650 °C, and $Ca(IO_3)_2$ at 640 °C) or 30 min ($LiIO_3$ at 900 °C, $Mg(IO_3)_2$ and $Ca(IO_3)_2$ at 800 °C) in argon and collected for X-ray diffraction crystallography (XRD PANanalytical Empyrean Series 2 diffractometer) analysis.

8.3.6 Temperature jump time of flight mass spectrometry (T-Jump/TOFMS)

The details of T-Jump/TOFMS can be found in previous publications from our group[22–24]. Briefly, size-reduced alkali metal iodate or synthesized alkaline metal iodate

was suspended in hexane and sonicated briefly. The resultant suspension was coated to be a thin layer on a Pt wire (diameter=76 μm, 0.9-1.1 cm in length, OMEGA Engineering Inc.) that was soldered between two copper leads of a T-Jump probe. The probe was then loaded into the high-vacuum T-Jump MS chamber and the Pt wire was resistively heated with a 3 ms pulsed square wave signal from a direct current voltage supply. Thermometry of the Pt wire was acquired and temperature profile of the wire was obtained by applying the calibration relationship between the temperature of the wire and its corresponding resistance from the Callendar-Van Dusen equation. The temperature of the thin sample layer on Pt wire was roughly the same with the wire. A 70 eV electron gun ionizer was used to ionize gas phase species produced from heating. A Teledyne LeCroy 600 MHz oscilloscope was used for mass spectra collection as well as current and voltage readings over a 10 ms period with 0.1 ms interval.

8.4 Result and discussion

8.4.1 Time-of-flight mass spectrometry under rapid heating rate (~10^5 K/s)

T-Jump/TOFMS was utilized to analyze the decomposition products of metal iodates under high heating rates (~10^5 K/s) and the resulting mass spectra are displayed in Figure 8-2 (a). O_2, as the main volatile species, appears in relatively large quantities for all the iodates. While for I, a representative of the I-containing species including I, and I_2, the peak intensities from $Mg(IO_3)_2$, $Ca(IO_3)_2$, and $LiIO_3$ are significantly higher than $NaIO_3$ and KIO_3. It is noteworthy that the formation of I arises from the ionization of I_2 by the electron gun ionizer. Semiquantitative analysis of the I release is conducted by measuring its peak intensity as well as relative intensity compared to KIO_3, as shown in Figure 8-2

(b), which clearly illuminates that the I release of $Mg(IO_3)_2$, $Ca(IO_3)_2$, and $LiIO_3$ is about 10 times higher than $NaIO_3$ and KIO_3. This analysis suggests the existence of two different decomposition mechanisms among these iodates. Stern reported that metal iodates may decompose according to three different routes: (a) metal iodide and O_2 are produced, (b) metal oxide, I_2, and O_2 are produced, and (c) metal orthoperiodate, I_2, and O_2 are produced[25]. Ito *et al*. and Morton *et al*. argued that orthoperiodate is not the final decomposition product, which can further decompose into metal oxide, I_2, and O_2[26,27]. Therefore, based on the T-Jump/TOFMS analysis, it is proposed that $Mg(IO_3)_2$, $Ca(IO_3)_2$, and $LiIO_3$ follow pathway α, while $NaIO_3$ and KIO_3 follow pathway β.

$$\{Mg(IO_3)_2, Ca(IO_3)_2, \text{and } LiIO_3\} \quad MIO_3 \rightarrow MO + O_2 + I_2 \qquad (\alpha)$$

$$\{NaIO_3 \text{ and } KIO_3\} \quad MIO_3 \rightarrow MI + O_2 \qquad (\beta)$$

where M=metal. It is also noteworthy that metal ions are present for alkali metal iodates (Li, Na, and K for $LiIO_3$, $NaIO_3$, and KIO_3, respectively), while for alkaline metal iodates, the peaks of their metal ions are absent. These metal signatures indicate the formation of metal iodides because the iodides are more volatile than oxides, which is due to the lower melting and boiling points of alkali metal iodides compared to their corresponding oxides, as evident in Table S1. O_2 and I release profiles of $Mg(IO_3)_2$, $Ca(IO_3)_2$, and $LiIO_3$ are displayed in Figure 8-2 (c)-(e) and these temporal profiles suggest that O_2 and I are released at the same temperature for all the three iodates, which will be discussed further in the subsequent sections. O_2 and I release profiles of $NaIO_3$ and KIO_3 displayed in Figure 8-2 (f) and (g) demonstrate the low intensity of I release over time.

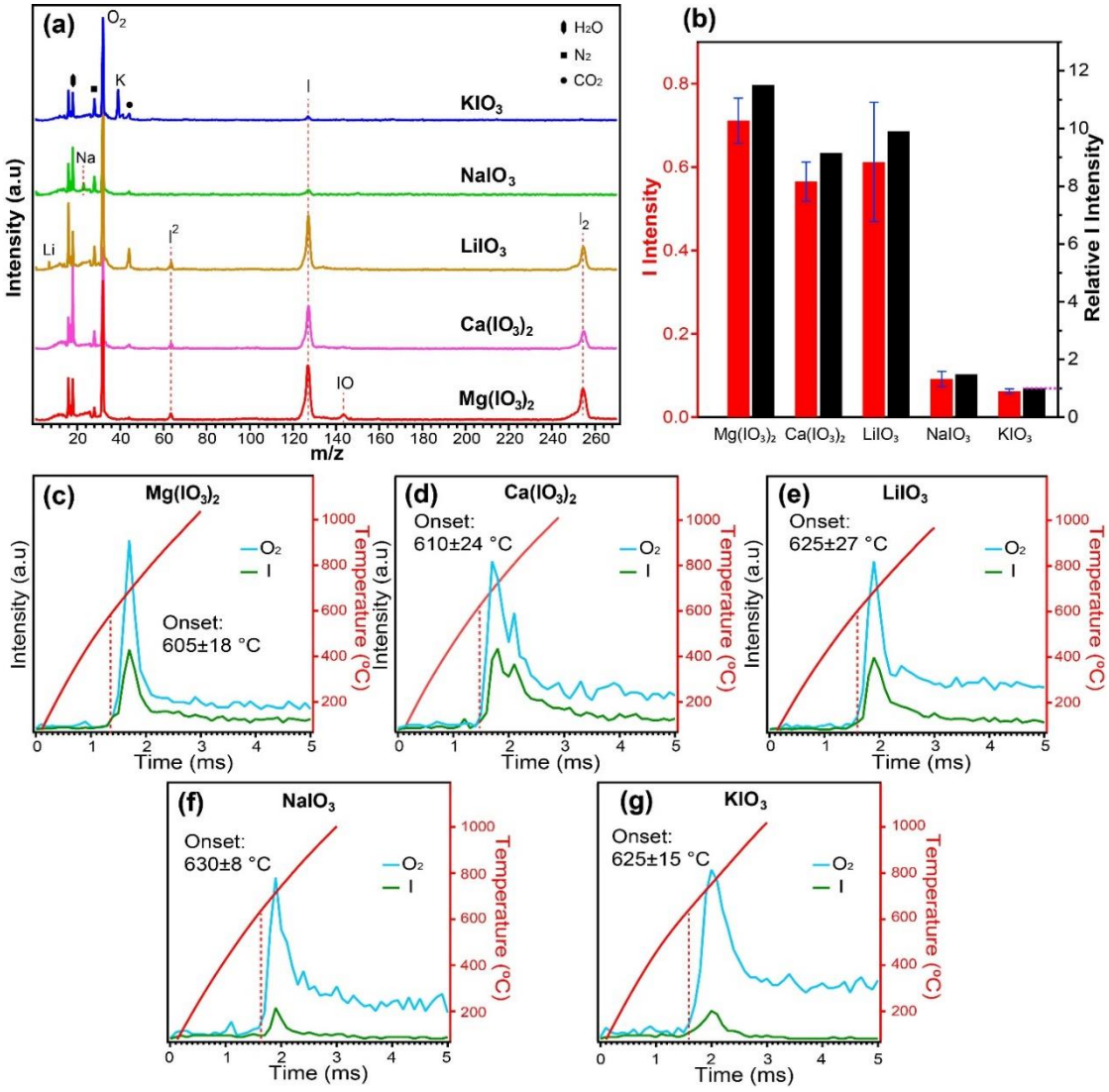

Figure 8-2 Mass spectrum of rapidly heated alkali and alkaline metal iodates (a). Most notable mass species are labeled. The measured I release of these iodates and their relative intensity to KIO_3 (b). O_2 and I release over time and the corresponding heating profile of $Mg(IO_3)_2$ (c), $Ca(IO_3)_2$ (d), $LiIO_3$ (e), $NaIO_3$ (f), and KIO_3 (g). The onset release temperature averaged over a minimum of three experiments is labeled.

8.4.2 Thermochemical analysis under slow heating rate (10 K/min)

Thermochemical analysis of the metal iodates is performed by slow heating TGA/DSC in an argon environment for supplementing the lack of gravimetric and calorimetric diagnostics from T-Jump/TOFMS. XRD is utilized to analyze the condensed

phase products around featured temperature points of decomposition identified by TGA/DSC. TGA/DSC result and temperature dependent XRD analysis of $Mg(IO_3)_2$ are displayed in Figure 8-3.

A two-step decomposition of $Mg(IO_3)_2$ is proposed by Ito *et al*., where magnesium orthoperiodate ($Mg_5(IO_6)_2$) is produced from the first step while MgO is formed after the second step, and I_2 and O_2 are released at each step, as shown in Equation (1) and (2)[26]. However, the verification of the decomposition products of each step is lacking.

$$Mg(IO_3)_2 = 0.2\ Mg_5(IO_6)_2 + 0.8\ I_2 + 1.8\ O_2 \quad (1)$$

$$0.2\ Mg_5(IO_6)_2 = MgO + 0.2\ I_2 + 0.7\ O_2 \quad (2)$$

The DSC in Figure 8-3 (a) reveals that $Mg(IO_3)_2$ does indeed follow a two-step decomposition process, although this two-step is not as evident in TGA. The measured mass losses of 71.9% and 89.6% after the first and the second step decomposition, respectively, are very close to the theoretical mass loss of $Mg(IO_3)_2$ at 69.7% and 89.3% predicated from Equation (1) and (2), respectively. Also, as mentioned in 8.4.1, I_2 and O_2 are released at the same temperature for $Mg(IO_3)_2$ from T-Jump TOFMS (Figure 8-2 (c)), consistent with the proposed mechanism. XRD analysis of the solid-state products collected after each step in Figure ***8-3*** (b) illuminates that $Mg_5(IO_6)_2$ is formed at the end of the first decomposition step (650 °C), although MgO is also detected, indicating a portion of $Mg_5(IO_6)_2$ is further decomposed. After the second step (680 °C), MgO is produced. This analysis verifies the decomposition of $Mg(IO_3)_2$ follows Equation (1) and

(2), and the overall decomposition is consistent with the decomposition route (pathway (α)) proposed in 8.4.1.

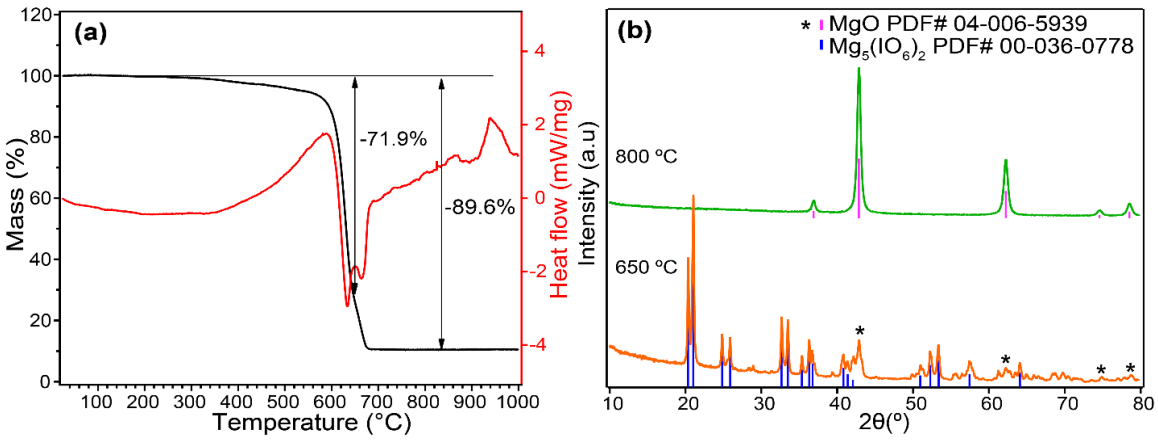

Figure 8-3 TGA/DSC of $Mg(IO_3)_2$ under and argon environment (a), and temperature dependent XRD analysis of $Mg(IO_3)_2$ heated products (b).

Figure 8-4 (a) displays the TGA/DSC for the decomposition of $Ca(IO_3)_2$ as well as the XRD analysis of the solid product collected by the end of each mass loss step. Similar to $Mg(IO_3)_2$, $Ca(IO_3)_2$ demonstrates the previously documented two-step decomposition[27], and these two steps are shown in Equation (3) and (4).

$$Ca(IO_3)_2 = 0.2\ Ca_5(IO_6)_2 + 0.8\ I_2 + 1.8\ O_2 \quad (3)$$

$$0.2\ Ca_5(IO_6)_2 = CaO + 0.2\ I_2 + 0.7\ O_2 \quad (4)$$

The measured mass loss of 64.5% after the first decomposition step is close to the theoretically predicted mass loss of 66.9%, and the measured mass loss of 85.4% after the second decomposition step is nearly identical to the theoretically predicted mass loss of 85.6%. XRD analysis reveals that $Ca_5(IO_6)_2$ is produced after the first decomposition step (640 °C) while the final product is CaO (740 °C). These results, combined with the

observation that I_2 and O_2 are released at the same temperature from T-Jump TOFMS (Figure 8-2 (d)), confirm that the decomposition of $Ca(IO_3)_2$ is consistent with the two-step decomposition mechanism.

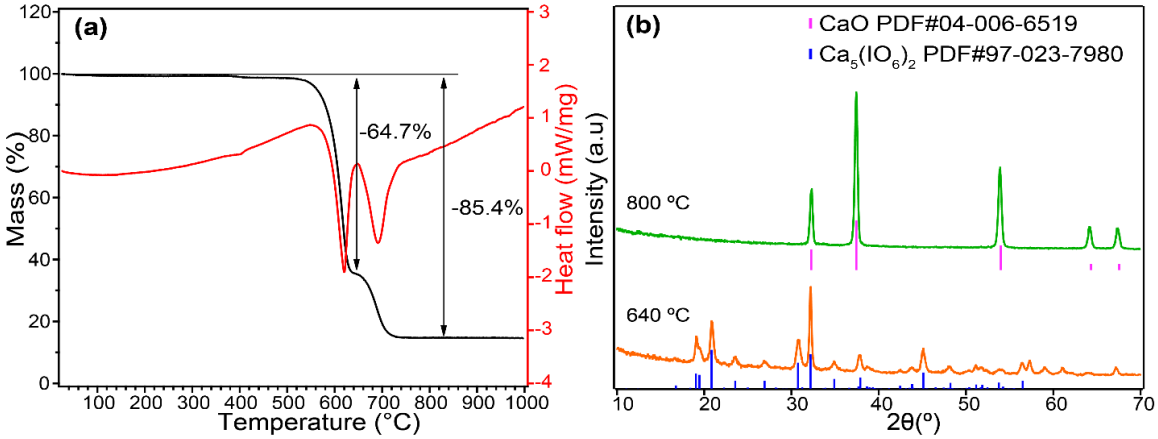

Figure 8-4 TGA/DSC of $Ca(IO_3)_2$ under and argon environment (a), and temperature dependent XRD analysis of $Ca(IO_3)_2$ heated products (b).

As discussed in 8.4.1, $LiIO_3$, $Mg(IO_3)_2$, and $Ca(IO_3)_2$ demonstrate a similar decomposition characteristic from the T-Jump TOFMS analysis (Figure 8-2), therefore it is proposed that the decomposition of $LiIO_3$ follows the two steps represented in Equation (5) and (6) based on the decomposition process of $Mg(IO_3)_2$ and $Ca(IO_3)_2$.

$$LiIO_3 = 0.2\ Li_5IO_6 + 0.4\ I_2 + 0.9\ O_2 \quad (5)$$

$$0.2\ Li_5IO_6 = 0.5\ Li_2O + 0.1\ I_2 + 0.35\ O_2 \quad (6)$$

Figure 8-5 displays the TGA/DSC of $LiIO_3$ as well as XRD analysis of temperature dependent decomposition products of $LiIO_3$. TGA/DSC of $LiIO_3$, as displayed in Figure 8-5 (a), shows a two-step mass loss process. The measured mass loss at the end of each step is 70.8% and 92.5%, respectively, which are approximate to the predicted theoretical

mass loss of 71.7% and 91.8% according to Equation (5) and (6), respectively. XRD analysis reveals that the solid product collected after the first decomposition (650 °C) is Li_5IO_6, consistent with the expectation from Equation (5). The product from the second step that ends at 870 °C is a mixture of Li_2O, LiI, and undecomposed Li_5IO_6. While Li_2O and undecomposed Li_5IO_6 are expected to form based on Equation (6), the presence of LiI suggests a different decomposition pathway from $Mg(IO_3)_2$ and $Ca(IO_3)_2$, whose final decomposition product does not contain MgI_2 and CaI_2, respectively. This difference will be discussed in more details in the subsequent section.

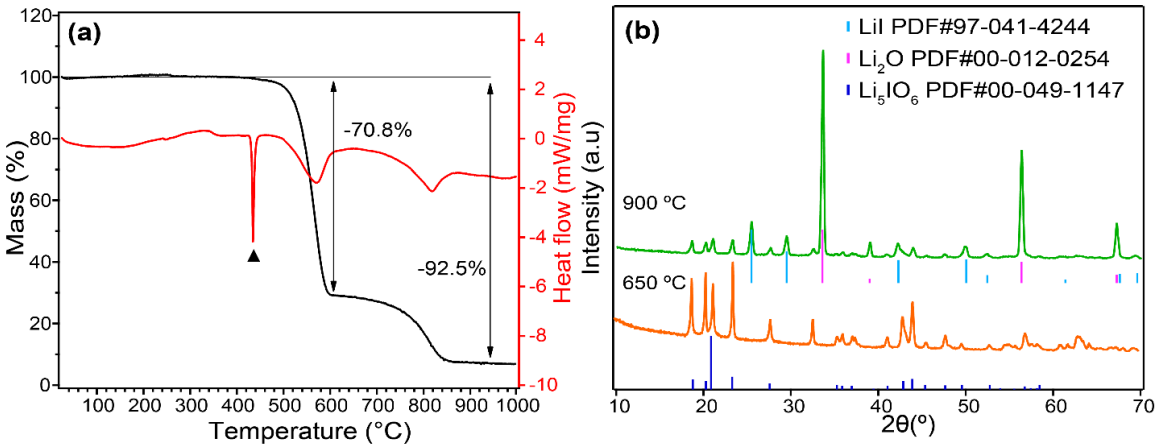

Figure 8-5 TGA/DSC of $LiIO_3$ under and argon environment (a), and temperature dependent XRD analysis of $LiIO_3$ heated products (b). ▲indicates melting of $LiIO_3$[20].

It has been demonstrated from T-Jump TOFMS, TGS/DSC, and XRD analysis that the decomposition of $LiIO_3$, $Mg(IO_3)_2$, and $Ca(IO_3)_2$ occur via two steps, with the first step forming metal orthoperiodate, I_2 and O_2, and the second step producing metal oxide, I_2 and O_2. $NaIO_3$ and KIO_3 are expected to follow a different decomposition pathway as they produce minimal I_2 during decomposition from the T-Jump TOFMS analysis (Figure 8-2). TGA/DSC of $NaIO_3$, as displayed in Figure 8-6, shows multiple-stepped mass loss. XRD

analysis shows that the solid residue collected at the end of the first mass loss step (575 °C) is NaI. The attempt to collect residue at 900 °C was unsuccessful. The formation of NaI and the absence of intense I_2 peak from T-Jump TOFMS (Figure 8-2) suggest the following decomposition of $NaIO_3$:

$$NaIO_3 = NaI + 1.5\ O_2 \quad (7)$$

Additionally, I observe Na peak from T-Jump/TOFMS (Figure 8-2), which also indicates NaI formation. The theoretical mass loss based on Equation (7) is 24.4%, which is much lower than the measured first step mass loss of 53.7%, and this is attributed to the sublimation of NaI[28,29]. The mass loss after the first step is attributed to the evaporation of NaI, whose TGA/DSC shows rapid mass loss after the melting point at 661.6 °C (Figure S2).

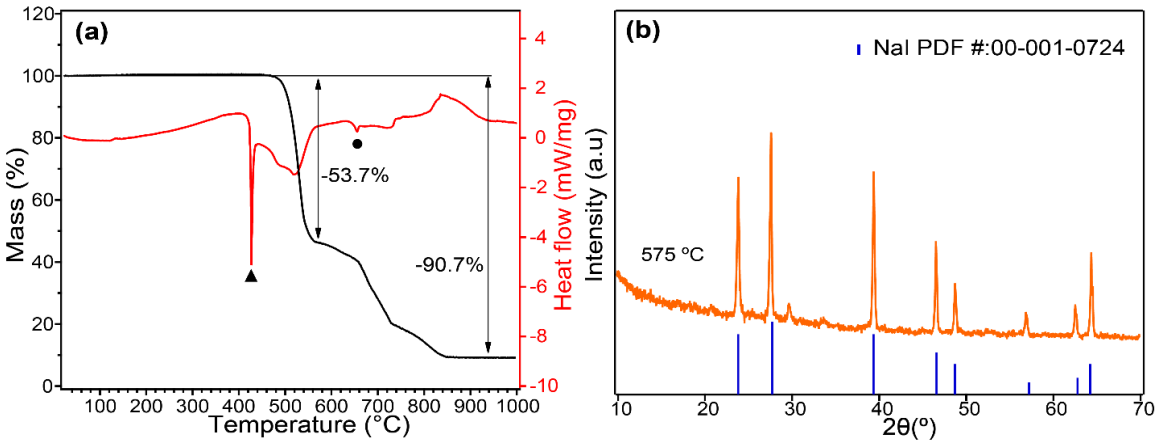

Figure 8-6 TGA/DSC of $NaIO_3$ under and argon environment (a), and temperature dependent XRD analysis of $NaIO_3$ heated products (b). ▲indicates melting of $NaIO_3$ and ● indicates melting of produced NaI[20,30].

KIO_3 displays a similar decomposition mechanism to $NaIO_3$ based on the presence of metal ion peak and minimal release of iodine, as shown in Figure 8-2. Therefore I expect the following decomposition pathway for KIO_3:

$$KIO_3 = KI + 1.5\ O_2 \quad (8)$$

TGA/DSC of KIO_3 displays a two-stepped mass loss (Figure 8-7 (a)). The measured mass loss of the first step that ends at 585 °C is 22.4%, which is the same with the theoretical mass loss of 22.4% predicted from Equation (8). XRD analysis (Figure 8-7 (b)) of decomposition product after the first mass loss step reveals the formation of KI. The second mass loss step in TGA/DSC is attributed to the evaporation of KI[31].

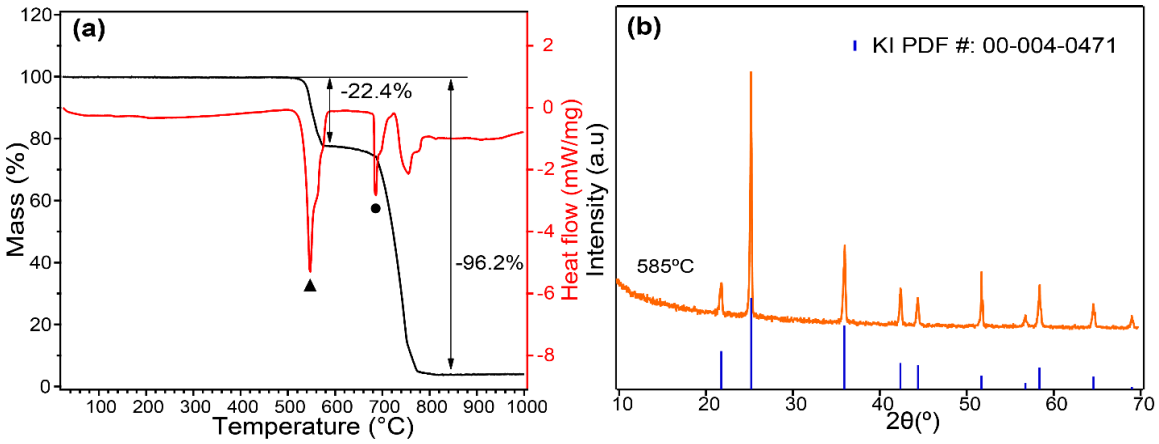

Figure 8-7 TGA/DSC of KIO_3 under and argon environment (a), and temperature dependent XRD analysis of KIO_3 heated products (b). ▲indicates melting of KIO_3 and ● indicates melting of produced KI[20,30].

8.4.3 Thermodynamic prediction of iodate decomposition mechanism

Gibbs free energy change determines whether a reaction is feasible. A negative Gibbs free energy indicates a spontaneous reaction[31]. Decomposition of metal iodates can follow pathway α, which produces metal oxide, O_2, and I_2, or β, which leads to metal iodide

and O_2. For simplicity, all the calculations for Gibbs free energy change is performed with standard values of ΔH and ΔS at room temperature. All the calculated values of ΔG are positive as none of the iodates decompose at room temperature, as shown in Figure S3. The decomposition temperatures of both pathways are estimated, assuming ΔG is 0, while ΔH and ΔS are held constant. These estimated decomposition temperatures are then normalized to the measured decomposition temperatures from T-Jump MS and are displayed in Figure 8-8. For $Mg(IO_3)_2$ and $Ca(IO_3)_2$, the estimated decomposition temperature of pathway α is lower than pathway β, suggesting that pathway α is more favorable. This finding is consistent with the observations from T-Jump TOFMS, TGA/DSC and XRD. In the case of $NaIO_3$ and KIO_3, pathway β is the more favorable due to its significantly lower estimated decomposition temperature than pathway α, which is also supported by evidence from T-Jump TOFMS, TGA/DSC and XRD. However, for $LiIO_3$, the estimated decomposition temperature of pathway α is higher than pathway β, indicating that pathway β is more favorable. This contradicts the experimental result demonstrating that pathway α is more feasible. This discrepancy is not well understood. Overall, the trend is clear that as the metal descends within the same group, from Mg to Ca and Li to K, the estimated decomposition temperature of pathway α increases, while the calculated decomposition temperature of pathway β decreases. Consequently, pathway α becomes less favorable while pathway β becomes more favorable as metal moves downward in the same group. A similar argument can be made that when metal moves rightward in the same period, from Na to Mg and K to Ca, pathway β becomes less favorable while pathway α becomes more favorable.

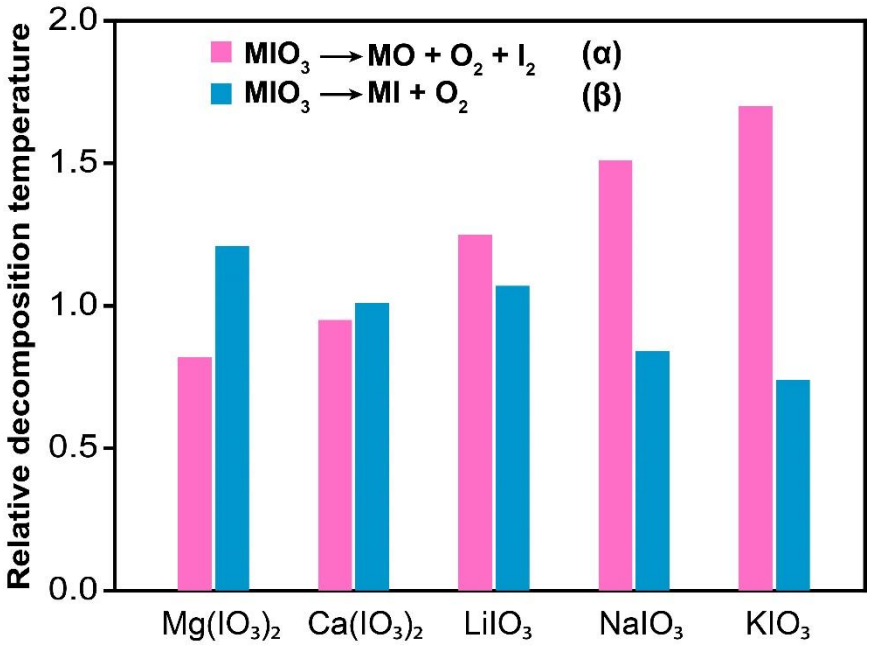

Figure 8-8 Calculated decomposition temperature of metal iodates assuming Gibbs free energy change being zero at room temperature relative to the measured decomposition temperature from T-Jump MS for different decomposition pathways. More details about the calculation can be found in Table S2.

8.5 Conclusions

This study investigates the decomposition mechanism of alkali and alkaline metal iodates ($LiIO_3$, $NaIO_3$, KIO_3, $Mg(IO_3)_2$, and $Ca(IO_3)_2$). T-Jump TOFMS demonstrates that all iodates release O, but not all iodates release I_2. $Mg(IO_3)_2$, $Ca(IO_3)_2$, and $LiIO_3$ release significant amount of I_2, while $NaIO_3$ and KIO_3 have minimal I_2 release. TGA/DSC measurement of metal iodates and XRD analysis of the temperature dependent condensed phase species reveals that the decomposition of these metal iodates follows different pathways. $Mg(IO_3)_2$, $Ca(IO_3)_2$, and $LiIO_3$ follow a two-step decomposition pathway: (1) Decomposition from metal iodates (MIO_3. M=Mg, Ca, and Li) into metal orthoperiodate ($M_x(IO_6)_y$) with I_2 and O_2 release, and (2) decomposition from metal orthoperiodate to

metal oxide (MO) with I_2 and O_2 release. $NaIO_3$ and KIO_3 follow a one-step decomposition pathway, where they decompose into NaI and KI, respectively, with O_2 release. Thermodynamic predictions of decomposition pathways are made by comparing decomposition temperatures estimated from thermodynamic data, and these estimations roughly predict the decomposition pathway of the investigated metal iodates. This study reveals that not all metal iodates are potential candidates for biocidal application and provides a simple strategy to predict the feasibility of I_2 release from metal iodates.

8.6 References

(1) Gray, M. J.; Wholey, W.-Y.; Jakob, U. Bacterial Responses to Reactive Chlorine Species. *Annu. Rev. Microbiol.* **2013**, *67*, 141–160. https://doi.org/10.1146/annurev-micro-102912-142520.

(2) Chang, J.; Zhao, G.; Zhao, X.; He, C.; Pang, S.; Shreeve, J. M. New Promises from an Old Friend: Iodine-Rich Compounds as Prospective Energetic Biocidal Agents. *Acc. Chem. Res.* **2021**, *54* (2), 332–343. https://doi.org/10.1021/acs.accounts.0c00623.

(3) Kaiho, T. *Iodine Chemistry and Applications*; John Wiley & Sons, 2014.

(4) Hu, X.; DeLisio, J. B.; Li, X.; Zhou, W.; Zachariah, M. R. Direct Deposit of Highly Reactive Bi(IO3)3- Polyvinylidene Fluoride Biocidal Energetic Composite and Its Reactive Properties. *Adv. Eng. Mater.* **2017**, *19* (1), 1500532. https://doi.org/10.1002/adem.201500532.

(5) Wang, H.; Jian, G.; Zhou, W.; DeLisio, J. B.; Lee, V. T.; Zachariah, M. R. Metal Iodate-Based Energetic Composites and Their Combustion and Biocidal Performance. *ACS Appl. Mater. Interfaces* **2015**, *7* (31), 17363–17370. https://doi.org/10.1021/acsami.5b04589.

(6) Wheelis, M. *Deadly Cultures: Biological Weapons Since 1945*; Harvard University Press, 2006.

(7) Aly, Y.; Zhang, S.; Schoenitz, M.; Hoffmann, V. K.; Dreizin, E. L.; Yermakov, M.; Indugula, R.; Grinshpun, S. A. Iodine-Containing Aluminum-Based Fuels for Inactivation of Bioaerosols. *Combust. Flame* **2014**, *161* (1), 303–310. https://doi.org/10.1016/j.combustflame.2013.07.017.

(8) Wang, S.; Abraham, A.; Zhong, Z.; Schoenitz, M.; Dreizin, E. L. Ignition and Combustion of Boron-Based Al·B·I2 and Mg·B·I2 Composites. *Chem. Eng. J.* **2016**, *293*, 112–117. https://doi.org/10.1016/j.cej.2016.02.071.

(9) Zhang, S.; Schoenitz, M.; Dreizin, E. L. Iodine Release, Oxidation, and Ignition of Mechanically Alloyed Al−I Composites. *J. Phys. Chem. C* **2010**, *114* (46), 19653–19659. https://doi.org/10.1021/jp108171k.

(10) Grinshpun, S. A.; Adhikari, A.; Yermakov, M.; Reponen, T.; Dreizin, E.; Schoenitz, M.; Hoffmann, V.; Zhang, S. Inactivation of Aerosolized Bacillus Atrophaeus (BG) Endospores and MS2 Viruses by Combustion of Reactive Materials. *Environ. Sci. Technol.* **2012**, *46* (13), 7334–7341. https://doi.org/10.1021/es300537f.

(11) Zhang, S.; Badiola, C.; Schoenitz, M.; Dreizin, E. L. Oxidation, Ignition, and Combustion of Al·I2 Composite Powders. *Combust. Flame* **2012**, *159* (5), 1980–1986. https://doi.org/10.1016/j.combustflame.2012.01.004.

(12) Martirosyan, K. S.; Wang, L.; Luss, D. Novel Nanoenergetic System Based on Iodine Pentoxide. *Chem. Phys. Lett.* **2009**, *483* (1), 107–110. https://doi.org/10.1016/j.cplett.2009.10.038.

(13) R. Clark, B.; L. Pantoya, M. The Aluminium and Iodine Pentoxide Reaction for the Destruction of Spore Forming Bacteria. *Phys. Chem. Chem. Phys.* **2010**, *12* (39), 12653–12657. https://doi.org/10.1039/C0CP00473A.

(14) Xu, F.; Biswas, P.; Nava, G.; Schwan, J.; Kline, D. J.; Rehwoldt, M. C.; Mangolini, L.; Zachariah, M. R. Tuning the Reactivity and Energy Release Rate of I2O5 Based Ternary Thermite Systems. *Combust. Flame* **2021**, *228*, 210–217. https://doi.org/10.1016/j.combustflame.2020.12.047.
(15) Johnson, C. E.; Higa, K. T. Iodine-Rich Biocidal Reactive Materials. *MRS Online Proc. Libr.* **2013**, *1521* (1), 307. https://doi.org/10.1557/opl.2013.46.
(16) Wang, H.; Kline, D. J.; Rehwoldt, M.; Zachariah, M. R. Ignition and Combustion Characterization of Ca(IO3)2-Based Pyrotechnic Composites with B, Al, and Ti. *Propellants Explos. Pyrotech.* **2018**, *43* (10), 977–985. https://doi.org/10.1002/prep.201800041.
(17) Sullivan, K. T.; Piekiel, N. W.; Chowdhury, S.; Wu, C.; Zachariah, M. R.; Johnson, C. E. Ignition and Combustion Characteristics of Nanoscale Al/AgIO3: A Potential Energetic Biocidal System. *Combust. Sci. Technol.* **2010**, *183* (3), 285–302. https://doi.org/10.1080/00102202.2010.496378.
(18) Zhou, W.; DeLisio, J. B.; Wang, X.; Zachariah, M. R. Reaction Mechanisms of Potassium Oxysalts Based Energetic Composites. *Combust. Flame* **2017**, *177*, 1–9. https://doi.org/10.1016/j.combustflame.2016.05.024.
(19) Wu, T.; SyBing, A.; Wang, X.; Zachariah, M. R. Aerosol Synthesis of Phase Pure Iodine/Iodic Biocide Microparticles. *J. Mater. Res.* **2017**, *32* (4), 890–896. https://doi.org/10.1557/jmr.2017.6.
(20) Wang, Y.; Wang, H.; Xu, F.; Ghildiyal, P.; Zachariah, M. R. Effect of Alkali Metal Perchlorate and Iodate Type on Boron Ignition: The Role of Oxidizer Phase Change. *Chem. Eng. J.* **2022**, *446*, 136786. https://doi.org/10.1016/j.cej.2022.136786.
(21) Wang, H.; DeLisio, J. B.; Wu, T.; Wang, X.; Zachariah, M. R. One-Step Solvent-Free Mechanochemical Synthesis of Metal Iodate Fine Powders. *Powder Technol.* **2018**, *324*, 62–68. https://doi.org/10.1016/j.powtec.2017.10.024.
(22) Jian, G.; Piekiel, N. W.; Zachariah, M. R. Time-Resolved Mass Spectrometry of Nano-Al and Nano-Al/CuO Thermite under Rapid Heating: A Mechanistic Study. *J. Phys. Chem. C* **2012**, *116* (51), 26881–26887. https://doi.org/10.1021/jp306717m.
(23) Jian, G.; Chowdhury, S.; Sullivan, K.; Zachariah, M. R. Nanothermite Reactions: Is Gas Phase Oxygen Generation from the Oxygen Carrier an Essential Prerequisite to Ignition? *Combust. Flame* **2013**, *160* (2), 432–437. https://doi.org/10.1016/j.combustflame.2012.09.009.
(24) Rehwoldt, M. C.; Wang, Y.; Xu, F.; Ghildiyal, P.; Zachariah, M. R. High-Temperature Interactions of Metal Oxides and a PVDF Binder. *ACS Appl. Mater. Interfaces* **2022**, *14* (7), 8938–8946. https://doi.org/10.1021/acsami.1c20938.
(25) Stern, K. H. *High Temperature Properties and Thermal Decomposition of Inorganic Salts with Oxyanions*; CRC Press, 2000.
(26) Ito, N.; Obata, K.; Shindo, Y.; Hakuta, T.; Yoshitome, H. Catalytic Thermal Decomposition of Magnesium Iodate in the Presence of Metal Oxides or Carbon. *Thermochim. Acta* **1984**, *73* (1), 33–40. https://doi.org/10.1016/0040-6031(84)85174-6.
(27) Morton, R. C. B.; McKelvey, V. E. UNITED STATES DEPARTMENT OF THE INTERIOR.

(28) Hilpert, K. Vaporization of Sodium Iodide and Thermochemistry of (NaI)2(g) and (NaI)3(g): An Experimental and Theoretical Study. *Berichte Bunsenges. Für Phys. Chem.* **1984**, *88* (2), 132–139. https://doi.org/10.1002/bbpc.19840880211.
(29) Kotter, L. N.; Groven, L. J. Boron Carbide Based Biocide Compositions: A Study of Iodate Particle Size on Combustion and Iodine Output. *Propellants Explos. Pyrotech.* **2020**, *45* (3), 509–516. https://doi.org/10.1002/prep.201900278.
(30) Haynes, W. M. *CRC Handbook of Chemistry and Physics, 95th Edition.*; CRC Press: Hoboken, 2014.
(31) Smith, J. M.; Ness, H. C. V.; Abbott, M. *Introduction to Chemical Engineering Thermodynamics*; McGraw-Hill Education, 2005.

8.7 Supporting information

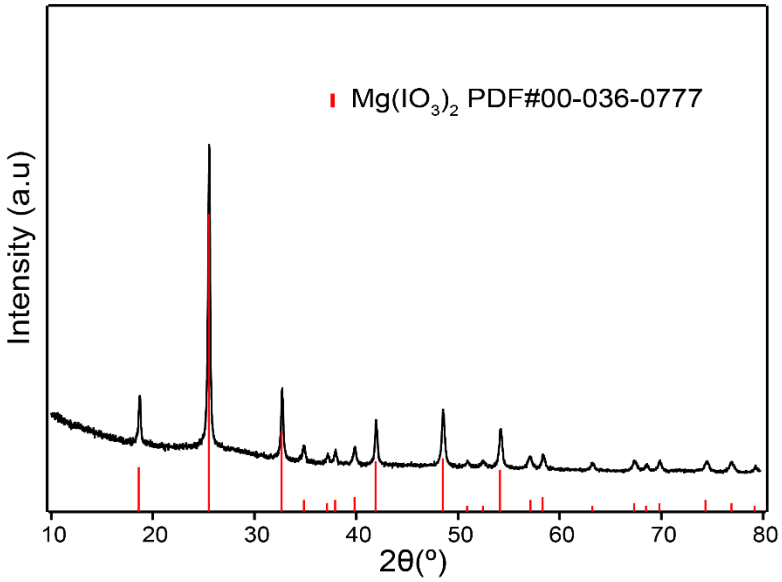

Figure S1 XRD of as-synthesized $Mg(IO_3)_2$ from ASP.

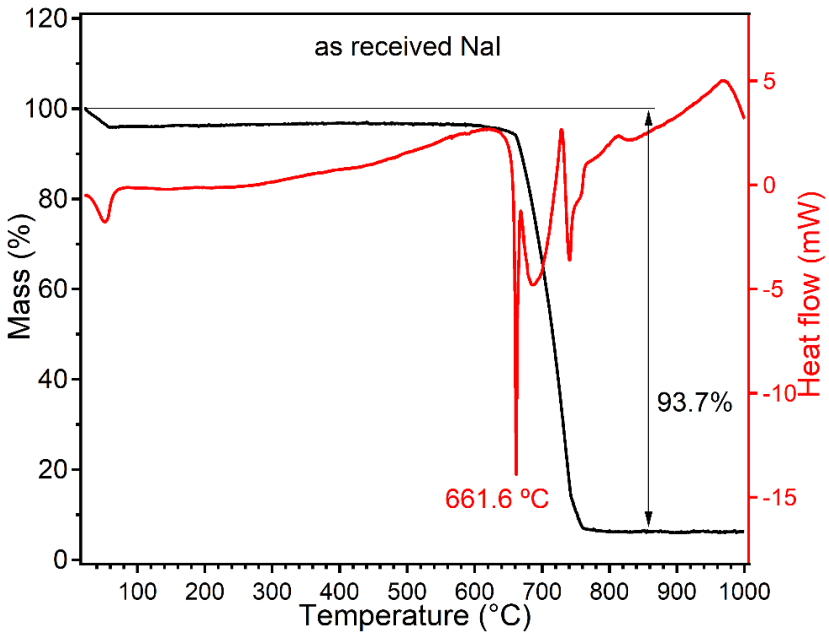

Figure S2 TGA/DSC of NaI.

Table S1 Physical properties

	Melting pointing (°C)	Boiling pointing (°C)
MgI_2	634 (2)	--
MgO	2825 (2)	3600 (2)
CaI_2	783 (2)	1100 (2)
CaO	2613 (2)	2853 (3)
LiI	469 (2)	1171 (2)
Li_2O	1438 (2)	2563 (4)
NaI	661 (2)	1304 (2)
Na_2O	1134 (2)	--
KI	681 (2)	1323 (2)
K_2O	740 (2)	--

Table S2 Thermodynamic data used for calculation

	$\Delta_f H°$ kJ·mol^{-1}	S° J·K^{-1}·mol^{-1}
$LiIO_3$	-503.4 (1)	151.5 *
$NaIO_3$	-481.8 (2)	151.5*
KIO_3	-501.4 (2)	151.5 (2)
$Ca(IO_3)_2$	-1002.5 (1)	230 (1)
$Mg(IO_3)_2$	-903.7 (5)	230 ^
Li_2O	-597.9 (2)	37.6 (2)
Na_2O	-414.2 (2)	75.1 (2)
K_2O	-361.5 (2)	94.1 (1)
CaO	-634.9 (2)	38.1 (2)
MgO	-601.6 (2)	27.0
LiI	-270.4 (2)	86.8 (2)
NaI	-287.8 (2)	98.5 (2)
KI	-327.9 (2)	106.3 (2)
CaI_2	-533.5 (2)	142 (2)
MgI_2	-364.0 (2)	129.7 (2)
O_2	0 (1)	205.15 (1)
I_2	0 (1)	116.14 (1)

* data cannot be found. The values are taken from KIO_3 assuming the entropy of $LiIO_3$, $NaIO_3$, and KIO_3 are the same.

^ data cannot be found. The values are taken from $Ca(IO_3)_2$ assuming the entropy of $Mg(IO_3)_2$ and $Ca(IO_3)_2$ are the same.

(1)http://course.sdu.edu.cn/G2S/eWebEditor/uploadfile/20120211220619_326063273396.pdf

(2) (CRC Handbook of Chemistry & Physics) William M. Haynes - CRC Handbook of Chemistry and Physics 2015-2016-CRC Press (2015)

(3) Ropp, R. C. Group 16 (O, S, Se, Te) alkaline earth compounds. Encyclopedia of the alkaline earth compounds (2013): 105-197.

(4) Kessinger, G. F., A. R. Jurgensen, D. M. Missimer, and J. S. Morrell. The high-temperature chemical reactivity of Li2O. Nuclear technology 171, no. 1 (2010): 108-122.

(5) BROWN, LC. "IODINE ON DEMAND." (2002).

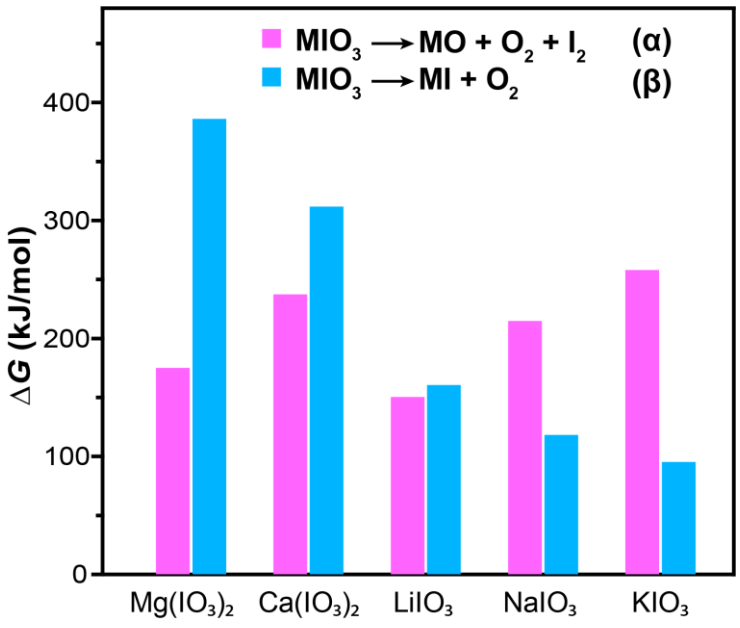

Figure S3 Calculated Gibbs free energy change of alkali and alkaline metal iodates with different decomposition pathways at room temperature. More details about the calculation can be found in Table S2.

9 Combustion Behavior of Aluminized Metal Iodate Composites. Part 2: Iodine and Energy Release Rate

9.1 Summary

Metal iodates are attractive oxidizers in the biocidal application due to their high oxygen and iodine content. In this study, I systematically investigate the iodine release, ignition, and reactivity of aluminized alkali and alkaline metal iodate thermites, namely Al-$Mg(IO_3)_2$, Al-$Ca(IO_3)_2$, Al-$LiIO_3$, Al-$NaIO_3$ and Al-KIO_3, as well as the combustion behavior of assembled high-loading aluminized metal iodate composites. Temperature-jump/time-of-flight mass spectrometry (T-Jump/TOFMS) results demonstrate that Al-$Mg(IO_3)_2$, Al-$Ca(IO_3)_2$, and Al-$LiIO_3$ release a substantial amount of iodine at approximately the same temperature, whereas Al-$NaIO_3$ and Al-KIO_3 exhibit minimal iodine release. In contrast, combustion cell result reveals that the reactivity of Al-$Mg(IO_3)_2$, Al-$Ca(IO_3)_2$, and Al-$LiIO_3$ is lower than Al-$NaIO_3$ and Al-KIO_3, indicating a trade-off between iodine release and reactivity among aluminized metal iodates. Iodine release rate, derived from the combination of T-Jump TOFMS and combustion cell data, reveals that Al-$Mg(IO_3)_2$ and Al-$Ca(IO_3)_2$ have significantly higher iodine release rates than Al-$LiIO_3$. Free-standing Al-metal iodate composites with nearly 50 wt% iodine content are successfully assembled by 3D printing and their combustion behaviors are characterized by high-speed videography and pyrometry for flame temperature measurement. It is found that only Al-$Ca(IO_3)_2$, Al-$LiIO_3$ and Al-$NaIO_3$ achieve complete propagation in an inert environment, and their microscopic combustion characteristics are similar. The propagation rate and flame temperature of Al-$Ca(IO_3)_2$ and Al-$LiIO_3$ are lower than Al-

$NaIO_3$, resulting in a higher energy release rate of Al-$NaIO_3$ compared to Al-$Ca(IO_3)_2$ and Al-$LiIO_3$, which suggests a trade-off between iodine release and energy release rate. This study demonstrates that, while not all aluminized metal iodate composites show promise in biocidal application, Al-$Ca(IO_3)_2$ and Al-$LiIO_3$ composites hold promise as biocidal agents due to their combined heat and iodine release capabilities.

9.2 Introduction

As discussed in Part 1 of this study[1], viruses, bacteria, formulated into weapons pose serious concerns. These threats necessitate a strategy for bioagent deactivation. One effective and environmentally friendly strategy for destroying microorganism is the application iodine as a disinfectant.[2–4] Nevertheless, the high vapor pressure of iodine often renders it inefficient and inconvenient to be implemented for destroying large-scale microorganism. An alternative strategy for bioagent deactivation is the employment of energetic materials for a thermal neutralization.[5–7] However, the disadvantage of this method is the likely incomplete neutralization as the thermal event is often short. To solve the problems and take advantage of both strategies, it has been proposed that, agent defeat weapons (ADWs), a new class of energetic material that releases large amounts of strong biocides after the delivery of a thermal event, could be effective in deactivation biological materials.[7–9]

Nanothermites, energetic composites typically consisting of metal fuel and oxidizer nanoparticles that undergo highly exothermic reaction upon ignition, have advantages of higher energy density and higher tunability over the conventional monomolecular CHNO

energetics.[10–18] Nanothermites are particularly well-suited for application of AWDs when a suitable iodine-releasing oxidizer is used. I_2O_5 is an attractive oxidizer for this purpose due to its high iodine and oxygen content, and various studies investigated the destruction of spore forming bacteria and energy release of energetic composites containing I_2O_5.[9,19,20] However, the practical application of I_2O_5 is limited by its hygroscopic properties. Metal iodates are potentially very attractive due to their high iodine content and strong oxidizing nature. Iodine release and combustion behavior of thermite with various metal iodates including $Cu(IO_3)_2$, $AgIO_3$, $Bi(IO_3)_2$, $Fe(IO_3)_2$, and $Ca(IO_3)_2$, have been investigated.[6,7,21,22] These studies reveal that not all metal iodates release I_2 during decomposition.

In part 1 of this work, a systematical study was performed on the decomposition mechanism of alkali and alkaline metal iodates ($LiIO_3$, $NaIO_3$, KIO_3, $Mg(IO_3)_2$, and $Ca(IO_3)_2$), which have high iodine and oxygen content. It was demonstrated that while the iodine in $LiIO_3$, $Mg(IO_3)_2$, and $Ca(IO_3)_2$ are released as I_2 during thermal decomposition, the iodine in $NaIO_3$ and KIO_3 are trapped as metal iodide, which has limited utility as a biocide. This study reveals that not all metal iodates are promising candidates in biocidal application and provides a simple thermodynamic calculation strategy to predict the feasibility of I_2 release of metal iodates.

A key step forward to real-world application is the fabrication of these metal iodates into composites with mechanical integrity at high loading to achieve high energy density and iodine content, as well as the subsequent combustion behavior of the composites. However, the fabrication of high loading nanothermite composites is limited by processing challenges due to the high viscosity, which makes the traditional casting methods unpractical.[13]

Additive manufacturing techniques such as 3D printing has attracted attention in energetic composite preparation due to its relative simplicity, customizability, and convenience.[13,23–25] Recently, free-standing composites with 90 wt% nanothermite loading were successfully prepared with 3D printing and their combustion behaviors were investigated.[13,23,26–28] Nevertheless, these studies mostly use a metal oxide as the oxidizer, and a systematic study focusing on the combustion behavior of high loading energetic composite with iodine-containing oxidizer is still lacking.

In this chapter, I utilize aluminum (Al), the most commonly used fuel due to its high energy density, ready availability, and high reactivity, as the fuel to study the iodine release, ignition, and reactivity of alkali and alkaline metal iodates ($LiIO_3$, $NaIO_3$, KIO_3, $Mg(IO_3)_2$, and $Ca(IO_3)_2$).[10,12,29] Temperature-jump time of flight mass spectrometry (T-Jump/TOFMS) and temperature-jump ignition (T-Jump ignition) are employed to analyze the iodine release and ignition behavior of aluminized metal iodate thermites, respectively. Combustion cell measurement is utilized to determine the reactivity of these thermites. More importantly, free-standing composites with 90 wt% loading of aluminized metal iodate thermites with iodine content as high as nearly 50 wt% are successfully prepared by 3D printing and their combustion behaviors are studied by high-speed videography and pyrometry.

9.3 Materials and Methods

9.3.1 Materials

$NaIO_3$ (99%) was obtained from Alfa Aesar. $LiIO_3$ (97%), KIO_3 (≥98%), $MgCl_2$ (≥98%), HIO_3 (≥99.5%), $Ca(NO_3)_2 \cdot 4H_2O$ (≥99%), and polyvinylidene fluoride (PVDF, average molecular weight: ~534,000) were purchased from Sigma Aldrich (Millipore Sigma). HPLC grade water, hexanes (99.9%), N, N dimethylformamide (DMF, 99.8%), and NaOH (≥97%) were purchased from Fisher Scientific. METHOCEL™ F4M Hydroxypropyl Methylcellulose (HPMC) was obtained from Dow Chemical Company. Aluminum nanoparticles (Al NPs, ~50 nm, 67 wt% active) were obtained from Argonide Corporation. The active content of Al NPs was determined utilizing thermogravimetry and differential scanning calorimetry (TGA−DSC, Netsch STA449 F3 Jupiter)[13,14].

9.3.2 Size reduction of alkali metal iodate particles

Size of as-received alkali metal iodates was reduced via ball milling with a Retsch CryoMill operated at ambient condition. Briefly, 0.75 g alkali metal iodate, ~0.75 ml hexanes, and three steel balls (7/32″ in diameter, obtained from GlenMills) were loaded into a plastic centrifuge tube (FisherBrand 2 mL) and then milled with a Retsch CryoMill operated at ambient conditions for 30 min at a frequency of 25.0 Hz for 10 mins. After settling for ~ 5 min for cooling, the sample was ball milled again for 10 mins. This process was repeated two more times so that the total milling time was 40 mins. Then the sample was transferred into a desiccator for drying. SEM (scanning electron microscope) images of the obtained samples are shown in Figure S1.

9.3.3 Synthesis of alkaline metal iodates

Details for the synthesis of $Ca(IO_3)_2$ micron particle can be found in our previous publication.[30] Briefly, 236 mg $Ca(NO_3)_2 \cdot 4H_2O$, 428 mg KIO_3, three alumina balls (7/32″ in diameter, purchased from GlenMills), and 0.5 mL ethanol were added to a centrifuge tube (FisherBrand, 2 mL) and milled for 20 min at a frequency of 25.0 Hz. The resultant suspension was centrifuged at 7000 rpm for 5 min. The obtained precipitate was washed three times with 30 mL water every time and then dried in a vacuum oven overnight for water removal. The dried solid powder was baked in a tube furnace at 350 °C for 40 min in air for the removal of crystal water. [22] SEM image of the obtained $Ca(IO_3)_2$ is shown in Figure S1.

Details of synthesizing $Mg(IO_3)_2$ can be found in Part 1[1]. SEM image of the synthesized $Mg(IO_3)_2$ is shown in Figure S1.

9.3.4 T-Jump ignition and TOFMS

The details of the T-Jump ignition and TOFMS tests can be found in our previous publications.[11,31,32] Briefly, Al nanoparticles and the corresponding amounts of metal iodates were physically mixed in hexane. Following 30 min of ultrasonication, a small amount of the suspension was coated on Pt wire (diameter=76 μm, 0.8-1.1 cm length, OMEGA Engineering Inc.), which was then resistively heated by a direct current voltage supply. Temperature readings of the Pt wire was obtained through calibrating with Callendar-Van Dusen equation. It is assumed the temperature of the thin coating on Pt wire is the same with temperature of the wire. A minimum of three tests were performed for every sample.

For T-Jump ignition tests, the samples were ignited inside a chamber filled with argon at 1 atm and the ignition process was recorded by a high-speed camera (Vision Research Phantom V12.1). The ignition delay time was determined from the obtained video as well as the measured wire temperature. For T-Jump TOFMS, a 70 eV electron gun ionizer was used for ionizing gas phase species produced from the sample inside the TOFMS chamber held at ~10^{-6} Torr. For both T-Jump ignition and TOFMS, measurements were repeated at least three times.

9.3.5 Combustion cell measurements

Reactivity of the Al-metal iodate thermites at stoichiometric ratio were evaluated in a constant volume combustion cell (~20 cm^3), from which PV/m (P is the maximum pressure, V is the volume of the combustion cell, and m is the mass for each measurement), pressurization rate, and burn time (half width of the optical signal) were evaluated. Details of combustion cell measurements can be found in our previous studies.[33,34] 25 mg of a thermite powder was used for each measurement, which was repeated with a minimum of three times in total.

As Part 1 demonstrated, these metal iodates have two decomposition mechanisms[1]. The amount of Al and metal iodate was determined from the following equations (Equation 1-5) for prescribing the stoichiometric ratio and are based on the decomposition paths I previously determined.

$$10Al + 3Mg(IO_3)_2 = 5Al_2O_3 + 3MgO + 3I_2 \quad (1)$$

$$10Al + 3Ca(IO_3)_2 = 5Al_2O_3 + 3CaO + 3I_2 \quad (2)$$

$$10Al + 6LiIO_3 = 5Al_2O_3 + 3Li_2O + 3I_2 \quad (3)$$

$$2Al + NaIO_3 = Al_2O_3 + NaI \quad (4)$$

$$2Al + KIO_3 = Al_2O_3 + KI \quad (5)$$

9.3.6 Preparation of ink and direct ink writing of 90 wt% loading aluminized metal iodate composites

The details of ink preparation and direct ink writing can be found in our previous publication.[13] Briefly, 4 wt% PVDF and 6 wt% HPMC were dissolved into DMF. Metal iodate was added to the solution and the obtained suspension was ultrasonicated for 30 min. Stoichiometric amount of Al nanoparticles was then added to the suspension and the obtained sample was ultrasonicated for 30 min and magnetically stirred overnight before printing with a printer (Hyrel System 30 M). For printing, the ink was extruded through an 18-gauge needle and directly written on a preheated (~75 °C) glass substrate with a pre-designed pattern. Each layer was ensured to be dried visibly before depositing the next layer. Following printing, the obtained films were heated for 30 min at ~75 °C for removing the residual solvent. The films were then cut into ~2 cm long sticks for combustion characterizations.

9.3.7 Microscopic and macroscopic imaging

The details of the imaging process can be found in our previous study.[35] Generally, two imaging systems were utilized for studying the combustion behavior of the printed composites. One imaging system was macroscopic imaging system with high-speed camera (Vision Research Phantom Miro M110) and the other one was microscopic imaging system that uses high-speed camera (Vision Research Phantom VEO710L) coupled with Infinity Photo-Optical Model K2 DistaMax. For a typical measurement, one stick was placed on a stage inside an argon filled chamber that was mounted between the two imaging systems. The stick was ignited with a Joule-heated nichrome wire and the combustion process was recorded with both imaging systems.

9.3.8 Three-color imaging pyrometry

The details of three-color imaging pyrometry can be found in our previous publications.[36–38] Briefly, three color (red, green, and blue) intensities from the Bayer filter and their ratios were utilized for measuring the flame temperature of a sample assuming graybody emission behavior of the sample. A blackbody source (Mikron M390) was used for obtaining calibration factors. The temperature uncertainty was estimated to be nominally 200-300 K.[28,38]

9.3.9 Scanning electron microscope

The morphology of the metal iodate micron particles as well as the cross section of the 3D-printed composites were characterized by scanning electron microscope (SEM, Thermo-Fisher Scientific NNS450).

9.4 Results and discussion

9.4.1 Time-of-flight mass spectrometry and ignition of Al-iodate thermites under rapid heating rate (~10^5 K/s)

T-Jump/TOFMS was used to analyze iodine release from the metal iodates with Al and the resulting mass spectra are shown in Figure 9-1 (a). As demonstrated in Part 1, alkali and alkaline metal iodates follow two different decomposition pathways: (1) decomposition into metal oxide, oxygen, and iodine, and (2) decomposition into metal iodide and oxygen[1]. $Ca(IO_3)_2$, $Mg(IO_3)_2$, and $LiIO_3$ follow pathway (1) while $NaIO_3$ and KIO_3 follow pathway (2). Therefore, upon thermal decomposition, $Ca(IO_3)_2$, $Mg(IO_3)_2$, and $LiIO_3$ release significant amount of iodine, while $NaIO_3$ and KIO_3 have minimal iodine release. Similar results are obtained with the addition of Al, where Al-$Ca(IO_3)_2$, Al-$Mg(IO_3)_2$, and Al-$LiIO_3$ release significantly higher amount of iodine than Al-$NaIO_3$ and Al-KIO_3. Semiquantitative analysis of the release behavior of I, a representative of I_2, was performed by measuring its intensity in different Al-iodate systems and relative intensity to Al-KIO_3. The results are shown in Figure 9-1 (b), which clearly demonstrates the iodine release difference and verifies that Al-$Ca(IO_3)_2$, Al-$Mg(IO_3)_2$, and Al-$LiIO_3$ are promising in biocidal application. One important evaluating parameter for biocidal energetics is the biocide release temperature, which is iodine in this case. Iodine release profiles of Al-$Ca(IO_3)_2$, Al-$Mg(IO_3)_2$, and Al-$LiIO_3$ displayed in Figure 9-1 (c)-(e) demonstrate that the iodine release temperature of these thermites are roughly the same. Such an analysis is not conduced on Al-$NaIO_3$ and Al-KIO_3 due to their low iodine release.

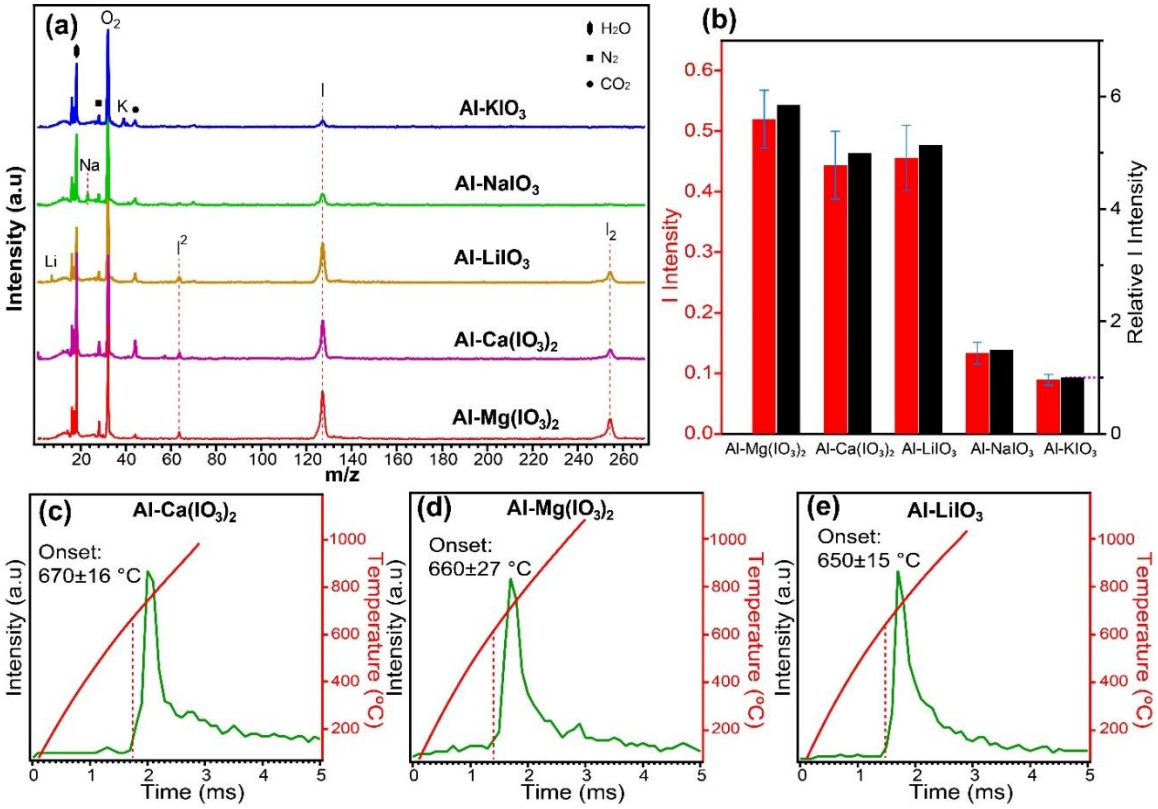

Figure 9-1 T-Jump/TOFMS spectrum of alkali and alkaline metal iodate with Al (a). Most notable mass species are labeled. The measured I intensities of the iodate with Al and their relative intensity to Al-KIO_3 (b). I release over time and the corresponding heating profile of Al-$Ca(IO_3)_2$ (c), Al-$Mg(IO_3)_2$ (d), and Al-$LiIO_3$ (e). The onset I release temperature averaged over a minimum of three experiments is labeled.

Ignition studies of Al with metal iodates were conducted in 1 atm argon and the representative snapshots of ignition are shown in Figure 9-2 (a). These results demonstrate that all the Al-iodate systems ignite in an inert environment, although Al-$Mg(IO_3)_2$ and Al-$LiIO_3$ have less vigorous flames. Figure 9-2 (b) displays the O_2 release onset temperature obtained from T-Jump TOFMS of metal iodates as well as ignition temperature of Al-iodate systems. Previous studies demonstrated that polymorphic phase change in alumina (~880 K, from amorphous to γ-Al_2O_3) causes accelerated outwardly diffusion of Al and

initiates the thermite reaction when gas-phase oxygen is readily available.[11,39] In the current study, O_2 release onset temperature of metal iodate and ignition temperature of Al-metal iodate are nearly the same at about 630 °C (~900 K) for all the thermites, which is slightly higher than the phase transition temperature of alumina at ~880 K, indicating the ignition is possibly limited by the availability of gaseous oxygen from metal iodate. The ignition temperature at about 630 °C is very close to the melting point of Al at 660 °C though. Therefore, it is also possible that the ignition is limited by the availability of Al from melting.

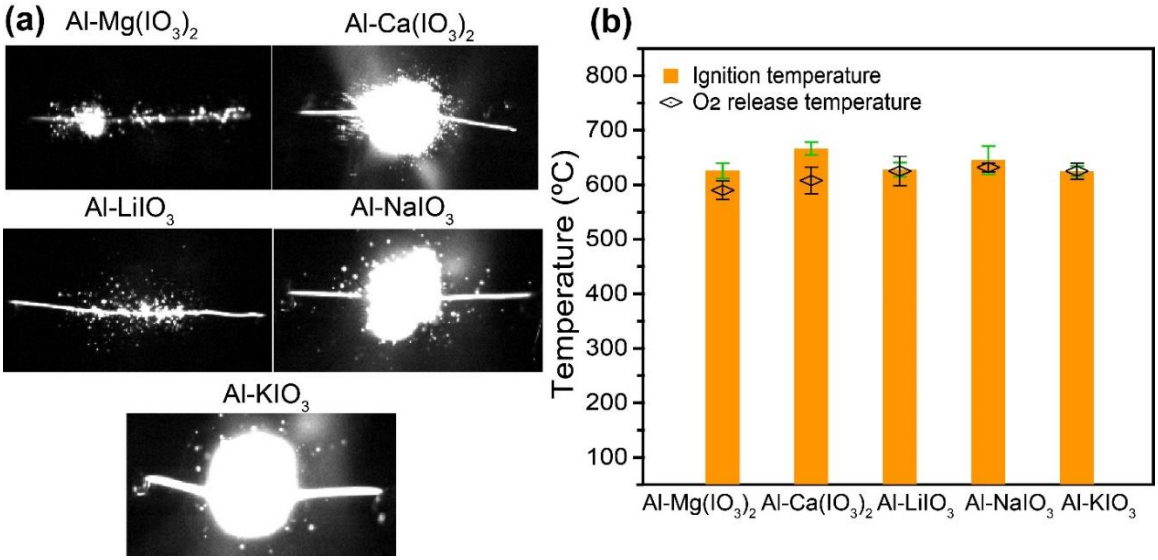

Figure 9-2 T-Jump ignition snapshots of Al with alkali and alkaline metal iodate (a). O_2-release onset temperature of metal iodate estimated from T-Jump/TOFMS and T-Jump ignition temperature of metal iodate with Al.

9.4.2 Reactivity and iodine release rate of Al-iodate thermites

Constant-volume cell measurements were conducted on the Al-iodate thermites to evaluate their reactivity and combustion characteristics including PV/m, pressurization rate, and burn time.[33] Figure 9-3 displays the combustion parameters of the Al with

different metal iodates. Al-$NaIO_3$ and Al-KIO_3 have significantly higher peak pressure and pressurization rate, shorter burn time as compared to Al-$Mg(IO_3)_2$, Al-$Ca(IO_3)_2$, and Al-$LiIO_3$, demonstrating their superior reactivity. These differences cannot be explained on the basis of energy density that are displayed in Figure 9-3 (d), which shows that differences are insignificant. It is well-known that particle size has significant effect on the reactivity of a thermite,[40–42] however Figure S1 shows that the particle size is similar among these metal iodates. Further I show in Figure 9-2 (b), that the onset temperature of O_2 release is roughly the same for all the metal iodates, suggesting that it is unlikely the contributing factor for the reactivity difference.

Another factor that influences the PV/m and pressurization rate is the amount of gas released during the combustion process. Equation (1-5) demonstrates that for Al-$Mg(IO_3)_2$, Al-$Ca(IO_3)_2$, and Al-$LiIO_3$, Al_2O_3, metal oxide, and I_2 are produced. The boiling point of Al_2O_3, MgO, CaO, Li_2O, and I_2 is 2967 °C, 3600 °C, 2853 °C, 2563 °C, and 184 °C, respectively,[43–46] The measured flame temperature of the 3D printed composite of Al-$Ca(IO_3)_2$ and Al-$LiIO_3$ below 1700 °C, which will be discussed further in 3.3, is significantly lower than the boiling point of Al_2O_3, CaO, Li_2O. This indicates that Al_2O_3, CaO, Li_2O will remain in the condensed phase, and the only gas product is I_2. A similar temperature comparison for Al-$Mg(IO_3)_2$ cannot be performed as the flame temperature of its printed composite cannot be obtained. However, MgO has much higher boiling point and Al-$Mg(IO_3)_2$ has similar reactivity to Al-$Ca(IO_3)_2$ and Al-$LiIO_3$. Therefore it is reasonable to speculate that MgO also remains in the condensed phase during combustion. This analysis indicates that the only gaseous product during combustion for Al-$Mg(IO_3)_2$,

Al-$Ca(IO_3)_2$, and Al-$LiIO_3$ is I_2. While for the combustion of Al-$NaIO_3$ and Al-KIO_3, Al_2O_3 and metal iodide are produced, and the boiling point of NaI and KI is 1304 °C and 1323 °C, respectively.[44] The measured flame temperature of 3D printed Al-$NaIO_3$ composite of ~ 2350 °C is much higher than the boiling point of NaI, which means NaI is gaseous during combustion. It is speculated that KI is also gaseous during combustion for Al-KIO_3 as the boiling point of KI is closed to NaI and the reactivity of Al-$NaIO_3$ and Al-KIO_3 is similar. Figure 9-3 (d) displays the relative amount of gas release during combustion for different thermite systems and shows Al-$NaIO_3$ and Al-KIO_3 have significantly higher amount of gas release compared to Al-$Mg(IO_3)_2$, Al-$Ca(IO_3)_2$, and Al-$LiIO_3$. This higher amount of gas release likely explains the higher PV/m and pressurization rate of Al-$NaIO_3$ and Al-KIO_3.

Al-$Mg(IO_3)_2$ and Al-$Ca(IO_3)_2$ have nearly the same reactivity as they have similar peak pressure, pressurization rate, and burn time. Al-$LiIO_3$ underperforms Al-$Mg(IO_3)_2$ and Al-$Ca(IO_3)_2$ although $LiIO_3$, $Mg(IO_3)_2$, and $Ca(IO_3)_2$ follow the same decomposition pathway and all the three thermites have similar energy density[1]. It is noteworthy that energy density of these thermite systems is calculated from the standard enthalpy of reaction at room temperature, which means endothermicity of phase change of the involved chemicals during combustion is not considered. Now a primary question arises: Why does Al-$LiIO_3$ has a lower reactivity than Al-$Mg(IO_3)_2$ and Al-$Ca(IO_3)_2$? As shown in Part 1[1], $Mg(IO_3)_2$ and $Ca(IO_3)_2$ decompose without a noticeable melting process, while $LiIO_3$ melts at 434 °C that corresponds to a sharp endothermic peak. [44] The endothermicity of $LiIO_3$ melting leads to less heat release during the combustion process. In addition, the condense

phase decomposition product of $Mg(IO_3)_2$, $Ca(IO_3)_2$, and $LiIO_3$ are MgO, CaO, and Li_2O, respectively. The melting point of Li_2O at 1438 °C is much lower than MgO and CaO at 2825 °C and 2613 °C, respectively.[44] The flame temperature is higher than the melting point of Li_2O for Al-$LiIO_3$ but lower than the melting point of CaO and MgO in the case of Al-$Mg(IO_3)_2$ and Al-$Ca(IO_3)_2$, respectively, which will be discussed further in 3.3. This means the Li_2O melts while MgO and CaO remain as solid during the combustion process. The endothermicity of Li_2O melting will result in a further reduction in heat release from the combustion of Al-$LiIO_3$ compared to Al-$Mg(IO_3)_2$ and Al-$Ca(IO_3)_2$. Therefore, although the theoretical energy release for Al-$Mg(IO_3)_2$, Al-$Ca(IO_3)_2$, and Al-$LiIO_3$ is comparable, the actual energy release of Al-$LiIO_3$ is lower due to the endothermic nature of melting $LiIO_3$ and Li_2O during combustion. This likely explains the lower reactivity of Al-$LiIO_3$ than Al-$Mg(IO_3)_2$ and Al-$Ca(IO_3)_2$.

Iodine release rate of an energetic composite is a critical factor for the application as biocidal agent, and different iodine release rate may be preferred in different circumstances.[2,21] Figure 9-3 (e) displays the relative iodine release rate for thermites with significant iodine release and demonstrates that the iodine release rate of Al-$Mg(IO_3)_2$ and $Ca(IO_3)_2$ is similar and dramatically higher than Al-$LiIO_3$. This result suggests that the iodine release rate of Al-based thermite can be manipulated simply by utilizing different iodates as oxidizer, or perhaps by making mixtures.

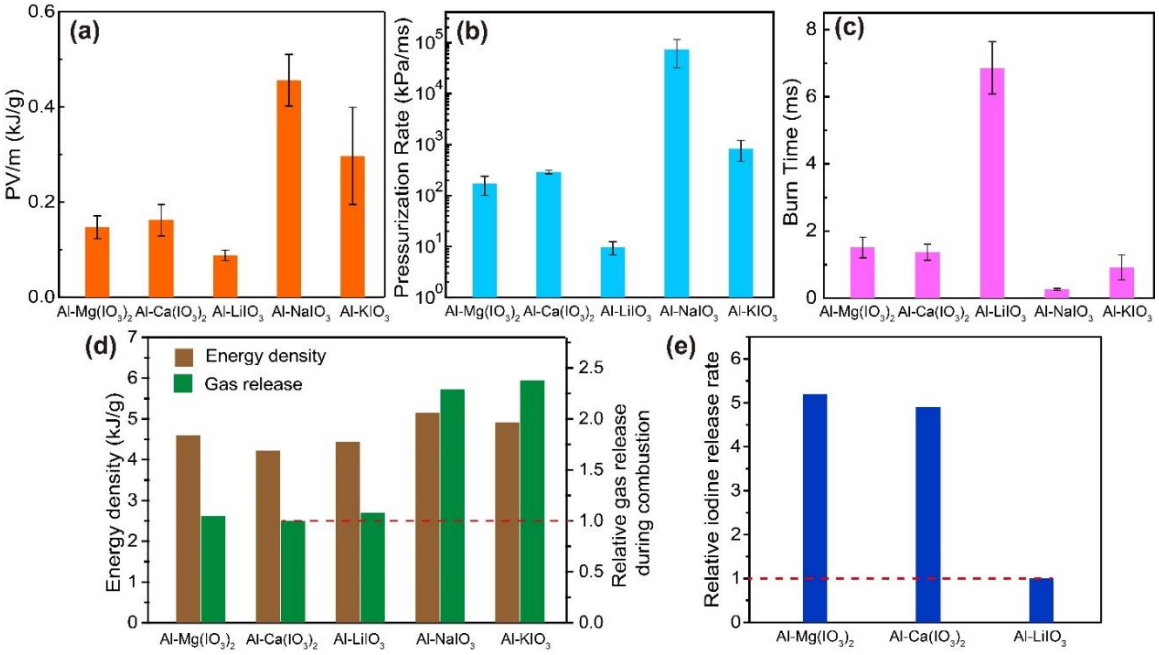

Figure 9-3 PV/m (a), pressurization rata (b), and burn time (c) of Al with different metal iodates. Combustion enthalpies of Al with different metal iodates at stoichiometric ratio as well as their relative amount of gas release to Al-$Ca(IO_3)_2$ during combustion (d).[47] Estimated relative iodine release rate of Al with different metal iodates based on the iodine release rate of Al-$LiIO_3$ (e). The iodine release rate is calculated via dividing the average iodine release intensity from TOFMS by the average burn time from pressure cell measurement.

9.4.3 Combustion performance of printed high loading Al-iodate composites

As mentioned above, fabrication of high particle loading composite with good mechanical properties is essential to obtain high energy density for real-world application.[23] All the Al-iodate thermites can be 3D printed into free-standing composites with 90 wt% thermite loading. The photo of a representative printed composite shows the smooth and crack-free surface and cross-section SEM images of all the printed composites are shown in Figure 9-4 (a). Iodine content and energy release rate are two key parameters in evaluating biocidal agent in addition to the aforementioned iodine release rate. These composites have high iodine content (nearly 50 wt%, as shown in Figure 9-4 (b)).

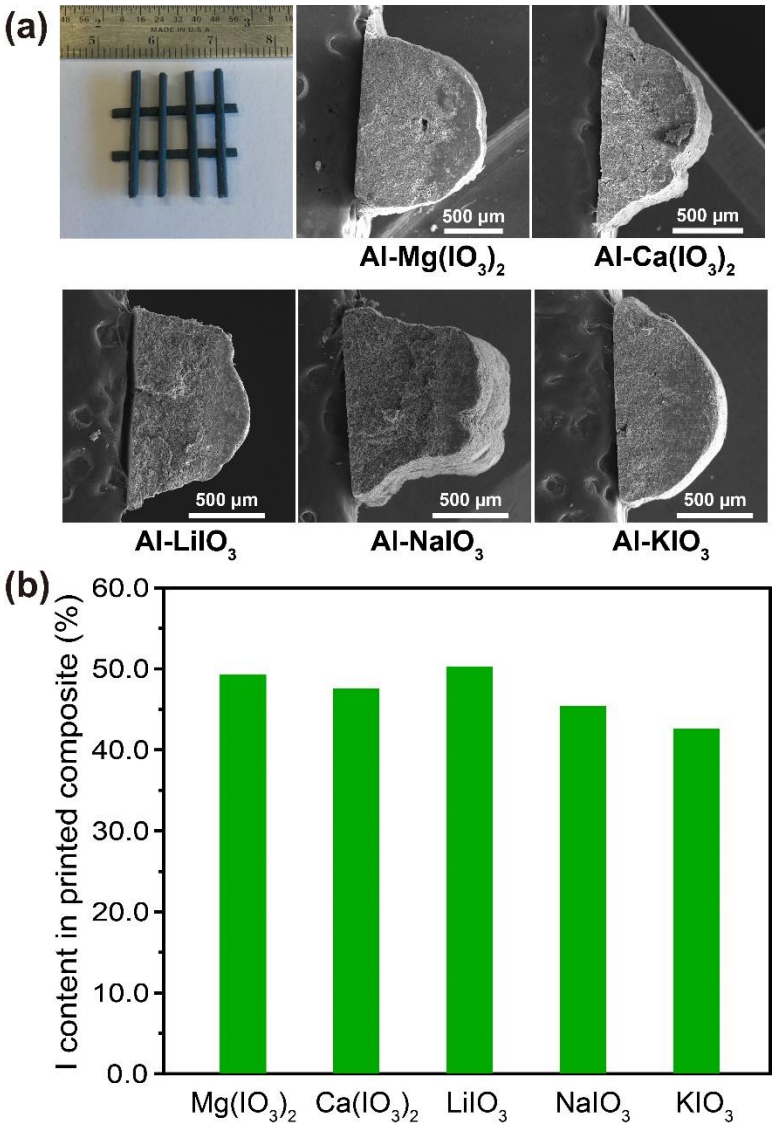

Figure 9-4 SEM cross-section of the assembled composites (a). Theoretically gravimetric iodine content in the printed composite of Al with metal iodates (b). Note: Inactive content of Al is not considered for this calculation.

Combustion behavior of the printed composites were investigated in argon (1 atm) with high-speed microscopic imaging and macroscopic imaging coupled with pyrometry.[26,35] Interestingly, although all the Al-iodate thermites ignite in argon (1 atm), not all the printed composites can fully propagate. Al-$Ca(IO_3)_2$, Al-$LiIO_3$, and Al-$NaIO_3$

composites propagate fully, while Al-$Mg(IO_3)_2$ and Al-KIO_3 composites have incomplete propagation. The feasibility of propagation does not follow the reactivity trend or the decomposition pathway of metal iodates and is not well understood.

For the composites that propagate fully in argon, the microscopic combustion characteristic is essentially the same, where Al droplet with dark cap (aluminum oxide) forms on the burning surface, as shown in Figure 9-5 (a). These droplets have a size of tens of micrometer and there is no significant size difference among different composites. It is worth noting that the initial Al particles incorporated into the composite is 50 nm, which suggests extensive sintering/agglomeration of Al occurs during the combustion process.[26] SEM images of the post-combustion product for Al-$Ca(IO_3)_2$, Al-$LiIO_3$, and Al-$NaIO_3$ shown in Figure S2 further confirm the similarity in agglomerate size among the three composites. SEM/EDS was utilized to analyze the element distribution of post-combustion product of Al-$Ca(IO_3)_2$ and Al-$NaIO_3$, as shown in Figure S3 and Figure S4, respectively. The presence of Na and I overlaps for Al-$NaIO_3$, suggesting the formation of NaI. While for Al-$Ca((IO_3)_2$, the presence of Ca overlaps with O instead of I, implying the formation of CaO. This is consistent to the proposed reaction in Equation (2) and (4) based on Part 1, which demonstrates the decomposition of $Ca(IO_3)_2$ and $NaIO_3$ follow different pathway and produces CaO and NaI, respectively[1]. The same analysis from EDS is not performed for Al-$LiIO_3$ as Li is undetectable in the instrument utilized.

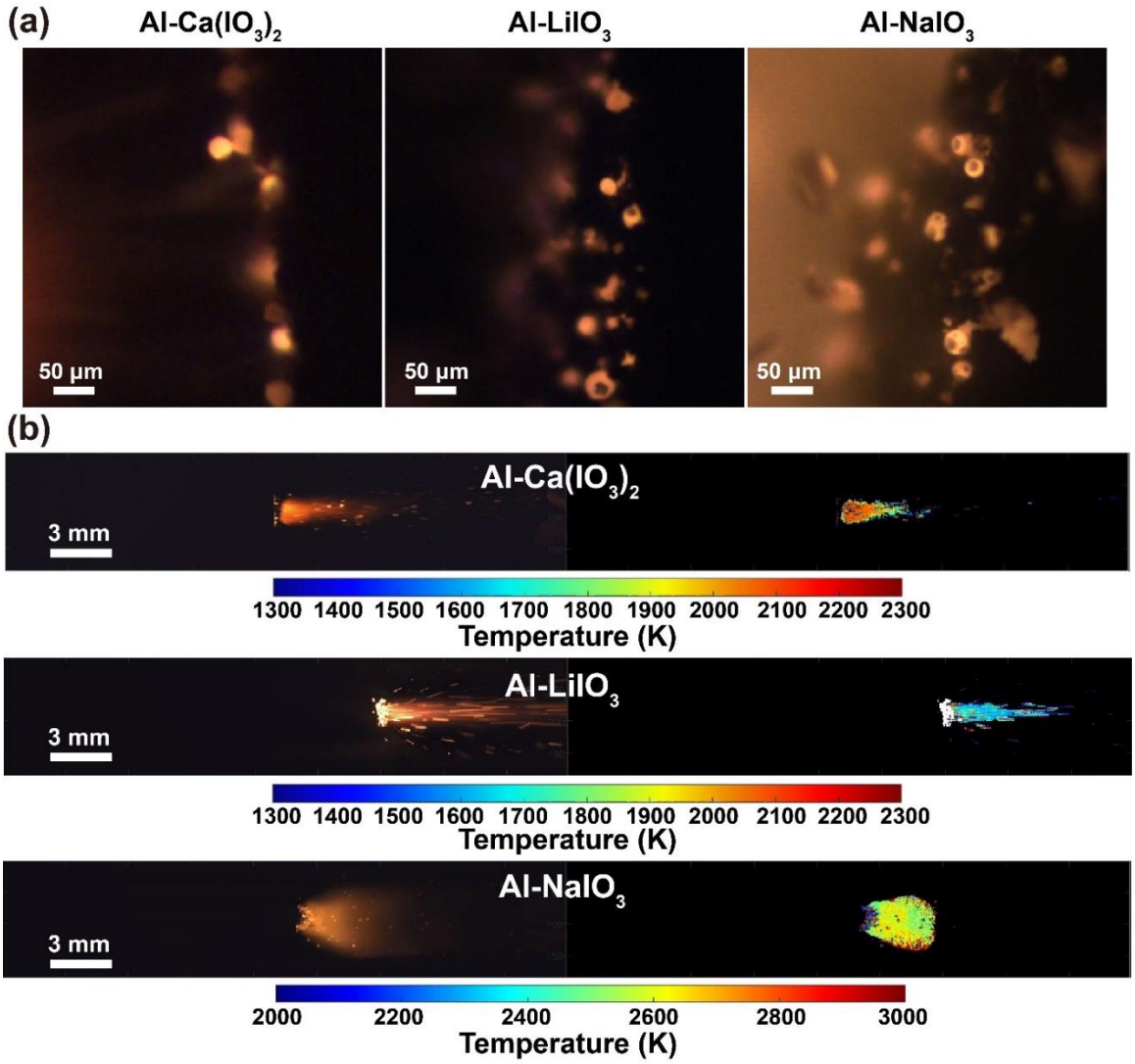

Figure 9-5 Representative images from microscopic videos (a), and representative snapshots (left) as well as corresponding flame temperature maps (right) from macroscopic videos (b) of Al-$Ca(IO_3)_2$, Al-$LiIO_3$, and Al-$NaIO_3$. Note: the temperature scale bar is different for Al-$NaIO_3$ as its flame temperature is much higher than the other two composites.

Three-color (RGB) pyrometry is employed to measure the temperature of the agglomerates on the burning surface from microscopic imaging as well as the flame temperature from macroscopic imaging. Figure S5 shows that the agglomerate temperature is ~2100 K for all the three composites from microscopic imaging. Figure 9-5 (b) displays

the representative flame snapshot from macroscopic imaging of for Al-$Ca(IO_3)_2$, Al-$LiIO_3$, and Al-$NaIO_3$ and their corresponding temperature map, which demonstrate flame temperature is different among the three composites. Flame temperature profiles displayed in Figure 9-6 (a)-(c) show that the average flame temperature of Al-$Ca(IO_3)_2$, Al-$LiIO_3$, and Al-$NaIO_3$ is 1930 K, 1820 K, and 2620 K, respectively. The significantly higher flame temperature of Al-$NaIO_3$ is attributed to its higher reactivity, as discussed in 9.4.2.

In 9.4.2, the lower thermite reactivity of Al-$LiIO_3$ compared to Al-$Mg(IO_3)_2$ and Al-$Ca(IO_3)_2$ is attributed to the endothermicity of $LiIO_3$ and Li_2O melting with the assumption that the flame temperature of Al-$LiIO_3$ is higher than the melting point of Li_2O at 1438 °C (1711 K). The flame temperature of Al-$LiIO_3$ thermite should be higher than the printed composite at 1820 K as the composite has 10% polymer binder that reduces the overall energy density. This is consistent with our proposition that Li_2O melts during the combustion of the thermite and the endothermicity contributes to the lower reactivity of Al-$LiIO_3$. As for Al-$Ca(IO_3)_2$, the melting point of CaO at 2613 °C (2886 K) is almost 1000 K higher than the flame temperature of the printed Al-$Ca(IO_3)_2$ composite, which means the flame temperature of Al-$Ca(IO_3)_2$ thermite is unlikely to be sufficiently high for melting CaO.

A comparison of the combustion performance of the printed composites is displayed in Figure 9-6 (d), where the burn rate is obtained from the macroscopic imaging and the relative energy release rate is estimated based on Equation S1.[27] Al-$Ca(IO_3)_2$ and Al-$LiIO_3$ have nearly the same burn at ~1 cm/s, which is about half of the burn rate of Al-$NaIO_3$ at ~2.2 cm/s. The estimated energy release rate of Al-$NaIO_3$ is much higher than

Al-$Ca(IO_3)_2$ and Al-$LiIO_3$, consistent with the aforementioned analysis from pressure cell tests that demonstrate Al-$NaIO_3$ has significantly higher reactivity than Al-$Ca(IO_3)_2$ and Al-$LiIO_3$. This means the printed composite of Al-$NaIO_3$ is more effective in releasing heating than Al-$Ca(IO_3)_2$ and Al-$LiIO_3$. However, as discussed in 9.4.1, Al-$NaIO_3$ only releases minimal amount of iodine compared with Al-$Ca(IO_3)_2$ and Al-$LiIO_3$, implying there is a trade-off between iodine release and heat release among these printed composites.

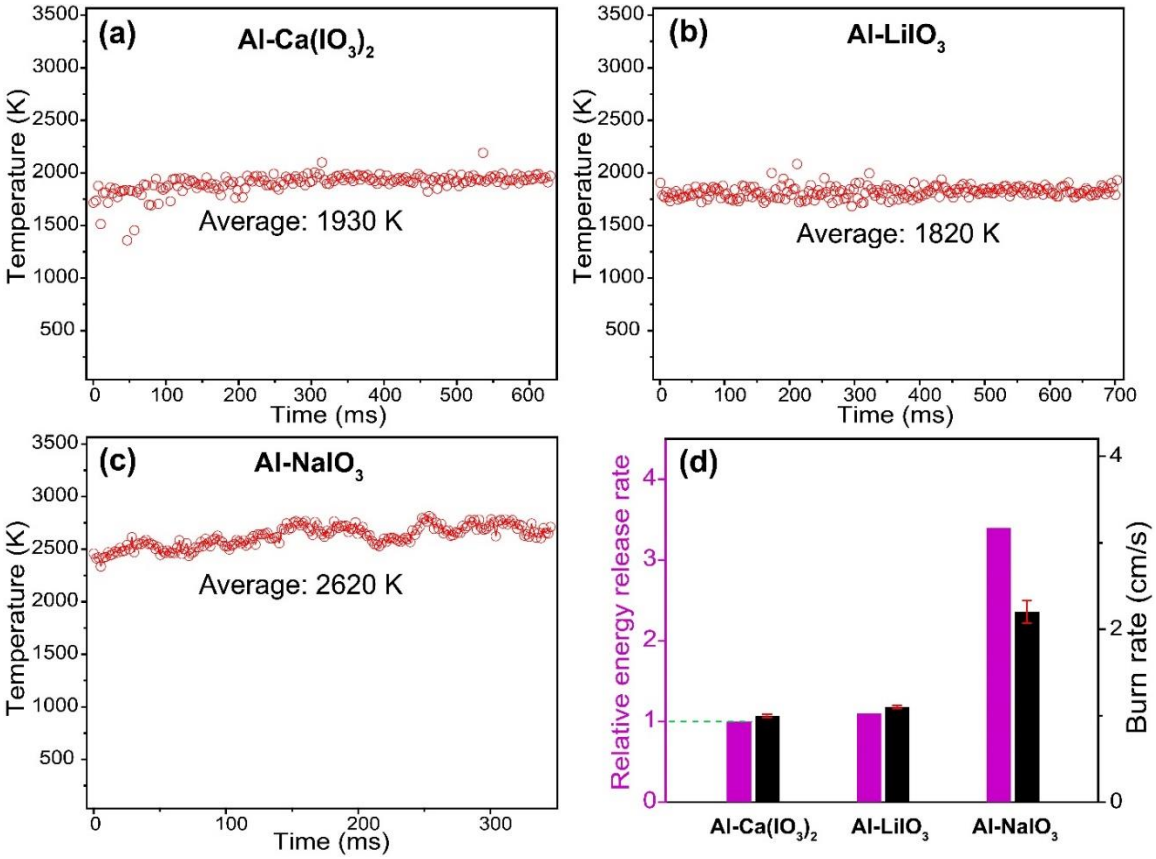

Figure 9-6 Time-resolved average flame temperature from macroscopic imaging of Al-$Ca(IO_3)_2$ (a), Al-$LiIO_3$ (b), and Al-$NaIO_3$ (c). Note: Each data point represents the average temperature of the entire flame at a specific time, while the average temperature inserted is the average of all the shown data points in the figure. Burn rate and relative energy release rate of Al-$Ca(IO_3)_2$, Al-$LiIO_3$, and Al-$NaIO_3$ (d). The relative energy release rate is based on the energy release rate of Al-$Ca(IO_3)_2$.

9.5 Conclusions

In this part 2, I conduct a systematic exploration of the iodine release, ignition, and reactivity of aluminized thermites containing alkali and alkaline metal iodate ($LiIO_3$, $NaIO_3$, KIO_3, $Mg(IO_3)_2$, and $Ca(IO_3)_2$) and the combustion behavior aluminized metal iodate composites. T-Jump TOFMS demonstrates that Al-$Mg(IO_3)_2$, Al-$Ca(IO_3)_2$, and Al-$LiIO_3$ release significant amount of iodine at roughly the same temperature, while $NaIO_3$ and Al-KIO_3 have minimal iodine release. Combustion cell analysis demonstrates the reactivity of Al-$Mg(IO_3)_2$, Al-$Ca(IO_3)_2$, and Al-$LiIO_3$ underperforms Al-$NaIO_3$ and Al-KIO_3, suggesting the trade-off between reactivity and iodine release. Incorporating data from both T-Jump TOFMS and combustion cell, I find that Al-$Mg(IO_3)_2$ and Al-$Ca(IO_3)_2$ have a similar iodine release rate, which is significantly higher than Al-$LiIO_3$. Free-standing Al-metal iodate composites with 90 wt% thermite loading and nearly 50 wt% iodine content are successfully prepared by 3D printing and their combustion behavior is characterized utilizing high-speed videography and pyrometry. It is found that only Al-$Ca(IO_3)_2$, Al-$LiIO_3$ and Al-$NaIO_3$ completely propagate in an inert environment and they display analogous microscopic combustion behavior characterized by spherical droplets formation on the burning surface. Comparing the macroscopic combustion behavior of the Al-$Ca(IO_3)_2$ and Al-$LiIO_3$ composites, minimal difference in propagation rate and flame temperature is identified, leading to comparable energy release rates. In contrast, the higher propagation rate and flame temperature of Al-$NaIO_3$ composite result in a significantly higher energy release rate than Al-$Ca(IO_3)_2$ and Al-$LiIO_3$, highlighting the trade-off between iodine release and heat release. This study reveals that while not all aluminized

metal iodate composites are potential candidates in biocidal application, Al-$Ca(IO_3)_2$ and Al-$LiIO_3$ composites are promising biocidal agents due to both heat and iodine release.

9.6 References

(1) Wang, Y.; Shi, K.; Paul, G. I.; Biswas, P.; Zachariah, M. R. Combustion Behavior of Aluminized Metal Iodate Composites. Part 1: Decomposition Mechanism of Metal Iodates. *Combust. Flame* **2024**, *262*, 113372. https://doi.org/10.1016/j.combustflame.2024.113372.

(2) Chang, J.; Zhao, G.; Zhao, X.; He, C.; Pang, S.; Shreeve, J. M. New Promises from an Old Friend: Iodine-Rich Compounds as Prospective Energetic Biocidal Agents. *Acc. Chem. Res.* **2021**, *54* (2), 332–343. https://doi.org/10.1021/acs.accounts.0c00623.

(3) Gray, M. J.; Wholey, W.-Y.; Jakob, U. Bacterial Responses to Reactive Chlorine Species. *Annu. Rev. Microbiol.* **2013**, *67*, 141–160. https://doi.org/10.1146/annurev-micro-102912-142520.

(4) Wheelis, M. *Deadly Cultures: Biological Weapons Since 1945*; Harvard University Press, 2006.

(5) Wu, T.; SyBing, A.; Wang, X.; Zachariah, M. R. Aerosol Synthesis of Phase Pure Iodine/Iodic Biocide Microparticles. *J. Mater. Res.* **2017**, *32* (4), 890–896. https://doi.org/10.1557/jmr.2017.6.

(6) Hu, X.; DeLisio, J. B.; Li, X.; Zhou, W.; Zachariah, M. R. Direct Deposit of Highly Reactive Bi(IO3)3- Polyvinylidene Fluoride Biocidal Energetic Composite and Its Reactive Properties. *Adv. Eng. Mater.* **2017**, *19* (1), 1500532. https://doi.org/10.1002/adem.201500532.

(7) Sullivan, K. T.; Piekiel, N. W.; Chowdhury, S.; Wu, C.; Zachariah, M. R.; Johnson, C. E. Ignition and Combustion Characteristics of Nanoscale Al/AgIO3: A Potential Energetic Biocidal System. *Combust. Sci. Technol.* **2010**, *183* (3), 285–302. https://doi.org/10.1080/00102202.2010.496378.

(8) Kaiho, T. *Iodine Chemistry and Applications*; John Wiley & Sons, 2014.

(9) Xu, F.; Biswas, P.; Nava, G.; Schwan, J.; Kline, D. J.; Rehwoldt, M. C.; Mangolini, L.; Zachariah, M. R. Tuning the Reactivity and Energy Release Rate of I2O5 Based Ternary Thermite Systems. *Combust. Flame* **2021**, *228*, 210–217. https://doi.org/10.1016/j.combustflame.2020.12.047.

(10) Zhao, W.; Ren, H.; Yan, T.; Ou, Y.; Jiao, Q.; Wang, H.; Kline, D. J.; Zachariah, M. R. Tailoring Energy Release of Nano-Si Based Thermites via Incorporation of Ti Nanoparticles. *Chem. Eng. J.* **2020**, *396*, 124559. https://doi.org/10.1016/j.cej.2020.124559.

(11) Zhou, W.; DeLisio, J. B.; Wang, X.; Zachariah, M. R. Reaction Mechanisms of Potassium Oxysalts Based Energetic Composites. *Combust. Flame* **2017**, *177*, 1–9. https://doi.org/10.1016/j.combustflame.2016.05.024.

(12) Jian, G.; Piekiel, N. W.; Zachariah, M. R. Time-Resolved Mass Spectrometry of Nano-Al and Nano-Al/CuO Thermite under Rapid Heating: A Mechanistic Study. *J. Phys. Chem. C* **2012**, *116* (51), 26881–26887. https://doi.org/10.1021/jp306717m.

(13) Wang, H.; Shen, J.; Kline, D. J.; Eckman, N.; Agrawal, N. R.; Wu, T.; Wang, P.; Zachariah, M. R. Direct Writing of a 90 Wt% Particle Loading Nanothermite. *Adv. Mater.* **2019**, *31* (23), 1806575. https://doi.org/10.1002/adma.201806575.

(14) He, W.; Liu, P.-J.; He, G.-Q.; Gozin, M.; Yan, Q.-L. Highly Reactive Metastable Intermixed Composites (MICs): Preparation and Characterization. *Adv. Mater.* **2018**, *30* (41), 1706293. https://doi.org/10.1002/adma.201706293.
(15) Zhu, Y.; Zhou, X.; Xu, J.; Ma, X.; Ye, Y.; Yang, G.; Zhang, K. In Situ Preparation of Explosive Embedded CuO/Al/CL20 Nanoenergetic Composite with Enhanced Reactivity. *Chem. Eng. J.* **2018**, *354*, 885–895. https://doi.org/10.1016/j.cej.2018.08.063.
(16) Yen, N. H.; Wang, L. Y. Reactive Metals in Explosives. *Propellants Explos. Pyrotech.* **2012**, *37* (2), 143–155. https://doi.org/10.1002/prep.200900050.
(17) Comet, M.; Martin, C.; Klaumünzer, M.; Schnell, F.; Spitzer, D. Energetic Nanocomposites for Detonation Initiation in High Explosives without Primary Explosives. *Appl. Phys. Lett.* **2015**, *107* (24), 243108. https://doi.org/10.1063/1.4938139.
(18) Prakash, A.; McCormick, A. V.; Zachariah, M. R. Synthesis and Reactivity of a Super-Reactive Metastable Intermolecular Composite Formulation of Al/KMnO4. *Adv. Mater.* **2005**, *17* (7), 900–903. https://doi.org/10.1002/adma.200400853.
(19) R. Clark, B.; L. Pantoya, M. The Aluminium and Iodine Pentoxide Reaction for the Destruction of Spore Forming Bacteria. *Phys. Chem. Chem. Phys.* **2010**, *12* (39), 12653–12657. https://doi.org/10.1039/C0CP00473A.
(20) Martirosyan, K. S.; Wang, L.; Luss, D. Novel Nanoenergetic System Based on Iodine Pentoxide. *Chem. Phys. Lett.* **2009**, *483* (1), 107–110. https://doi.org/10.1016/j.cplett.2009.10.038.
(21) Wang, H.; Jian, G.; Zhou, W.; DeLisio, J. B.; Lee, V. T.; Zachariah, M. R. Metal Iodate-Based Energetic Composites and Their Combustion and Biocidal Performance. *ACS Appl. Mater. Interfaces* **2015**, *7* (31), 17363–17370. https://doi.org/10.1021/acsami.5b04589.
(22) Wang, H.; Kline, D. J.; Rehwoldt, M.; Zachariah, M. R. Ignition and Combustion Characterization of Ca(IO3)2-Based Pyrotechnic Composites with B, Al, and Ti. *Propellants Explos. Pyrotech.* **2018**, *43* (10), 977–985. https://doi.org/10.1002/prep.201800041.
(23) Shen, J.; Wang, H.; Kline, D. J.; Yang, Y.; Wang, X.; Rehwoldt, M.; Wu, T.; Holdren, S.; Zachariah, M. R. Combustion of 3D Printed 90 Wt% Loading Reinforced Nanothermite. *Combust. Flame* **2020**, *215*, 86–92. https://doi.org/10.1016/j.combustflame.2020.01.021.
(24) Ruz-Nuglo, F. D.; Groven, L. J. 3-D Printing and Development of Fluoropolymer Based Reactive Inks. *Adv. Eng. Mater.* **2018**, *20* (2), 1700390. https://doi.org/10.1002/adem.201700390.
(25) Ghosh, S.; Parker, S. T.; Wang, X.; Kaplan, D. L.; Lewis, J. A. Direct-Write Assembly of Microperiodic Silk Fibroin Scaffolds for Tissue Engineering Applications. *Adv. Funct. Mater.* **2008**, *18* (13), 1883–1889. https://doi.org/10.1002/adfm.200800040.
(26) Wang, Y.; Hagen, E.; Biswas, P.; Wang, H.; Zachariah, M. R. Imaging the Combustion Characteristics of Al, B, and Ti Composites. *Combust. Flame* **2023**, *252*, 112747. https://doi.org/10.1016/j.combustflame.2023.112747.

(27) Wang, H.; Wang, Y.; Garg, M.; Moore, J. S.; Zachariah, M. R. Unzipping Polymers Significantly Enhance Energy Flux of Aluminized Composites. *Combust. Flame* **2022**, *244*, 112242. https://doi.org/10.1016/j.combustflame.2022.112242.
(28) Wang, H.; Kline, D. J.; Rehwoldt, M. C.; Zachariah, M. R. Carbon Fibers Enhance the Propagation of High Loading Nanothermites: In Situ Observation of Microscopic Combustion. *ACS Appl. Mater. Interfaces* **2021**. https://doi.org/10.1021/acsami.1c02911.
(29) Yetter, R. A.; Risha, G. A.; Son, S. F. Metal Particle Combustion and Nanotechnology. *Proc. Combust. Inst.* **2009**, *32* (2), 1819–1838. https://doi.org/10.1016/j.proci.2008.08.013.
(30) Wang, H.; DeLisio, J. B.; Wu, T.; Wang, X.; Zachariah, M. R. One-Step Solvent-Free Mechanochemical Synthesis of Metal Iodate Fine Powders. *Powder Technol.* **2018**, *324*, 62–68. https://doi.org/10.1016/j.powtec.2017.10.024.
(31) Wang, Y.; Wang, H.; Xu, F.; Ghildiyal, P.; Zachariah, M. R. Effect of Alkali Metal Perchlorate and Iodate Type on Boron Ignition: The Role of Oxidizer Phase Change. *Chem. Eng. J.* **2022**, *446*, 136786. https://doi.org/10.1016/j.cej.2022.136786.
(32) Rehwoldt, M. C.; Wang, Y.; Xu, F.; Ghildiyal, P.; Zachariah, M. R. High-Temperature Interactions of Metal Oxides and a PVDF Binder. *ACS Appl. Mater. Interfaces* **2022**. https://doi.org/10.1021/acsami.1c20938.
(33) Sullivan, K.; Zachariah, M. Simultaneous Pressure and Optical Measurements of Nanoaluminum Thermites: Investigating the Reaction Mechanism. *J. Propuls. Power* **2010**, *26* (3), 467–472. https://doi.org/10.2514/1.45834.
(34) Sullivan, K.; Young, G.; Zachariah, M. R. Enhanced Reactivity of Nano-B/Al/CuO MIC's. *Combust. Flame* **2009**, *156* (2), 302–309. https://doi.org/10.1016/j.combustflame.2008.09.011.
(35) Wang, H.; Julien, B.; Kline, D.; Alibay, Z.; Rehwoldt, M.; Rossi, C.; Zachariah, M. Probing the Reaction Zone of Nanolaminates at ∼μs Time and ∼μm Spatial Resolution. *J. Phys. Chem. C* **2020**, *124* (25), 13679–13687. https://doi.org/10.1021/acs.jpcc.0c01647.
(36) Wang, H.; Kline, D. J.; Zachariah, M. R. In-Operando High-Speed Microscopy and Thermometry of Reaction Propagation and Sintering in a Nanocomposite. *Nat. Commun.* **2019**, *10* (1), 3032. https://doi.org/10.1038/s41467-019-10843-4.
(37) Jacob, R. J.; Kline, D. J.; Zachariah, M. R. High Speed 2-Dimensional Temperature Measurements of Nanothermite Composites: Probing Thermal vs. Gas Generation Effects. *J. Appl. Phys.* **2018**, *123* (11), 115902. https://doi.org/10.1063/1.5021890.
(38) Kline, D. J.; Alibay, Z.; Rehwoldt, M. C.; Idrogo-Lam, A.; Hamilton, S. G.; Biswas, P.; Xu, F.; Zachariah, M. R. Experimental Observation of the Heat Transfer Mechanisms That Drive Propagation in Additively Manufactured Energetic Materials. *Combust. Flame* **2020**, *215*, 417–424. https://doi.org/10.1016/j.combustflame.2020.01.020.
(39) Trunov, M. A.; Schoenitz, M.; Dreizin, E. L. Effect of Polymorphic Phase Transformations in Alumina Layer on Ignition of Aluminium Particles. *Combust. Theory Model.* **2006**, *10* (4), 603–623. https://doi.org/10.1080/13647830600578506.

(40) Sullivan, K. T.; Kuntz, J. D.; Gash, A. E. The Role of Fuel Particle Size on Flame Propagation Velocity in Thermites with a Nanoscale Oxidizer. *Propellants Explos. Pyrotech.* **2014**, *39* (3), 407–415. https://doi.org/10.1002/prep.201400020.
(41) Huang, Y.; Risha, G. A.; Yang, V.; Yetter, R. A. Effect of Particle Size on Combustion of Aluminum Particle Dust in Air. *Combust. Flame* **2009**, *156* (1), 5–13. https://doi.org/10.1016/j.combustflame.2008.07.018.
(42) Sundaram, D. S.; Yang, V.; Zarko, V. E. Combustion of Nano Aluminum Particles (Review). *Combust. Explos. Shock Waves* **2015**, *51* (2), 173–196. https://doi.org/10.1134/S0010508215020045.
(43) Chen, Y.; Guildenbecher, D. R.; Hoffmeister, K. N. G.; Cooper, M. A.; Stauffacher, H. L.; Oliver, M. S.; Washburn, E. B. Study of Aluminum Particle Combustion in Solid Propellant Plumes Using Digital In-Line Holography and Imaging Pyrometry. *Combust. Flame* **2017**, *182*, 225–237. https://doi.org/10.1016/j.combustflame.2017.04.016.
(44) Haynes, W. M. *CRC Handbook of Chemistry and Physics, 95th Edition.*; CRC Press: Hoboken, 2014.
(45) Ropp, R. C. Group 16 (O, S, Se, Te) Alkaline Earth Compounds. In *Encyclopedia of the Alkaline Earth Compounds*; Elsevier, 2013; pp 105–197. https://doi.org/10.1016/B978-0-444-59550-8.00003-X.
(46) Kessinger, G. F.; Jurgensen, A. R.; Missimer, D. M.; Morrell, J. S. The High-Temperature Chemical Reactivity of Li2O. *Nucl. Technol.* **2010**, *171* (1), 108–122. https://doi.org/10.13182/NT10-A10775.
(47) *Materials Project*. https://materialsproject.org/ (accessed 2021-12-09).

9.7 Supporting information

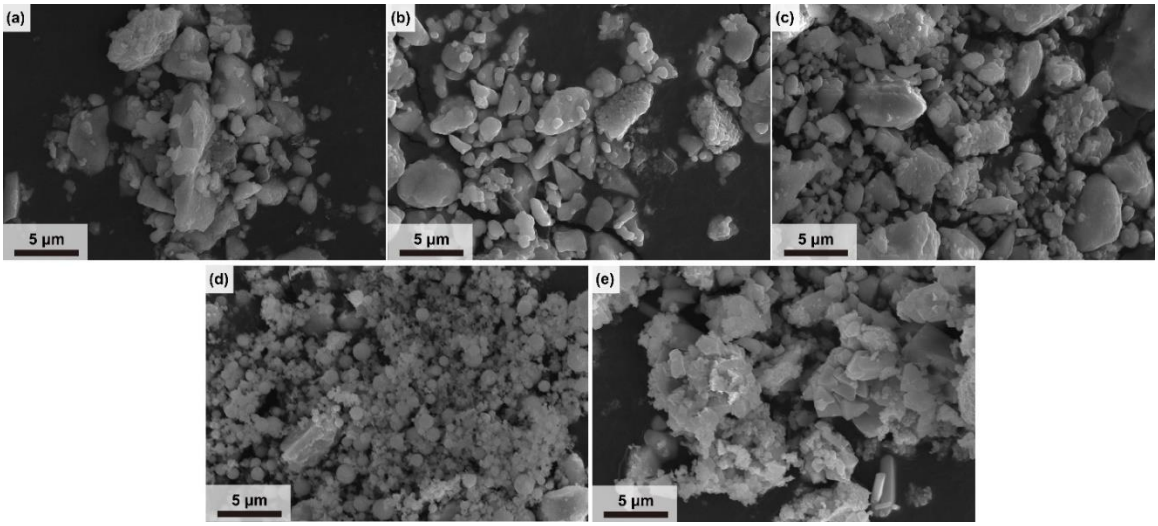

Figure S1 SEM images of $LiIO_3$ (a), $NaIO_3$ (b), KIO_3 (c), $Mg(IO_3)_2$ (d) and $Ca(IO_3)_2$ (e).

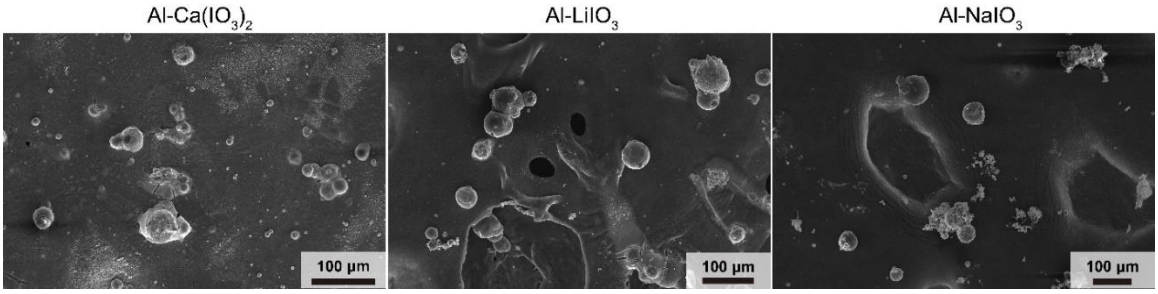

Figure S2 SEM images of post-combustion product for Al-$Ca(IO_3)_2$, Al-$LiIO_3$, and Al-$NaIO_3$.

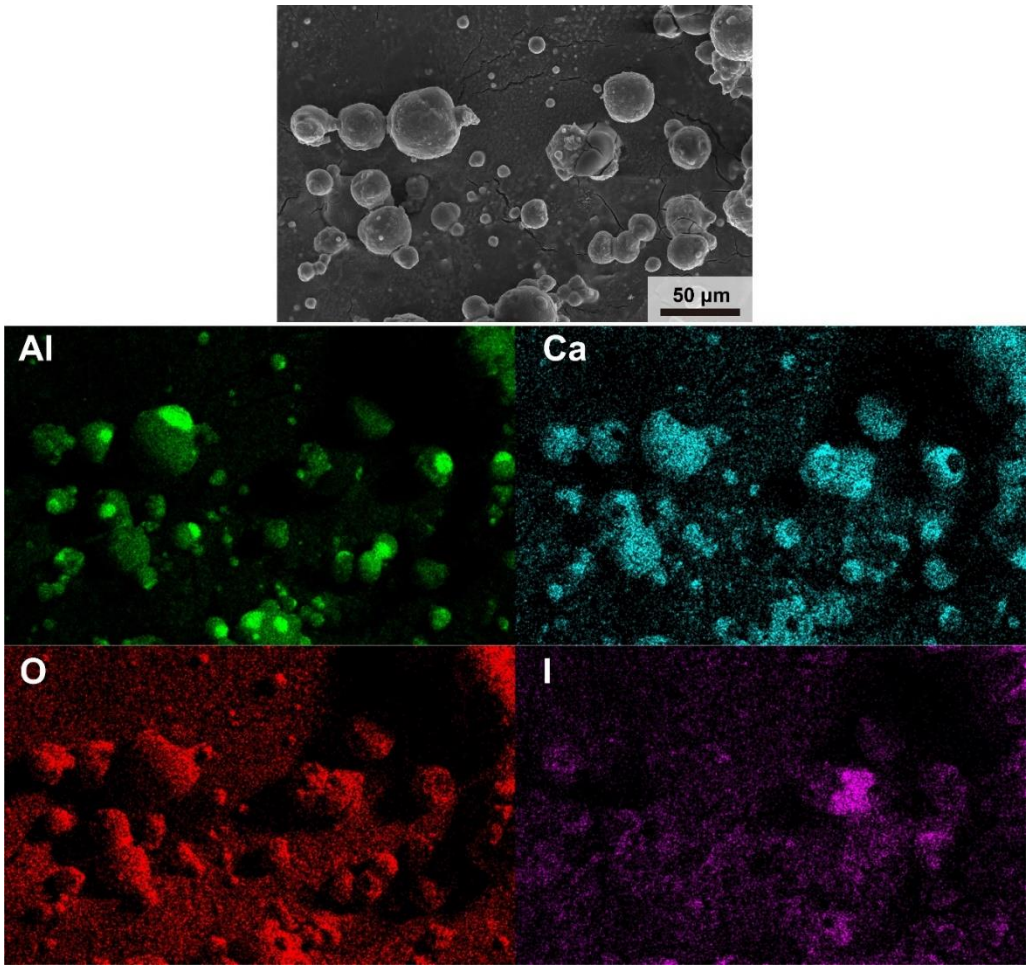

Figure S3 EDS of post-combustion product for Al-Ca$(IO_3)_2$.

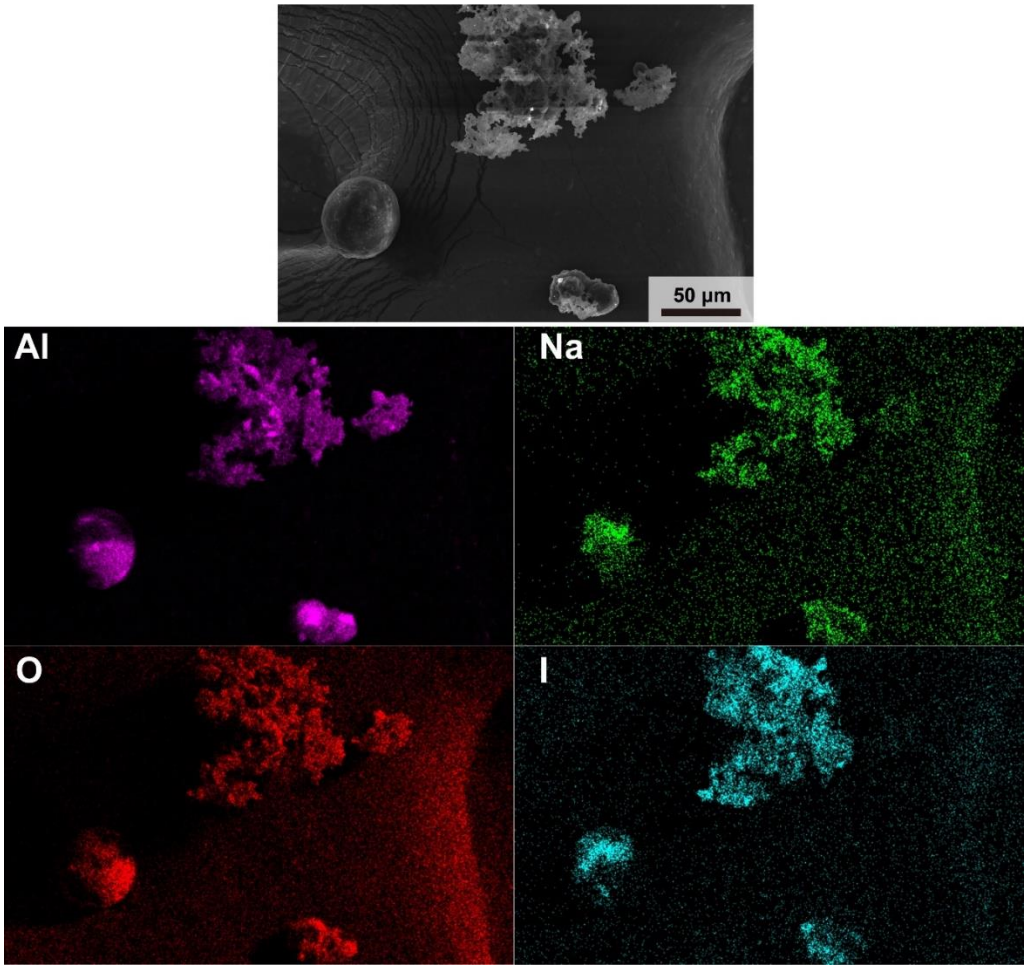

Figure S4 EDS of post-combustion product for Al-$NaIO_3$.

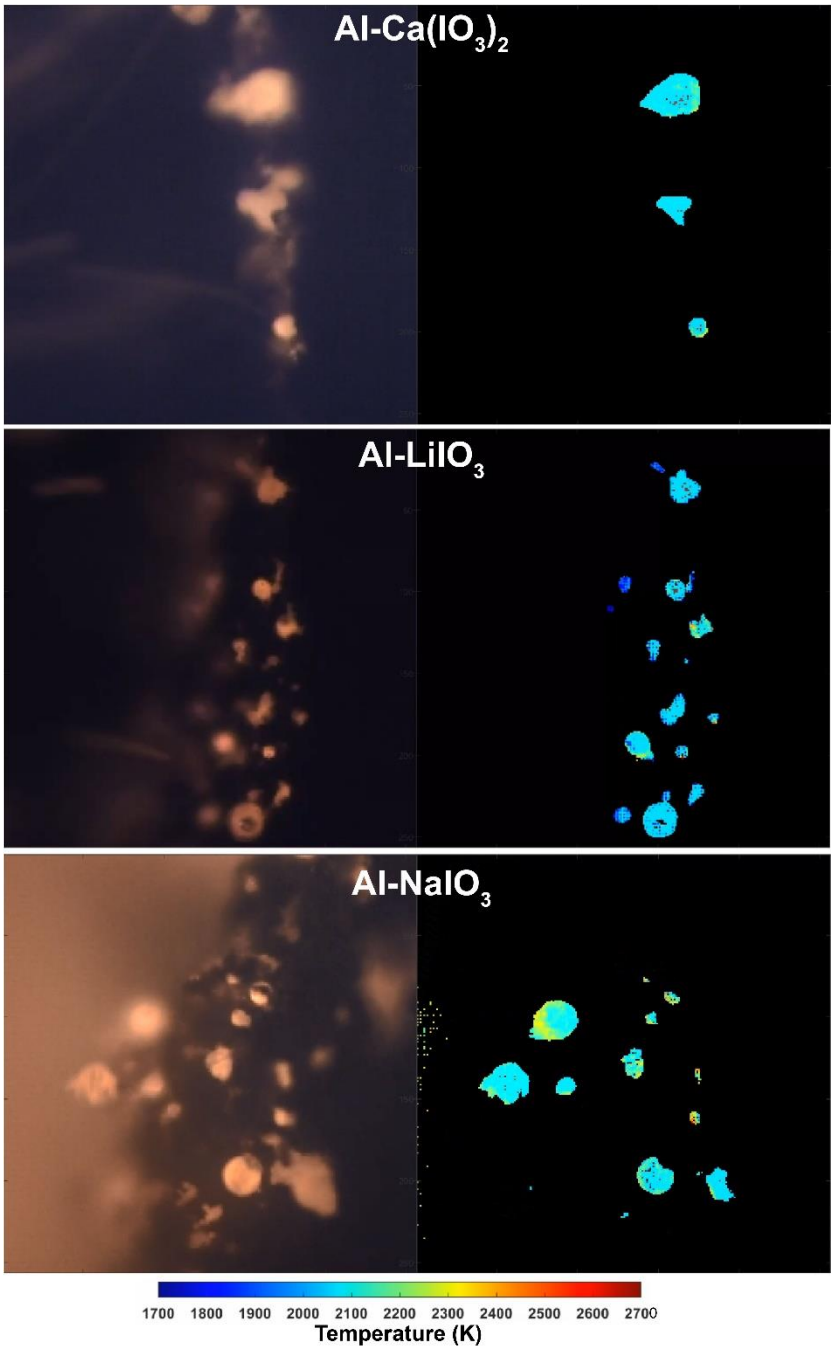

Figure S5 Temperature map of from three-color (RGB) pyrometry for an image from microscopy video of Al-$Ca(IO_3)_2$ (top), Al-$LiIO_3$ (middle), and Al-$NaIO_3$ (bottom). High error points and low-intensity points were excluded from the calculation.

Energy release rate of the printed composites is determined in Equation S1.

$$E = \rho \times v \times A \times Cp \times \Delta T \quad \text{(S1)}$$

Where ρ is the density of the printed composite, which is determined by combining the length, cross-section area and the corresponding mass of the printed sticks. v represents the burn rate, A is the cross-section area of the composite, C_p is the heat capacity of the composite and is assumed to be the same for all three composites, and ΔT is the difference between flame temperature and room temperature.

10 Summary and Future Work

10.1 Conclusions

The objective of this dissertation was to gain a comprehensive understanding of the reaction dynamics of energetic materials by investigating the influence of physical properties and heat transfer on the ignition and combustion characteristics of condensed-phase energetic materials. Various characterization techniques were employed, including temperature-jump ignition, temperature-jump time-of-flight spectrometry, scanning electron microscopy, X-ray diffraction, thermogravimetric-differential scanning calorimetry, as well as in-operando microscopic and macroscopic imaging coupled with color pyrometry, to analyze the phenomena occurring at the reactive interface of these materials. Below, I summarize the key findings of each chapter of this dissertation and offer suggestions for future studies.

Chapters 3 and 4 delve into the crucial impact of the physical properties on the ignition and combustion characteristics of energetic materials. Chapter 3 investigates a series of oxidizers (alkali metal perchlorates and iodates) with similar chemistries to elucidate the controlling mechanisms in boron ignition. It is discovered that nanoscale boron exhibits different ignition behaviors when paired with these metal perchlorates and iodates. Despite the similar chemistries, B/$LiClO_4$, B/$NaClO_4$, B/$LiIO_3$, and B/$NaIO_3$ ignite while B/$KClO_4$ and B/KIO_3 do not, in an inert environment. Additionally, the boron incorporation into $LiClO_4$, $NaClO_4$, $LiIO_3$, and $NaIO_3$ promotes their decomposition due to heat release from the redox reactions. However, the boron addition to $KClO_4$ and KIO_3

has minimal impact on their decomposition. The variance in ignition behavior is attributed to the discrepancy in the interval between melting and decomposition of the oxidizers. $KClO_4$ and KIO_3 melt and decompose concurrently, rendering limited time for the oxidizers to envelop the boron nanoparticles as a liquid. Consequently, only boron nanoparticles in close initial contact with the oxidizer particles have immediate access to gaseous oxygen, resulting in minimal ignition events. Conversely, perchlorates and iodates with a relatively large interval between melting and decomposition, such as $LiClO_4$, $NaClO_4$, $LiIO_3$, and $NaIO_3$, there is time for the oxidizers to melt and surround the boron nanoparticles before decomposition. This facilitates easier access to gaseous oxygen for the boron nanoparticles and leads to more robust ignition. This revelation underscores the influence of oxidizer physical properties and transport phenomena on ignition behaviors.

Chapter 4 reveals that the microscopic combustion behavior of an energetic composite is significantly influenced by the physical properties of the fuel and its oxide. Energetic composites containing nanoscale aluminum, boron, and titanium as fuels are investigated. Microscopic imaging unveils notable sintering and agglomeration in all three composites. However, distinct combustion characteristics are observed among them. In the case of aluminum composites, molten and mobile droplets with dark caps form on the burning surface, attributed to the droplet temperature surpassing the melting points of both aluminum and aluminum oxide. Conversely, boron and titanium composites exhibit fractal-shaped agglomerates on the burning surface. The discrepancy in combustion features between boron and titanium stems from the fractal-shaped agglomerates of titanium exhibiting a greater propensity to transition into a more spherical form compared to boron.

For boron composites, the temperature of the agglomerates is measured to be higher than the melting point of B_2O_3 but lower than the melting point of boron, explaining the fractal shape. In contrast, the temperature of titanium agglomerates is slightly higher than the melting point of titanium and TiO_2 but lower than the melting point of Ti_2O_3, which forms at the interface of titanium and TiO_2. It is proposed that Ti_2O_3 contributes to the fractal shape of the agglomerates, and its transition into TiO_2, with a lower melting point, explains the heightened tendency for the fractal-shaped agglomerates to adopt a spherical shape than that of boron.

Chapters 5-7 delve into various strategies aimed at manipulating the heat transferred from the flame or reaction front back to the unburnt material, thereby tuning the energy release rate from energetic composites. In Chapter 5, one approach explored is tuning the equivalence ratio between the fuel and oxidizer. Investigation into aluminum/ammonium perchlorate (AP) composites reveals that a composite with an equivalence ratio of 2 exhibits a significantly higher burn rate compared to the stoichiometric ratio. This is attributed to the prolonged residence time of agglomerates on the burning surface due to the formation of larger agglomerates, resulting in increased heat feedback.

Chapter 6 presents another method to manipulate heat feedback by tuning agglomerate surface tension. Silicon is introduced as an additive to lower the surface tension of aluminum, leading to a reduced droplet growth rate from agglomerate, enhancing the overall agglomerate residence time on the burning surface. This leads to

improved conductive heat feedback and subsequently higher energy release rates in composites of Al/$KClO_4$.

In Chapter 7, carbon fiber is introduced as a means to intercept agglomerates near the burning surface in composites of mesoparticles. The inclusion of carbon fiber addresses the issue of noncontinuous propagation observed in mesoparticle-only composites, attributed to inadequate heat feedback. By intercepting hot agglomerates, carbon fiber significantly enhances heat feedback by prolonging the residence time of agglomerates near the burning surface, resulting in steady propagation behavior in the composite.

Chapters 8-9 provide a systematic investigation into the potential application of alkali and alkaline metal iodates ($LiIO_3$, $NaIO_3$, KIO_3, $Mg(IO_3)_2$, and $Ca(IO_3)_2$) as energetic biocidal agents. The study reveals that these metal iodates undergo two distinct decomposition pathways, yielding different products. Some produce metal oxide, oxygen, and iodine (e.g., $Mg(IO_3)_2$, $Ca(IO_3)_2$, and $LiIO_3$), while others yield metal iodide and oxygen (e.g., $NaIO_3$ and KIO_3). A thermodynamic calculation is presented, which effectively predicts the decomposition pathway of metal iodates. Additionally, the combustion behavior of thermites utilizing these metal iodates as oxidizers and nanoscale aluminum as fuel is investigated. It is found that Al-$NaIO_3$ and Al-KIO_3 exhibit higher reactivity compared to Al-$Mg(IO_3)_2$, Al-$Ca(IO_3)_2$, and Al-$LiIO_3$, albeit with minimal iodine release. This indicates a trade-off between iodine release and reactivity. Furthermore, high loading free-standing composites of aluminized metal iodates with high iodine content are fabricated and their combustion behavior is studied. Only Al-$Ca(IO_3)_2$, Al-$LiIO_3$, and Al-$NaIO_3$ demonstrate complete propagation in an argon environment, with similar

microscopic combustion characteristics. However, Al-$Ca(IO_3)_2$ and Al-$LiIO_3$ exhibit lower burning rates and flame temperatures compared to Al-$NaIO_3$, resulting in lower energy release rates. This highlights the trade-off between iodine release and energy release rate. Overall, the findings suggest that not all metal iodates are suitable candidates for biocidal applications. Aluminized $Ca(IO_3)_2$ and $LiIO_3$ emerge as promising energetic biocidal agents due to their combined heat and iodine release properties.

Therefore, this dissertation has addressed multiple challenges related to understanding and manipulating the ignition and combustion behavior of energetic materials, opening new avenues for improving energy release rate of high-energy systems and developing energetic biocidal agents.

10.2 Recommendation for future work

10.2.1 Investigating the noncontinuous combustion behavior of printed composites of nanoenergetic mesoparticles

The objective of this study is to investigate an alternative method for adjusting the burn rate and energy release rate of energetic composites. The approach involves incorporating two systems with distinct combustion behaviors into a single composite. One system produces a steady flame with a relatively slow propagation rate, such as polymers, which can be used to ignite the other system with a higher propagation rate and higher flame temperature, such as nanoenergetic mesoparticles. As elucidated in Chapter 7, the printed composite consisting of 90% mesoparticles (Al/CuO/NC) and 10% PMMA as the binder exhibited a noncontinuous and oscillating propagation behavior. This phenomenon is attributed to the inadequate heat feedback from the flame due to the rapid departure of hot agglomerates from the burning surface. The reignition is hypothesized to occur due to the heat accumulation from the continuous combustion of PMMA, reaching the ignition temperature of Al/CuO and reigniting the Al/CuO/NC mesoparticles. Consequently, the time interval between two consecutive visible combustion events is regulated by the combustion of PMMA. It is inferred that a higher PMMA content results in faster reignition of the mesoparticles due to accelerated heat accumulation, thereby reducing the time interval between two consecutive visible combustion events.

I have produced a composite comprising 80% mesoparticles (Al/CuO/NC) combined with 20% PMMA as the binder. This composite exhibited a reduced interval between two consecutive visible combustion events compared to the composite with a 10%

PMMA binder. This indicates that the mesoparticles in the composite ignite at a higher rate. This initial finding lends support to the hypothesis that the burn rate of a composite containing highly reactive mesoparticles can be controlled by adjusting the relative content of the polymer binder and the mesoparticles. However, to comprehensively investigate this concept, it is necessary to fabricate composites with various polymer binder contents containing mesoparticles or other highly reactive energetic components and evaluate their combustion behaviors systematically.

10.2.2 Investigating the effect of oxidizer type on the combustion behavior

The findings presented in Chapter 4 underscore the significant influence of the physical properties, specifically the melting and boiling points, of the fuel and their corresponding oxides on the microscopic combustion characteristics of an energetic composite. This observation prompts an inquiry into how the oxidizer impacts the combustion behavior of such composites. Initial results indicate distinct combustion behaviors between 90% loading Al-CuO and Al-KClO4 composites manufactured using the same printing technique. Illustrated in Figure 10-1, the agglomerates formed on the burning surface of the Al-CuO composite are notably smaller than those of the Al-$KClO_4$ composite. Furthermore, the agglomerates exhibit a shorter residence time on the burning surface in the Al-CuO composite compared to the Al-$KClO_4$ composite. This disparity in agglomerate surface residence time may contribute to the differing burn rates observed in these two composites, approximately 3 cm/s for Al-CuO and 10 cm/s for Al-$KClO_4$, respectively, as inferred from the heat feedback argument. However, further investigation

is needed to explore the influence of various oxidizer types, such as Bi_2O_3, CoO, and Fe_2O_3, in order to fully understand their effects on the combustion characteristics of energetic composites.

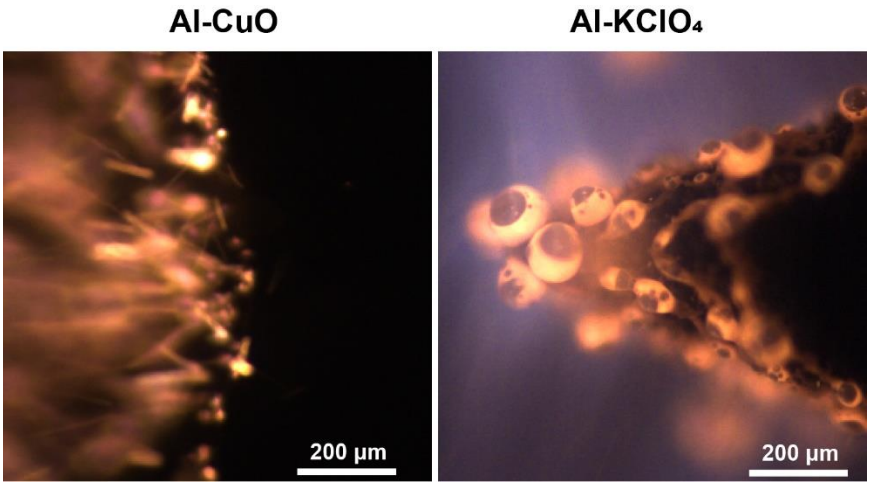

Figure 10-1 Microscopic combustion characteristic of 90% loading composite of Al-CuO (left) and Al-$KClO_4$ (right) with 4% PVDF and 6% HPMC as the binder.

10.2.3 Surface modification of boron nanoparticles for improved combustion performance

As discussed previously, the reactivity of boron is hindered by the presence of a boron oxide shell, which acts as a barrier, limiting the diffusion of reactants for boron oxidation. One potential approach to remove this oxide shell and enhance the reactivity of boron is to expose the nanoparticles to hydrofluoric acid (HF), as previous studies have shown that the oxide layer removal rate of boron is significantly increased in the presence of HF[1]. PVDF is known to melt at approximately 150 °C and generate HF during

decomposition[2]. Therefore, I propose to coat boron nanoparticles with PVDF to facilitate the in-situ removal of boron oxide during heating. Exploiting the relatively low melting point of PVDF, I physically mixed boron nanoparticles with PVDF at mass ratios of 9:1 and 4:1, then heated the mixtures in a furnace set to 160 °C for 2 hours within an argon environment. The objective of this annealing process is to melt the PVDF and allow the molten polymer to wet the boron nanoparticles, thereby promoting their contact.

T-Jump ignition conducted in an oxygen environment reveals that the annealed boron with PVDF mixtures exhibit clear ignition events, whereas the bare boron shows no ignition, as illustrated in Figure 10-2 (a). This suggests that the PVDF coating promotes the ignition of boron nanoparticles. Furthermore, thermogravimetric-differential scanning calorimetry (TGA/DSC) of the mixture of PVDF and B_2O_3 at a mass ratio of 1:1 was conducted in an argon environment. The results, depicted in Figure 10-2 (b), show a distinct exothermic peak at 323.5 °C accompanied by a mass loss, indicating a reaction between PVDF and B_2O_3, implying that B_2O_3 is partially removed by PVDF. These preliminary findings indicate that PVDF is effective in removing B_2O_3 and facilitating the ignition of boron nanoparticles. However, further investigations are necessary to delve into this behavior and apply this approach in practical applications. Specifically, transmission electron microscopy (TEM) coupled with energy dispersive X-ray spectroscopy (EDS) is required to confirm the coating of PVDF on the boron nanoparticles. Additionally, the reaction mechanism between PVDF and B_2O_3 needs to be explored through different characterization techniques including T-Jump TOFMS and Fourier-transform infrared spectroscopy (FTIR). Furthermore, the boron nanoparticles coated with PVDF must be

incorporated into composites, and their combustion behavior needs to be studied and compared with that of composites containing bare boron to examine the effect of PVDF coating.

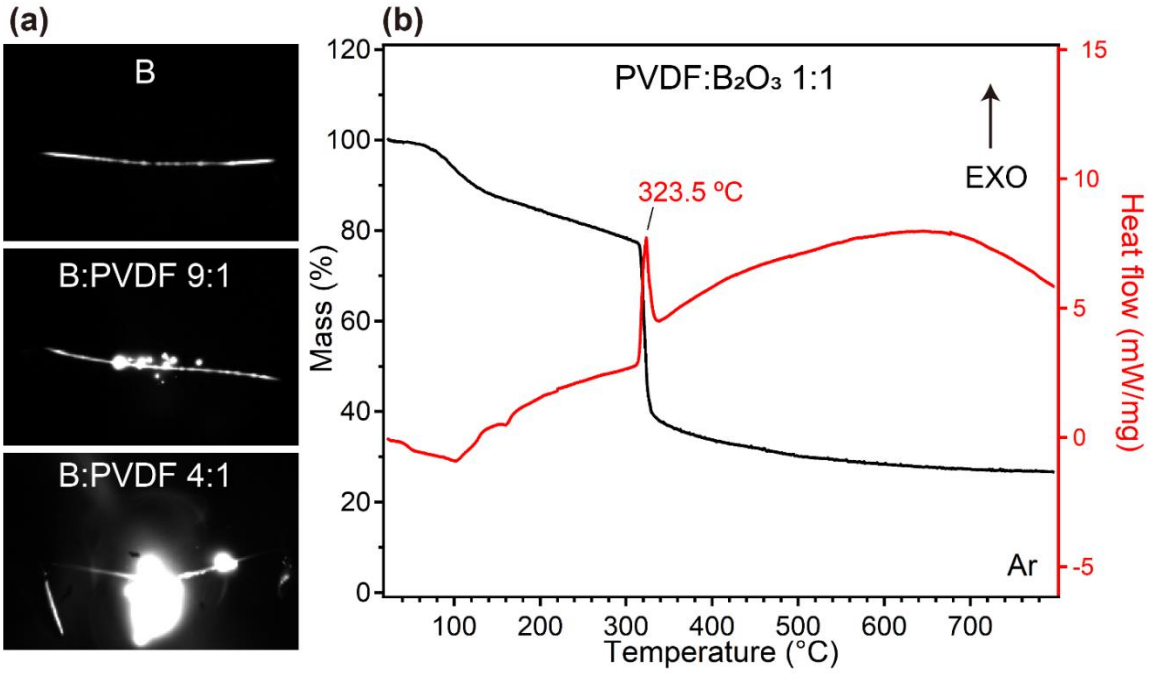

Figure 10-2 Representative T-Jump ignition snapshots for B (top), B-PVDF with a mass ratio of 9:1 (middle), and B-PVDF with a mass ratio of 4:1 (bottom) in an oxygen environment (a), and TGA/DSC of mixture of PVDF with B_2O_3 with a mass ratio of 1:1 in an argon environment (b).

10.3 References

(1) Ulas, A.; Kuo, K. K.; Gotzmer, C. Ignition and Combustion of Boron Particles in Fluorine-Containing Environments. *Combust. Flame* **2001**, *127* (1), 1935–1957. https://doi.org/10.1016/S0010-2180(01)00299-1.

(2) Rehwoldt, M. C., Wang, Y., Xu, F., Ghildiyal, P., & Zachariah, M. R. (2022). High-temperature interactions of metal oxides and a PVDF binder. *ACS Applied Materials & Interfaces*, *14*(7), 8938-8946. https://doi.org/10.1021/acsami.1c20938

10.4 Publications

(1) Rehwoldt, M. C., **Wang, Y. (co-first author)**, Xu, F., Ghildiyal, P., & Zachariah, M. R. (2022). High-temperature interactions of metal oxides and a PVDF binder. *ACS Applied Materials & Interfaces*, *14*(7), 8938-8946.

(2) **Wang, Y.,** Wang, H., Xu, F., Ghildiyal, P., & Zachariah, M. R. (2022). Effect of alkali metal perchlorate and iodate type on boron ignition: The role of oxidizer phase change. *Chemical Engineering Journal*, *446*, 136786.

(3) **Wang, Y**., Hagen, E., Biswas, P., Wang, H., & Zachariah, M. R. (2023). Imaging the combustion characteristics of Al, B, and Ti composites. *Combustion and Flame*, *252*, 112747.

(4) Wang, H., **Wang, Y. (co-first author)**, & Zachariah, M. R. (2024). Observing coalescence of aluminum nanoparticles during burning using aluminum/ammonia perchlorate sandwiched films. *Combustion and Flame*, *260*, 113117.

(5) **Wang, Y.,** Shi, K., Issac Paul, G., Biswas, P., & Zachariah, M. R. (2024). Combustion behavior of aluminized metal iodate composites. Part 1: Decomposition mechanism of metal iodates. *Combustion and Flame*, *262*, 113372.

(6) **Wang, Y.,** Issac Paul, G., Hagen, E., Wang, H., & Zachariah, M. R. (2024). Combustion behavior of aluminized metal iodate composites. Part 2: Iodine and energy release rate. *Combustion and Flame, 262*, 113373.

(7) **Wang, Y.,** Issac Paul, G., Zachariah. M.R. Investigating the combustion behavior of Al/AP composites with high-speed videography. Under review in *International Journal of Energetic Materials and Chemical Propulsion.*

(8) Kumar Vasudevan. A., **Wang, Y. (co-first author)**, Biswas, P., Shi, K., Zachariah. M.R. Controlled Release of Diborane from Alkali Metal Borohydride using Ionic Liquid-Based Lewis Acids for Air Breathing Applications. Under review in *Angewandte Chemie.*

(9) Shi, K., **Wang, Y.(co-first author)**, Issac Paul, G., Zachariah. M.R. The Influence of Heat Feedback and Thermal Conductivity on the Burn Rate of Nanothermite Composites. Under review in *Combustion and Flame*.

(10) **Wang, Y.,** Xu, F., Issac Paul, G., Vidales Pasos, E., Shi, K., Wagner, B., Mangolini, L., Zachariah. M.R. Role of surface tension on heat feedback and power from energetic composites. Under review in *ACS Applied Materials & Interfaces*

(11) **Wang, Y.,** Chowdhury, M., Zhou, Y., Issac Paul, G., Shi, K., Zachariah. M.R. Oscillating-to-Continuous Combustion Transition in Mesoparticle Composites through Manipulation of Heat Feedback. Under review in *Advanced Functional Materials*

(12) **Wang, Y.,** Zhou, Y., Issac Paul, G., Miller Kelsea Quan, Tran., Jaramillo Nicholas. Pantoya, M., Zachariah. M.R. Replacing ammonium perchlorate with aluminum iodate hexahydrate for prolonged iodine and heat release from nanoenergetic composites. (*Under preparation*)